NUMERICAL MODELLING OF THE HUMAN ARTERIAL NETWORK IN CONJUNCTION WITH THE GTF TECHNIQUE TO IMPROVE CARDIOVASCULAR DIAGNOSTICS

Ahmed Tamkin Butt, B.Eng. (Hons)

A thesis submitted to the University of Nottingham for the Degree of Doctor of Philosophy

November 2018

ABSTRACT

The argument on the effectiveness of the Generalized Transfer Function (GTF) technique is currently ongoing. To resolve the dispute in experiment based studies, this thesis aims to use a well-validated numerical model as an alternative to experimental studies to test the validity of the GTF method. This thesis divides the work into four main inter-disciplinary areas of research.

Development of an existing non-linear one-dimensional (1-D) mathematical model that can comprehensively compute the propagation of blood in the human arterial network. The model developed was divided into large arteries and small arteries. The large arteries are based on physiological data while the small arteries were based on statistical relations. Instead of the more commonly used Windkessel model, the structured tree outflow boundary condition was used as the computation of pressure and flow in the small arteries provides a more dynamic and physiological boundary condition to the large arteries.

A multi-level validation of the developed model was undertaken in order to demonstrate the robustness and the applicability of the developed 1-D model to real life situations. The model was used to simulate pulse wave propagation along a single vessel (aorta) and the results compared against in-vivo data. The in-vivo systolic and diastolic pressures were 16.8 ± 0.4 kPa and 9.5 ± 0.4 kPa while the model estimated were 16.89 kPa and 10.94 kPa, respectively, showing excellent agreement. Simulation of pulse wave propagation in the entire arterial tree was then undertaken with two different geometries, from a 3-D model and physiological data. Comparison against the 3-D model showed a maximum percentage error of 2.5% while the excellent waveform amplitude and shape comparison with in-vivo data, confirmed the validity of the 1-D model.

The multi-level validation confirmed the robustness of the 1-D model to accurately simulate pulse propagation under varying geometric, elastic and fluid properties. This allowed the use of the 1-D model to create a database that recorded several different cardiovascular responses due to several

physiological and pathological conditions. The physiological conditions simulated were the variation in cardiac output and the variation in arterial stiffness while the pathological conditions simulated were abdominal aortic aneurysm and the coarctation of aorta. All physiological and pathological conditions agreed well with literature and were extremely well captured by the 1-D model.

Half of the pressure response database was used to estimate the GTFs between the ascending aorta and four different peripheral anatomical locations namely, the carotid artery, brachial artery, radial artery and the femoral artery. The estimated GTFs were multiplied with pulse pressures (PP) from the respective locations of the remaining half of the database and the yielding GTF-estimated Central Aortic Pressure (CAP) were statistically compared with the known, model-generated CAP to evaluate the validity of the GTF technique. The Pearson's r values for the carotid, brachial, radial and femoral artery generated CAP of 0.991, 0.981, 0.978 and 0.873 ($p < 0.001$), 0.996, 0.996, 0.993 and 0.971 ($p < 0.001$) and 0.999, 1.000, 1.000 and 0.934 ($p < 0.001$) for the systolic, diastolic and mean pressures, respectively, showed that the GTF technique is capable of estimating the CAP with extremely high accuracy. These results were further cemented by carrying out a Bland-Altman analysis as well as a linear regression which demonstrate that the GTF estimated CAP are highly correlated with model-generated CAP with the carotid artery being the most preferable and femoral artery being the least preferable site of PP measurement.

This thesis, in addition to comprehensively validating the 1-D model with structured tree outflow condition and demonstrating disease modelling, uses an alternative to experimental studies, which is free from human and calibration errors, to exhibit the accuracy of the GTF technique. The pressure response database created using the validated 1-D model for 194 physiological and pathological conditions introduces variations in PP as well as CAP. The GTFs estimated using half of these responses agrees well with GTFs found in literature and when put to test for CAP estimation using the remaining half of the responses, performs extremely well.

ACKNOWLEDGEMENTS

First and foremost, I am most grateful to almighty Allah who has blessed me with favorable circumstances in all walks of life and without whom none of this would be possible.

I would like to extend my heartiest gratitude to my former Supervisor, Dr. Yubing Shi for all the knowledge he shared with me and his ever so inspiring help throughout the time that I worked under him. I would also like to thank my current supervisors, Dr. Abakr and Dr. Mustapha whose patience, advice and insight enabled me to complete this thesis successfully. Their unending guidance and support has been a major driving force in completing this work.

I would like to acknowledge the help and support of Dr. Mette Olufsen and Dr. Umar Qureshi for providing me with reference codes and aiding me in implementing the structured tree outflow boundary condition.

I would also like to acknowledge the help and support I received from the technical staff of the University of Nottingham, especially Ms. Muna and Ms. Asyiqin.

A big thanks is in order for all my friends and teachers, past and present, for making me the person I am today and for always being extremely supportive.

My greatest appreciation and gratitude to the single most important blessing in my life, my fiancé, Maryam who supported me, taught me how to pick myself up when I was down and shared each and every joy with me in the best of times. I would not be here without her continued support and I am forever in debt for her kindness and compassion.

Finally, I would like to thank my parents and siblings for their support, patience and the sacrifices they have made throughout the course of my studies. None of the work done here would be meaningful or possible without my prayers parents.

TABLE OF CONTENTS

LIST OF JOURNAL PUBLICATIONS

- A. T. Butt, Y. A. Abakr, and K. B. Mustapha, “Blood Flow Modelling to Improve Cardiovascular Diagnostics : a Preliminary Review of 1-D Modelling,” Int. J. Eng. Technol., vol. 7, no. 4.26, pp. 25–34, 2018.
- A. T. Butt, Y. A. Abakr, and K. B. Mustapha, “Blood Flow Modeling to Improve Cardiovascular Diagnostics : Application of A GTF to Predict Central Aortic Pressure using a 1-D Model,” Int. J. Eng. Technol., vol. 7, no. 4.26, pp. 146–152, 2018.

RESEARCH AND TEACHING AWARDS

International Conference on Biomechanics and Medical Engineering (ICBME2018), Kuala Lumpur, Malaysia

- **Best paper award**- A.T. Butt, Y.A. Abakr, K.B. Mustapha "*Blood Flow Modelling to Improve Cardiovascular Diagnostics: Application of a GTF to Predict Central Aortic Pressure using a 1- D Model.*"
- **Best presenter award**- Ahmed Tamkin Butt, "*Blood Flow Modelling to Improve Cardiovascular Diagnostics: A Preliminary Review of 1-D Modelling*"
- **Best presenter award**- Ahmed Tamkin Butt, "*Blood Flow Modelling to Improve Cardiovascular Diagnostics: Application of a GTF to Predict Central Aortic Pressure using a 1- D Model.*"

University of Nottingham Malaysia, Student's Association awards. Kuala Lumpur, Malaysia

- **Best Research/Teaching assistant award** (2016).
- **Best Teaching assistant/ Lecturer award** (2017).

LIST OF FIGURES

LIST OF TABLES

LIST OF ABBREVIATIONS

0-D	0-dimensional
1-D	1-dimensional
2-D	2-dimensional
3-D	3-dimensional
AAA	Abdominal Aortic Aneurysm
BC	Boundary Condition
CAP	Central aortic Pressure
cine PC-MRI	Cine Phase Contrast Magnetic Resonance Imaging
CO	Cardiac Output
CoA	Coarctation of Aorta
CR	Compliance-Resistance
CVD	Cardiovascular Disease
DCAP	Derivation Central Aortic Pressure
DFT	Discrete Fourier Transform
DP	Diastolic Pressure
DPP	Derivation Peripheral Pressure
ECAP	Estimated Central Aortic Pressure
EDP	Estimated Diastolic Pressure
EMP	Estimated Mean Pressure
ESP	Estimated Systolic Pressure
FDM	Finite Difference Method
FEM	Finite Element Method
FVM	Finite Volume Method

GTF	Generalized Transfer Function
HR	Heart Rate
IC	Initial Condition
IDFT	Inverse Discrete Fourier Transform
ISH	Isolated Systolic Hypertension
ITF	Individualized Transfer Function
LA	Left Atrium
LV	Left Ventricle
MP	Mean Pressure
ODE	Ordinary Differential Equation
PDE	Partial Differential Equation
PP	Pulse Pressure
RA	Right Atrium
RCR	Resistance-Compliance-Resistance
RV	Right Ventricle
SP	Systolic Pressure
SV	Stroke Volume
TF	Transfer Function
VCAP	Validation Central Aortic Pressure
VDP	Validated Diastolic Pressure
VMP	Validated Mean Pressure
VPP	Validation Peripheral Pressure
VSP	Validated Systolic Pressure
WIA	Wave Intensity Analysis

LIST OF SYMBOLS

$\pm$	Plus-minus sign
%	Percent
$<$	Less than
$>$	Greater than
$=$	Equal
$\geq$	Greater than or equal to
∞	Infinity
$\boldsymbol{A}$	Area
$\boldsymbol{A_0}$	Unstressed Area
$\boldsymbol{\alpha}$	Scaling factor
$\boldsymbol{a}$	Integration constant
$\boldsymbol{\beta}$	Scaling factor
$\boldsymbol{b}$	Integration constant
$\boldsymbol{cm}$	Centimeter
$\boldsymbol{C}$	Compliance
$\boldsymbol{\Delta}$	Difference
$\boldsymbol{\delta}$	Boundary layer thickness
$\boldsymbol{e}$	Exponential function
$\boldsymbol{E}$	Young's Modulus
$\boldsymbol{\eta}$	Cross sectional area ratio
$\boldsymbol{g}$	Gram
$\boldsymbol{\gamma}$	Asymmetry ratio
$\boldsymbol{h}$	Vessel wall thickness
$\boldsymbol{H_{A-B}}$	Transfer function between locations A and B
$\boldsymbol{Hz}$	Hertz
$\boldsymbol{I}$	Current
$\boldsymbol{i}$	Imaginary unit
$\boldsymbol{J_0}$	Bessel function of the first kind and zero order
$\boldsymbol{J_1}$	Bessel function of the first kind and first order
$\boldsymbol{kPa}$	kilopascal

k_n	Vessel Elastic properties parameter
k	Wave number
kg	Kilogram
L	Length
l	Liter
lrr	Length to radius ratio
$\lim$	Limit of a function
log	Logarithm
M	Magnitude
m	Meter
mm	Millimeter
$mmHg$	Millimeters of mercury
min	Minute
ml	Milliliter
μ	Dynamic viscosity
v	Kinematic viscosity
ω	Angular Frequency
p	Pressure
p_0	Nominal pressure
P_S	Systolic pressure
P_D	Diastolic pressure
P_m	Mean pressure
Pa	Pascal
π	Pi
φ	Phase
Q_{in}	Flow at inlet
Q_0	Peak flow value
q	Flow
$\mathcal{R}$	Reynolds number
R	Resistance
r	Radius
r_0	Unstressed radius

r_{min}	Minimum radius
rad	Radians
ρ	Densiy
s	second
T	Time period
t	Time
τ	Time parameter that marks the end of systole
u_x	Longitudinal velocity
$\mathbf{V}$	Volume
w_0	Womersley number
x	Spatial position
ξ	Radius exponent
Z	Impedance

CHAPTER 1

INTRODUCTION

1.1 Background

As per the World Health Organization, cardiovascular diseases are the leading cause of death globally [1]. Hypertension is now identified as the single most important cause of mortality worldwide [2] and by 2025 it is predicted that 1.56 billion people will suffer from hypertension [3]. 30% of all deaths annually are due to cardiovascular diseases; the actual number of deaths lies somewhere between 17 to 18 million. This percentage is expected to increase in the future due to the lifestyle of the modern age. Indeed, the number of deaths annually due to cardiovascular diseases is estimated to be an alarming 23.6 million in 2030 [1], [4].

In clinical diagnoses, a very important physiological index is blood pressure. The central aortic pressure (blood pressure at the aortic root) represents the systemic after load on the heart. However, measuring the central aortic pressure in routine clinical practice is tedious, expensive and invasive and has to be approximated using blood pressures measured non-invasively from peripheral locations. Some tools and techniques used include sphygmomanometer (Blood pressure cuff), carotid artery tonometry [5]–[7] and brachial oscillometry [8]–[11]. There has been an increased interest in measuring the relationship between the central aortic pressure and peripheral pressure (for instance brachial, radial, carotid, femoral arteries) due to systolic hypertension being recognized as a risk factor for cardiovascular diseases [12]–[16].

Previous research has shown that the waveforms of peripherally measured pressure and central aortic pressures are significantly different in regards to the wave shapes as well as amplitude [17] and these differences are intensified in more critical, diseased conditions. This makes peripheral pressure an unreliable measurement of blood pressure in clinical diagnosis. It has been demonstrated

that the peripheral systolic pressure when compared to central aortic pressure is 11-22 mmHg higher [13]. It has also been shown that a number of blood pressure-lowering drugs have similar effects on the peripheral pressure but very different effects on the central aortic pressure [18], implying that central aortic pressure is a better indicator physiologically for diagnosing diseases [19]–[21] making it's measurement an absolute must.

1.2 Problem statement

In view of the findings described in the previous section, a statistics-based technique called the generalized transfer function (GTF) technique was proposed [13], [22]. This population-based technique allows estimation of central aortic pressure from peripheral pressure measured non-invasively. Multiple central and peripheral pressures undergo a Fourier analysis and a generalized transfer function is calculated. The central pressures of individual patients can be estimated by simply multiplying this GTF with the peripheral pressures of these patients in the frequency domain and converting the result back to the time domain [23]–[28]. The patent to this technique [29] is in use of SphygmoCor® system (SphygmoCor®,AtCor Medical, West Ryde, NSW, Australia), a commercially available blood pressure measurement equipment. However, there has been some debate that the general transfer function varies from person-to-person due to a variety of physiological differences, making the general transfer function an unreliable tool of choice in such analyses as it lacks adaptability [30]–[32]. Cloud et al. [31] undertook a study with 30 patients and found that the SphygmoCor® system underestimated the systolic central aortic pressure and overestimated the diastolic central aortic pressure by 13.3mmHg and 11.5mmHg, respectively. To put things into perspective, a blood pressure measuring equipment should not have a standard deviation greater than ±8mmHg [33]. Consequently, individualized transfer functions (ITF) were introduced to account for individual differences amongst patients [34]–[37], and although promising, they still lack complete personalization.

With the on-going disagreement between the research groups for and against the GTF technique, it is essential to use an independent method to test the GTF technique, which also serves as an alternative to experimental studies. Numerical modeling provides such an alternative research method. Pressure changes in arteries can be more accurately analyzed by deriving and solving the mathematical equations that govern the pressure wave dynamics in the arteries [38]. This can serve as the judging tool to check the validity of the transfer function method.

Numerical modeling has been used comprehensively, to investigate a diverse range of problems in the study of cardiovascular dynamics. Research has already been carried out using numerical modelling of the pulse wave propagation to study the changes in flow as it goes from the heart towards the peripheral arteries. Stergiopulos et al.[39] used peripheral pressure and velocity to model the pulse wave transmission effect in a vessel segment. Based on the reflection coefficient in the periphery and the time taken for pulse wave transmission, a transfer function was defined that relates the central and peripheral pressures. Since the simulation is carried out on a vessel segment, it does not provide information about pressure in other parts of the arterial network. Segers et al. [40] and Thore et al. [41] used transmission line models to simulate pulse wave dynamics. Another study conducted by Jiang et al [42] extends the electrical circuits analogy to the entire human arterial network to predict the central aortic pressure. Although the entire network is simulated, the analogy to electrical circuits does not represent wave propagation effects satisfactorily. Additionally, important parameters such as Young's modulus, vascular thickness and cross sectional areas of the arteries are assumed constant, which is not the case in physiological conditions.

All these studies use simplified models that either do not take into consideration material, geometric and flow non-linearities such as inhomogeneous vessel wall elasticity, vessel tapering etc. or consider stand-alone simulation cases. To our knowledge, a full-scale cardiovascular model that incorporates non-linearities as well, has not been used to systematically evaluate the GTF technique.

1.3 Aims and objectives

The aim of this work is to conduct an independent evaluation of the GTF technique using a comprehensive numerical model that is well validated and can accurately represent blood flow in the arterial network under physiological conditions while incorporating non-linearities of blood flow propagation. The motivation behind using such a model is twofold. Firstly, to improve the evaluation of the GTF technique by using a comprehensive model rather than an isolated or simplified model. Secondly, majority of the previous researches conducted to evaluate the GTF technique were experimental, raising questions about the accuracy of the equipment used as well as the errors arising due to calibration procedures. This model provides an alternative to experimental studies for said evaluation.

In order to achieve these aims, the work here was broken down into specific objectives which are as follows:

- Mathematical Modelling (Chapter 4)- Developing a one-dimensional fluid dynamical model that takes into consideration realistic features of blood flow propagation such as vessel tapering, vessel branching, inhomogeneous vessel wall elasticity etc.
- Numerical validation (Chapter 5) - Carrying out a systematic, multi-level validation against data published in literature to increase the reliability of the code and its capability to simulate various clinical conditions.
- Parametric study (Chapter 6) - Conducting a parametric study of the one-dimensional model to simulate various physiological and pathological conditions, to create a pressure response data.
- GTF estimation (Chapter 7) - Carrying out a Fourier analysis on half of the central and peripheral pressure response data to estimate transfer functions between ascending aorta and multiple physiological peripheral locations.

- CAP reconstruction (Chapter 7) - Using the estimated GTFs to estimate central aortic waveforms from multiple peripheral locations for the remaining half of the pressure response database.
- Validity test (Chapter 7) - Carrying out a statistical analysis on the GTF estimated central aortic waveforms to test the validity of the GTF technique.

1.4 Research scope

The scope of this study is restricted to the deployment of a 1-D numerical model to simulate the propagation of blood flow in large systemic arteries. Downstream boundary conditions are defined using a structured tree outflow condition proposed by Olufsen et al [43]. This boundary condition solves linearized governing equations of blood flow in the tree of small arteries and finds the impedance at the root of this tree. This impedance then provides a physiological boundary condition at the distal ends of large arteries and represents the resistance to flow due to downstream vasculature. Blood is assumed as a Newtonian fluid throughout the study, which is justified in the large arteries as will be seen in later sections. The geometry of large systemic arteries is based on physiological data. Since the physiological geometric properties of capillaries and small arteries is hard to measure, the small arteries are based on statistical relations while the model does not encompass capillaries. Additionally, the blood in capillaries can not be assumed Newtonian. Considering that modelling capillaries and the entire arterial system is not computationally feasible and detailed data on their properties is still largely unknown, the model has to be truncated at some point which justifies the use of the given boundary condition. More importantly, the main aim of this work is to test the validity of the GTF technique, which is used only in systemic arteries to estimate CAP from peripheral pressures in large systemic arteries. Hence, the venous system, pulmonary circulation and cerebral circulations are not investigated/ included in this study. The GTF technique despite being a population based statistical technique is evaluated by using a virtual

database created using the 1-D model, the implication being that actual human patient is not used. However, a primary objective is to use an alternative to experimental studies to test the validity of the GTF technique, in doing so the inherent errors of experimental studies are removed.

1.5 Organization of thesis

This work is organized into eight chapters and two appendices. A summary is provided at the end of each chapter, reiterating the key points from each chapter. The outline of these chapters is as follows:

Chapter 1: Introduction

This chapter provides a formal background and general introduction to the problem and how the problem is addressed via specific aims and objectives.

Chapter 2: Physiological basis and mechanical idealization of the cardiovascular system

This chapter provides a review of the anatomy and physiology of blood flow in the human cardiovascular system

Chapter 3: Numerical modelling of the cardiovascular system: Review of one-dimensional modelling

This chapter provides a critical review of the literature available on the numerical modelling of the cardiovascular system with special focus on 1-D modelling.

Chapter 4: Mathematical model of the arterial network

This chapter provides the details of the mathematical formulation used to simulate blood flow in the large and small arteries and modelling its interaction with the elastic walls of vessels. It also describes the boundary conditions used to extend the governing equations to an entire arterial network and the numerical method used to solve the equations.

Chapter 5: One-dimensional model validation

This chapter provides an in-depth, multi-level validation of the 1-D model. The model results are compared with models published in literature as well as in-vivo data found in literature.

Chapter 6: Physiological and pathological pressure response database

This chapter provides the details of the parameters used for the 1-D model parametric study to simulate various physiological and pathological conditions. The results from each study are then used to create a pressure response database.

Chapter 7: Generalized Transfer Function

This chapter provides details of how the pressure response database is used to estimate GTFs between the central aortic waveforms and waveforms from multiple peripheral anatomical locations. The estimated GTFs are then used to estimate CAP waveforms. A statistical analysis is then carried out to test the validity of the GTF technique.

Chapter 8: Conclusions and perspectives

This chapter summarizes the achievements of this work and discusses the limitation of this study while recommending potential future work.

Appendix A Fluid and Elastic parameters for the 1-D model

Provides the parameters used to simulate various models.

Appendix B Work flow of 1-D model simulations

Provides a pseudocode for the simulations carried out to setup the arterial network.

Appendix C Matlab routines for data extraction and GTF estimation

Provides the Matlab programs used to generate estimated central aortic waveforms via the GTF technique.

CHAPTER 2

PHYSIOLOGICAL BASIS AND MECHANICAL IDEALIZATION OF THE CARDIOVASCULAR SYSTEM

2.1 Introduction

This chapter details the physiological description of the cardiovascular system. The workings of the heart (2.2.1) are explained followed by an elaboration of the hierarchy of blood vessels (2.2.3). 2.2.4 pays special attention to the systemic arteries of the circulation, as these are the arteries of interest in this work. 2.2.5 presents the structure of blood and justifies the assumptions about blood. 2.3 gives an overview of the propagation of blood and how the fluid and the structures interact during blood propagation. Finally, 2.4 summarizes the entire chapter and presents the research gap in a concise manner.

2.2 Cardiovascular system

At its core, the cardiovascular system consists of a cardiac pump (the heart), circulatory network (blood vessels) and the fluid (blood). This system is responsible for the transport of nutrients and Oxygen among the several organs of the mammalian body through the convective transport of blood. This convective transport of blood has two main purposes; the first is to allow for the diffusive transport of oxygen and other nutrients to the tissues and the second is to remove carbon dioxide and harmful waste products from the tissues. These waste products are a result of cell metabolism. Due to the large diffusional resistance, this interchange of nutrients would not be possible without the convective transport [44]. The cardiovascular system can be further divided into two systems; namely the systemic circulation and pulmonary circulation, with the heart being at the helm of both these systems. (**Fig. 2-1**)

The systemic circulation starts at the left ventricle and ends at the right atrium, while the pulmonary circulation originates at the right ventricle and ends at the left atrium. To fully comprehend these systems, it is first necessary to understand the basic functioning of the heart.

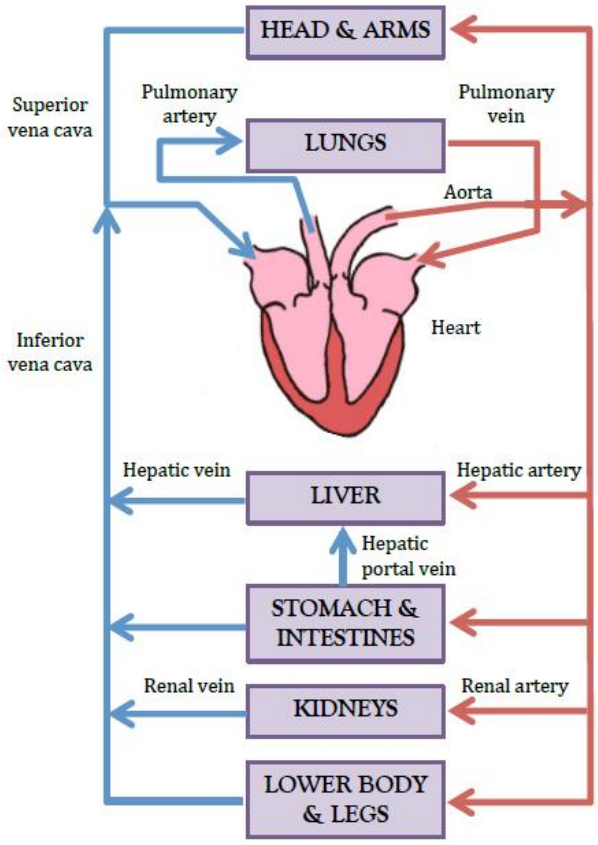

Fig. 2-1: Schematic of the cardiovascular system. Red arrows represent vessels carrying oxygenated blood while blue arrows represent vessels carrying deoxygenated blood Taken from [45].

2.2.1 The heart

The heart, essentially, consists of two synchronized pumps that are parallel to each other (the left and the right heart). Both of them comprise of two chambers each; the upper ones are called the atria (right and left atrium) while the lower chambers are called the ventricles (right and left ventricle).

At the end of each chamber, there is a valve. These valves regulate blood flow and ensure that the blood only flows in one direction [46]. All four chambers and their corresponding valves can be seen in **Fig. 2-2**

Blood enters the right atrium (RA) via the Venae Cavae. This is the point of entry of the blood into the heart. The blood that enters the right atrium is deoxygenated blood, this is the blood that has transported its oxygen to the organs and is returning to the heart with the carbon dioxide it removed from these organs. From the right atrium, the blood goes into the right ventricle (RV) and from this point on, the pulmonary circulation begins. The objective of the pulmonary circulation is to transport deoxygenated blood to the lung tissues, where a gaseous exchange takes place; the blood picks up oxygen and the lungs remove the carbon dioxide from the blood. This gaseous exchange is known as respiration. Once the blood is oxygenated, it is transported to the left atrium (LA) via the pulmonary vein. The oxygenated blood is now ready to be transported from the left atrium to the rest of the body thus concluding the pulmonary circulation.

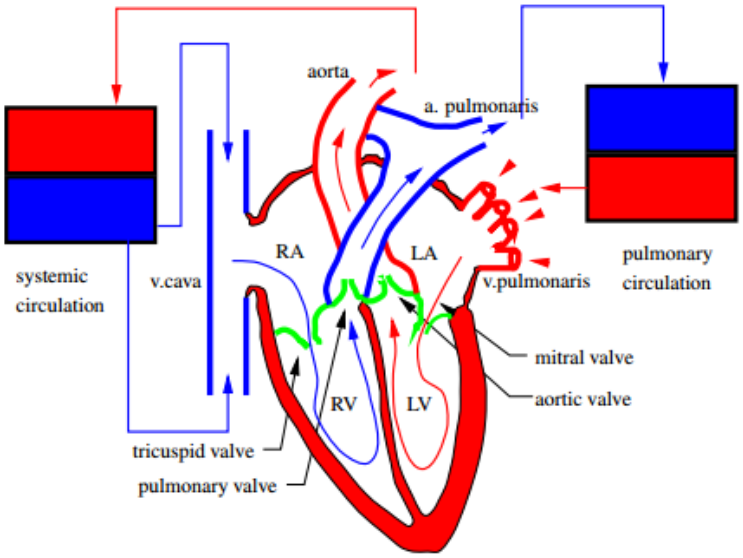

Fig. 2-2: Schematic representation of the heart and the circulatory system [44].

The blood flows from the left atrium to the left ventricle (LV) and at this point, the systemic circulation is put into motion. The blood flows from the left ventricle into the aorta and the rest of the body. The objective of the systemic circulation is to transport oxygen rich blood to all the organs and tissues. When the blood reaches an organ, it exchanges oxygen with carbon dioxide. Once the gaseous exchange with all the organs is complete, the deoxygenated blood goes back in the right atrium and the whole process starts again. This concludes one cardiac cycle or one cycle of systemic and pulmonary circulation.

Fig. 2-3 is a diagrammatic representation of the route taken by the blood in one cardiac cycle.

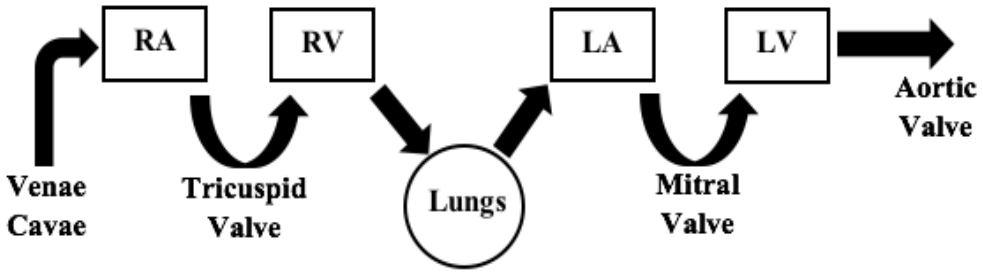

Fig. 2-3: Block diagram illustration of the route taken by the blood.

2.2.2 Cardiac Cycle

A single cardiac cycle comprises of two phases namely systole and diastole. When the blood is in the left atrium, the heart muscles contract causing the blood to flow from the left atrium to the left ventricle. Once the blood flows into the left ventricle, the valve between the left atrium and ventricle, the mitral valve, closes so that none of the blood flows back into the left atrium. Consequently, the pressure in the left ventricle increases until a certain pressure level called the aortic pressure is reached. At this pressure, the valve between the left ventricle and ascending aorta, the aortic valve, opens and a large amount of blood is ejected into the aorta at a high flow rate. This is known as the systolic phase or simply systole.

When the pressure in the left ventricle falls below the aortic pressure, the aortic valve shuts and remains shut until the next cardiac cycle. This is known as the diastolic phase or simply diastole. During diastole, the heart muscles relax and the blood moves from the atrium into the ventricular cavity.

The systole and diastole alternate and repeat periodically. This is what produces the "lub" "dub" sounds. The lub being systole and dub being diastole. It is the periodic repetition of a high outflow and no outflow which in turn, leads to flow and pressure pulsations in the arteries [47]. Under resting conditions, systole constitutes one-third of the cardiac cycle (about 0.25s) while diastole contributes to the remaining two-thirds (about 0.55s) [48]. The systolic and diastolic pressure are the measurements taken in a routine blood pressure checkup. This cardiac cycle is better presented with the aid of **Fig. 2-4**.

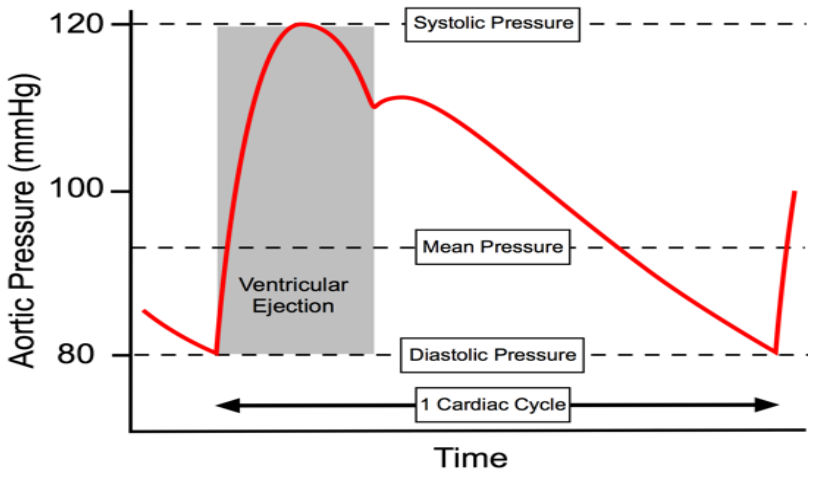

Fig. 2-4: A cardiac cycle representing the Systolic, Diastolic and Mean Pressures in the Aorta [49].

Diastole takes approximately twice the time as systole. In a healthy human being, the cardiac cycle lasts about 0.8s, which equates to 75 beats per minute. In each stroke, the left ventricle ejects approximately 70ml of blood into the ascending aorta [50]. This is known as the stroke volume (SV).

Based on these values, two important terms can be defined now; the heart rate (HR*)*, which is the number of times the heart beats per minute and the cardiac output (CO), which is the amount of blood pumped by the heart per minute. It has already been established that the heart rate is 75 beats/min which yields a cardiac output of 5 l/min (CO=SV x HR) [50].

2.2.3 Venous system

The organization of systemic and pulmonary circulation is very similar, in that they both have an arterial part (arteries) and a venous part (veins). The arteries (with the exception of pulmonary artery) take oxygenated blood from the heart to the tissues while the veins (with the exception of pulmonary vein) take deoxygenated blood away from the tissues and into the heart.

Branches and networks of vessels constitute and aid the cardiovascular system. The size of these vessels and their geometrical properties vary [51]. The aorta is the largest artery. In order to understand how the nutrient exchange between the blood and the organ/tissue takes place, it is necessary to understand the hierarchy of these blood vessels.

The large arteries branch repeatedly into smaller arteries that continue to branch further into even smaller vessels called arterioles. The arterioles branch into even smaller vessels called capillaries. Due to the branching of the arterial network, the number of vessels increases away from the heart, therefore the collective cross-sectional area increases downstream. The branching of the arterial network ensures the flow of blood is slowed down. Additionally, vascular resistance increases downstream to aid the slowing down of blood flow.

Capillaries are the smallest of the blood vessels and they merge into venules. The venules converge into small veins that ultimately converge into the larger vessels called veins.

These vessels can be divided into the arterial system, capillary system and venous system. ***Table 2-1*** summarizes the functions of the different types of systems and the vessels in them [48], [52].

Table 2-1: Different Vessels and their functions.

System	Vessels	Function
Arterial system	Arteries	Distribute oxygenated blood throughout body and maintain blood pressure between heartbeats
Capillary system	Arterioles	Transport blood to capillary beds from arteries
	Capillaries	Diffuse oxygen and nutrients to cells of the organ
	Venules	Collect deoxygenated blood from capillaries
Venous system	Veins	Return deoxygenated blood to the heart

For the exchange of nutrients and oxygen to occur, the blood first goes from arteries to arterioles and from there on into a network of capillaries that cover all organs/tissues. The arterioles act as control valves between the arteries and capillaries. The purpose of these control valves is to regulate the amount of blood flowing into the capillaries in response to the needs of a certain organ [47]. This is why the arterioles are theoretically resistance vessels [53], consequently they exhibit the largest pressure drop.

The permeability of the capillary walls is enough to let small molecules diffuse across. Through the walls of the capillaries the oxygen, hormones and nutrients from the blood are diffused to the interstitial fluid of the cells of the organ while removing carbon dioxide and other waste products of cell metabolism. The blood that now contains the waste products and carbon dioxide is collected by the venules from the capillaries and is transported back to the heart via larger veins. The larger

veins take the deoxygenated blood to the heart and the pulmonary circulation begins. **Fig. 2-5** shows how the exchange of nutrients takes place with a tissue.

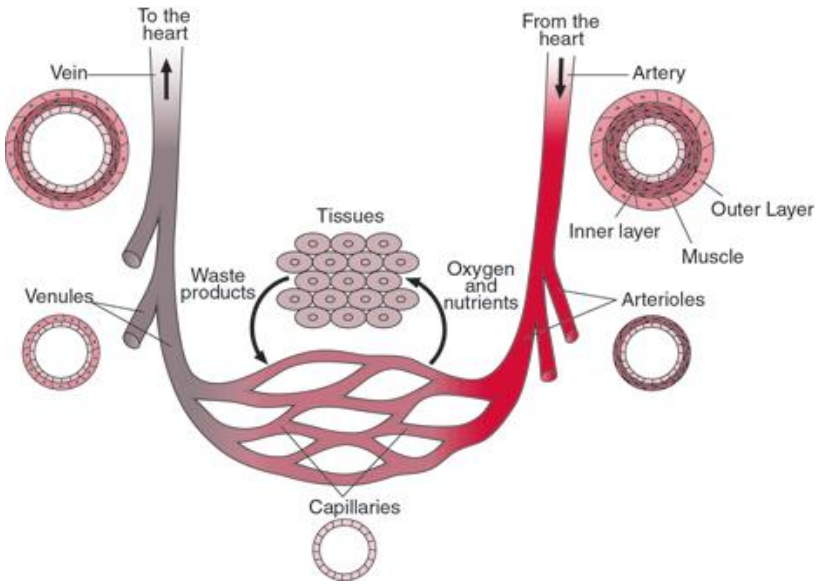

Fig. 2-5: The exchange of nutrients between the capillaries and the tissues. The artery brings oxygen and nutrient rich blood and to the capillaries. The vein takes waste products from the capillaries and transports them back to the heart [54].

It is abundantly clear that all the vessels need to be well adapted in order to carry out their function. This is the reason why the vessels in the arterial, capillary and venous system have varying geometrical and mechanical properties.

From **Fig. 2-6**, it can be seen that the vessels of the capillary system have the smallest diameter **Fig. 2-6 (A)** and the greatest cross-sectional areas **Fig. 2-6 (B)** to help in diffusing the nutrients and oxygen to the surrounding tissue. The large number of vessels in the capillary system **Fig. 2-6 (E)** is because these vessels need to be distributed in a structured way so that they can cover the tissue

evenly by minimizing their volume and maximizing their surface, again to facilitate the diffusion of oxygen and nutrients [55].

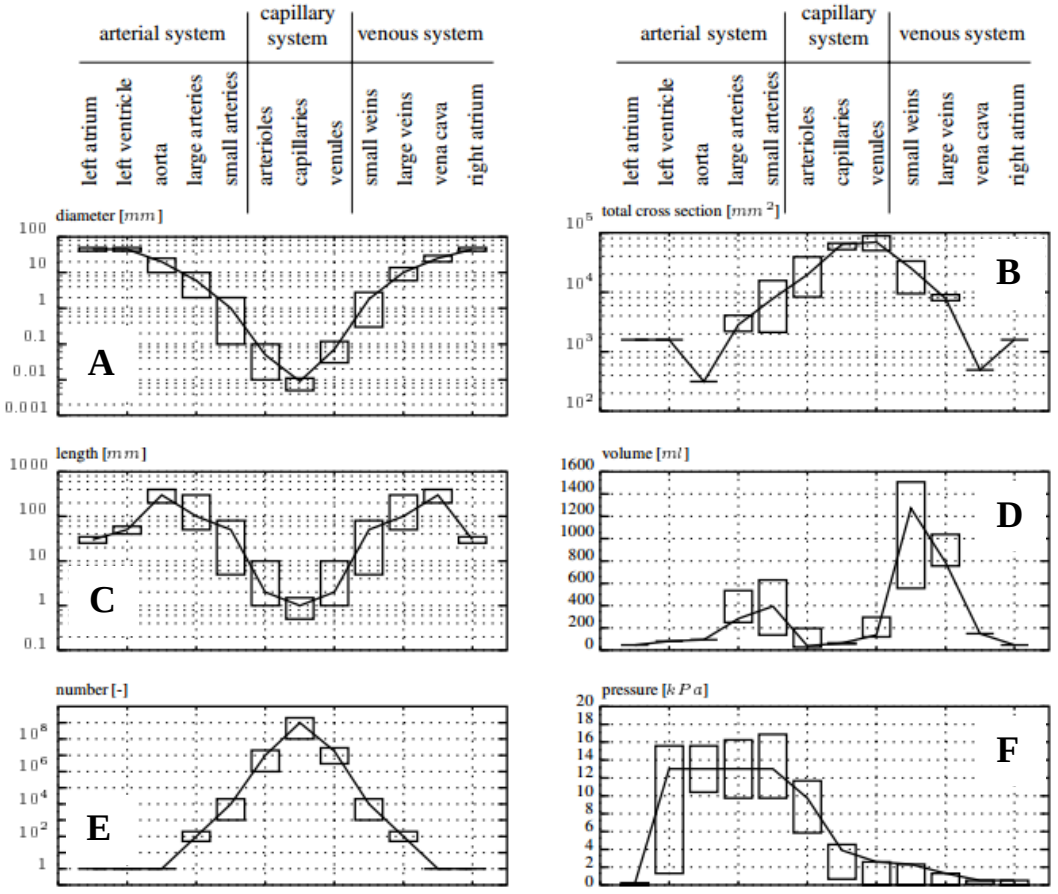

Fig. 2-6: Rough estimates of the diameter, length and number of vessels, their total cross-section and volume and the pressure in the vascular system [44].

As mentioned before, the oxygenated blood ejected by the heart is transported to the organs via the arterial system. Naturally, the pressure in the systemic arteries is much higher as compared to the rest of the veins and capillaries. The higher pressure in larger arteries can be seen in the **Fig. 2-6 (F)** Lastly from the figure **Fig. 2-6 (D)** it can be seen that the large veins have the highest blood volume. This implies that veins, in addition to transporting deoxygenated blood back to the heart,

also act as a reservoir. Due to their size and abundance, veins and venules contain about two-thirds of the blood at any given instance.

2.2.4 Systemic Arteries and their elastic properties

Systemic arteries are the ones responsible for delivering oxygenated blood to all the organs. Larger arteries, smaller arteries and arterioles constitute the systemic arteries by forming a network of branching vessels (**Fig. 2-8**).

Arterial walls consist of three layers (**Fig. 2-7**):

The innermost layer is known as the tunica intima. This layer is composed of a thin basal lamina, a sub endothelial layer and a layer of endothelial cells. Smooth muscle cells, fibroblasts and collagen constitute the sub endothelial layer. The circular cavity in which the blood flows is called the lumen. The purpose of this layer is to ensure plasma does not seep in through the wall of the vessel [52].

The middle layer is called the tunica media. This layer consists of smooth muscle and elastic (elastin and collagen) and is responsible for the ability to contract and the mechanical strength of the vessel [52].

The strong outer covering is known as the tunica adventitia. This layer consists of fibro elastic tissues. This layer regulates the local flow by regulating the local resistance [52].

Elastin is the primary factor in determining the dynamics of blood flow. It allows temporary blood storage in the large arteries in each heartbeat by expanding to accommodate the surge of blood from the heart. While expanding, elastin stores the mechanical energy. During diastole, when the heart stops ejecting blood, this stored mechanical energy is used to overcome the downstream resistance to keep the blood flowing in the smaller vessels while maintaining the blood pressure above the diastolic pressure (80 mmHg). On the other hand, collagen is not as distensible as elastin and its purpose is to ensure the vessels do not expand excessively when the blood pressures increases.

Each layer of the arteries comprises of cells that serve different roles in order to accommodate the flow of blood in different parts of the body. The variation in the proportion of the three layers is dependent on the location and size of the vessel. Due to the varying amounts of elastic fibres and muscles, arteries are able to expand and contract to accommodate the pulsation of blood propagation. This complex composition of arterial walls make its elastic properties non-linear [56]. The behavior of the arteries is not purely elastic, in fact, arteries exhibit some viscoelastic behavior [47]. However, the effects of viscoelasticity under physiological conditions are small [57].

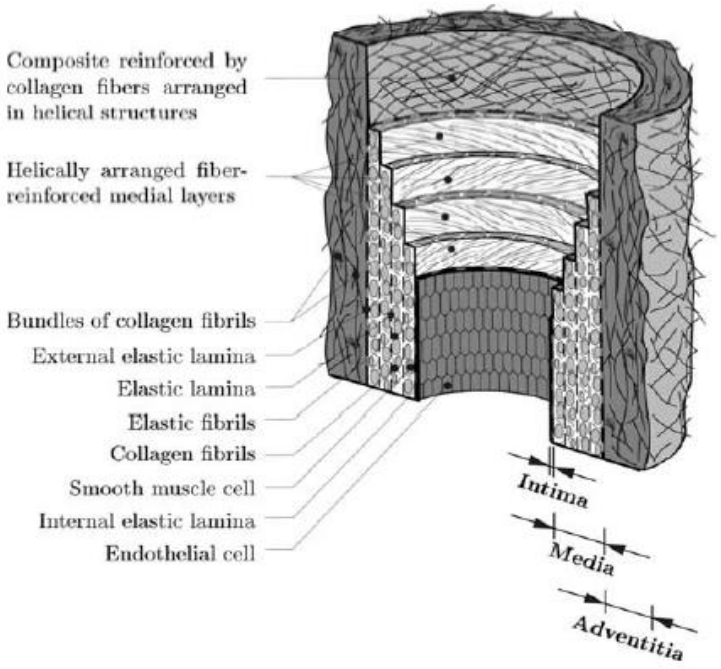

Fig. 2-7: Cross section of an artery [58].

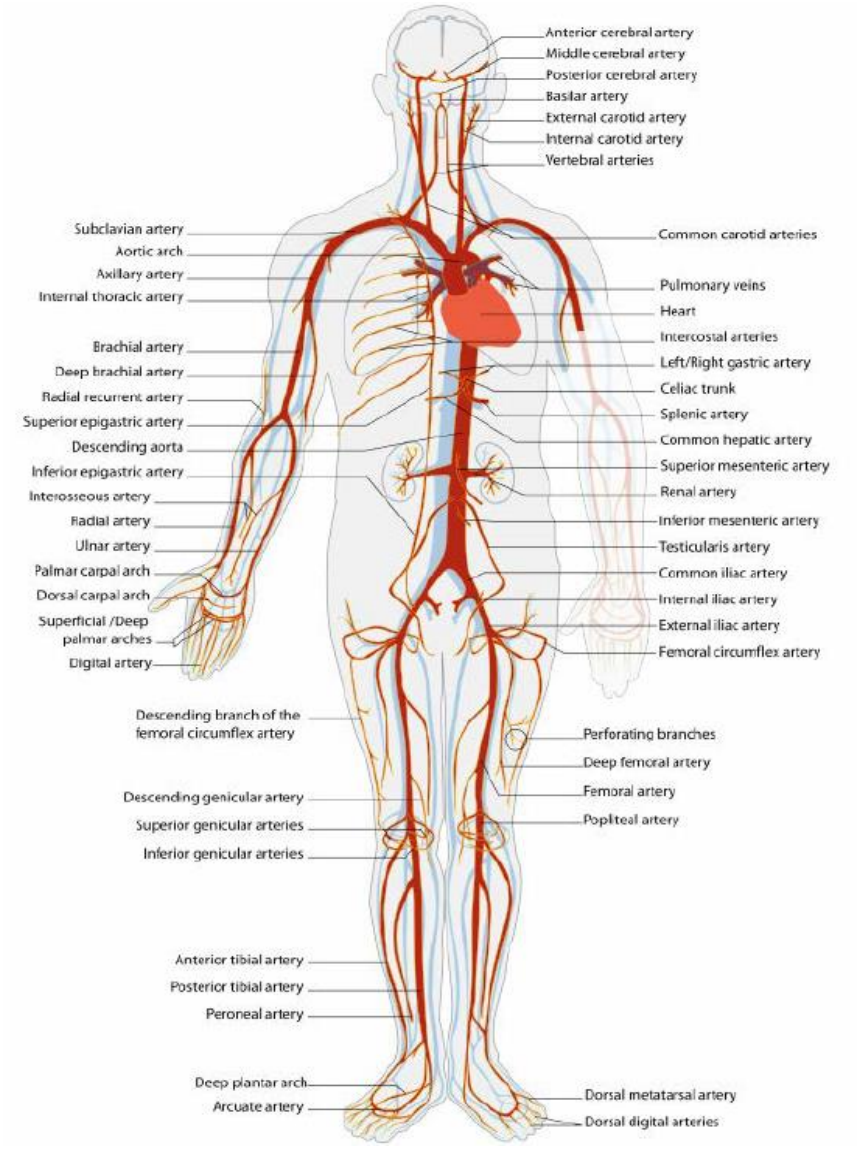

Fig. 2-8: The systemic arteries [59].

The structure of the systemic arteries changes gradually from larger arteries to the smaller arterioles. According to Wheater et al, [60] as the arteries become smaller, the elastic tissues decrease, while the smooth muscles become more prominent. The implication being that elastin and collagen decrease downstream. Due to this, the arteries become stiffer (their Young's modulus increases) as

the distance from the heart increases. These changes in stiffness regulate blood flow and are an important aspect to be considered while modelling blood flow.

Aging leads to a decrease in elastin overtime and an increase in collagen build up. Therefore, collagen contributes more to the elastic properties of vessels with aging. As mentioned earlier, collagen is not as distensible as elastin (approximately 100 times lesser) hence with aging; vessels tend to become stiffer, a process known as arteriosclerosis. [61]

2.2.5 Mechano-physical properties of the blood

Blood is a fluid in which various nutrients, cells, waste materials and hormones are dissolved. All these are exchanged with various tissues in the body as the blood flows through the venous system, as discussed earlier. The fluid part of blood is plasma. Blood has been consistently recognized as a non-Newtonian fluid because, although, plasma is Newtonian [62], red blood cells are suspended in plasma making blood non-Newtonian. This implies that the viscosity is dependent on shear rate [63], [64]. However, for flow in larger arteries (systemic circulation), the diameters of large arteries is large compared to the suspended particles in blood. Additionally, the viscosity is independent of the shear rates because the shear rates are high in larger vessels [47]. This makes the non-Newtonian behavior of blood inconsequential in larger vessels. Hence, blood is treated as a Newtonian fluid in numerical modelling of systemic arteries. According to Pedley, [65] blood can be approximated as a homogeneous and incompressible fluid[1] as 90% of plasma is water and the nutrients and cells in the plasma are much smaller than the diameter of the arteries. Usually, the density of blood is taken as $\rho = 1055\ Kg/m^3$ while the viscosity is $\mu = 4.0\ mPas$.

[1] Note: here that these assumptions are valid for large systematic arteries, which will be the only ones, being considered in this work.

2.3 Pressure and flow propagation of the blood

As seen in earlier sections, flow waves are generated due to the ejection of blood from the left ventricle and the interaction of this ejection with the flexible (distensible) arterial walls. Since blood is assumed as an incompressible fluid, it implies that the arteries have to be elastic to accommodate the flow of increased blood volume caused when the heart muscles contract. Due to the distension of the vessels, the pressure and flow of blood within the artery keeps changing. The vessels expand when blood pressure increases during systole and store elastic energy, and contract when they release the absorbed elastic energy during diastole when the pressure decreases. This contraction and expansion initiates a continuous and regular beating (pulse). These variations can be studied as flow and pressure waves running forwards and backwards. Backward waves are generated due to reflections of forward running waves. (**Fig. 2-9**) The speed of propagation is such that the pulse wave has ample time to travel to the peripheral arterioles from the aorta and be reflected back to the heart multiple times during a heartbeat.

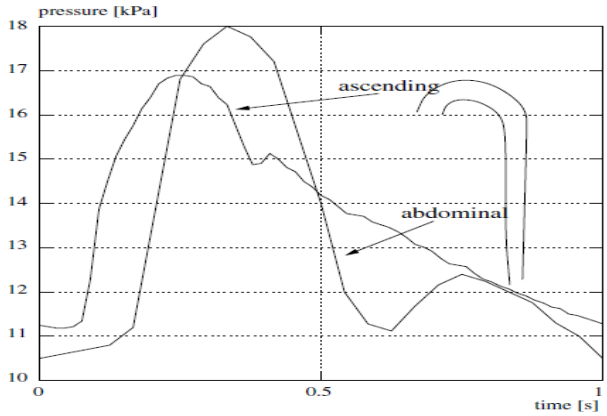

Fig. 2-9: Pressure at two different sites in the aorta [44].

It will be shown in future sections that the velocity of the pulse wave depends on the stiffness (Elastic Modulus or Young's modulus) of the arterial wall. The cross sectional area of the vessel walls

depends on the pressure difference over the wall [44]. Due to the nonlinear anisotropic properties of the arterial walls, the relation between area and pressure is also nonlinear.

The elasticity of the arteries also causes the pressure and flow to be smooth in the arterial system. Had these arteries been rigid, the blood flow rate into and out of the system would be equal hence during diastole the blood flow would be zero. This smoothing mechanism was first described by Reverend Stephen Hales (1677-1761) and is called the Windkessel effect [66]. Hales compared the arterial system and the heart to a medieval fire cart. In this comparison, the air-filled chamber is analogous to the compliance of the arteries and the fire hose nozzle represents the peripheral resistance (**Fig. 2-10**).

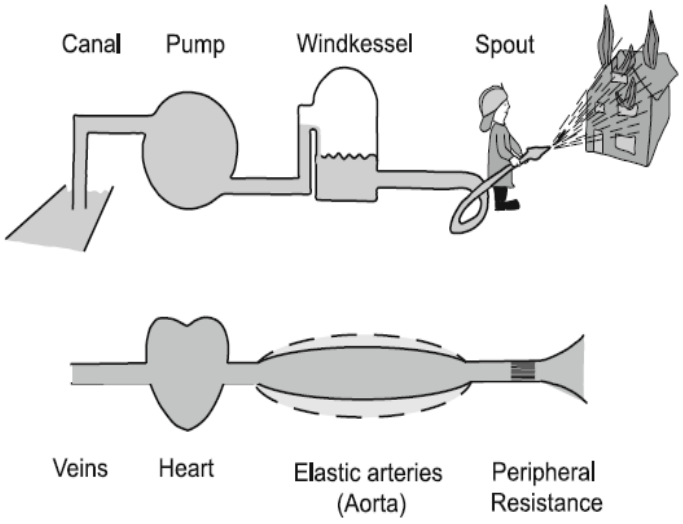

Fig. 2-10: The Windkessel concept. Large arteries are analogous to the air chamber (acts as the Windkessel) [66].

When the blood reaches the capillaries, the flow is slow, smooth and fairly constant and this allows for efficient transference of nutrients and waste products to and fro the blood and the tissue. This is a result of the Windkessel effect.

The shape and amplitude of pressure and flow waveforms varies throughout the arterial network. **Fig. 2-11** shows the waveforms of pressure and flow velocity of a canine under normal conditions.

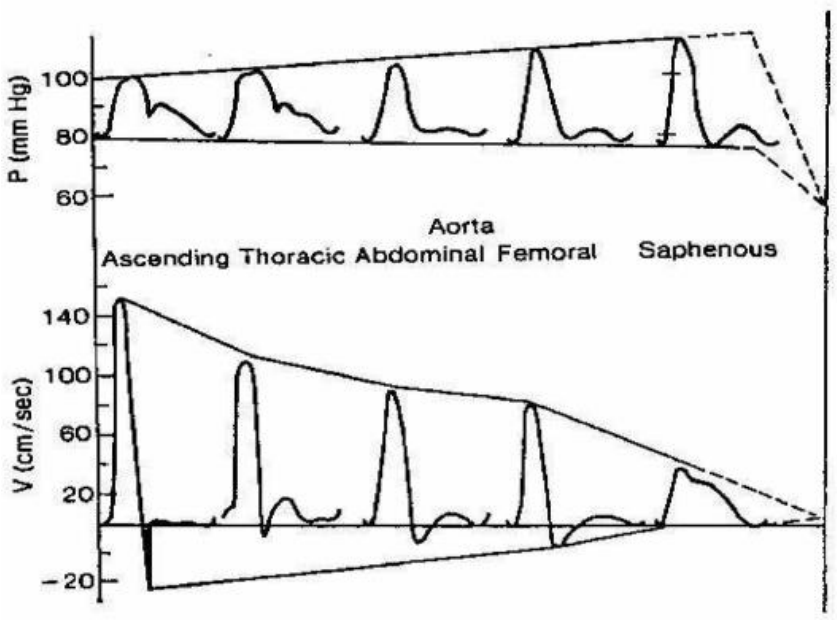

Fig. 2-11: Pressure waveforms (top) and velocity waveforms (bottom) in various arteries of a canine. The systolic pressure increases away from the heart while the amplitude of the velocity waves decreases [17].

From **Fig. 2-11**, it can be seen that during systole, the blood pressure increases and declines sharply until diastole. During diastole, the pressure rises forming a second peak, which forms the dicrotic notch, again followed by a smooth decrease in pressure. This second pressure peak disappears farther away from the heart.

The systolic pressure in large arteries increases as the distance from the heart increases however mean pressure decreases gradually. This increase in systolic pressure is due to wave reflections that occur because of the tapering and bifurcating nature of the arteries and most importantly due to the impedances at the terminal ends of the arteries where they branch into smaller arteries and arterioles [67]. Wave reflections also occur due to the shutting of the aortic valve at the end of diastole as well as due to structural changes of the vessel walls. The reflected waves superimpose on the pressure waves, hence increasing the systolic pressure.

It can also be seen that the amplitude and mean value of the velocity wave decreases downstream. This decrease is due to flow division at the branching points, increase in the impedance to flow, a decrease in reverse flow and an increase in width [63].

2.4 Summary

In this chapter, a summary of the workings of the cardiovascular system is provided, with special attention to systemic arteries, as these are the only arteries that are simulated using the one-dimensional model in later sections.

Key points from this chapter are as follows:

- The cardiovascular system can be further divided into two systems; namely the systemic circulation and pulmonary circulation. The objective of the pulmonary circulation is to transport deoxygenated blood from the body to the lung tissues, where a gaseous exchange takes place; the blood picks up oxygen and the lungs remove the carbon dioxide from the blood. This oxygenated blood taken back to the heart and is now ready to be transported to all the organs. The objective of the systemic circulation is to transport oxygen rich blood to all the organs and tissues.
- Pressure in the systemic circulation is much higher as compared to pulmonary circulation.

- A single cardiac cycle comprises of two phases namely systole and diastole. Systole occurs when the heart muscles contract to pump blood into the large arteries causing the "lub" sound. Diastole occurs when the heart muscles relax and the aortic valve shuts causing the "dub" sound. Pressure in large arteries is highest during systole and lowest during diastole. The systolic and diastolic pressure are the measurements taken in a routine blood pressure checkup. In a healthy human being, the cardiac cycle lasts about 0.8s, which equates to 75 beats per minute. In each stroke, the left ventricle ejects approximately 70ml of blood into the ascending aorta.
- The arteries (with the exception of pulmonary artery) take oxygenated blood from the heart to the tissues while the veins (with the exception of pulmonary vein) take deoxygenated blood away from the tissues and into the heart. Capillaries allow the diffusion of oxygen and nutrient to the tissue and take carbon dioxide and other waste products away from the tissue. The size of these vessels and their geometrical properties vary in order to adapt to the pulsating flow. Changes include thicknesses, stiffness, and inlet and outlet radii of the vessels to name a few.
- Large arteries branch into smaller arteries and arterioles, which further branch into the smallest vessels capillaries. The capillaries merge into venules and ultimately large veins.
- The constituents of blood are plasma, various nutrients, cells, waste materials and hormones. For flow in larger arteries (systemic circulation), blood is considered a Newtonian fluid, homogeneous and incompressible fluid with density, $\rho = 1050 - 1055\ Kg/m^3$ while the viscosity is $\mu = 4.0 - 5.0\ mPas$.
- Arteries have non-linear elastic behavior due to variation in their properties. This variation is necessary to provide a smoothing mechanism to the flow of blood as blood is incompressible.

- The systolic pressure in large arteries increases as the distance from the heart increases due to wave reflections that occur because of the tapering of vessels, bifurcations and impedances at the terminal ends of the arteries.
- Amplitude and mean velocity/flow wave downstream. This decrease is due to flow division at the branching points, increase in the impedance to flow, a decrease in reverse flow and an increase in width.

CHAPTER 3

NUMERICAL MODELLING OF THE CARDIOVASCULAR SYSTEM: REVIEW OF ONE-DIMENSIONAL MODELLING

3.1 Introduction

The research into the cardiovascular system has come a long way over the years. An important research area in this field is the propagation of the pulse wave in the arterial network and how this propagation is affected by various factors ranging from the tapering of arteries to the reflections caused to the flow due to branching of the arteries. Even with state of the art technology, hemodynamical ailments of the arterial network are challenging to evaluate using clinical studies. Given the advancements in computational methods, numerical modelling of the cardiovascular system provides a viable alternative to invasive clinical studies.

In this chapter, 3.2 provides a brief historical review of the main influences on the understanding of the cardiovascular system and how this understanding has evolved into mathematical models and numerical techniques. 3.3 justifies the choice of the 1-D model used to simulate blood propagation in this work followed by the types of the 1-D models currently available (3.4) and the applications of these models (3.5). 3.6, 3.7 justify and describe the choice of solution methods and boundary conditions. Finally, Section 3.9 summarizes the key take aways from this chapter.

3.2 Brief historical review

Although not a prerequisite in understanding the underlying physics of blood propagation, the knowledge of its historical background does provide insight into how the concept of blood propagation has evolved over a period that spans from the Common Era to the present day.

The first known writing which corrected some of the wrong understandings of blood propagation of the time came from a Roman Physician, Galen. (129 – 210 AD). He found that the arteries contained blood, rather than air which was the common belief at the time. Additionally, he believed that there were two systems at work in the body, a venous system that provides nutrition and the arterial system that was the source of heat for the body [68], [69]. Like Greek physician Erasistratus (304 -250 BC), Galen falsely believed the blood originated in the Liver and was consumed by the organs instead of circulating periodically. He also put forth the inaccurate idea that the heart has two chambers.

Most of these beliefs were amazingly unquestioned for the next 1500 years. The first physician to actually oppose these beliefs was Ibn An-Nafis (1210 – 1288 AD) who was also responsible for the first ever description of pulmonary circulation [70]. Leonardo Da Vinci (1452 – 1519 AD) took great interest in human anatomy and produced numerous drawings of the visible anatomical features. In drawings of the heart, he used his knowledge of engineering to understand how the heart functions and correctly described the closure mechanism of the Aortic valve. Not long after, Andreas Vesalius (1514 – 1564) wrote one of the most influential books on human anatomy, "De Humani Corporis Fabrica" (On the Fabric of the Human Body) which questioned Galen's universally accepted views.

Gradually, Galen's views started becoming less popular until William Harvey (1578-1657) completely deconstructed the incorrect views of blood circulation in his book "De motu Cordis et Sanguinis in Animalibius" (Movement of the heart and blood in Animals, an anatomical essay) [71]. Harvey deduced that the blood flows from the heart to the rest of the body and instead of the organs consuming the blood; the blood goes back to the heart. He put forth the idea that the pulsatile behavior of blood flow through the arterial network was due to the contraction of the heart. He also realized that the variations of the pulsation in an unhealthy body was due to the anomalies in the function of the heart and blood vessels which directly leads to the establishment of the effect wave

reflection has on the arterial pulse. Harvey was limited by the technology of his time, which did not allow him to conclusively discover capillaries. Nevertheless, he still deduced the existence of capillaries until Marcello Malpighi (1628 – 1694), Jacob van Swammerdam (1637-1680) and Anthony van Leeuwenhoek (1632 -1723) finally discovered them. They used a microscope to describe the capillary networks that connect the arterioles and venules and explained the shape of the red blood cells [69]. Actual measurement of pressure in the circulation system started with experiments of Reverend Stephen Hales (1677-1761) who is often credited with the first ever blood pressure measurement. Hales compared the arterial system and the heart to a medieval fire cart. In this comparison, the air-filled chamber is analogous to the compliance of the arteries and the fire hose nozzle represents the peripheral resistance. This idea came to be known as the Windkessel effect.

Through his experiments, Hales showed that the greatest resistance to blood flow came from arterioles and capillaries [63]. A major contribution was made by Leonhart Euler (1707-1783), who derived the general equations of mass and momentum conservation of an inviscid fluid. Euler was the first one to apply these equations to blood flow but failed to find a solution to these equations because he did not identify the wave like nature of blood flow [72]. Euler's close friend, Daniel Bernoulli (1700-1782), although known for being a prominent mathematician, used his multidisciplinary knowledge to come up with the Bernoulli equation. This equation directly led to the conversion of pressure to potential and kinetic energy [73]. The first person to describe the wave like nature of blood flow scientifically was Thomas Young (1773 – 1829). Young is often described as "The last man who knew everything" [74]. He contributed immensely to the study of elasticity, with the modulus of elasticity (Young's modulus) being a direct consequence of his work. His work in hemodynamics led him to propose a relationship between propagation velocity of the arterial pulse and elastic properties of the vessel walls [75]. Moens [76] and Korteweg [77] later formally formulated an equation that related propagation velocity and Young's modulus. The Moens

Korteweg equation combined with the one-dimensional Navier-Stokes equations, which resemble the equations derived by Euler, form a mathematical model of pulse wave propagation. Bernhard Riemann (1826 – 1866) introduced a method in 1860, [78] that was vital in solving this mathematical model. The method is known as the method of characteristics, which finds characteristics, or curves along which the partial differential equation is reduced to an ordinary differential equation.

Refererring back to Euler's model, the non-linear equations he proposed become analogous to electrical transmission line equations once they are linearized. As a result, several studies were conducted in the frequency domain [17], [79]. Noordergraaf and Westerhof [80] constructed the model for the large systemic human arteries, which, since the advent of computers have been improved upon by various researchers such as Avolio [81], Olufsen et al [82], Sherwin et al [83], and Stergiopulos [15] among others.

3.3 Choice of model

As it was seen earlier, in the cardiovascular system the blood vessels have a structure that resembles that of a tree, the vessels start off with larger vessels (arteries) and branch into smaller vessels (arterioles, capillaries and venules). While this branching occurs, not only does the size of the vessels change but other properties change as well. For instance, the diameters of the vessels decrease progressively while the area of the lumen along with the stiffness of the vessels increases downstream. The varying properties and the bifurcating nature of the arterial network, has an effect on the heart loading and coronary perfusion [38]. This in turn effects the aortic blood pressure waveform as well as the relationship of this waveform to peripheral blood pressure waveforms. These effects are yet to be fully investigated [84]. However, in-vivo and in-vitro studies to examine these factors are difficult, time consuming and costly to carry out. Therefore, numerical modelling offers an alternative to experimental studies as a non-invasive and feasible tool. Pressure changes in arteries can be more accurately analyzed by deriving and solving the mathematical equations that

govern the pressure wave dynamics in the arteries [38]. In most studies [15], [43], [82], [83], [85]–[88], large arteries of the systemic circulation are solely simulated as the assumptions of blood propagation models are more applicable to large arteries. Additionally, the material properties and the geometric complexity of the smaller vessels are difficult to measure; hence, large arteries are simulated and truncated through various methods.

Numerous modelling techniques (zero-dimensional, one-dimensional, two-dimensional or three-dimensional models) have been put forth to study several physiological phenomenon. Each of these techniques has its own merits; however, the accuracy and aims of the research are the prerequisite to selecting which kind of model should be used to simulate propagation of pulse wave in the arterial network i.e., whether to use a zero-dimensional, one-dimensional, two-dimensional or three-dimensional model.

Zero-dimensional (0-D) models or lumped parameter models describe blood propagation using two ordinary differential equations (ODEs) and an algebraic equation. In 0-D models, the variable properties; pressure, flow and volume are assumed uniform. The two ODEs (conservation of mass and momentum) are only dependent on time. Since 0-D models do not depend on spatial variable, they do not consider spatial wave propagation effects. 0-D models are most suitable for evaluating hemodynamical interactions among organs and providing outflow boundary conditions for one-dimensional [89] and three- dimensional [90] models.

One-dimensional (1-D) models simulate blood propagation in the axial direction. Axial symmetry of the geometry is assumed. The 1-D models give rise to two non-linear hyperbolic partial differential equations (PDEs) that describe the conservation of mass and momentum (Navier-Stokes equations) which are dependent on time and axial distance. A third equilibrium equation is used to close the system. This third equation often referred to as the constitutive equation considers the mechanical properties of the arterial wall. In 1-D models radial velocity is neglected and local

pressure at cross sections is assumed constant. 1-D models are used to study wave propagation effects and are widely used for clinical applications (3.5).

Two-dimensional (2-D) models are the least used models out of all the modelling techniques. Similar to 1-D models, two partial differential equations (PDEs) describe the conservation of mass and momentum and a third equilibrium equation is used to close the system. In 2-D models, axial and radial velocities are computed while circumferential velocity is neglected. The non-linear convective term is ignored and the solutions are computed in the frequency domain [64]. 2-D models are most commonly used as an improved boundary condition to three-dimensional models for specific applications [38].

Three-dimensional (3-D) models describe blood propagation based on the full Navier-Stokes equations and the system of hyperbolic PDEs is closed off by an equilibrium equation. 3-D models compute complex flow patterns in any small region of the system [38]. 3-D models are computationally, the most expensive models and need several input parameters. They are most suitable for applications that consider flow in specific segments of the arterial network.

Fig. 3-1 shows a diagrammatic illustration of the different scales of models used.

Zero-dimensional models are suitable if the general distribution of the pressure, flow and volume of blood needs to be inspected. However, for a more specific research, higher models are used where these flow variables are assumed to be non-uniform. Another important difference between zero-dimensional and higher models is that zero-dimensional models do not include the nonlinear convective acceleration term whereas other models do [38].

On the other hand, two-dimensional and three-dimensional models give more details about the distribution of variable properties in a small segment of the vascular system. For instance, these models can be used to reveal the meticulous pressure and flow distribution in a specific section of a

certain vessel. In order to simulate the entire systemic circulation, which is extremely vast, modelling the entire arterial tree using two-dimensional and three-dimensional models is impractical. Additionally, the exact geometrical and material properties of the entire arterial tree are still unknown.

Two-dimensional and three-dimensional modelling are not only costly but the computational times of simulations with these models for a few arteries takes far too long [91]–[94]. When using a one-dimensional model in comparison to a three-dimensional model, the computation cost reduces by at least 1000 times [95]. According to Alastruey et al., [85] a simulation of one cardiac cycle for approximately 100 segments takes less than a minute. A detailed comparison of one-dimensional and three-dimensional formulations can be found in [95].

The various models used to simulate the cardiovascular system are shown in **Fig. 3-1**.

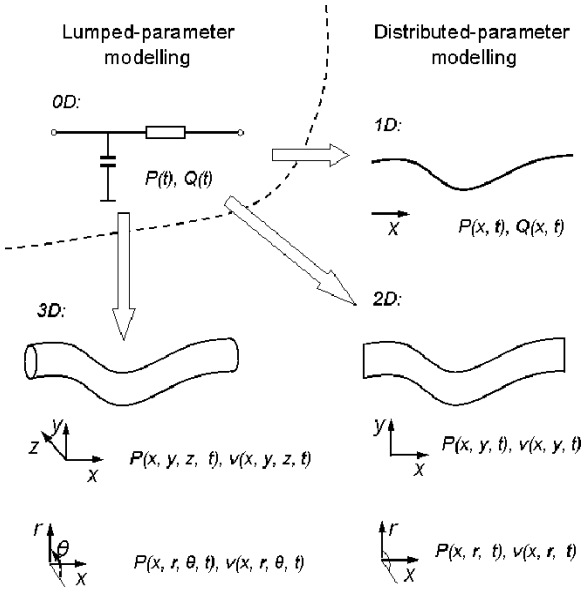

Fig. 3-1: Various Cardiovascular computational models [38].

Unlike higher order models, one-dimensional models cannot simulate intricate details of blood flow such as flow separation or vortex formation. However, in-vivo measurements [82], [87], [96]–[103], in-vitro experiments [85], [104]–[108] as well as three-dimensionally modelled numerical data [86], [95] demonstrate that one-dimensional models can successfully capture the main features of pressure, flow and area waveforms in the systemic circulation's arterial network.

Canic and Kim [109] investigated the characteristics of the governing equations of blood propagation. They demonstrated that the wavelengths of the pressure and flow waves from the heart are larger than the vessel diameters. Hence it is rational to consider the flow quasi one-dimensional [80], [110]–[112].

Table *3-1* summarizes the comparison between the various degrees of models used to simulate the cardiovascular system.

Table 3-1: General comparison of modelling techniques for cardiovascular dynamics studies

Model	Assumed distribution of variable properties.	Types of Governing equations	Applications of model
0-D	Uniform	• 2 ODE's (Conservation of mass and momentum) • Algebraic equilibrium equation (relates volume to Pressure)	Suitable for inspection of overall pressure distribution, flow and volume of blood. Can, at times, provide boundary conditions for 3-D model
1-D	Non-Uniform	• 2 PDE's (Conservation of mass and momentum) • Equilibrium Equations	Represents wave reflection/transmission effect which allows for better boundary conditions for 3-D models

2-D	Non-Uniform	• 2 PDE's (Conservation of mass and momentum) • Equilibrium Equations	Represents radial variation of velocity in an axisymmetric tube allows for even improved boundary conditions for 3-D models but to a certain limit off applicability
3-D	Non-Uniform	• 2 PDE's (Conservation of mass and momentum) • Equilibrium Equations	Compute complex flow patterns in any small region of the system.

As seen in Chapter 2, the systemic circulation is constituted by a large network of branching vessels. This makes high dimensional modelling of the arterial network tedious, expensive and simply unfeasible. Keeping in mind that the consideration of flow being quasi one-dimensional is justified, a 1-D model is sufficient to model the entire arterial tree, as it can easily represent the changes in the variable properties along the entire tree while being economically feasible at the same time. Additionally, it can easily take non-linearities such as vessel tapering, vessel branching and wave propagation effects into consideration making it the optimum model for this particular work.

3.4 Types of one-dimensional models

A number of one-dimensional models for pulse wave propagation in the arterial network have been developed previously for various applications. [55], [87], [110], [113]–[127]. The equations governing these models are alike, with differences arising in the types of methods used to solve these equations, the boundary conditions applied to these models, whether non-linear effects are considered and if they are, which non-linear effects are considered [38].

Modelling pulse wave propagation in an artery using a one-dimensional model is simulated as a fluid-structure interaction problem between the flow of blood and the displacement of the arterial wall. The axisymmetric form of the one-dimensional incompressible continuity and momentum equations (Navier-Stokes equations) govern the propagation of blood in a vessel (Section 4.2.1) while the motion of the arterial wall is governed by the equation of equilibrium. (Equation (4.4))

Although intricate models exist [120], the much simpler linear or non-linear constitutive equations are most commonly used to describe the pressure/cross-sectional area relationship [55], [83], [87], [110], [113]–[119], [121]–[128].

Details of other pressure-area relations used in previous research can be found here [86].

Other variations include the study of vessel tapering [83], [114], [116], [117], [122], [123] as well as vessel collapse [113], [116], [125]. The methods to include effects of blood viscosity also bring about slight variations in the model. Majority of authors assume Poiseuille flow (over a given cross section, the fully developed flow has a parabolic velocity profile) [123], [129]–[131]. Variations of these approximations can be found here [15], [111], [112]. There are some other models which simulate with the assumption that the blood is non-Newtonian, again introducing a slight variation in the formulation [132], [133].

The one-dimensional model used in this work is the one developed by Olufsen [43]. The propagation of blood in the systemic arteries is described by the Navier-Stokes equations. The equations are integrated over the cross-sectional area of an arterial segment to produce the one-dimensional model. Each vessel is modelled as an impermeable axisymmetric compliant cylinder and the blood is assumed as an incompressible, homogeneous and Newtonian fluid.

3.5 Where is the one-dimensional model used?

One-dimensional models have been used for blood propagation in arterial segments [110], [121], [127] as well as entire arterial networks [43], [63], [82], [85], [87], [118], [119] as well as blood flow in the pulmonary circulation [53]. A variety of models have been used to study diseased vessels such as ones with stenosis or bypass grafts [96], [114], [120], [122]–[124], [134]. Other studies have looked into animal arterial networks [116], [135], [136]. Wave Intensity Analysis (WIA), developed by Parker and Jones [121], helps in understanding forward and backward pulse propagation and is a direct application of one-dimensional models. WIA has been applied to the left ventricle [137], [138], systemic arteries [139], coronary vessels [140] as well as pulmonary arteries [141], [142] to study pulse wave propagation. One-dimensional models, as pointed out earlier, are also used as boundary conditions for three-dimensional models [91], [117], [143], [144].

3.6 Solution methods

In order to solve the system of non-linear hyperbolic equations that govern the one-dimensional propagation of the pulse wave, several analytical and numerical methods have been used.

Method of characteristics was used by Schaaf [111], Anliker et al [145], Stergiopulos [15], Parker and Jones [121], Bodley [127], Wang and Parker [118], Wang et al. [119], Stettler et al [146] and Steeter et al. [110]. In the method of characteristics, the governing equations (continuity and momentum) are transformed from partial differential equations to ordinary differential equations along the direction of certain curves called characteristic curves (or lines). These characteristic curves correspond to the two characteristic variables (Riemann invariants). Once they have been transformed, these ordinary differential equations can be easily solved.

Finite difference methods (FDM) have also been used to discretize and solve the governing equations [15], [47], [87], [104], [113], [120], [125], [128], [130], [147], [148]. In FDM, the derivatives of the governing equations form the basis of the discretization. Each of these derivatives

is substituted with an approximate difference formula. Details of the finite difference method can be found in [149]–[152]. Within the finite difference method, the Lax-Wendroff scheme [82], [113], [125], [153]–[155] and MacCormack scheme [104], [125], [156]–[158] have been used to discretize the governing equations.

Recently, Finite volume methods (FVM) have also been used to discretize and solve the governing equations [159], [160]. In FVM, the integrals of the governing equations form the basis of the discretization. The governing equations are first discretized into finite volumes after which they are solved in each of these finite volumes. For details about the finite volume method see [161]–[163]. Within the finite volume methods, the Godunov scheme is the most popularly used [116], [135] scheme to discretize the governing equations.

Finite element methods (FEM) have also been a popular method to discretize the governing equations. In FEM, a piecewise representation of the solution in terms of specified basis functions forms the basis of the discretization. The domain where the computations is carried out is broken down into smaller domains or finite elements, see [164]–[166] for details on the finite element method. Comparison of the three methods is difficult, primarily due to the many variations of all three methods. FVM and FDM provide discrete solutions, while FEM provides a continuous solution. Generally, it is believed that FVM and FDM are easier to implement when compared to FEM however, FEM can handle irregular boundaries with relative ease when compared to FDM and FVM. Within FEM, the Galerkin scheme [83], [85], [86], [99], [100], [122], [123], [167], [168], discontinuous Galerkin scheme [88], [114], [115], [134], Taylor-Galerkin scheme [114], [147], Galerkin Least Squares [129] and Yoshida projection scheme [117] have been used amongst others to discretize and solve the governing equations.

Other solution methods include hybrids of one-dimensional models with Womersley flow (classic linear analytical solution) [80], [81], [169], [170]. These methods do not take into account the effects

of non-linearities. [114], [127], [131]. Details of these methods are beyond the scope this work but can be found here, [83], [171].

A comparative study was conducted by Boileau et al. [156] to compare the most popularly used numerical schemes for 1-D modelling. The models used were the finite difference MacCormack method, finite volume method, finite element methods and a simplified trapezium method. All the models demonstrated excellent abilities to capture the important features of blood flow in large arteries.

Since, all these methods show good ability to capture the important aspects of blood flow propagation the choice of solution method chosen for this work is an explicit FDM schemes, more specifically the two-step Lax-Wendroff method. This method is easy to implement in order to discretize and solve the governing equations.

3.7 Boundary conditions

When modelling pulse wave propagation using a one-dimensional model in an arterial network or an artery (for simplicity), three boundary conditions have to be imposed, one at the proximal end, one at the distal end and one at the bifurcating end [73]. The one on the proximal end is a rather simple boundary condition where either pressure or flow (derived from experimental data or literature) can be specified. The one on the distal end, however, needs deliberation.

In various arterial tree one-dimensional models [81], [114], [129], [172], the aorta has been used as the point for the initial boundary condition. A pressure wave is either imposed as the initial condition [114] or a derived function of flow rate is specified [79], [123], [173], [174]. This makes the formulation simpler as the values are prescribed instead of modelling the aortic valve. Additionally, reverse flow into the left ventricle is not considered.

Vessel branching is another boundary condition that needs consideration. A number of researchers have applied conservation of flow (i.e. the flow in the parent vessel must be equal to the sum of flows in the daughter vessels) and continuity of pressure (the pressure in the parent vessel is equal to the pressures in each of the daughter vessels) [55], [123], [134]. Some researchers, applied wave reflection coefficients to estimate changes in flow and pressure [87] [118].

Flow characteristics in the smaller vessels is not the same as that in the larger arteries as was pointed out earlier. The fluid properties as well as the material properties change which effects the characteristics of flow. This, in addition to the arterial tree's branching structure means there is a necessity to truncate the model. Moreover, modelling each vessel from large arteries all the way to the capillaries is simply not feasible. This need for truncation of the one-dimensional model gives rise to boundary conditions at the distal ends of the vessels. Anything beyond the truncation point (i.e. smaller vessels) needs to be consolidated.

Like the inlet condition, various researchers have prescribed a combination of pressure and flow rate [110], [113], [116], [121], [125], [127], [134] for the distal boundary condition.

In an attempt to introduce boundary conditions that represent physiological downstream conditions, some researchers used purely resistive loads [80], [81], [111], [114], [115], [118], [122]. However, there is no method available yet, that allows for the calculation of the values used for these loads. It has also been recognized that this method does not take into consideration the compliance of the vessels [130]. This results in a reflection coefficient, which depends on frequency (inversely proportional to any given harmonic of the pressure change).

Another way to represent the distal end of vessels is to derive a model based on the impedance at the terminal end of a vessel. This is done by using a three-element Windkessel model [15], [87], [120], [123], [129], [130] as the boundary condition. The Windkessel model characterizes the compliance as well as the resistance of the vessels by using an electric analog model. This model

immensely improves the distal representation. However, this model cannot capture wave propagation effects [55] which causes undulations in the input impedance. A solution to this problem is to directly prescribe the wave reflection coefficient at the terminals [114], [118], [124] or to use the structured tree outlet boundary condition [47], [55], [82], [175], [176] in which the impedance at the terminal is estimated by the linear form of the Navier-Stokes equations. In the structured tree outlet boundary condition model, the small arteries are joined to the distal ends of the large arteries and modelled as binary asymmetric structured trees. Similar to large arteries, the equations that govern blood propagation in small arteries can be derived from the axisymmetric form of Navier-Stokes equations. However viscous effects are more prominent in small arteries as compared to inertial effects hence the Navier-Stokes equations can be linearized by neglecting the non-linear terms [82]. Once the equations are derived [82] they predict the flow $Q(x, \omega)$ and pressure $P(x, \omega)$ in the frequency domain. A no-slip boundary condition is used to link the equations together. A convolution integral of the impedance and flow rate computes the pressure at each outlet providing a physiological outflow condition for the large arteries. This boundary condition can be used for one-dimensional, two-dimensional and three-dimensional models [89], [177], [178] and captures wave propagation effects well, however applying this type of boundary condition to a non-linear model is tedious [86] and the computation is costly especially for 3-D models [179].

For this work, the aorta has been used as the point for the initial boundary condition. A derived function of flow rate is specified to describe the ejection profile. This makes the formulation simpler as the values are prescribed instead of modelling the aortic valve.

At bifurcations, it is assumed that there is no leakage, therefore, the flow going out of the parent vessel must be equal to the sum of the flow going into the two daughter vessels. At the bifurcation points, albeit minor, some energy is lost. This loss of energy can be accounted for by modelling it in terms of loss coefficients, however, these coefficients cannot be estimated analytically in a one-

dimensional model [82]. A viable approximation of this energy loss is assuming continuity of pressure [15] at the bifurcation.

For the outflow condition, the structured tree outlet condition is used. Small arteries are joined to the terminal ends of the large arteries. These small arteries and arterioles are modelled as a structured tree and a semi analytical approach is used to express the root impedance of this tree. This in turn provides the outflow condition for the large arteries [43]. The need to use such a boundary condition lies in its advantage over lumped parameter models; structured tree outflow condition is a physiologically based boundary condition and may correctly account for the effect of the downstream vasculature on wave propagation in the arterial network.

3.8 Arterial segments

For one-dimensional modelling, the arterial network is broken down into smaller arterial sections that are connected to each other. The number of arterial segments used in one-dimensional modeling has increased in recent years from 29 to over 4 million [47], [81], [86], [87], [132], [172], [180]. Inherently, the greater the amount of arterial sections a network is broken down into, the more information required for the input parameters.

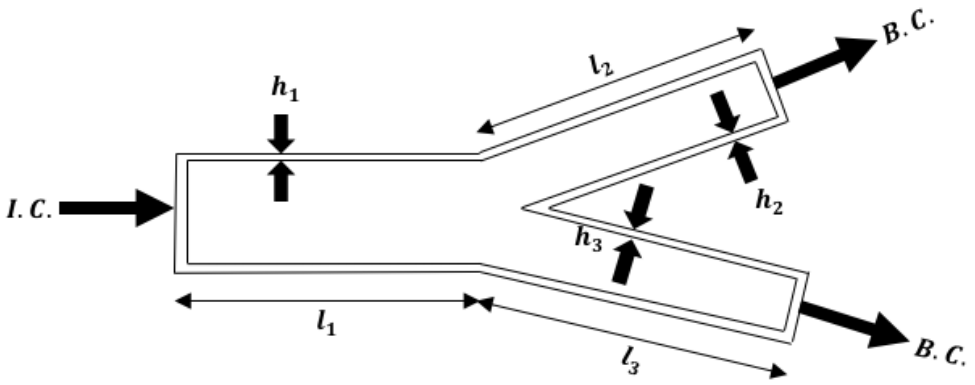

Fig. 3-2: A bifurcating artery

For instance, if a simple bifurcating artery is broken down into three segments, that is, the parent vessel and the two daughter vessels it bifurcates into (**Fig. 3-2**), parameters are required for each of these segments. The parameters include (but are not limited to) the lengths of each of these vessels (L_1, L_2, L_3), their inlet and outlet radii, the vessel thickness' (h_1, h_2, h_3), the stiffness of each of these vessels, the inlet boundary condition $(I.C.)$ for the parent vessel and the outlet boundary condition $(B.C.)$ for the daughter vessels.

If a multi-branched model is being made for the arterial network, it will have multiple bifurcations and with each generation of bifurcation, the input parameters needed increases. Moreover, these input parameters vary from person to person, making patient-specific multi branched modelling extremely tedious. A method is needed to minimize the arterial segments the network is broken down into, so that lesser input parameters are needed for patient-specific modelling [2]. Olufsen's structured tree boundary condition [47] provides a viable option for this purpose and can be taken further to incorporate patient specific models.

3.9 Summary

In this chapter, an examination is provided of the various existing one-dimensional models, their differences, the methods with which their governing equations are discretized and solved as well as the treatment of boundary conditions in these models.

Key points from this chapter are as follows:

- Owing to the lack of wide scale experimental studies, the limitations associated with it and the immense advances in computational technology, in recent years, numerical modelling of the cardiovascular system has gained popularity as a viable alternative.

- Since 0-D models do not depend on spatial variable, they do not consider spatial wave propagation effects. For a comprehensive model, wave propagation effects need to be considered, hence higher order models need to be used.
- 1-D models as compared to higher dimensional models provide a feasible and efficient means to study the dynamics of pulse wave propagation in order to increase the comprehension of circulatory physiology.
- In a 1-D model, a system of hyperbolic PDEs (axisymmetric Navier-Stokes equations) and a state equation to close the system are used to describe flow of a fluid in a compliant vessel.
- Various 1-D models are available based on the solution methods used, boundary conditions applied, consideration of geometrical features such as tapering and whether non-linearities are included or not. This work uses a comprehensive model, hence non-linearities, vessel tapering, vessel branching, etc. have to be included.
- In order to solve the system the governing equations several methods are available such as FDM, FVM, FEM, Method of characteristics, Spectral methods. Literature demonstrates that all these methods show good ability to capture the important aspects of blood flow propagation. Explicit FDM schemes are easy to implement, therefore for this work an FDM scheme (Lax-Wendroff method) is used to discretize and solve the governing equations.
- For this work, the aorta has been used as the point for the initial boundary condition. A derived function of flow rate is specified to describe the ejection profile.
- At bifurcations, it is assumed that there is no leakage pressure continuity is assumed.
- For the outflow condition of large arteries, the structured tree outlet condition is used as it a physiologically based boundary condition and correctly accounts for the effect of the downstream vasculature on wave propagation in the arterial network

CHAPTER 4

MATHEMATICAL MODEL OF THE ARTERIAL NETWORK

4.1 Introduction

The one-dimensional model used in this thesis is the one developed by Olufsen [43]. The propagation of blood in the systemic arteries is described by the incompressible axisymmetric Navier-Stokes equations. The equations are integrated over the cross-sectional area of an arterial segment to produce the one-dimensional model. The blood flow is modelled in a bifurcating binary tree of 24 vessels where each vessel is modelled as an impermeable axisymmetric compliant cylinder and the blood is assumed as an incompressible, homogeneous and Newtonian fluid with density, ρ and viscosity, μ. The geometry of the arterial tree is based on the paper by Olufsen [82] and imitates the geometry of physiological arteries (**Table *2-1***). This model permits all the important aspects of physiological fluid-structure interaction to be captured accurately without increasing the computational load. Additionally, more vessels can be easily simulated but the arterial tree has been simplified for this study as the aim is to study the application of one-dimensional modelling rather than the blood flow itself.

The model is divided into two parts; the large arteries and the small arteries. The large arteries originate at the heart and are truncated after a maximum of two generations. The small arteries and arterioles are joined at the distal ends of the large arteries and modelled as binary asymmetric structured trees. The small arteries do not imitate physiologically accurate data instead are based on statistical relationships estimated from literature [82].

4.2 Large arteries

The blood flow in large arteries is modelled as a bifurcating binary tree where each vessel is modelled as an impermeable axisymmetric compliant cylinder and the blood is assumed as an incompressible, homogeneous and Newtonian fluid with density, ρ and viscosity, μ. Each arterial segment is assumed to taper exponentially and the radius, $r(x)$ is modelled via the following equation

$$r(x) = r_{in}\, e^{\log\left(\frac{r_{out}}{r_{in}}\right)\left(\frac{x}{L}\right)} = r_{in}\left(\frac{r_{out}}{r_{in}}\right)^{\frac{x}{L}} \qquad (4.1)$$

Where, x is the position along the vessel, r_{in} is the inlet (or proximal) radius, r_{out} is the outlet (or distal) radius of the vessel and L is the length of the vessel [82]. For a complete description of the artery it is necessary to define L, r_{in} and r_{out}.

The arterial wall described in section is known to be constituted by various layers to give it its elastic properties. The volume compliance C can be mathematically modelled as follows:

$$C = \frac{dV}{dp} \approx \frac{3A_0 L}{2}\frac{r_0}{Eh} \qquad (4.2)$$

Where V is the volume of the artery under consideration, p is the pressure in this artery, A_0 is the cross sectional area and it is equal to πr_0^2, r_0 being the unstressed radius, L is the length of the artery, E is the Young's modulus and h is the thickness of the arterial wall.

The elastic properties in this study are evaluated using a relationship (Equation (4.3)) of the Young's modulus, the radius of the artery and thickness of the arterial wall.

$$\frac{Eh}{r_0} = k_1 e^{k_2 r_0} + k_3 \tag{4.3}$$

Where $k_1 = 2 \times 10^7\ g/s^2cm, k_2 = -22.53\ cm^{-1} and\ k_3 = 8.65 \times 10^5\ g/s^2cm.$ A plot of this relationship as a function of r_0 is fitted to the elastic data from Stergiopulos [15] demonstrating the relationship between the E, h and r_0.

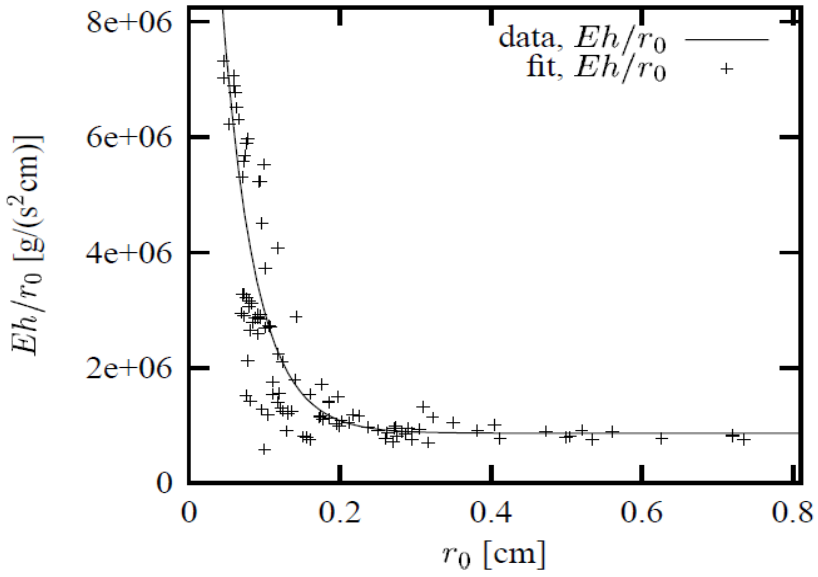

Fig.4-1: Graph of Eh/r_0 as a function of r_0 [47]

A few discrepancies seen between the fitted and observed data are due to variable compliance throughout the arterial network. Some vessels with the same radii may have dissimilar compliance leading to different values of the relationship between E, h and r_0.

4.2.1 Fluid dynamics in large arteries

Now that the geometrical and structural properties of large arteries have been considered, a fluid dynamical model can be built. The 1-D model uses three equation to describe the flow of blood in an artery. The continuity and momentum equations (Navier-Stokes equations) and a state equation. These equations describe the flow of blood in the axial direction in a compliant tube, the motion of the walls of the compliant tube and the fluid structure interaction of blood and the walls of the compliant tube. The distensible properties of the walls are incorporated in the state equation.

In order to reduce the complex 3-D problem to a 1-D problem, the necessary assumptions are :

- The flow is axisymmetric and the all the vessels modelled have a circular cross section.
- If the velocity profile is known, it can be integrated over the cross sectional area to give a 1-D model. It is assumed that the velocity profile of blood is parabolic across the cross-sectional area of the vessel, therefore a relationship between the cross-sectional area of the vessel, $A(x,t)$ and pressure, $p(x,t)$ exerted on the arterial wall can be defined as the following:

$$p(x,t) - p_0 = \frac{4}{3}\frac{Eh}{r_0}\left(1 - \sqrt{\frac{A_0(x)}{A(x,t)}}\right) \tag{4.4}$$

Where p_0 is the diastolic (nominal) pressure, $r_0$is the equilibrium radius (the radius when the pressure is nominal)

Equations (4.5) and (4.6) are the continuity and momentum equations that govern the one-dimensional flow in large arteries, respectively. A detailed derivation of these equations can be found here [47], [82], [181]

$$\frac{\partial A}{\partial t} + \frac{\partial q}{\partial x} = 0 \tag{4.5}$$

$$\frac{\partial q}{\partial t} + \frac{\partial}{\partial x}\left(\frac{q^2}{A}\right) + \frac{A}{\rho}\frac{\partial p}{\partial x} = -\frac{2\pi v\, r}{\delta}\frac{q}{A} \tag{4.6}$$

Where, v is the kinematic viscosity $\left(\frac{\mu}{\rho}\right)$ and δ is the thickness of the boundary layer. Equations (4.3)-(4.6) are used to calculate the pressure $p(x,t)$ and flow $q(x,t)$ in each arterial segment.

4.2.2 Boundary conditions for large arteries

The equations described in the previous section are applicable to a single artery. In order to extend the equations introduced in the previous section to an entire arterial network, three boundary conditions are imposed. Firstly, to the inlet of the arterial tree (inflow condition), secondly, at each vessel bifurcation in which a parent vessel bifurcates into two daughter vessels and lastly a boundary condition is imposed at the terminal ends of the tree (outflow condition).

For the inflow condition, an ejection profile acquired through clinical measurement or derived using simple relationships of flow in the ascending aorta [82] is imposed. The ejection profile as a function of time is shown in **Fig. 4-2**, enforced using

$$Q_{in}(t) = \begin{cases} Q_0 \sin\left(\frac{\pi t}{\tau}\right) & if\ t < \tau \\ 0 & otherwise \end{cases} \tag{4.7}$$

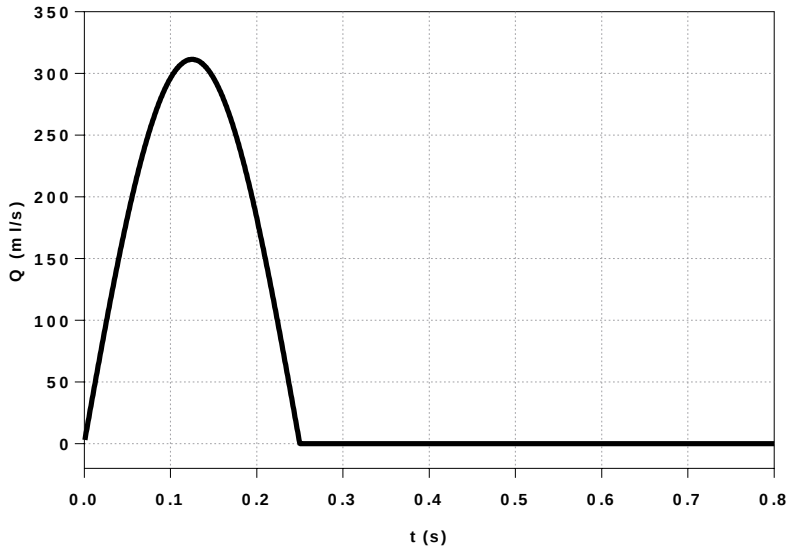

Fig. 4-2: Ejection profile used as the inflow boundary condition for the one-dimensional model.

At the bifurcations (**Fig. 4-3**), it is assumed that there is no leakage, therefore, the flow going out of the parent vessel (P) must be equal to the sum of the flow going into the two daughter vessels (d_1, d_2)

$$q_P(\mathrm{L},\mathrm{t}) = q_{d_1}(0,\mathrm{t}) + q_{d_2}(0,t) \tag{4.8}$$

At the bifurcation points, albeit minor, some energy is lost. This loss of energy can be accounted for by modelling it in terms of loss coefficients, however, these coefficients cannot be estimated analytically in a one-dimensional model [82]. A viable approximation of this energy loss is assuming continuity of pressure [15] at the bifurcation.

$$p_P(\mathrm{L},\mathrm{t}) = p_{d_1}(0,\mathrm{t}) = p_{d_2}(0,\mathrm{t}) \tag{4.9}$$

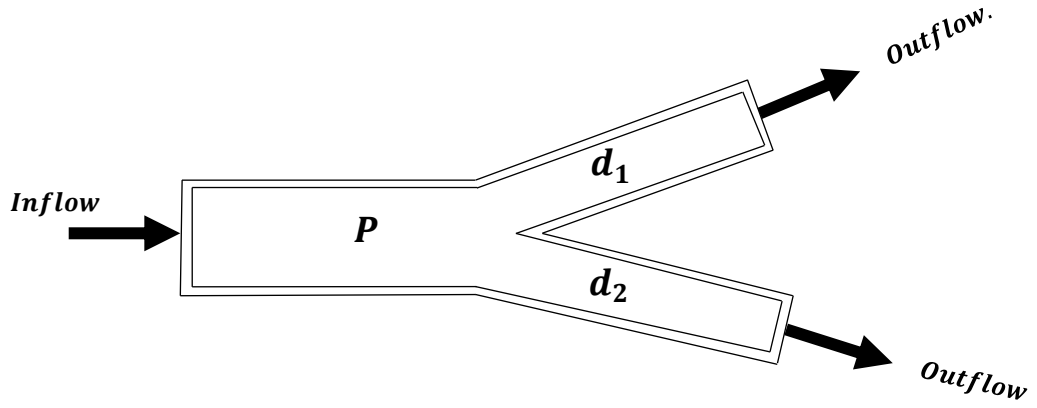

Fig. 4-3: A bifurcating artery

For the outflow condition, small arteries are joined to the terminal ends of the large arteries. These small arteries and arterioles are modelled as a structured tree and a semi analytical approach is used to express the root impedance of this tree. This in turn provides the outflow condition for the large arteries [43]. The frequency dependent impedance $Z(x,\omega)$ determined from the model of small arteries is a relation between the Pressure $P(x,\omega)$ and flow $Q(x,\omega)$ in the small arteries. This impedance (analogous to $R = \frac{V}{I}$ in electrical circuits) is given as follows:

$$Z(x,\omega) = \frac{P(x,\omega)}{Q(x,\omega)} \tag{4.10}$$

Where, $P(x,\omega)$ is analogous to voltage, V and $Q(x,\omega)$ is analogous to current, I in electric circuits.

Given that the inflow profile is periodic, it can be assumed that $P(x,\omega)$ and $Q(x,\omega)$ can be expressed as a complex periodic Fourier series. This allows separate determination of any feature of the system response.

$$p(x,t) = \sum_{k=-\infty}^{\infty} P(x,\omega_k) e^{i\omega_k t} \tag{4.11}$$

$$q(x,t) = \sum_{k=-\infty}^{\infty} Q(x,\omega_k) e^{i\omega_k t} \tag{4.12}$$

Where, $\omega_k = 2\pi k/T$ is the angular frequency, $P(x,\omega_k)$ and $Q(x,\omega_k)$ are

$$P(x,\omega_k) = \frac{1}{T}\int_{-T/2}^{T/2} p(x,t) e^{-i\omega_k t} dt$$

$$Q(x,\omega_k) = \frac{1}{T}\int_{-T/2}^{T/2} q(x,t) e^{-i\omega_k t} dt$$

The impedance calculated in the frequency domain $Z(x,\omega)$ can be transformed to the time domain representation of impedance $z(x,t)$ using an inverse Fourier transform. Further, a convolution theorem provides an analytical relation between $p(x,t)$ and $q(x,t)$ as follows:

$$p(x,t) = \int_{t-T}^{t} q(x,\tau) z(x,t-\tau) d\tau \tag{4.13}$$

This analytical relation is the outflow boundary condition applied at the terminal of the large arteries.

4.3 Small Arteries

The small arteries and arterioles attached to the ends of the large arteries are modelled separately as binary asymmetric structured trees. Similar to large arteries, the equations that govern blood propagation in small arteries can be derived from the axisymmetric form of Navier-Stokes

equations. However viscous effects are more prominent in small arteries as compared to inertial effects hence the Navier-stokes equations can be linearized by neglecting the non-linear terms [82].

In the binary asymmetric structured tree model of small arteries, each of these small arteries keep bifurcating into generations of even smaller arteries until a specified radius, r_{min} has been reached. The value of r_{min} can be the same for all arteries or variable hence the generation of the structured tree vary. The radii of the daughter vessels, $r_{d_1} and\ r_{d_2}$ are linearly scaled, relative to the radius of the parent vessel, r_P via constants that characterize the asymmetry of the tree, $\alpha\ and\ \beta$ (**Fig. 4-4**)

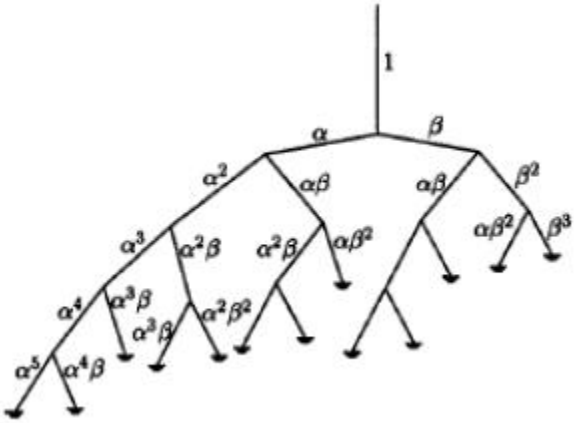

Fig. 4-4: Diagrammatic description of the binary asymmetric tree model of the small arteries [47]

The bifurcations of the small arteries in the structured tree are administered using a power law derived by Uylings [182] based on the principle of minimum work. This law assumes flow in cylindrical vessels.

$$r_P^{\xi} = r_{d_1}^{\xi} + r_{d_2}^{\xi}, \tag{4.14}$$

Where, $\xi = 3$ is used for laminar flows and $\xi = 2.33$ is used for turbulent flows.

In addition to the power law described in equation (4.14), creating an asymmetric tree requires two other relations. These are:

- A ratio relating the cross sectional areas of the daughter vessels to the parent vessel, η

$$\eta = \frac{r_{d_1}^2 + r_{d_2}^2}{r_P^2} \tag{4.15}$$

- A ratio relating the areas of the daughter vessels,

$$\gamma = \frac{r_{d_1}}{r_{d_2}} \tag{4.16}$$

The three equations, equations (4.14)-(4.16) describe the structured tree. The three relations, ξ, η and γ are related to each other by equation (4.17)

$$\eta = \frac{1+\gamma}{(1+\gamma^{\xi/2})^{2/\xi}} \tag{4.17}$$

Based on these equations, the scaling parameters α and β can now be defined as:

$$\alpha = \frac{r_{d_1}}{r_P} = \left(1+\eta^{\xi/2}\right)^{-1/\xi} \tag{4.18}$$

$$\beta = \frac{r_{d_2}}{r_P} = \alpha\sqrt{\gamma} \tag{4.19}$$

In order to find the values of α and β, the values of ξ, η and γ need to be defined. The values used are $\xi = 2.76$, $\eta = 1.16$ and $\gamma = 0.41$. These values are the most well documented values from literature [82], [182]–[185]. These values yield the values of the scaling parameters, $\alpha \; and \; \beta$ as 0.9 and 0.6, respectively.

Equations (4.14)-(4.19) and the values used in these equations set up the structured tree for the small arteries. One last equation is necessary for this structure, the length of each segment within the structured tree. In order to find the length of each vessel, a length to radius ratio has been used as follows:

$$l_{rr} = \frac{L}{r_0} \tag{4.20}$$

Again, the value of the length to radius ratio is taken from literature as $l_{rr} \approx 50$ [47], [82].

Once the equations are derived, they predict the flow $Q(x, \omega)$ and pressure $P(x, \omega)$ in the frequency domain. A no-slip boundary condition is used to link the equations together.

4.3.1 Fluid dynamics in small arteries

As mentioned earlier, for the small arteries, a linear model is used to govern the propagation of blood. This method is based on Womersley's linearized theory [79] which has been used in past by a number of researchers [65], [186], [187] to study flow in distensible vessels. More recently it has been used by Qureshi et al [53], Vaughan [188] and Clipp & Steele [189], [190]. For this work, the approach proposed by Olufsen [43], [47], [82] is used. In this work, a brief description of the equations governing blood flow in small vessels is provided. Detailed derivations of these equations can be found in [47].

Similar to large arteries, three equations describe changes in pressure, flow and area for small arteries. However, implementing a non-linear model in small vessels is not computationally feasible. Additionally, the non-linear model does not describe wall shear stresses well [47]. Therefore a few assumptions are made in order to linearize the governing equations for small arteries as follows:

- In small arteries, the viscous forces are more dominant as compared to inertial forces [47].

- Small vessels have uniform cross sectional areas A_0, that is, they do not taper along their lengths unlike the large arteries.
- The flow in small vessels again is assumed to be axisymmetric.

Owing to these assumptions, the axial momentum equation is reduced to equation (4.21)

$$\frac{\partial u_x}{\partial t} + \frac{1}{\rho}\frac{\partial p}{\partial x} = \frac{v}{r}\frac{\partial}{\partial r}\left(r\frac{\partial u_x}{\partial r}\right) \tag{4.21}$$

Where u_x is the longitudinal flow velocity in a small artery. With the assumption that all variables are periodic with a time period T, using complex Fourier series, the pressure and flow can be stated in the frequency domain as

$$p(x,t) = \sum_{k=-\infty}^{\infty} P(x,\omega_k)e^{i\omega_k t}$$

$$q(x,t) = \sum_{k=-\infty}^{\infty} P(x,\omega_k)e^{i\omega_k t} = 2\pi\int_0^{r_0} u(r,x,t)rdr$$

Where,

$$u(r,x,t) = \sum_{k=-\infty}^{\infty} U(r,x,\omega_k)e^{i\omega_k t}$$

and $\omega_k = 2\pi k/T$ is the angular frequency, $P(x,\omega_k)$, $Q(x,\omega_k)$ and $U(r,x,\omega_k)$are

$$P(x,\omega_k) = \frac{1}{T}\int_{-T/2}^{T/2} p(x,t)e^{-i\omega_k t}dt$$

$$Q(x,\omega_k) = \frac{1}{T}\int_{-T/2}^{T/2} q(x,t)e^{-i\omega_k t}dt$$

$$U(r,x,\omega_k) = \frac{1}{T}\int_{-\frac{T}{2}}^{\frac{T}{2}} u(r,x,\omega_k)e^{-i\omega_k t}$$

Putting these back in equation (4.21) yields,

$$i\omega U_x + \frac{1}{\rho}\frac{\partial P}{\partial x} = \frac{v}{r}\frac{\partial}{\partial r}\left(r\frac{\partial u_x}{\partial r}\right) \tag{4.22}$$

With the assumption that the vessels do not taper, the solution to equation (4.22) is,

$$U_x = \frac{1}{i\omega\rho}\frac{\partial P}{\partial x}\left(1 - \frac{J_0(rw_0/r_0)}{J_0(w_0)}\right)$$

Where, $w_0^2 = i^3 w^2$, and $w^2 = \frac{r_0^2\omega}{v}$ is the squared Womersley number and $J_0(x)$ is the Bessel function of the first kind and zero order.

The volumetric flow rate as a function of velocity can be stated in the frequency domain as

$$Q = 2\pi\int_0^\infty U_x r dr,$$

Which yields the momentum equation of small arteries as the following:

$$i\omega Q + \frac{A_0}{\rho}\frac{\partial P}{\partial x}\left(1 - F_J\right) = 0 \tag{4.23}$$

Where, $F_J = \frac{2J_1(w_0)}{w_0 J_0(w_0)}$ and $J_1(x)$ is a Bessel function of the first kind and first order.

The continuity equation for larger arteries is stated again

$$\frac{\partial q}{\partial x} + \frac{\partial A}{\partial t} = 0,$$

Using the state equation (equation (4.4(4.3)), the continuity equation can be re-written as

$$C\frac{\partial p}{\partial t}+\frac{\partial q}{\partial x}=0 \tag{4.24}$$

Where C is the compliance or distensibilty of the vessel and can be written as,

$$C=\frac{\partial A}{\partial p}=\frac{3A_0r_0}{2Eh}\left(1-\frac{3pr_0}{4Eh}\right)^{-3}\approx\frac{3A_0r_0}{2Eh}$$

Again, assuming periodicity and using Fourier expansions, the continuity equation for the small arteries becomes

$$i\omega CP+\frac{\partial Q}{\partial x}=0 \tag{4.25}$$

Differentiating the continuity equation (Equation (4.25)) with respect to x and substituting it back into the momentum equation (Equation (4.23)) yields a wave equation of the form

$$\frac{\omega^2}{c^2}Q+\frac{\partial^2 Q}{\partial x^2}=0,\quad or\quad \frac{\omega^2}{c^2}P+\frac{\partial^2 P}{\partial x^2}=0, \tag{4.26}$$

Where, c is the wave propagation velocity and is given as

$$c=\sqrt{\frac{A_0\left(1-F_J\right)}{\rho C}} \tag{4.27}$$

Solution to equation (4.26) yields the frequency domain representations of pressure $P(x,\omega)$ and flow $Q(x,\omega)$ as

$$Q(x,\omega)=a\cos(\omega x/c)+b\sin(\omega x/c) \tag{4.28}$$

$$P(x,\omega)=i\sqrt{\frac{\rho}{CA_0\left(1-F_J\right)}}\left(-a\cos(\omega x/c)+b\sin(\omega x/c)\right) \tag{4.29}$$

Where, a and b are arbitrary constants of integration. It was stated in Equation (4.10) that the frequency dependent impedance $Z(x,\omega)$ can be defined as

$$Z(x,\omega) = \frac{P(x,\omega)}{Q(x,\omega)}$$

Substituting equations (4.28) and (4.29) into equation (4.10) yields

$$Z(x,\omega) = \frac{ig^{-1}(b\cos(\omega x/c) - a\sin(\omega x/c))}{a\cos(\omega x/c) + b\sin(\omega x/c)} \tag{4.30}$$

$where,\ g = \sqrt{CA_0(1-F_J)/\rho},$

At the distal end of the vessel, $x = L$

$$Z(L,\omega) = \frac{ig^{-1}(b\cos(\omega L/c) - a\sin(\omega L/c))}{a\cos(\omega L/c) + b\sin(\omega L/c)} \tag{4.31}$$

At the proximal end of the vessel, $x = 0$

$$Z(0,\omega) = \frac{i}{g}\frac{b}{a} \tag{4.32}$$

With the assumption that the impedance at the distal end $Z(L,\omega)$ is known, $\frac{b}{a}$ can be found as

$$\frac{b}{a} = \frac{\sin(\omega L/c) + igZ(L,\omega)\cos(\omega L/c)}{\cos(\omega L/c) + igZ(L,\omega)\sin(\omega L/c)}$$

Substituting $\frac{b}{a}$ into equation (4.32) yields the proximal impedance or the root impedance of any vessel as a function of its distal (terminal) impedance

$$Z(0,\omega) = \frac{ig^{-1}\sin(\omega L/c) + Z(L,\omega)\cos(\omega L/c)}{\cos(\omega L/c) + igZ(L,\omega)\sin(\omega L/c)} \tag{4.33}$$

For any given vessel, the proximal (terminal) impedance for zero frequency is,

$$Z(0,0) = \lim_{\omega \to 0} Z(0,\omega) = \frac{8\mu l_{rr}}{\pi r_0^3} + Z(L,0) \tag{4.34}$$

4.3.2 Boundary conditions for small arteries

Similar to large arteries, the governing equations of the small arteries can be solved by implementing suitable boundary conditions. This allows pressure and flow to be computed at any point in the small arteries. It must be noted, however, that the aim for this work is not to compute pressure and flow in the small arteries; rather, it is to use the small arteries to provide a physiological outflow condition for the large arteries. Consequently, the impedances computed in the previous section are of utmost importance with special focus on the root impedance as that provides the outflow condition for the large arteries.

The inflow to the small arteries is the flow coming in from the large arteries.

For the bifurcations in the small arteries, the assumptions remain the same as that of the large arteries (section 4.2.2). These are

- Pressure continuity
- There is no leakage; the flow going out of the parent vessel must be equal to the sum of the flow going into the two daughter vessels.

Bifurcation conditions for small arteries, analogous to of impedances in electrical take the form of

$$\frac{1}{Z_P} = \frac{1}{Z_{d_1}} + \frac{1}{Z_{d_2}} \tag{4.35}$$

Where, Z_P is the impedance of the parent vessel while Z_{d_1} and Z_{d_2} are the impedances of the daughter vessels.

It has been stated before, that viscous forces dominate flow in the smaller arteries. In the fluid dynamical model of small arteries, viscosity has already been accounted for; hence, inclusion of

lumped resistance elements at the terminals of small arteries becomes redundant. Consequently the terminal resistance (Z_t) can be set to zero. It must be noted that the peripheral resistance from various parts of the body is not the same, which can be taken into account by using different values of r_{min} [47].

The boundary conditions described discussed in this section, the definition of r_{min} and the known values of the terminal impedance allow the impedance at the root of the structured tree be computed using equation (32) which provides a physiological outflow to the 1-D model of the larger arteries.

4.4 Numerical Method

The governing equations namely the continuity equation (Equation (4.5)), the momentum equation (Equation (4.6)) and the state equation (Equation (4.4)) need to be solved numerically as analytical solutions are not possible. Before numerically solving them, it is useful to represent the equations in their non-dimensional form. The non-dimensional quantities can be defined as

$$\tilde{x} = \frac{x}{r_c} \quad \tilde{t} = \frac{tq_c}{r_c^3} \quad \tilde{\delta} = \frac{\delta}{r_c}$$
$$\tilde{r_0} = \frac{r_0}{r_c} \quad \tilde{A} = \frac{A}{r_c^2} \quad \tilde{h} = \frac{h}{r_c}$$
$$\tilde{q} = \frac{q}{q_c} \quad \tilde{p} = \frac{pr_c^4}{\rho q_c^2} \quad \tilde{E} = \frac{E}{\rho g r_c}$$

Where, r_c is the characteristic radius of the vessels. q_c is the characteristic flow in the Aorta, ρ is the density of blood and g is the acceleration due to gravity. The values chosen for r_c, ρ, g and q_c are 1 cm, 1.055 g/cm^3, 981 cm/s^2 and 10 cm^3/s, respectively [47][191]. Using the non-dimensional quantities in the continuity gives us the dimensionless continuity equation

$$\frac{\partial \tilde{A}}{\partial \tilde{t}} + \frac{\partial \tilde{q}}{\partial \tilde{x}} = 0 \tag{4.36}$$

While the dimensionless momentum equations is

$$\frac{\partial \tilde{q}}{\partial \tilde{t}} + \frac{\partial}{\partial \tilde{x}}\left(\frac{\tilde{q}^2}{\tilde{A}}\right) + \tilde{A}\frac{\partial \tilde{p}}{\partial \tilde{x}} = -\frac{2\pi\tilde{r}}{\delta\mathcal{R}}\frac{\tilde{q}}{\tilde{A}} \tag{4.37}$$

Where $\mathcal{R} = \frac{q_c}{\nu r_c}$ is the Reynold's number.

The dimensionless state equation is

$$\tilde{p}(\tilde{A}) = \frac{4}{3}\frac{\tilde{E}\tilde{h}}{\tilde{r_0}}\left(1 - \sqrt{\frac{\tilde{A}_0}{\tilde{A}}}\right) \tag{4.38}$$

For simplicity, the tildes can be dropped from the non-dimensional equations from this point on

To numerically solve the system, the Lax-Wendroff method is adopted as mentioned earlier. Following Olufsen [47] and Qureshi [191], the governing equations have to be first expressed in the conservation form. In order to do so a function, B is introduced in its dimensionless form as

$$B\big(r_0(x), p(x,t)\big) = \frac{1}{\rho}\int_{p_0}^{p(x,t)} A[r_0(x), p']dp' \tag{4.39}$$

Makin $A(x,t)$ the subject of the formula in the state equation,

$$A(x,t) = A_0\left(1 - \frac{p(x,t)}{f(r_0)}\right)^{-2} \tag{4.40}$$

where, $f(r_0) = \frac{4}{3}\frac{Eh}{r_0}$

Substituting equation (4.40) into equation (4.39) and differentiating the resulting equation with respect to x gives

$$B = f(r_0)\sqrt{A_0 A}$$

$$\frac{\partial B}{\partial x} = \frac{\partial B}{\partial A}\frac{\partial A}{\partial p}\frac{\partial p}{\partial x} + \frac{\partial B}{\partial r_0}\frac{dr_0}{dx} = A\frac{\partial p}{\partial x} + \frac{\partial B}{\partial r_0}\frac{dr_0}{dx}$$

The momentum equation can now be re-written as

$$\frac{\partial q}{\partial t} + \frac{\partial}{\partial x}\left(\frac{q^2}{A} + B\right) = -\frac{2\pi\nu qR}{\delta A} + \frac{\partial B}{\partial r_0}\frac{dr_0}{dx} \tag{4.41}$$

Coupling the dimensionless state equation (equation (4.38)) with the dimensionless momentum equation (equation (4.37)), $\frac{\partial B}{\partial r_0}\frac{dr_0}{dx}$ can be evaluated as

$$\frac{\partial B}{\partial r_0}\frac{dr_0}{dx} = \left(2\sqrt{A}\left(\sqrt{\pi}\,f + \sqrt{A_0}\frac{df}{dr_0}\right) - \frac{df}{dr_0}\right)\frac{dr_0}{dx}, \tag{4.42}$$

Substituting (4.42) in equation (4.37) and combining it with equation (4.36), the system in the conservation form $\left(\frac{\partial}{\partial t}\,U + \frac{\partial}{\partial x}\,R = S\right)$ can be expressed as

$$\frac{\partial}{\partial t}\begin{pmatrix} A \\ q \end{pmatrix} + \frac{\partial}{\partial x}\begin{pmatrix} q \\ \frac{q^2}{A} + f\sqrt{A_0 A} \end{pmatrix} = \begin{pmatrix} 0 \\ -\frac{2\pi r}{\delta\mathcal{R}}\frac{q}{A} + \left(2\sqrt{A}\left(\sqrt{\pi}\,f + \sqrt{A_0}\frac{df}{dr_0}\right) - A\frac{df}{dr_0}\right)\frac{dr_0}{dx} \end{pmatrix} \tag{4.43}$$

4.4.1 Lax-Wendroff Scheme

This section details the explicit scheme used to solve the governing equations in the arterial tree, namely the Richtmeyer's two-step Lax-Wendroff scheme. This is a second-order method and

requires the system of governing equations be expressed in the conservation form (Equation (4.43)). A basic scheme for each of the following is required

- The interior of the arteries
- Inflow
- Outflow
- Bifurcation

4.4.1.1 Interior

Some intermediate values need to be determined before finding the solution of all the interior points. The intermediate values are computed at steps $\left(m+\frac{1}{2}, n+\frac{1}{2}\right)$ shown in ***Fig. 4-5***.

The conservation form as shown in equation (4.43) is of the form

$$\frac{\partial}{\partial t}U + \frac{\partial}{\partial x}R = S$$

Where, U represent the dependant variables, R is the system flux while S represents the right hand side of the system of equations. Equation (4.43)

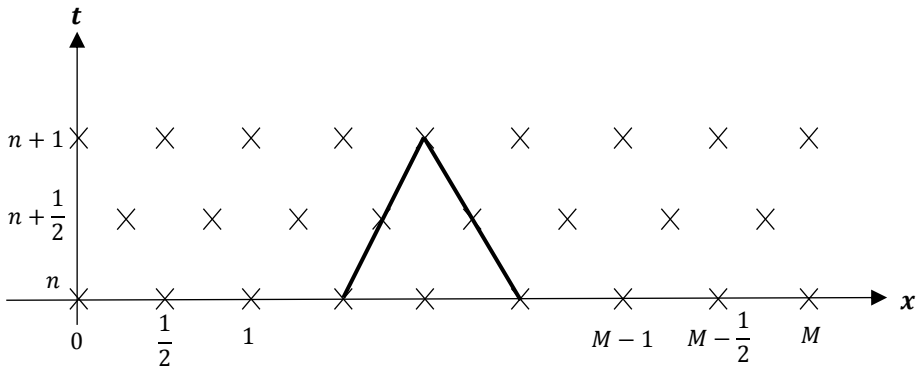

Fig. 4-5: In order to determine values at $n+1$, intermediate values must be determined [47]

Let $U_m^{n+1} = U(m\Delta x, n\Delta t)$ and using the same convention for R and S. By means of a uniform grid, a four point formula can be derived which predicts the flow at time-level $(n+1)$ as

$$U_m^{n+1} = U_m^n = \frac{\Delta t}{\Delta x}\left(R_{m+1/2}^{n+1/2} - R_{m-1/2}^{n+1/2}\right) + \frac{\Delta t}{2}\left(S_{m+1/2}^{n+1/2} - S_{m-1/2}^{n+1/2}\right) \tag{4.44}$$

By means of two intermediate points at time-level, $(n+1)$ the following can be determined

$$\begin{matrix} R_{m+1/2}^{n+1/2} & S_{m+1/2}^{n+1/2} \\ R_{m-1/2}^{n+1/2} & S_{m-1/2}^{n+1/2} \end{matrix}$$

Using the flux and right hand side of the system of equations via the definition

$$U_j^{n+1/2} = \frac{U_{j+1/2}^n + U_{j-1/2}^n}{2} + \gamma\left(-\frac{R_{j+1/2}^n - R_{j-1/2}^n}{h} + \frac{S_{j+1/2}^n - S_{j-1/2}^n}{2}\right) \tag{4.45}$$

Where $j = m + \frac{1}{2}$ and $j = m - \frac{1}{2}$

4.4.1.2 Inflow

As mentioned earlier, the inflow to the system is defined using a periodic function given by equation (4.7). Along with the flow, Q , the area, A is also computed using the boundary condition for q. For the purpose of finding A, a ghost point is introduced (Fig. ***4-6***) that will evaluate $q_{-1/2}^{n+1/2}$ as follows

$$q_0^{n+1/2} = \frac{1}{2}\left(q_{-1/2}^{n+1/2} + q_{1/2}^{n+1/2}\right) \Leftrightarrow$$
$$q_{-1/2}^{n+1/2} = 2q_0^{n+1/2} - q_{-1/2}^{n+1/2} \tag{4.46}$$

From equation (4.44)

$$A_0^{n+1} = A_0^n - \frac{\Delta x}{\Delta t}\left((R_1)_{1/2}^{n+1/2} - (R_1)_{-1/2}^{n+1/2}\right) + \frac{\Delta t}{2}\left((S_1)_{1/2}^{n+1/2} - (S_1)_{-1/2}^{n+1/2}\right)$$

Where,

$$(R_1)_{-1/2}^{n+1/2} = q_{-1/2}^{n+1/2} \qquad and \qquad (S_1)_{-1/2}^{n+1/2} = 0$$

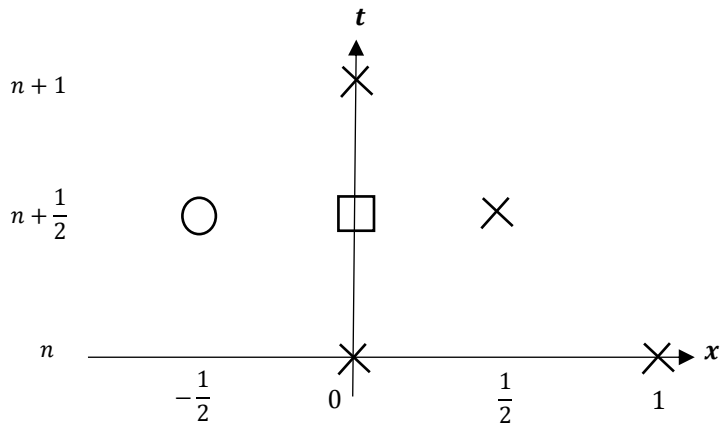

Fig. 4-6: Left boundary: Ghost point a half step $(-1/2)$ before the opening of the vessel and at time-step $n + 1/2$ is marked with a circle. Points specified with a cross are known and the point marked with a square is found by finding the average between adjacent time-steps.

4.4.1.3 Outflow

The convolution integral at the right boundary is expressed and further discretized as

$$q(M\Delta x, t) = \int_0^T p(M\Delta x, t-\tau) q(M\delta x, \tau) d\tau$$

$$q_M^n = p(\mathrm{M}, A_M^n) y_M^0 \Delta t + (q_{tms})_M^n$$

Where, $t = n\Delta t$ and $(q_{tms})_M^n = \sum_{k=1}^{N-1} p_M^{<n-k>_N} y_M^k \Delta t$. In this term, N signifies the number of time steps per period and the power of P_M represents the modulo operator. This boundary condition requires more deliberation as $q(x_M, t)$ is known only as a function of p (or A). From equation (4.44),

$$A_M^{n+1} = A_M^n - \frac{\Delta x}{\Delta t}\left((R_1)_{M+1/2}^{n+1/2} - (R_1)_{M-1/2}^{n+1/2}\right) + \frac{\Delta t}{2}\left((S_1)_{M+1/2}^{n+1/2} - (S_1)_{M-1/2}^{n+1/2}\right)$$

$$= A_M^n - \frac{\Delta x}{\Delta t}\left((R_1)_{M+1/2}^{n+1/2} - (R_1)_{M-1/2}^{n+1/2}\right) \quad (4.47)$$

$S_1 = 0$ and

$$q_M^{n+1} = q_M^n - \frac{\Delta x}{\Delta t}\left((R_2)_{M+1/2}^{n+1/2} - (R_2)_{M-1/2}^{n+1/2}\right) + \frac{\Delta t}{2}\left((S_2)_{M+1/2}^{n+1/2} + (S_2)_{M-1/2}^{n+1/2}\right) \quad (4.48)$$

The unknown variable from these equations are

$$q_M^{n+1} \qquad A_M^{n+1}$$

$$R\left(q_{M+1/2}^{n+1/2}, A_{M+1/2}^{n+1/2}\right) \quad S_2\left(q_{M+1/2}^{n+1/2}, A_{M+1/2}^{n+1/2}\right)$$

For the right boundary, a ghost point is established as shown

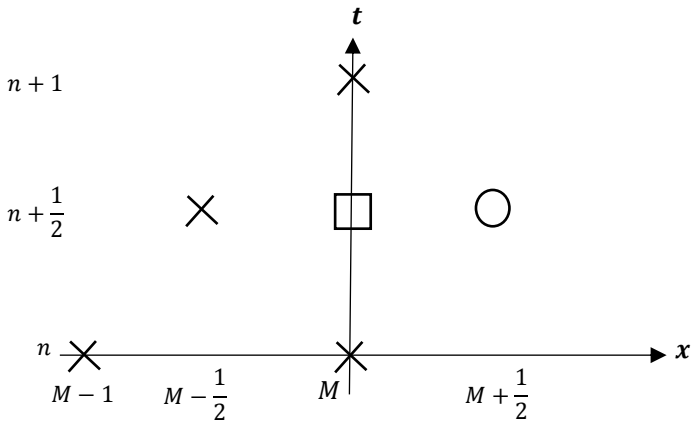

Fig. 4-7: Right boundary: Ghost point a half step $(M + 1/2)$ after the end of the vessel and at time-step $n + 1/2$ is marked with a circle. Points specified with a cross are known and the point marked with a square is found by finding the average between adjacent time-steps.

Using the ghost point,

$$q_M^{n+1/2} = \frac{q_{M-1/2}^{n+1/2} + q_{M+1/2}^{n+1/2}}{2} \tag{4.49}$$

$$A_M^{n+1/2} = \frac{A_{M-1/2}^{n+1/2} + A_{M+1/2}^{n+1/2}}{2} \tag{4.50}$$

The two unknown variables from the equations (4.49) & (4.50) can be determined using the boundary condition at the time-interval $(n + 1/2)$ and $(n + 1)$ as follows

$$q_M^{n+1/2} = p\left(\mathrm{M}, A_M^{n+1/2}\right) y_M^0 \Delta t + (q_{tms})_M^{n+1/2} \tag{4.51}$$

$$q_M^{n+1} = p(\mathrm{M}, A_M^{n+1}) y_M^0 \Delta t + (q_{tms})_M^{n+1} \tag{4.52}$$

The equations (4.51) & (4.52) have the following unknowns

$$\begin{matrix} q_M^{n+1} & A_M^{n+1} & q_M^{n+1/2} \\ A_M^{n+1/2} & q_{M+1/2}^{n+1/2} & A_{M+1/2}^{n+1/2} \end{matrix}$$

For simplicity, equations (4.49) and (4.50) are substituted into equation (4.51) to give

$$\frac{q_{M-1/2}^{n+1/2} + q_{M+1/2}^{n+1/2}}{2} = p\left(\mathrm{M}, \frac{A_{M-1/2}^{n+1/2} + A_{M+1/2}^{n+1/2}}{2}\right) y_M^0 \Delta t + (q_{tms})_M^{n+1/2} \tag{4.53}$$

Signifying that equations (4.47), (4.48), (4.52) and (4.53) need to be solved and the unknowns from these equations are

$$\begin{matrix} x_1 = q_{M+1/2}^{n+1/2} & x_2 = A_{M+1/2}^{n+1/2} \\ x_3 = q_M^{n+1} & x_4 = A_M^{n+1} \end{matrix}$$

4.5 Summary

In this chapter, the one-dimensional model used to simulate blood flow in the arterial network has been set up. The governing equations of the fluid-structure interaction problem in large and small arteries has been comprehensively described. In order to extend the governing equations to the systemic arteries, appropriate boundary conditions have also been prescribed and discussed.

Key points from this chapter are as follows:

- The propagation of blood in the systemic arteries is described by the incompressible axisymmetric Navier-Stokes equations.
- The blood flow is modelled in a bifurcating binary tree of 24 vessels where each vessel is modelled as an impermeable axisymmetric compliant cylinder and the blood is assumed as an incompressible, homogeneous and Newtonian fluid with density, ρ and viscosity, μ.
- The model is divided into two parts; the large arteries and the small arteries. The large arteries originate at the heart and are truncated after a maximum of two generations. The small arteries and arterioles are joined at the distal ends of the large arteries and modelled as binary asymmetric structured trees.
- The elastic properties are evaluated using a relationship of the Young's modulus, the radius of the artery and thickness of the arterial wall.
- In order to extend the incompressible axisymmetric Navier-Stokes equations to an entire arterial network, three boundary conditions are imposed. Firstly, to the inlet of the arterial tree (inflow condition), secondly, at each vessel bifurcation in which a parent vessel bifurcates into two daughter vessels and lastly a boundary condition is imposed at the terminal ends of the tree (outflow condition).
- For the inflow condition, an ejection profile derived using simple relationships of flow in the ascending aorta is imposed. At the bifurcations, pressure continuity and no flow leakage

is assumed. For the outflow condition, small arteries are joined to the terminal ends of the large arteries.

- The small arteries and arterioles attached to the ends of the large arteries are modelled separately as binary asymmetric structured trees. Similar to large arteries, the equations that govern blood propagation in small arteries can be derived from the axisymmetric form of Navier-Stokes equations. However viscous effects are more prominent in small arteries as compared to inertial effects hence the Navier-stokes equations can be linearized by neglecting the non-linear terms.
- In the binary asymmetric structured tree model of small arteries, each of these small arteries keep bifurcating into generations of even smaller arteries until a specified radius, r_{min} has been reached.
- For the bifurcations in the small arteries, the assumptions remain the same as that of the large arteries.
- The boundary conditions described for small arteries, the definition of r_{min} and the known values of the terminal impedance allow the impedance at the root of the structured tree be computed which provides a physiological outflow to the 1-D model of the larger arteries.
- To numerically solve the system, an explicit scheme, namely the Richtmeyer's two-step Lax-Wendroff scheme is used. This is a second-order method and requires the system of governing equations be expressed in the conservation form.
- A basic scheme is required for the interior of the arteries, the inflow and outflow as well as the bifurcations.

CHAPTER 5

ONE-DIMENSIONAL MODEL VALIDATION

5.1 Introduction

In order for a numerical model to be applicable to real life phenomenon, it has to be well validated against real time data. A 1-D cardiovascular model can be quantitatively validated using numerous techniques such as a single vessel [171] or multiple vessels connected to each other to form an arterial network [192]. In the former, the single vessel was a tapered vessel and the simulated and measured waveforms showed excellent agreement. The latter consisted of a silicone experimental model mimicking the arterial network. Again, the 1-D model showed excellent agreement with measured data and demonstrated that 1-D models are capable of capturing the main features of wave propagation in the arterial network of the systemic circulation, the prerequisite being that the geometrical, material and fluid properties are measured properly along with the proper implementation of suitable boundary conditions. These two cases are examples of in vitro validation, however 1-D models can also be validated using in vivo data. These in vivo validations can be further classified into qualitative validation and quantitative validation.

Avolio [81] carried out a qualitative validation, in which the data predicted by the model was compared to pressure and flow data found in literature. In a quantitative validation, the simulated data is compared to measured data from a specific subject (s). Examples of quantitative validation of the 1-D model include the studies by Olufsen et al. [53], Stettler et al. [146] and Reymond et al [193]. In these studies, results from a 1-D model of the arterial network were compared to measured data and showed excellent agreement.

An alternative to experimental studies is using data from a 3-D model and comparing it with the data acquired using a 1-D model. However it must be noted that 3-D models are generally used for

local geometries rather than entire arterial networks due to their computational cost. The implication being, 3-D models need reduced order models to represent downstream vasculature. Usually this is done using compartment or 0-D models to represent the downstream capillaries and smaller vessels [117], [194]–[196]. The models simulate geometries with smaller resistances and lesser outlets. In the case of more complex geometries, numerical instability is introduced which can be reduced at the expense of a higher computational cost.

It is noteworthy that validating a 1-D model against physiological data is tedious because the geometrical and elastic properties of physiological vessels is very difficult to quantify. Additionally, the geometrical, fluid and elastic properties of one subject are not necessarily the same as another subject. A study conducted by Mulder et al. [197] concluded that the geometrical properties and boundary conditions have an enormous impact on the propagation of blood flow in the arterial network, therefore, these geometrical properties and boundary conditions should be patient-specific.

The model in use for this work allows variation of geometric, elastic and fluid properties with much ease as well the variation of boundary conditions to simulate a multitude of pathophysiological conditions as will be seen in the next chapter. In this chapter, the results of the current model are compared with previous 1-D/3-D models as well as in-vivo data, in order to assess the validity of the model before using it to simulate physiological and pathophysiological conditions.

In this study, three case studies are presented for numerical validation. The first comparison is with the pulse wave propagation along a single vessel (section 5.2). The next comparison is with a 3-D model that has several branches (section 5.3) and finally the model is compared with a full-scale arterial network, which has been validated against in-vivo flow data (section 5.4).

5.2 Pulse propagation along the aorta (single vessel)

5.2.1 Introduction

In this section, the propagation along a single vessel namely the aorta is simulated. The vessel parameters are taken from literature [63]. The parameters used in [63] are for a healthy, young adult and the parameters were originally taken from the data published by Westerhof et al [80]. A 1-D model was used by Alastruey to simulate the aorta in [63] however, in that model the downstream vasculature (distal end of the vessel) is represented using a three-element Windkessel model. As mentioned before, the Windkessel model characterizes the compliance as well as the resistance of the vessels by using an electric analog model. Also known as, an RCR lumped parameter model, in the Windkessel model, two values of resistances are defined and a value of capacitance is defined. It extends upon the concept of a two-element Windkessel model in which a single resistance and capacitance are defined. The resistance in the two-element model describes the peripheral resistance which is the resistance to flow encountered by blood as it flows through the systemic circulation while capacitance describes the arterial compliance [38]. However, in the two-element CR model (**Fig. *5-1***, left), pressure and flow undulations are produced which can be reduced greatly by simply adding another resistor in series with the CR model [63]. This added resistor (**Fig. *5-1***, right) represents the characteristic impedance of the aorta, that is, it accounts for the resistance to flow due the aortic valve. **Fig. *5-1*** shows the representations of the CR and RCR models, where R_{μ_1} is the added resistor in the three-element model while R_{μ_2} and C represent the peripheral resistance and arterial compliance, respectively and Q and P represent the flow rate and time-varying pressure, respectively.

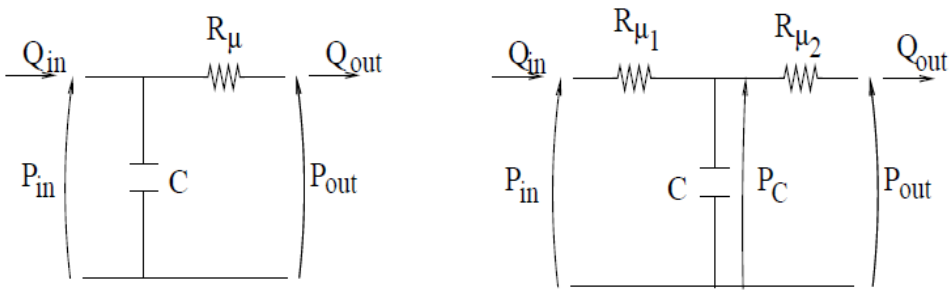

Fig. 5-1: Representation of Lumped parameter models as electric circuit analogues. The circuit of the left is a two-element (CR) model where the capacitor represents arterial compliance while the resistor represents peripheral resistance. The circuit on the right is the three-element (RCR) model where the second resistor represents the characteristic impedance of the aorta. Q and P represent the flow rate and time-varying pressure, respectively. [63]

The results from the current model are compared with simulation results of the model used by Alastruey [63]. The model used by Alastruey was validated against the data published by Simon et al. [198] and showed excellent capability of the model to approximate key hemodynamic features. Detailed validation can be found here: [63].

The geometric, elastic, fluid and RCR parameters used in Alastruey's model can be summarized in the **Table *5-1***:

Table 5-1: Geometric, elastic, fluid and boundary condition (RCR) parameter definition by Alastruey [63] to simulate pulse wave propagataion along the aorta (single vessel)

Parameter	Value
Length of aorta, L (m)	0.40
Radius of aorta at diastolic pressure, r_0 (m)	0.01

Young's Modulus of aorta, E (Pa)	4.0×10^5
Wall thickness, h (m)	0.0015
Blood density, ρ (kg/m^3)	1050
Blood viscosity, μ $(mPa\ s)$	4.0
Sum of the resistances of the RCR mode, $R_{\mu_1} + R_{\mu_2}$ $(Pa\ s\ m^{-3})$	1.89×10^8
Peripheral compliance, C (m^3/Pa)	6.31×10^{-9}

5.2.2 Methodology

At the inlet of the aorta, an ejection profile is prescribed, Q_{in}. This ejection profile is periodic with a period, $T = 0.8s$ ensuring a heart rate of 75 beats/min. The ejection flow profile is enforced via the equation:

$$Q_{in}(t) = \begin{cases} Q_0 \sin\left(\frac{\pi t}{\tau}\right) & if\ t < \tau \\ 0 & otherwise \end{cases} \quad (5.1)$$

Where, Q_0 is the peak value and $\tau = 0.25s$ marks the end of systole and hence the beginning of diastole, whereby the aortic valve shuts and no more blood flows into the aorta. Q_0 has a value of $311.5\ ml/s$. This value is used to ensure the cardiac output is $3.8\ l/min$ which is the measured cardiac output in the validation data from Simon et al. [198]. The ejection profile is shown in **Fig. *5-2***.

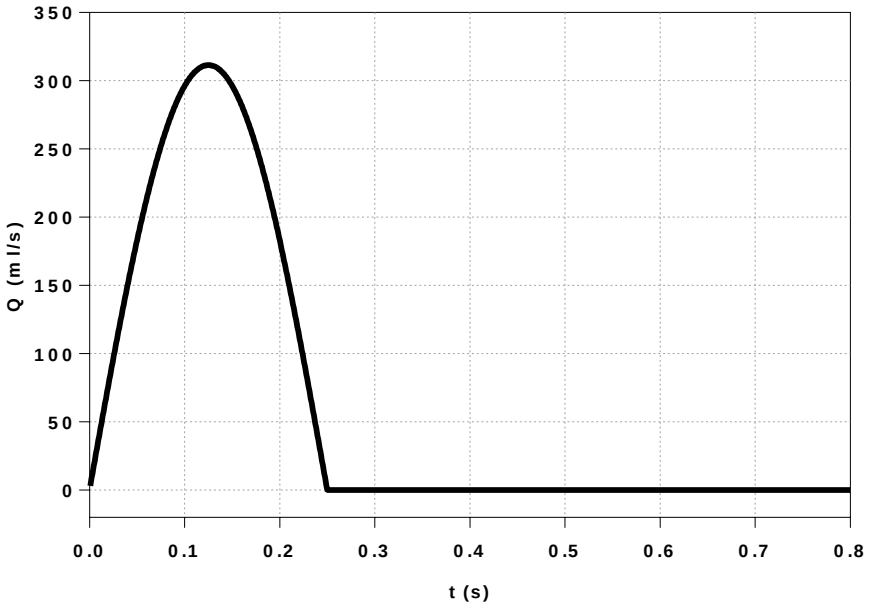

Fig. 5-2: Ejection profile used as the inflow boundary condition for the one-dimensional model

Using the parameters given in Appendix A and the 1D model described in the previous chapter, implemented via the algorithms given in Appendix B, the aorta was simulated. The variables were measured at 3 different locations by dividing the aorta into 3 main locations namely the inlet (proximal end), mid of the aorta and the outlet (distal end) of the aorta. This division is shown in **Fig. 5-3**.

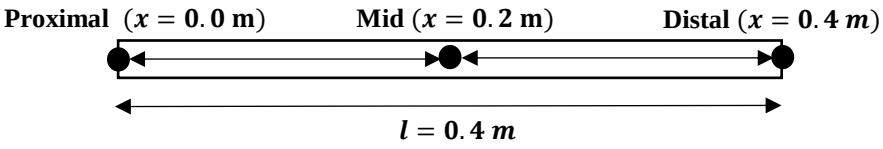

Fig. 5-3: Division of the human Aorta into three sections for the purpose of simulation

5.2.3 Results

Fig. *5-4* shows the comparison of the flow and pressure waveforms of the current 1-D model and Alastruey's 1-D model. The flow waveforms are taken from the mid and distal ends of the aorta. **Fig. *5-4*** (a) and (c) show the flow and pressure waveform comparison at the mid of the aorta, respectively, while **Fig. *5-4*** (b) and (d) show the flow and pressure waveform comparison at the distal end of the aorta, respectively.

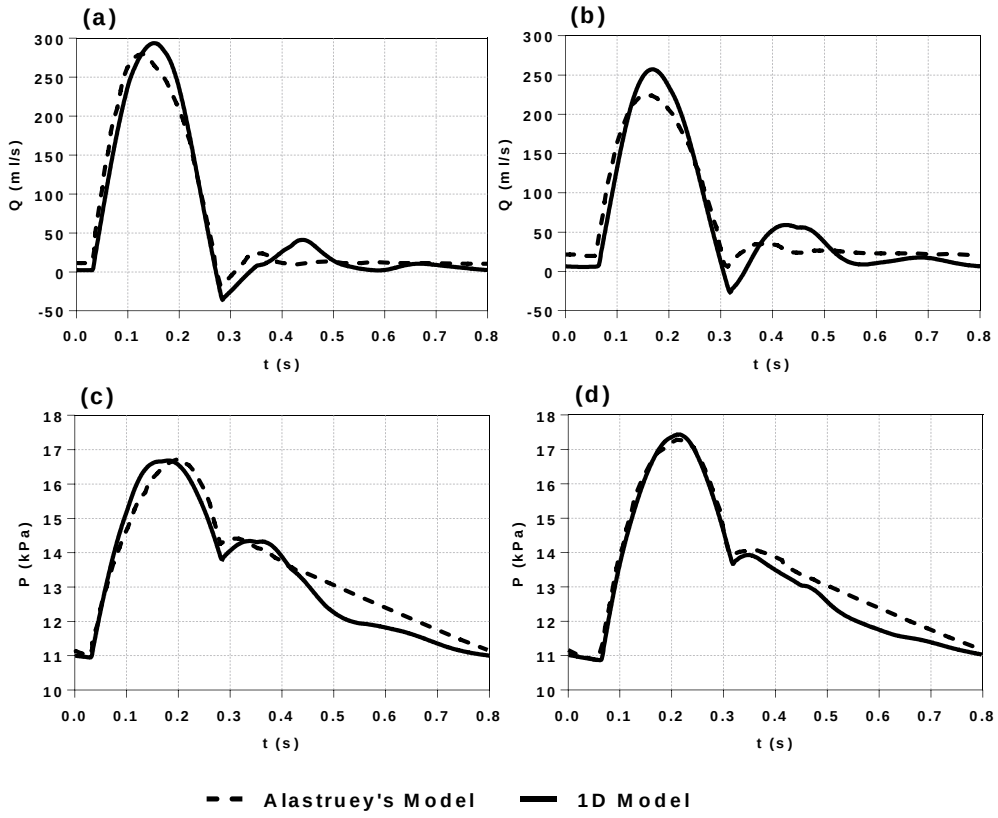

Fig. 5-4: Structured tree outflow model for a single aorta results (solid) compared with the results of Alastruey's RCR outflow model for a single aorta (dashed). (a) Flow comparison at mid-section ($x = 0.2\ m$) of the aorta (b) Flow comparison at the distal end ($x = 0.4\ m$) of the aorta (c) Pressure comparison at mid-section ($x = 0.2\ m$) of the aorta (b) Pressure comparison at the distal end ($x = 0.4\ m$) of the aorta.

Towards the distal end, it can be seen that the flow rate for both models, decreases. At the inlet, Q_0 has a value of 311.5 ml/s, but by the time the flow reaches the mid of the aorta, the flow decreases to approximately 280 ml/s in Alastruey's model and 293 ml/s in the current 1-D model. The flow rate keeps decreasing downstream and by the time the distal end is reached the flow has decreased to 223 ml/s in Alastruey's model and 255 ml/s in the current 1-D model. This decrease in flow downstream is better presented in **Fig. *5-5***. Downstream, during diastole the flow does not go to zero; instead, the flow increases slightly and decreases again. The delay in each flow waveform due to the distance of the waveform from the inlet can be clearly seen.

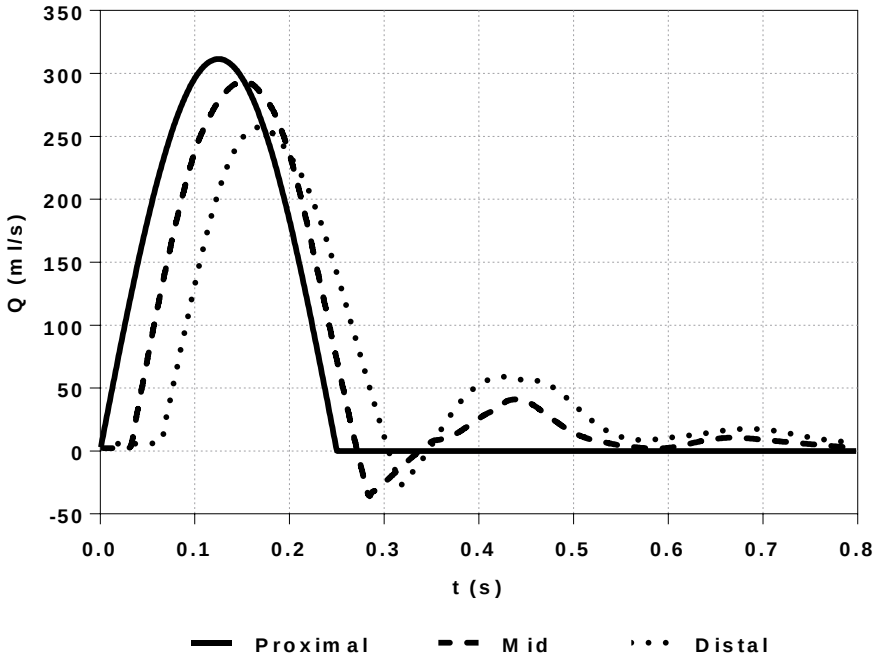

Fig. 5-5: Flow rate time histories at three locations along the aorta- Proximal (solid), mid (dashed) and distal (dotted). In terms of spatial dimension, the proximal, mid and distal sections are $x = 0.0\ m, x = 0.2\ m\ and\ x = 0.4\ m$.

The pressure increases downstream. The pressure in the mid of the aorta for Alastruey's model peaks at $16.70\ kPa$ while in the current model, the pressure in the mid of aorta peaks at $16.68\ kPa$. At the distal end Alastruey's model and the currents model, pressure peaks at $17.30\ kPa$ and $17.44\ kPa$, respectively. The dicrotic notch; a second peak in the pressure waveform which signifies the closure of the aortic valve is also observed. At the mid-section, the second peak, reaches its maximum value of $14.34\ kPa$ and $14.32\ kPa$ for Alastruey's and the current model, respectively. The same secondary peaks take the peak value of $14.10\ kPa$ and $13.93\ kPa$, at the distal ends for Alastruey's model and the current model, respectively. Downstream, although pressure increases, the second pressure peak decreases.

This can be clearly seen again, from **Fig. *5-4*** (c) and (d).

The pressure results obtained are compared quantitatively with Alastruey's model at the mid-section of the aorta as well as the distal end of the aorta (**Table *5-2***). The table summarizes the systolic pressure, P_S and the diastolic pressure, P_D in the mid and distal sections of the aorta for both the models. In both models, the P_S increases towards the distal end of the vessel. However, P_D reduces towards the distal end in both models. The percentage error is also provided between each value and is calculated via equation (5.2),

$$\%\ error = \frac{|Experimental\ value - Accepted\ value|}{Accepted\ value} \times 100 \qquad (5.2)$$

In this equation the experimental value is the one simulated using the 1-D model while the accepted value is the one taken from the data published by Alastruey [63].

Table 5-2: Summary of the comparison of systolic pressure, P_S and the diastolic pressure, P_D in the mid and distal sections of the aorta for both the models.

Location	**Mid**			**Distal**		
Variable	**Alastruey's Model**	**Current Model**	**% error**	**Alastruey's Model**	**Current Model**	**% error**
$\boldsymbol{P_S}$ **(kPa)**	16.70	16.68	0.12	17.30	17.44	0.81
$\boldsymbol{P_D}$ **(kPa)**	11.00	10.95	0.45	10.80	10.87	0.65

The simulated results are compared with in-vivo data from Simon et al. [198] as well as Alastruey's model [63] in **Table *5-3***. The current 1-D model's mean systolic and diastolic pressures correspond well with the model used by Alastruey and the P_S lies well within the range of the in-vivo data. P_D does not fall within the range of the in-vivo data, but fares well when compared to the model used by Alastruey.

Table 5-3: Comparison of the mean systolic, P_S and diastolic, P_D pressures between data measured in-vivo by Simon et al. [198], results from Alastruey's RCR outflow model [63] and the current 1-D model with structured outflow condition.

	In-Vivo	**Alastruey's Model**	**Current 1-D model**
Mean $\boldsymbol{P_S}$ **(kPa)**	16.8 ± 0.4	16.63	16.89
Mean $\boldsymbol{P_D}$ **(kPa)**	9.5 ± 0.4	11.0	10.94

5.2.4 Discussion

In section 5.2.2, the computed pressure and flow waveforms from the 1-D model were compared with a 1-D model from literature that uses an RCR model as it's boundary condition [63] as well as in-vivo data from literature [198]. The waveform shapes and amplitudes were compared to conclusively validate the model for a single vessel, both qualitatively as well as quantitatively. The simulation results showed excellent agreement with the model (***Fig. 5-4***) as well as the in-vivo data (***Table 5-3***). As mentioned in section earlier, in the systemic circulation, systolic pressure increases as the distance from the heart increases due to wave reflections and impedance at the terminal ends of the arteries. Additionally, the amplitude and mean flow rate decreases downstream. This decrease is due to the increase in the impedance to flow. These features are captured extremely well by the current 1-D model (***Fig. 5-4*** and ***Fig. 5-5***). Other key features of the pressure waveforms namely the dicrotic notch and the diastolic delay are also observed. The dicrotic notch signifies the closure of the aortic valve or simply the start of the diastolic phase. In this phase, no more blood enters the aorta. This is simulated by the inflow profile (***Fig. 5-2***). After $0.25s$, for the model used in this section, the flow goes to zero and there is a slight backflow, which gives rise to the dicrotic notch or the second peaking of the pressure waveforms. Downstream, the effect of the closure of the valve has reduced effect on the pressure waveforms, due to the distance from the heart, which explains why the amplitude of the second peak decreases downstream. The current 1-D model excellently captures this feature (***Fig. 5-4***).

The mean pressure decreases slightly towards the distal ends in both models. In Alastruey's model, the decrease is $0.01\ mmHg$ while in the current model the decrease is $0.05\ mmHg$. This slight decrease in mean pressure is because the fluid viscosity introduces resistance to flow. The resistance due to viscous dissipation is much smaller as compared to peripheral resistance, hence the mean pressure decrease very slightly.

Table *5-2* and ***Table 5-3*** summarized and compared the results of the 1-D model with that of Alastruey [63] and the data published by Simon et al. [198]. The percentage errors between the two models being compared remain under 1% signifying excellent agreement of the results between the two models despite having different outlet conditions. Both the numerical models perform well when compared to in-vivo data. Overall, the agreement of the results with the validation data was excellent and the exhibition of the key features of the pressure and flow waveforms ensures the capability of the model with structure tree outflow condition, to simulate blood flow in a single vessel.

The minimal discrepancies between the 1-D model and Alastruey's model can be explained by the choice of the downstream boundary conditions. In section 5.2, it was shown that the downstream boundary condition used by Alastruey is an RCR, three element Windkessel model while the downstream boundary condition used in the current model is a structured tree outflow condition. In the RCR models, values of resistances and capacitance define the resistance to flow and the arterial distensibilty, respectively. However, in the structured tree outflow condition, the governing equations explained in section 4.3 are used to simulate blood flow in smaller vessels providing a physiological boundary condition, which captures wave propagation/reflection effects very well. On the other hand, RCR models are known to lack the ability to capture wave reflection effects, well enough. From ***Fig. 5-4*** and ***Fig. 5-5***, it can be clearly seen the flow rates of the current model tend to have undulations in the mid-section as well as the distal end due to the incorporation of wave propagation effects. In contrast, Alastruey's models flow rates noticeably have minimal undulations.

Another important difference is that in Alastruey's model, the Young's modulus is defined explicitly. In the current model, the elastic properties are evaluated using a relationship (Equation (4.4)) of the Young's modulus, the radius of the artery and thickness of the arterial wall. The parameters used to define such a relationship have been reported in Appendix A. Due to the

difference in the method of describing the stiffness of the vessel, the vessel used in Alastruey's model does not have the same stiffness as the vessel used in the current 1-D model.

5.3 Pulse propagation in the arterial network- Comparison with a 3-D model

5.3.1 Introduction

In this section, the current 1-D model is compared with a 3-D model developed by Kim et al. [199]. The model used by Kim et al. is a 3-D finite-element model of the aorta. The model outputs pressure and flow waveforms in the descending aorta, more specifically the thoracic aorta. In their work, the heart is modelled as a lumped parameter model and coupled to the 3-D model to provide the inflow to the 3-D model. By modelling the heart, as such, provides physiologically realistic aortic flow waveforms [199]. The model is used to simulate a normal human thoracic aorta under rest and exercise conditions as well as a diseased thoracic aorta in the form of an aortic coarctation (narrowing of the aorta), present in the descending thoracic aorta. The parameters used for the 3-D simulation of the aorta under healthy conditions are summarized in **Table *2-1***:

Table 5-4: Elastic and fluid parameter definition by Kim et al. [199] to simulate pulse wave propagataion a 3-D model of the aorta and it's main branches.

Parameter	Value
Young's Modulus, E $(dynes/cm^2)$	6.0×10^6
Wall thickness, h (cm)	0.1
Blood density, ρ (g/cm^3)	1.06

Blood viscosity, μ $(dynes/cm^2\ s)$	0.04

The 3-D model starts at the root of the aorta, the inlet of the blood into the systemic circulation. The 3-D model includes the main upper branches, which are the right and left subclavian as well as left and right carotid arteries. The downstream vasculature as well as the terminal ends of the upper arteries are represented using a three-element Windkessel model (RCR) [199]. The RCR model was described in the previous section. RCR models are commonly coupled to 3-D computational domains to reduce the computational cost and to make the model simulations time efficient. This was seen earlier in section 5.2.1. The flow distribution to each of the outlets of the 3-D model is based on data from literature as well as data measured using cine phase contrast magnetic resonance imaging (cine PC-MRI) [199]. The 3-D model of the aorta with the main upper branches is shown in ***Fig. 5-6***. The description of the RCR models at different outlets is also shown in **Fig. *5-6*** (inset) along with the illustration of the RCR model.

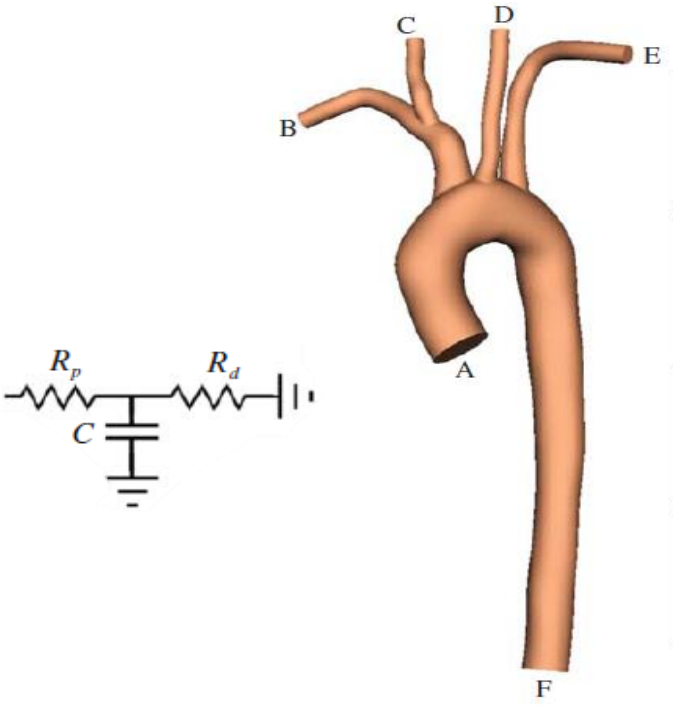

B: Right subclavian artery		
	Rest	Exercise
R_p (dynes·s/cm^5)	1040	1040
C (cm^5/dynes)	8.74E-5	8.74E-5
R_d (dynes·s/cm^5)	16300	16300

C,D: Right and left carotid arteries		
	Rest	Exercise
R_p (dynes·s/cm^5)	1180	1180
C (cm^5/dynes)	7.70E-5	7.70E-5
R_d (dynes·s/cm^5)	18400	18400

E: Left subclavian artery		
	Rest	Exercise
R_p (dynes·s/cm^5)	970	970
C (cm^5/dynes)	9.34E-5	9.34E-5
R_d (dynes·s/cm^5)	15200	15200

F: Descending thoracic aorta		
	Rest	Exercise
R_p (dynes·s/cm^5)	188	75
C (cm^5/dynes)	4.82E-4	4.82E-4
R_d (dynes·s/cm^5)	2950	1270

Fig. 5-6: Diagrammatic representation of the 3-D model of the aorta and its main upper branches used by Kim et al. [199]. The inset on the right shows the parameters used for the RCR model to represent the downstream vasculature as well as the terminal ends of the upper arteries while the inset on the left illustrates the RCR model used by Kim et al.

5.3.1 Methodology

Since the 3-D model represents the entire arterial network in a lumped manner, the model for a single vessel, validated in the previous section, is extended to simulate an entire arterial network. This arterial network is the one used in the next chapters, with a few variations in its parameters. Details of the boundary conditions and the mathematical formulation of such a model were given in chapter 4. Using the parameters given in Appendix A and the 1D model described in the previous chapter, implemented via the algorithms given in Appendix B, the entire arterial network was simulated.

The geometry of the arterial tree is based on the data published by Olufsen et al. [82] and imitates the geometry of physiological arteries (**Table 5-5**). This model has been validated qualitatively as well as quantitatively by comparing it with data measured using Magnetic resonance techniques. The model permits all the important aspects of physiological fluid-structure interaction to be captured accurately without increasing the computational load. The arterial tree is illustrated in **Fig. *5-7*** while the geometry of the arterial tree is given in **Table 5-5**.

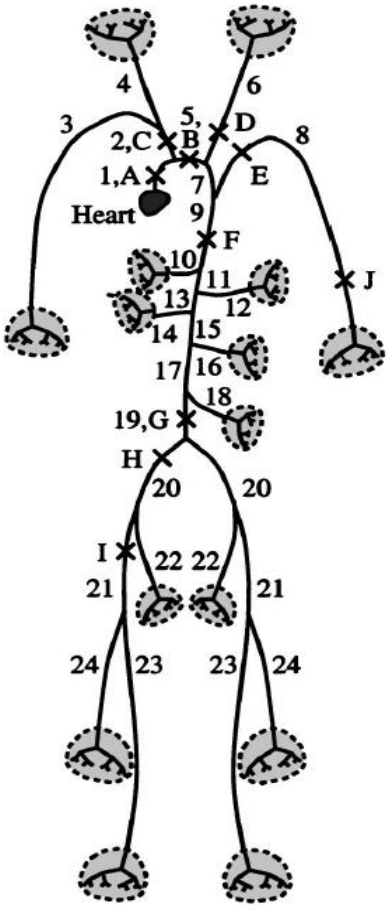

Fig. 5-7: Schematic of the arterial tree network taken from Olufsen et al. [82]. This arterial tree is used to simulate blood flow in the large arteries of the systemic circulation. The trees highlighted in grey at the terminal (outlet) ends of the arteries represent the structured tree of small arteries.

Table 5-5: Geometrical data for the one-dimensional model. Parameters L, r_{in} and r_{out} are the length, inlet radius and outlet radius of the artery. r_{min} is the truncation radius of the structured trees while R and L denote right and left. r_{min} is defined for only terminal arteries. (Taken from [82])

	Artery	$\boldsymbol{L}$ $(\boldsymbol{cm})$	$\boldsymbol{r_{in}}$ $(\boldsymbol{cm})$	$\boldsymbol{r_{out}}$ $(\boldsymbol{cm})$	$\boldsymbol{r_{min}}$ $(\boldsymbol{cm})$
1	Ascending aorta	7.0	1.25	1.14	-
2	Anonyma	3.5	0.7	0.7	-
3,8	R, L Subclavian and Brachial	43.0	0.44	0.28	0.01
4	Right common carotid	17.0	0.29	0.28	0.02
5	Aortic arch I	1.8	1.14	1.11	-
6	Left common carotid	19.0	0.29	0.28	0.03
7	Aortic arch II	1.0	1.11	1.09	-
9	Thoracic aorta	18.8	1.09	0.85	-
10	Celiac axis	3.0	0.33	0.30	0.02
11	Abdominal aorta I	2.0	0.85	0.83	-
12	Superior Mesenteric	5.0	0.33	0.33	0.02
13	Abdominal aorta II	2.0	0.83	0.80	-
14,16	R, L Renal	3.0	0.28	0.25	0.02
15	Abdominal aorta III	1.0	0.80	0.79	-
18	Inferior Mesenteric	4.0	0.20	0.18	0.01
17	Abdominal aorta IV	6.0	0.79	0.73	-
20	External Iliac	6.5	0.45	0.43	-
19	Abdominal aorta V	3.0	0.73	0.70	-

21	Femoral I	13.0	0.43	0.40	-
22	Internal Iliac	4.5	0.20	0.20	0.01
23	Deep femoral	11.0	0.20	0.20	0.01
24	R, L Femoral II	44.0	0.40	0.30	0.01

For the purpose of this validation, simulated results from the arterial network is compared with the data from the 3-D model for a healthy human aorta under rest conditions. As mentioned earlier, in the 3-D model, a lumped model of the heart is coupled to the 3-D model to provide the inflow. To make the simulations simpler, the inflow profile from the data published by Kim et al. [199] is taken instead of modelling the heart separately. Additionally, instead of attempting to model the exact inflow of the 3-D model through curve fitting, equation (5.1) is used again to provide the inflow for the 1-D model used here. By using a simple equation, a consistent and generic inflow profile is produced which reduces the complexity of modelling and at the same time reduces the number of subject-specific parameters required for the inflow profile. However, in order to make sure the inflow profile approximates the inflow taken from literature well enough, the parameters of the inflow equation are adjusted, accordingly. **Fig. *5-8*** shows the aortic inflow taken from Kim et al. [199] and the inflow profile used for the 1-D model by using equation (5.1). For ease of access, the equation is stated again,

$$Q_{in}(t) = \begin{cases} Q_0 \sin\left(\frac{\pi t}{\tau}\right) & if\ t < \tau \\ 0 & otherwise \end{cases}$$

Where, Q_0 is the peak value and $\tau = 0.28s$ marks the end of systole and hence the beginning of diastole, whereby the aortic valve shuts and no more blood flows into the aorta. Q_0 has a value of

$305\ ml/s$. The values of Q_0 and τ have been adjusted to approximate the inflow from the 3-D model as closely as possible as seen in **Fig. *5-8***.

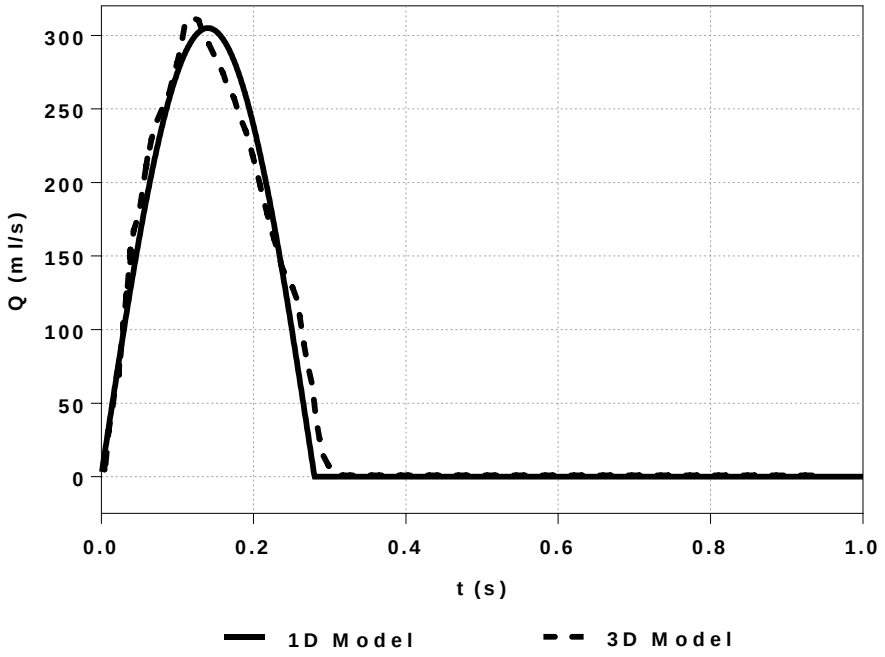

Fig. 5-8: Comparison between the inflow ejection profile used for 1-D model (Solid) and the inflow ejection profile used for the 3-D model (Dashed). The time period used for the 3-D model is $T = 0.952\ s$, the time period for the 1-D model is $T = 1.0\ s$.

5.3.2 Results

Using the geometrical properties defined in **Table 5-5** and the inflow profile described via **Fig. *5-8***, the arterial network of a healthy human subject was simulated. Additional parameter definition of the arterial network can be found in Appendix A. The computed pressures from this model at different locations are compared with the pressure data published by Kim et al. [199] in **Fig. *5-9***. The locations used for the pressure validation are the ascending aorta, Fig. ***5-9*** (a), the thoracic aorta **Fig. *5-9*** (b), the left subclavian **Fig. *5-9*** (c) and left carotid artery **Fig. *5-9*** (d) and finally the right

subclavian **Fig. *5-9*** (e), and right carotid artery **Fig. *5-9*** (f). The shape of the waveforms show extremely good agreement along with excellent computation of the systolic and diastolic pressures in all the locations.

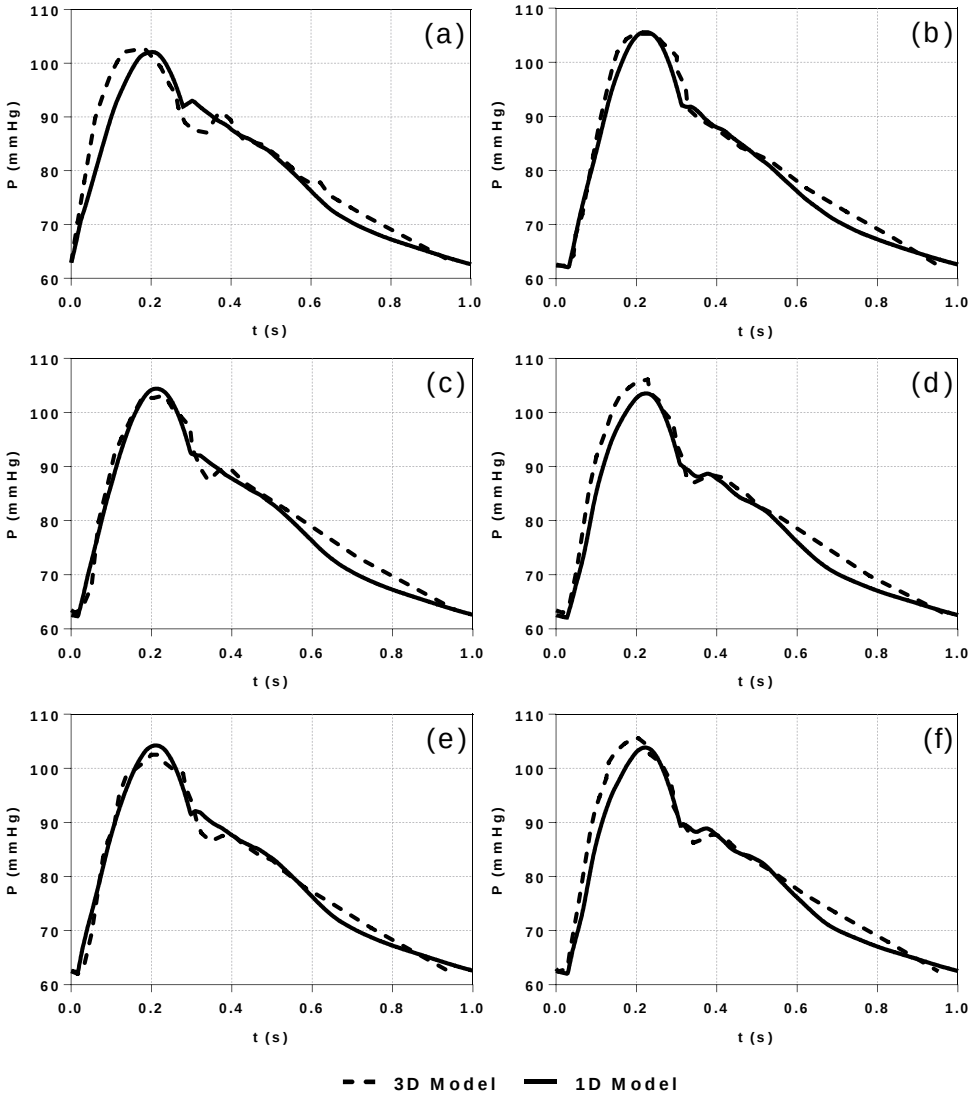

Fig. 5-9: Comparison between the pressure waveform time histories obtained from the 1-D model of the entire arterial network (solid) and the pressure waveform time histories obtained from the 3-

D model (dashed). The measurements locations are (a) ascending aorta (b) thoracic aorta (c) left subclavian artery (d) left carotid artery (e) right subclavian artery (f) right carotid artery.

Table *5-6* summarizes the systolic pressures, P_S, the diastolic pressures, P_D and the mean pressures, P_m measured at the six different locations for the 3-D and 1-D model and compared by calculating the percentage error. The percentage error is calculated via equation (5.2),

Table 5-6: Summary of the values of systolic pressure, P_S, the diastolic pressure, P_D and the mean pressure, P_m obtained from the 1-D model and the 3-D model at different anatomical locations. The comparison is quantified by finding the percentage error between the results obtained from the two models.

Location	P_S $(mmHg)$			P_D $(mmHg)$			P_m $(mmHg)$		
	3-D	**1-D**	**% error**	**3-D**	**1-D**	**% error**	**3-D**	**1-D**	**% error**
Ascending aorta (a)	102.6	102.1	0.5	62.9	62.9	0	82.8	82.5	0.3
Thoracic aorta (b)	105.3	105.6	0.3	63.4	62.6	1.3	84.4	84.1	0.3
Left subclavian (c)	102.7	104.3	1.5	63.5	62.6	1.4	83.1	83.5	0.4
Left carotid (d)	106.1	103.5	2.5	63.5	62.5	1.6	84.8	83.0	2.1
Right subclavian (e)	102.5	104.2	1.6	62.5	62.6	0.2	82.5	83.4	1.1
Right carotid (f)	105.6	103.8	1.7	63.5	62.6	1.4	84.6	83.2	1.6

The percentage errors lie in the range of 0% to 2.5%. The highest errors for P_S, P_D and P_m occur for the left carotid artery. The pressures tend to increase away from the heart. This increase is most prominent in the thoracic aorta.

The flow rates at different locations are not used for any applications of the 1-D model in the following chapters. However, for the purpose of completeness, the flow rates computed at the left subclavian and thoracic aorta by the 1-D model are compared to the flow rates published by Kim et al. [199]. **Fig. *5-10*** (a) shows the comparison of 1-D model computed flow rate with the 3-D model computed flow rate in the thoracic aorta while **Fig. *5-10*** (b) shows the computed flow rates in the left subclavian artery. The profiles of the waveforms show excellent agreement with the 1-D computed flow rates peaking at 180.1 ml/s and 29.1 ml/s for the thoracic and left subclavian arteries, respectively. In comparison, the 3-D model flow rates peak at 172 ml/s and 30.3 ml/s for the thoracic and left subclavian arteries, respectively.

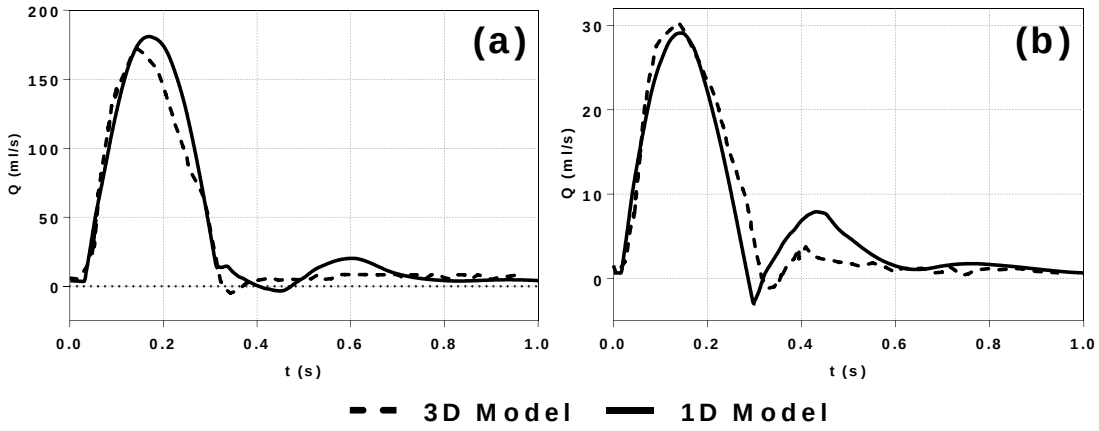

Fig. 5-10: Comparison of the periodic flow rate time histories between the 1-D model (solid) and the 3-D model (dashed) at two locations; (a) thoracic aorta (b) left subclavian artery

Fig. *5-11* shows the pressure in the right brachial artery simulated using the 1-D model. The pressure is measured approximately at the mid-section of the upper arm where the routine blood pressure measurements are made. The published data did not include the brachial waveform however; it did include the measured systolic and diastolic pressures in the brachial artery.

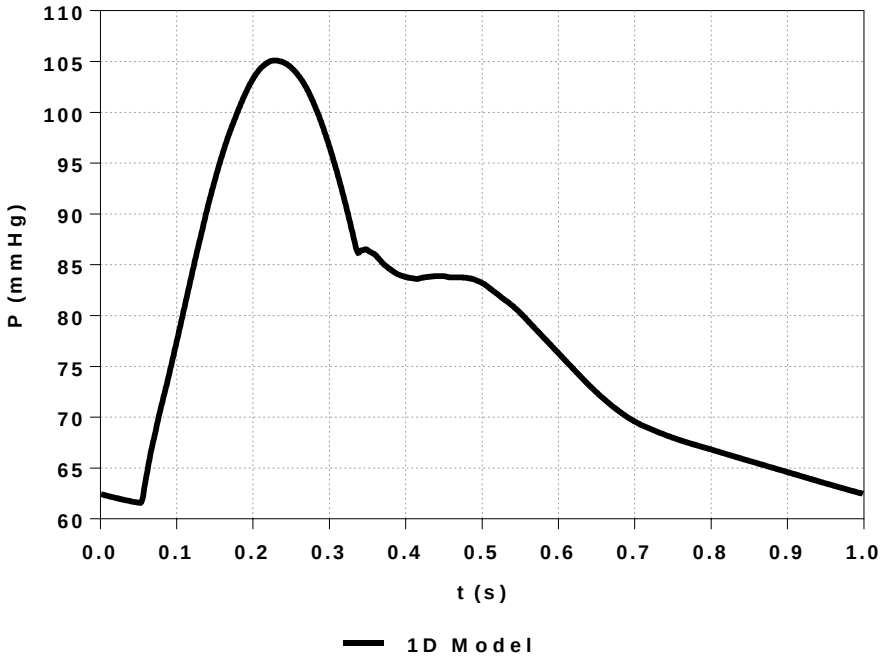

Fig. 5-11: Pressure waveform obtained from the 1-D model in the right brachial artery

This brachial pressure is compared with the brachial pressure simulated using the 3-D model as well as the brachial pressure data measured for a human subject under rest conditions by Kim et al. [199] in **Table *5-7***:

Table 5-7: Comparison of the systolic, P_S and diastolic, P_D pressures in the brachial artery between the 1-D model, the 3-D model and an actual human subject. Data for the 3-D model and the in-vivo measurement is taken from [199]

	Human subject	**3-D Model**	**1-D Model**
$P_S\ (mmHg)$	106	106	105.1
$P_D\ (mmHg)$	63	62	62.4

The corresponding values of the 1-D model show excellent agreement with both the human subject as well as the 3-D model.

5.3.3 Discussion

In section 5.3.1, the 1-D model is compared with a 3-D model. The 3-D model represents the entire arterial network in a lumped manner. Again, the outflow boundary conditions are described using an RCR model for the 3-D model. For this section, instead of using a single vessel or a group of a few branching vessels, the 1-D model is used to simulate the entire arterial tree (***Fig. 5-7***) with geometrical properties defined in **Table 5-5**. The comparison between the simulated results of the 1-D model and 3-D model are quite satisfactory. Not only is the 1-D model capable of reproducing the results attained from the 3-D model quantitatively but also qualitatively. The wave shape is preserved and the systolic and diastolic pressures are reproduced with excellent accuracy. The error analysis carried out in **Table *5-6*** testifies to the extent of accuracy of the 1-D model. The percentage errors lie in the range of 0% to 2.5%. Keeping in mind that a 1-D model being compared to a 3-D model has such a low percentage error, increases confidence in the robustness of the 1-D model.

Again, the model shows an increase in pressure downstream which agrees well with literature. The brachial pressure simulated using the 1-D model (***Fig. 5-11***) shows excellent agreement with the data measured for an actual human subject by Kim et al. [199] further cementing the capability of the 1-D model with a structured tree outflow condition.

The profiles of the flow waveforms also show excellent agreement with a decrease in flow downstream, which again, is in good agreement with literature.

Although the discrepancies are small, they can be explained again by the difference in the outflow boundary condition as well as the explicit definition of the Young's modulus in the 3-D model. These differences were explained in the previous section.

The geometry of the 3-D model is not the same as the arterial network used here. In an attempt to simplify modelling, the same arterial network is used for most of the simulations with variations arising only in the parameters that define arterial stiffness or the peripheral resistance. Owing to the difference in geometries between the 3-D and the 1-D model, discrepancies arise.

Lastly, as mentioned earlier, instead of modelling inflows iteratively, the inflow is modelled using a simple half-sinusoidal equation that approximates the inflow profiles taken from literature. The difference in inflow profile is another source of discrepancy.

5.4 Pulse propagation in the arterial network- Comparison with measured data and Olufsen's model

5.4.1 Introduction

In this section, the current 1-D model is compared with the model proposed by Olufsen et al. [43], [47], [82] with the data published by Olufsen et al [82]. Olufsen et al. compared their 1-D model with structured tree outflow condition with flow data measured using magnetic resonance techniques. Details of the subject used for the measurements are given in **Table *5-8***.

Table 5-8: Details of the subject used for the in-vivo measurement to compare the numerical results against.

Age ($\boldsymbol{years}$)	32
Height ($\boldsymbol{cm}$)	178
Weight ($\boldsymbol{kg}$)	65
Average heart rate ($\boldsymbol{bpm}$)	51

5.4.2 Methodology

Fig. *5-12* shows the aortic inflow taken from Olufsen et al. [82] and the inflow profile used for the 1-D model by using equation (5.1). Olufsen's inflow profile is the one measured in the ascending aorta for the human subject. For the inflow used in the current model, Q_0 has a value of $428\ ml/s$ while $\tau = 0.37s$. The period lasts $1.1s$. The values of Q_0 and τ have been adjusted to approximate the inflow from the taken from the published data as closely as possible as seen in **Fig. *5-12***.

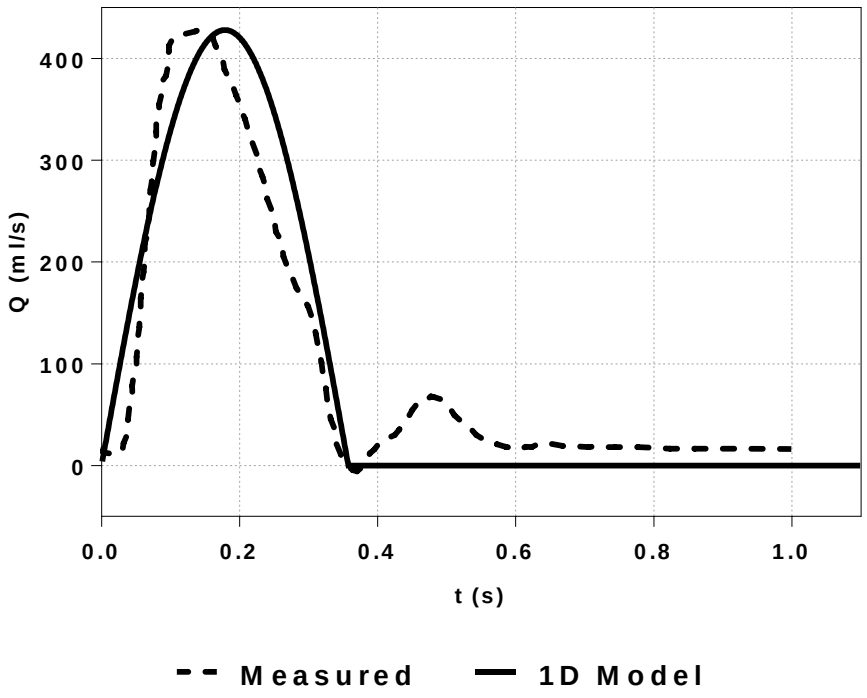

Fig. 5-12: Comparison between the inflow ejection profile used for 1-D model (solid) and the inflow ejection profile measured in-vivo (dashed). The time period is $T = 1.1\ s$.

The measured inflow peaks at $428\ ml/s$ and the diastole starts around $0.38s$. It can be noticed that the inflow has a slight undulation during diastole. In contrast, the half sinusoid used in the 1-D model has no such undulations. The peak flow rate is the same as the measured inflow profile while

diastole starts at $0.37s$. An important feature in **Fig. *5-12*** is the delay in the peeking of the flow rate. The measured data is physiological; hence, it is not based on a mathematical relation while our inflow is based on a mathematical equation (equation (5.1)). Using the parameters given in Appendix A and the 1D model described in the previous chapter, implemented via the algorithms given in Appendix B, the entire arterial network was simulated again.

The arterial tree used for this section for the 1-D model is illustrated in ***Fig. 5-7*** while the geometry of the arterial tree is given in **Table 5-5**.

5.4.3 Results

Fig. ***5-13*** (a), (b), (c), (d) and (e) show the comparison of the model predicted waveforms and data measured using Magnetic resonance imaging (MRI) at the aortic arch, thoracic aorta, abdominal aorta, external iliac and femoral artery, respectively. The shape of the waveforms show extremely good agreement along with excellent computation of the peak flowrates in all the locations. The slight deviation in the wave shape is due to different inflow used in the 1-D model. Nevertheless, majority of the peaks and nadirs do coincide which complement the overall agreement of the simulated data with measured data.

From the flow waveforms, it is obvious that away from the heart, the flow rate decreases gradually. Of all the measurement locations, the femoral artery is farthest away and demonstrates a very low flow rate as compared to locations near or around the heart such as the aortic arch or the thoracic aorta. To put this decrease into perspective, the flow rate in the 1-D model peaks at $345\ ml/s$ in the aortic arch, however by the time the flow rate reaches the femoral artery, the peak value is only $46.5\ ml/s$, implying a loss of approximately $300\ ml/s$ between the two locations. Additionally, the flow rate peaks at approximately 0.19 s in the aortic arch. While the peeking in flow rate in the femoral artery is seen at 0.28s. The delay is due to the distance of the two locations from the heart. Since the femoral artery is farther away, the peeking occurs later.

No measured pressure data was provided in the locations where the flow waveforms were validated. However, since pressure waveforms are of utmost importance as will be seen the next chapters, the pressure waveforms of the current 1-D model are compared with the validated 1-D model of Olufsen et al. [82].

Fig. *5-14* (a), (b), (c), (d) and (e) show the comparison of the 1-D model predicted pressure waveforms with the pressure waveforms from the 1-D model used by Olufsen et al to validate the flow data. The locations of measurement remain the same, that is, the aortic arch, thoracic aorta, abdominal aorta, external iliac and femoral artery, respectively.

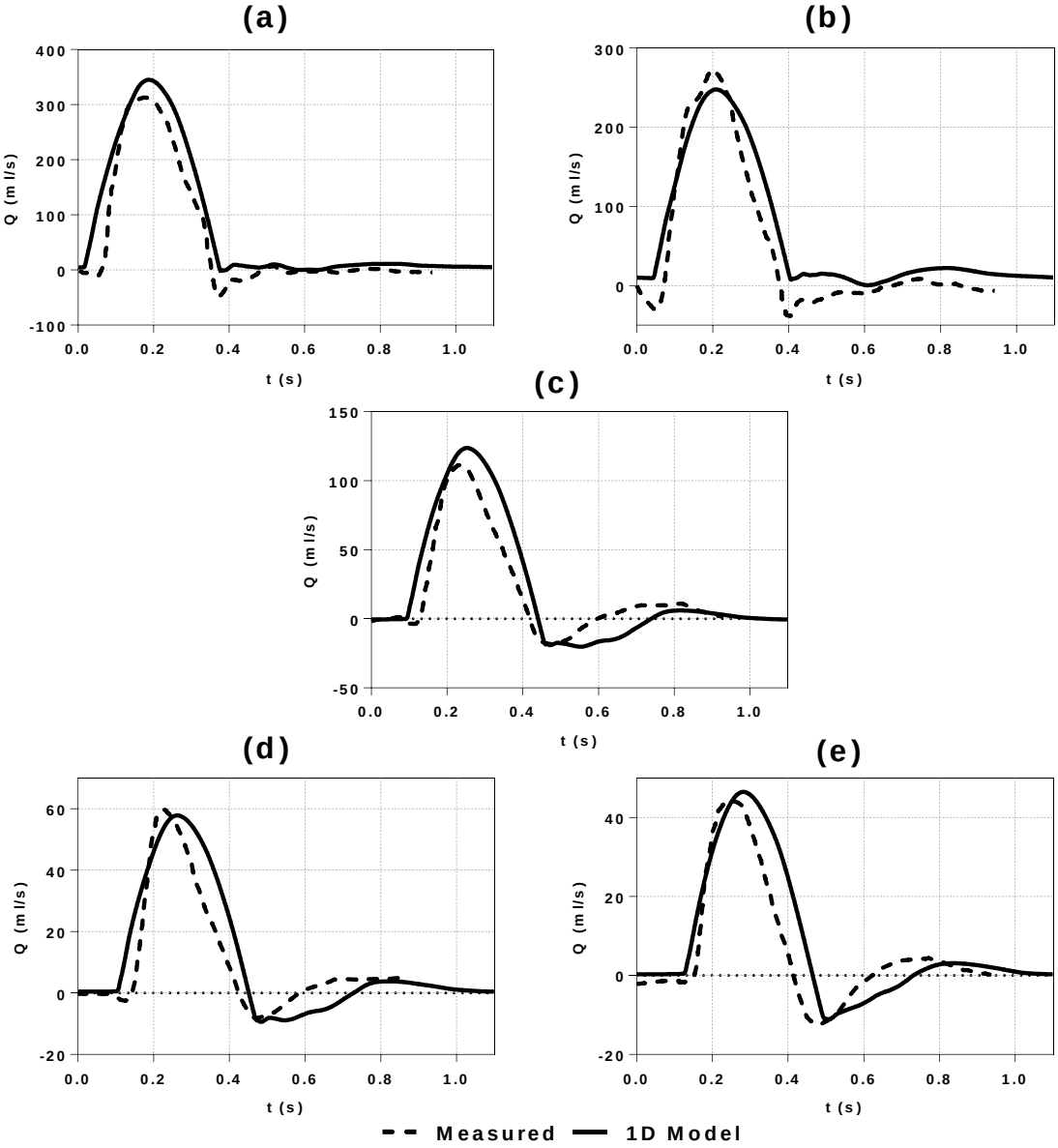

Fig. 5-13: Comparison between the flow waveform time histories obtained from the 1-D model of the entire arterial network (solid) and the flow waveform time histories measured in-vivo using MRI (dashed). The measurements locations are (a) aortic arch (b) thoracic aorta (c) abdominal aorta (d) external iliac (e) femoral artery.

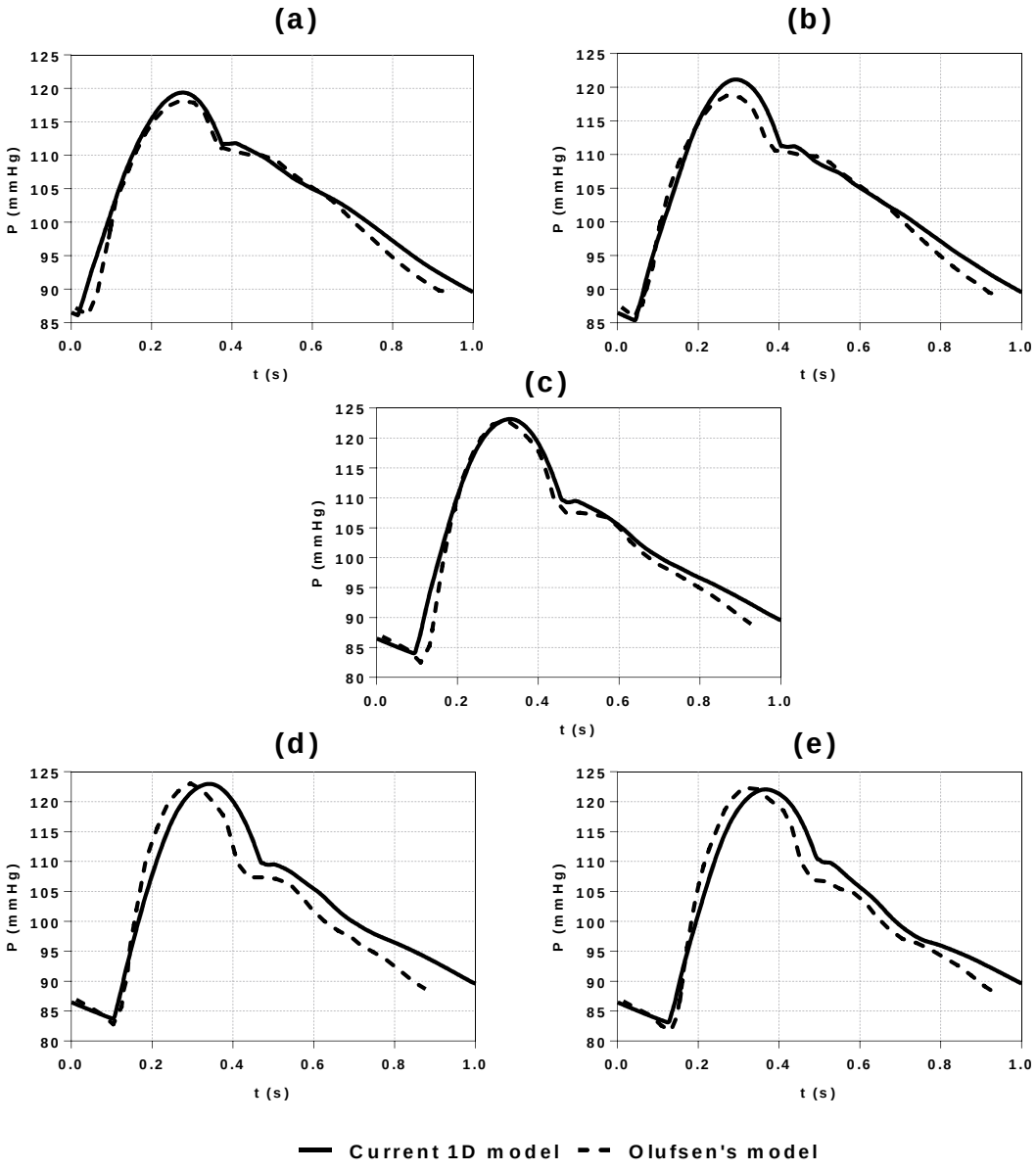

Fig. 5-14: Comparison between the pressure waveform time histories obtained from the 1-D model of the entire arterial network (solid) and the pressure waveform time histories obtained from the 1-D model of the entire arterial network used by Olufsen (dashed). The measurements locations are (a) aortic arch (b) thoracic aorta (c) abdominal aorta (d) external iliac (e) femoral artery.

The pressure waveforms of the current 1-D model show excellent agreement with the model output of Olufsen et al. Despite using different inflow profiles, the pressures peaks and nadirs align with near perfection. The percentage error is also provided (**Table *5-9***) between each value and is calculated via equation (5.2). In this equation the experimental value is the one simulated using the 1-D model while the accepted value is the one taken from the data published by Olufsen et al. [82].

Due to the flow rate peeking delay seen in the ejection profile, **Fig. *5-12***, there is some deviation in the pressure waveforms, however, it is very minimal. The delay becomes most obvious in the lower body, that is, in the external iliac and femoral artery.

Table 5-9: Summary of the values of systolic pressure, P_S and the diastolic pressure, P_D from the current 1-D model and the 1-D model used by Olufsen et al [82] at different anatomical locations. The comparison is quantified by finding the percentage error between the results obtained from the two models.

Location	P_S $(mmHg)$			P_D $(mmHg)$		
	Olufsen's Model	**Current Model**	**% error**	**Olufsen's Model**	**Current Model**	**% error**
Aortic Arch (a)	118.15	119.38	1.04	86.16	86.12	0.05
Thoracic Aorta (b)	118.74	121.16	2.04	85.86	85.40	0.54
Abdominal Aorta (c)	123.03	123.18	0.12	82.51	84.04	1.85
External Iliac (d)	123.06	122.97	0.07	82.78	83.75	1.17

Femoral (e)	122.34	122.05	0.24	81.71	83.13	1.74

The pressure increases as the distance from the heart increases. The dicrotic notch reduces with the distance from heart. This reduction in the second peeking was demonstrated in section 5.2.2 as well. Again, due to the distance from the heart, downstream, the peeking of the pressure is slightly delayed just as it was for the flow rate.

5.4.4 Discussion

In section 5.4.2, the 1-D model is compared with flow data measured experimentally. The data is taken from literature [82] and was measured using MRI for a human subject at various anatomical locations.

Olufsen et al. [43], [47], [82] proposed a model with a structured tree outflow boundary condition rather than using the more commonly used Windkessel model. In this model, the smaller vessels are modelled separately and the equations governing the fluid structure interaction are solved to simulate blood flow in the tree of smaller vessel, which provides the impedance for the large systemic arteries. This boundary condition, being physiological in nature, allows wave propagation effects to be incorporated in the 1-D model unlike the electrical models used to describe the downstream vasculature.

The model used in this work, is the one proposed by Olufsen et al, justifying the need to validate the current model against the simulated data of Olufsen's model as well. The comparison with in-vivo data as well as the original model conclusively validates the 1-D model, especially before using it to simulate various physiological and patho-physiological conditions as will be seen in the next chapter.

When compared to the measured flow data, the shape of the computed flow waveforms show extremely good agreement along with excellent computation of the peak flowrates in all the locations (**Fig. *5-13***). Majority of the peaks and nadirs coincide which reflect the overall agreement of the simulated data with measured data. Again, the flow rate decreases with increasing distance from the heart.

Since the pressure data for the locations of flow validation was not available, the current 1-D model's results are compared results from Olufsen's model that validates the flow waveforms. The pressure predictions when compared with Olufsen's model show excellent agreement (**Fig. *5-14***). The pressure increases away from the heart while the dicrotic notch decreases. From **Fig. *5-14*** it can be seen that the pressure predictions are extremely close to the pressures predicted by Olufsen's model despite using a different inflow profile as well as using slightly different parameters (Appendix A). The percentage errors (**Table *5-9***) all lie within a minimum value of 0.05% and a maximum value of 2.04%, conclusively validating the model developed here for the arterial network.

5.5 Summary

In this chapter, the one-dimensional model used in this work is validated. The validation is carried out by first simulating blood flow in a single vessel that mimics the human aorta, followed by a comparison with a 3-D model with several main upper body branches and finally the entire human arterial network. In each of these models, found in literature, in-vivo data has been provided as a benchmark. The 1-D model used here fares extremely well against the models as well as the in-vivo data. The significance of this multi-level validation is to demonstrate the robustness as well as the ability of the 1-D model with a structured tree outflow condition to simulate simple vessels as well as more complicated entire arterial networks. This increases confidence in the clinical applications of 1-D modelling.

Key points from this chapter are as follows:

- 1-D cardiovascular models have to be validated against in-vitro and in-vivo data before using them to simulate real world phenomenon.
- Validating a 1-D model against physiological data is tedious because the geometrical and elastic properties of all physiological vessels is very difficult to quantify.
- The current model is validated against the pulse wave propagation along a single vessel, a 3-D model that has several branches and finally a full-scale arterial network, which has been validated against in-vivo flow data.
- For the single vessel and 3-D models, the downstream vasculature (distal end of the vessel) is represented using a three-element Windkessel model while the full-scale model's downstream conditions are governed using the structured tree outflow boundary condition.
- The one-dimensional model shows excellent agreement with in-vivo data as well as the results from various models found in literature. The qualitative as well as quantitative validation is extremely satisfactory.
- Other key features of the pressure waveforms namely the dicrotic notch and the diastolic delay are also observed.
- The discrepancies between the one-dimensional model, Alastruey's model and the 3-D model can be explained by the difference in the treatment of the downstream vasculature In the RCR models, values of resistances and capacitance define the resistance to flow and the arterial distensibilty, respectively. However, in the structured tree outflow condition, flow is simulated in smaller arteries providing a physiological boundary condition, which captures wave propagation/reflection effects very well
- Another important difference is that in Alastruey's model and 3-D model, the Young's modulus is defined explicitly. In the current model, the elastic properties are evaluated

using a relationship of the Young's modulus, the radius of the artery and thickness of the arterial wall.

- A source of discrepancy between the 3-D model, the full-scale model and the current model is the inflow profile used in the current model. However, due to the proximity of the inflow profile used to the inflow profile compared against, the discrepancies are minimal.

CHAPTER 6

PHYSIOLOGICAL AND PATHOLOGICAL PRESSURE RESPONSE DATABASE

6.1 Introduction

1-D models allow modelling various physiological and pathological conditions making them extremely attractive as research tools. In addition to exhibiting key features of blood propagation in the cardiovascular system, 1-D models, if properly implemented, are flexible enough to allow variation of parameters, individually. The parameters can be broadly sub-categorized into geometrical, elastic and fluid parameters.

In this chapter, variations of these parameters is carried out to simulate a range of cardiovascular responses under different degrees of healthy and vascular disease conditions. From the simulated response data, the arterial pressure data is specifically collected to form a database for the next chapter, which is the estimation of the GTF. The flow responses from the simulated results are used to assist the interpretation of the pressure variations simulated.

6.2 Variation of cardiac output

6.2.1 Physiological implications and significance of cardiac output

The cardiac output (CO), is the amount of blood pumped by the heart per minute and is calculated via the equation [50]

$$CO = Stroke\ volume \times heart\ rate \tag{6.1}$$

where, the stroke volume is given in $liters/beat$ and the heart rate is given in $beats/min$. The physiological range of the cardiac output lies in the range of $4 - 8\ L/min$ [200], depending on the

cardiovascular needs of an individual. However lower cardiac inputs have been observed [198]. The mean average CO is approximately $5\ L/min$. In order to comprehensively take the range of the COs and the corresponding pressure responses of the cardiovascular system into account, simulations for thirteen cases are carried out. In these cases, the CO is increased from a minimum value of $3.1\ L/min$ to a maximum value of $6.83\ L/min$. The mean CO of this range then becomes $4.97\ L/min$ which is approximately the mean average CO.

6.2.2 Parametric study of cardiac output simulation

The inflow ejection profiles are enforced via equation (5.1). Using the generic inflow, it is much simpler to manipulate the cardiac output. For the uniformity of the database, the heart rate is not changed hence, the time period is kept constant at $T = 1.1\ s$. However, in order to change the cardiac output, the peak value Q_0 is changed for each of the thirteen cases. Table 6-1 shows the peak values used and the corresponding mean CO obtained. Fig. ***6-1*** (a-d) show the flow and pressure waveforms in the ascending aorta, brachial artery, abdominal aorta V (right before the iliac bifurcation) and the femoral artery, respectively for selected cardiac outputs.

Table 6-1: Various peak values, Q_0 used to simulate varying cardiac outputs.

Case	**Peak value, Q_0** (ml/s)	**Cardiac Output, CO** (l/min)
1	250	3.10
2	275	3.41
3	300	3.73
4	325	4.04
5	350	4.35
6	375	4.66
7	400	4.97
8	425	5.31

9	450	5.59
10	475	5.90
11	500	6.21
12	525	6.52
13	550	6.83

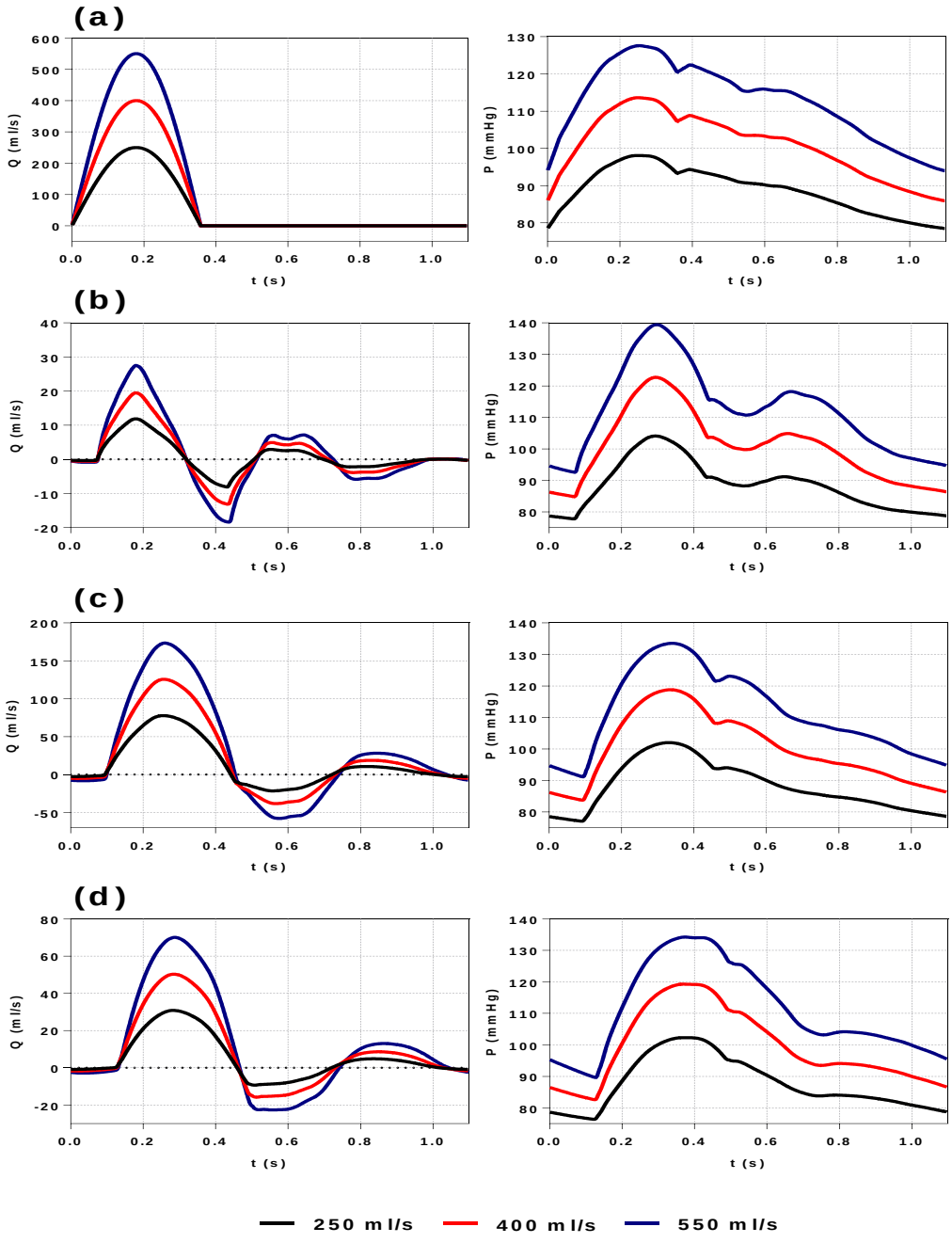

Fig. 6-1: Comparison of the flow (left) and pressure (right) waveform time histories obtained from the 1-D model by increasing cardiac outputs, when the peak flow values are $250ml/s$ (black), $400ml/s$ (red) and $550ml/s$ (blue). The anatomical measurement locations are (a) ascending aorta (b) brachial artery (c) abdominal aorta V (d) femoral artery

6.2.3 Discussion

It can be very clearly seen from **Fig. *6-1***, with each increment in the CO, the flow in the entire system increases causing pressure to increase in all arteries. However, the shape of the waveforms is preserved. The reason for the perseverance is because the variation brought about in the system is a physiological one rather than a pathological one. The increase in the system's flow and hence the pressure is because the size of the cardiovascular system has been kept constant while increasing the CO. The different COs used here allow enough variation of the CO in the pressure response database.

Although the flow rates described here represent physiological conditions, an increase or decrease of flow rate can also represent pathological conditions. For instance, severe dehydration or loss of blood through injury causes less availability of blood for pumping via the heart [201], hence reducing CO. On the other hand, waste removal diseases such as kidney failure, do not allow waste products to be expelled efficiently from the body, leading to an increase in the volume of blood, thereby increasing CO [201]. However, it has to be pointed out that under such a scenario, blood rich in waste materials would have the behavior of a Non-Newtonian fluid and the assumptions used here would fail to characterize the behavior of blood.

Quantifying the increase or decrease in blood volume under such circumstances is very complicated. Since GTF estimation needs a pressure response database with physiological and pathological conditions, quantification of the volume of blood is rendered trivial.

6.3 Variation of arterial stiffness

6.3.1 Physiological implications and significance of arterial stiffness

Arterial stiffening is the modification of the medial characteristics of an artery which cause a reduction in the compliance of the arterial wall causing a decrease in the buffering capability of the artery to the periodic pulsation of blood through it [202], [203]. The reduced compliance of the arterial walls results in arterial stiffening, which inevitably reduces the storage capacity of the artery and at the same time, increases the pulse wave velocity. The reduced storage capacity means the absorption of energy becomes inefficient, giving rise to increased pulse pressure [204]. The effects of arterial stiffening are the same as vasoconstriction, which is the narrowing of blood vessels due to the contraction of muscles in the arterial walls [205]. However, vasoconstriction is a natural response of the cardiovascular system to an external stimuli such as exposure to severe cold, to maintain mean arterial pressure. Vasoconstriction causes a loss in blood flow, increase in peripheral resistance and an increase in blood pressure. Vasoconstriction is also brought about via the use of blood pressure increasing medication.

Increase in pulse pressure over a long period of time due to damage to structural integrity of arteries caused by ageing and other pathological conditions, increase the risk factor for cardiovascular diseases (CVDs). The progression of risk of CVDs is worsened with progressing age [204], [206], [207]. Such diseases include (but are not limited to) diabetes, hypertension and renal disease [208], [209]. These conditions pose a cardiovascular risk as they cause symptoms characteristic of cardiovascular failure such as restriction of blood supply to tissues (ischaemia), increased stiffness of arteries and increased pulse pressure which are aggravated in severity with age [210].

The increase in arterial stiffening due to age is well documented, across different sex and ethnic groups [211]. The stiffening of arteries brings about an alteration to the response of the cardiovascular system to physiological needs such as changes in volume and pressure loading [208].

It has also been shown that the stiffness of the ventricles in the heart also increases with age [212]. Ageing leads to the widening of the arterial pulse that signifies stiffening of arteries [208] which is a risk factor for several CVDs [213], [214].

One such disease is hypertension, which is perhaps the most frequently recorded chronic disease in the world. 1 out of 4 people in the US have hypertension [215] and the prevalence increases drastically with age. It has been reported, between the ages of 18-39, 7.2% of people have hypertension while 30.1% of people, aged between 40-59 years are hypertensive. For people over 65 years, the prevalence is 65.4%. The lifetime risk of hypertension for individuals that are 55 years old is approximately 90% [215], [216]. After the age of 55 years, the systolic pressure progressively increases while the diastolic pressure decreases hence increasing the pulse pressure leading to the development of isolated systolic hypertension (ISH). Owing to this, ISH is the most prevalent form of hypertension in the older population [217], [218]. ISH can be easily characterized by the increase in the systolic pressure and a decrease in the diastolic pressure [219]. Studies have revealed that an increase in the systolic pressure increases the risk of CVDs significantly as compared to an increase in diastolic pressure [220].

There are various factors that contribute to ISH but the most important ones are arterial stiffening due to age as well as reduced compliance of the systemic arteries [218]. The decreased compliance leads to a less prominent cushioning of the volume ejected into the ascending aorta leading to a higher systolic pressure [221], [222]. As mentioned earlier, the bifurcating nature of arteries and the tapering of arteries along their respective length as well as the impedance at terminal sites, give rise to reflected waves. These waves superimpose on the incoming pressure waves and cause an increase in the systolic pressure. When arteries get stiffer, the wave reflections take place earlier in a cardiac cycle because of the increase in the pulse wave velocity [218], hence reaching the root of the aorta before the occurrence of the dicrotic notch. Thus increasing the systolic pressure and pulse pressure

further, especially at the root of the aorta [218]. This predictably strongly correlates hypertension with arterial stiffening [223].

Another extremely important contributor to CVDs and arterial stiffening is obesity. In a correlational study [224], it was shown that arterial stiffness was strongly correlated with higher body weight as well as hip and waist circumference. Interestingly, the study was independent of sex, age, ethnicity and the systolic blood pressure, making the correlation stronger. A key finding in the study is that the relationship between arterial stiffness and obesity becomes apparent at an early age.

Another disease associated with arterial stiffening is diabetes. It has been shown that impaired glucose metabolism or failing glucose tolerance as seen in type-2 diabetes causes a decrease in arterial distensibilty, thus an increase in arterial stiffness [225].

With the conclusive evidence presented here of how arterial stiffness increases with age and is the key contributor to several CVDs, this chapter seeks to use the 1-D model to simulate pressure/flow waveforms under the effects of increased stiffness. Due to a number of diseases associated with arterial stiffening and the common features seen in them (the recurring increase in arterial stiffness), classifying increased stiffness under one disease would do injustice to the characterization of the disease as well as the modelling capability of the 1-D model. Hence, this section is simply referred to as variation of arterial stiffness and can be seen under a multitude of perspectives such as ageing, hypertension, peripheral vasoconstriction, peripheral vasodilation and/or obesity.

6.3.2 Parametric study of arterial stiffness simulation

In order to comprehensively take arterial stiffness as well the increase in peripheral resistance into account for the generation of the pressure response database, the stiffness of the arteries is increased gradually.

In order to simulate arterial stiffening, the stiffness of the arteries is increased by changing the parameters of the stiffness relation (Equation (4.3)). The stiffness is increased from normal stiffness, which was validated in section 5.4, to a 100% increase in stiffness, that is, the stiffness is doubled. The incremental increase in stiffness is taken as 10% in order to take a wide range of stiffness' into consideration. Ten simulations are carried out, generating ten different stiffness cases for the pressure response database.

Fig. ***6-2*** shows the comparison of a healthy subject and the subjects with stiffness' increased by 50 and 100%. Fig. ***6-2*** (a-d) show the flow and pressure waveforms in multiple anatomical location, namely the ascending aorta, brachial artery, thoracic aorta and the femoral artery, respectively for selected incremental arterial stiffness'. The locations have been chosen arbitrarily in order to encompass parts of the body that lie in the upper body as well as the lower body.

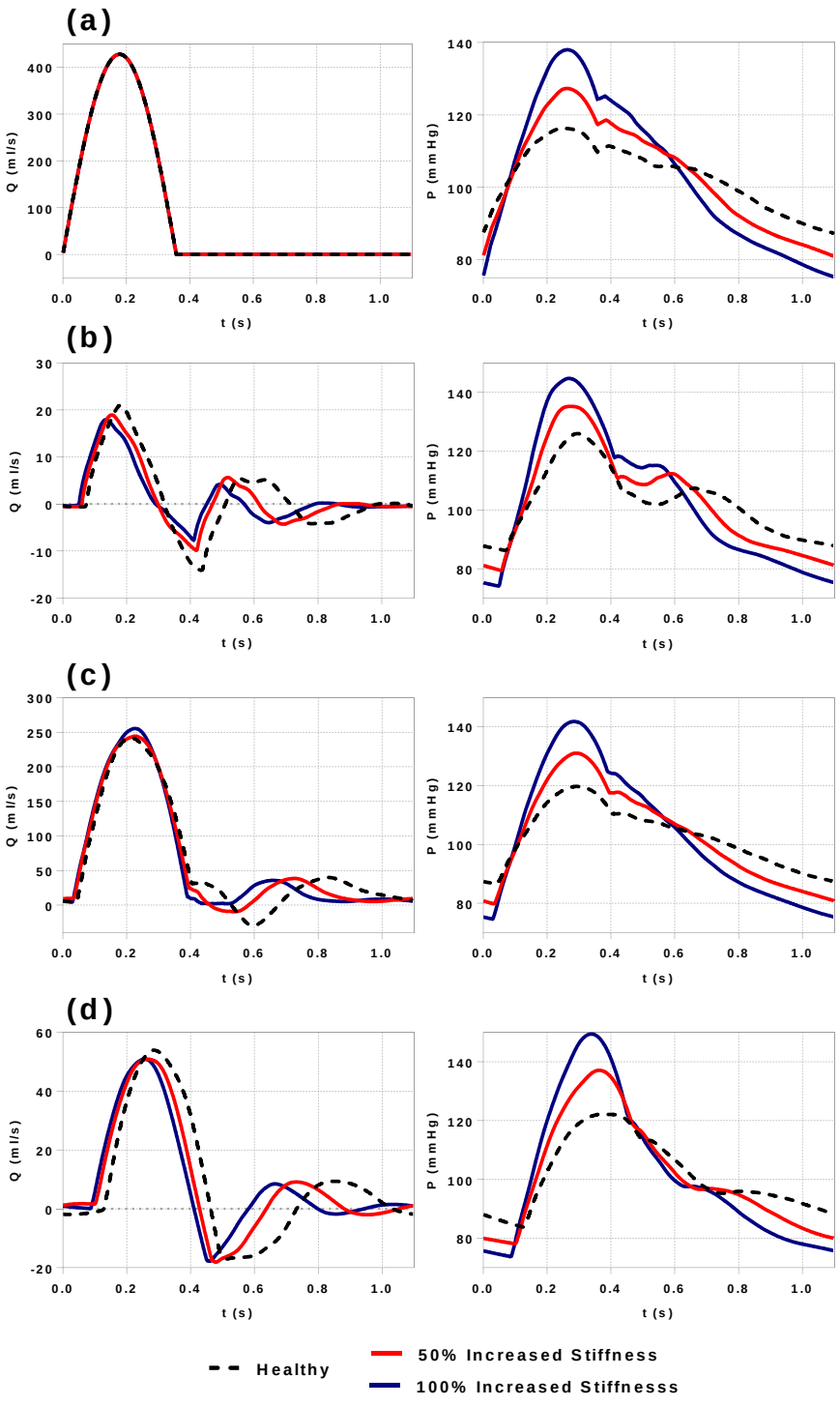
(a)
Q (ml/s)
400
300
200
100
0
0.0
0.2
0.4
0.6
0.8
1.0
t (s)
P (mmHg)
140
120
100
80
(b)
30
20
10
0
-10
-20
(c)
300
250
200
150
100
50
(d)
60
40
Healthy
50% Increased Stiffness
100% Increased Stiffnesss

Fig. 6-2: Comparison of the flow (left) and pressure (right) waveform time histories obtained from the 1-D model by increasing arterial stiffness. Selected increments 50% (red) and 100% (blue) in arterial stiffness are compared with a healthy human subject (black-dashed). The anatomical measurement locations are (a) ascending aorta (b) brachial artery (c) abdominal aorta V (d) femoral artery.

So far, cases where the arterial stiffness increases have been considered and they pertain to vasoconstriction. It is assumed that the validated model represents a healthy human subject, but the arterial stiffness of each individual is not the same. Since the validated model represents the arterial network for a 32 year old, subjects younger than this or more appropriately, subjects who have a lower arterial stiffness have not been considered. Keeping this in mind and reiterating the objective, that a comprehensive pressure response database is required for numerous subjects; it is only logical to reduce the arterial stiffness so that the database contains data from subjects having low arterial stiffness as well.

In order to encompass subjects with lower arterial stiffness', the stiffness is reduced by a maximum of 50% with decrements in stiffness by 10%. Five simulations are carried out, generating five different stiffness cases for the pressure response database.

Fig. *6-3* shows the comparison of a healthy subject and the subjects with stiffness' reduced by 30 and 50%. Fig. ***6-3*** (a-d) show the flow and pressure waveforms in multiple anatomical location, namely the ascending aorta, brachial artery, thoracic aorta and the femoral artery, respectively. The locations have been chosen arbitrarily in order to encompass parts of the body that lie in the upper body as well as the lower body.

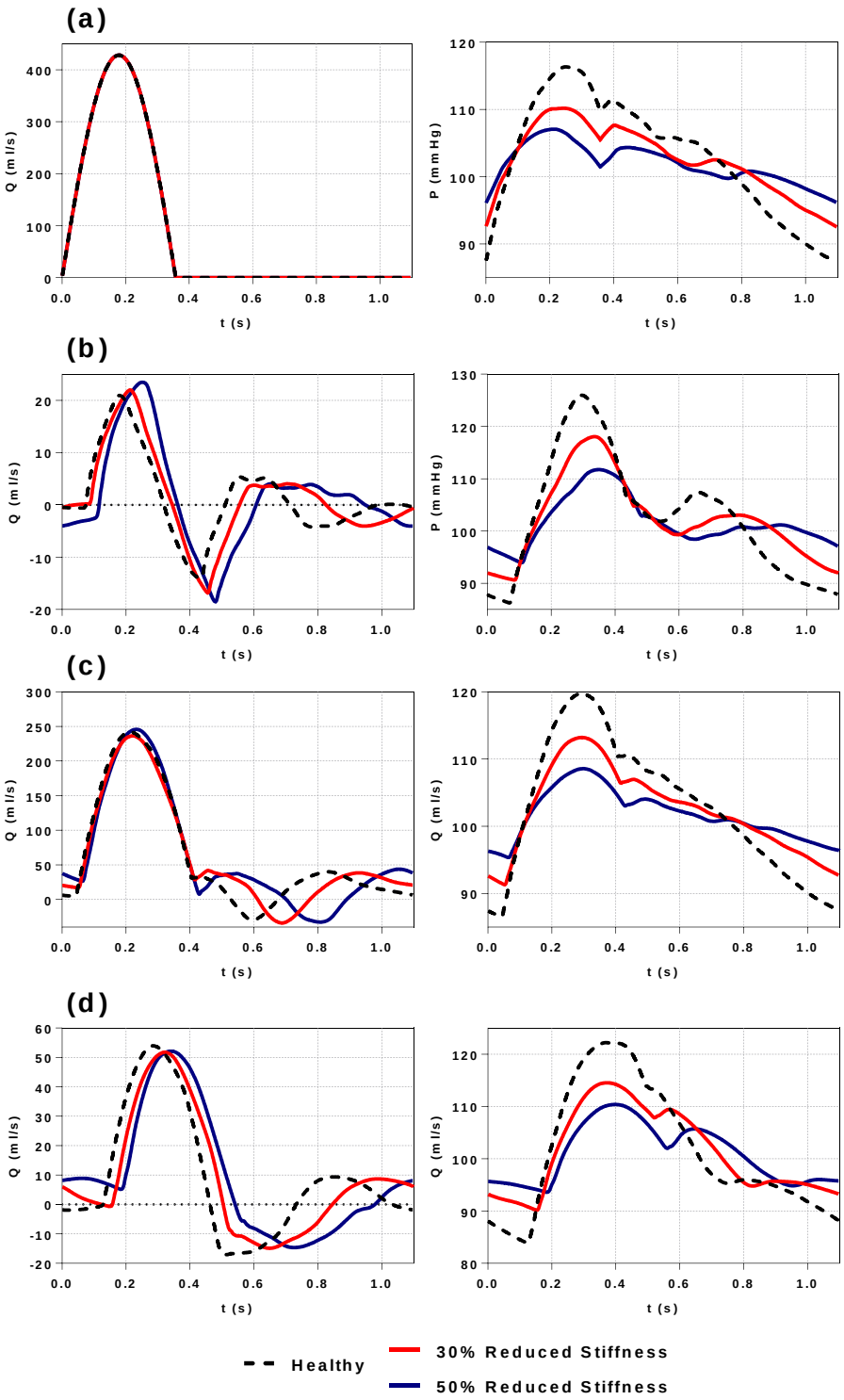
(a)
Q (ml/s)
P (mmHg)
t (s)
(b)
Q (ml/s)
P (mmHg)
t (s)
(c)
Q (ml/s)
Q (ml/s)
t (s)
(d)
Q (ml/s)
Q (ml/s)
t (s)
Healthy
30% Reduced Stiffness
50% Reduced Stiffness

Fig. 6-3: Comparison of the flow (left) and pressure (right) waveform time histories obtained from the 1-D model by decreasing arterial stiffness. Selected decrements 30% (red) and 50% (blue) in arterial stiffness are compared with a healthy human subject (black-dashed). The anatomical measurement locations are (a) ascending aorta (b) brachial artery (c) abdominal aorta V (d) femoral artery.

To create a full range of pressure response data, the effects of increasing or decreasing the minimum radius, r_{min} are also included. It was seen in section 4.3, that a minimum radius is prescribed for each terminal artery, r_{min}. This acts as a termination criterion. The small vessels keep bifurcating until this minimum radius is achieved after which the arteries terminate. However, in an actual cardiovascular system, the small vessels do not simply terminate. They keep branching further into smaller vessels until branching into capillaries after which the vessels merge again to become veins. In actuality, there are no terminal vessels [175]. Due to this reason r_{min} is a rather artificial parameter [175], hence making it's selection tedious. Sensitivity analyses carried out for the value of r_{min} in previous studies [47], [175] show that a decrease in the value of r_{min} increases the total impedance while an increased value of r_{min} decreases the total impedance at the terminal. Since there is no rule of thumb to determine the value of r_{min}, multiple values of r_{min} are incorporated in the 1-D model. For each change in stiffness and even under normal stiffness conditions, simulations are carried out for a range of r_{min} values that range from 0.09cm to 0.001cm (0.01cm is the generic value used for validation).

6.3.3 Discussion

At the ascending aorta or the inlet to the system, the flow waveforms coincide which signifies that the inlet conditions are the same for all the different stiffness models. It can be clearly seen from **Fig. *6-2***, in all the arteries, increasing the stiffness not only increases the systolic pressure but also decreases the diastolic pressure. This causes an increase in pulse pressure, as expected. The greater the increase in stiffness, the greater the increase in pulse pressure. This is physiologically sound, as

pointed out earlier in the description of arterial stiffening. Due to the increase in the stiffness of the arteries, the buffering or cushioning capability of the arteries has been reduced, which gives rise to an increased pulse pressure.

Due to the increased stiffness of the vessels, the diameters of the vessels are constricted from the lack of compliance. This causes a reduction in flow, which signifies an increase in vascular resistance. **Fig. *6-2*** shows that in all the locations the flow rate does, indeed decrease showing that the vascular resistance increases. The increase in vascular resistance can also be seen by simply comparing the peaking of both the flow and pressure waveforms. It is evident that the peaking at increased stiffness' occurs a little earlier as compared to a healthy subject. This early peaking is most obvious in the femoral artery. From Fig. ***6-2*** (d), it is obvious that the pressure waveform for 100% increased stiffness peaks at 0.34s, while the pressure waveform for a healthy subject peaks at 0.39s. This delay of 0.05s is what signifies the increase in vascular resistance and increase in the pulse wave velocity. As mentioned earlier, increase in vascular resistance and the reduced arterial distensibilty increases pulse wave velocity [17], [67], [226], which means the reflected waves from peripheral sites return earlier and superimpose on the systolic section of the pulse. What is also evident from all the arteries is that the dicrotic notch or the second peaking lasts for a smaller amount of time. When arteries get stiffer, the wave reflections take place earlier in a cardiac cycle because of the increase in the pulse wave velocity [218], hence reaching the root of the aorta before the occurrence of the dicrotic notch.

Decreasing the stiffness on the other hand as demonstrated by **Fig. *6-3*** has the exact opposite effect, as expected. For all the arteries it can be clearly seen that the systolic pressure decreases, the diastolic pressures increases while the mean pressure decreases. There are two important things to consider here; decreased stiffness as compared to the validated 'healthy' subject does not necessarily mean the stiffness reduces due to a pathological conditions. It simply represents a subject with lower

arterial stiffness and the results of the increased and decreased stiffness can be seen as a concatenation. However, if it is assumed that the validated model is descriptive for a healthy human subject, the decreased stiffness can be seen as vasodilation.

In the simplest terms, vasodilation occurs when the smooth muscles cells in the arterial walls relax, causing an increase in the arterial diameter [227]. This increase in area causes the blood flow to increase due to increased compliance or decreased arterial stiffness [228]. The increase in compliance also leads to a decrease in the blood pressure [229]. The objective of vasodilation is to reduce the total peripheral resistance by increasing the compliance through relaxation of the smooth muscle cells [230], [231]. The vasodilator response usually comes about when the ambient temperature is high and via vasodilation, the heated blood is taken to the skin [232], where the heat can be expelled to the atmosphere [233]. Ageing and other CVDs do not usually cause vasodilation however, the increased blood pressure due to arterial stiffening, triggers vasodilation in the cardiovascular system in order to contribute to the flow reserve [208]. The original finding that increasing flow pulsatility causes vasodilation in vivo was carried out in an experiment which was analyzing effects of arterial stiffening on mechanoenergetics [234]. Additionally, vasodilation occurs due to administration of certain drugs, especially blood pressure lowering drugs [235].

The reduced stiffness means increased compliance and decreased pulse wave velocity. The decrease in pulse wave velocity means the reflected waves now travel back slower. This causes in a more prominent and longer dicrotic notch because the second peeking is now effects by the reflected waves. The most obvious effect on the dicrotic notch can be seen for the femoral artery in the **Fig. *6-3*** (d).

6.4 Abdominal aortic aneurysm

6.4.1 Physiological problems associated with abdominal aortic aneurysm

The word aneurysm is derived from the Greek word, *aneurusma*, which means widening. In the medical world, an aneurysm can be broadly defined as an irreversible and permanent dilation of a vessel [236]. Although any dilation occurring in any section of the aorta below the diaphragm could be called an abdominal aortic aneurysm (AAA), an aneurysm is classified an AAA if it occurs in the infrarenal aorta (the section of aorta below the kidneys) (Fig. ***6-4***).

Under normal conditions, the diameter of the infrarenal aorta cannot be generalized as it is different for various age groups, sex and people with different bodyweight [237]. However, as a benchmark, diameter values of $1.5cm$ for women and $1.7cm$ for men are considered normal, for subjects older than 50 years [238]. This diameter of the infrarenal aorta decreases gradually from the point of its entry into the abdominal cavity to the point of its exit, the iliac bifurcation [236] (Fig. ***6-4***).

Conventionally, if the diameter of the infrarenal aorta dilates to $3cm$ or larger, it is deemed aneurysmal [239]. According to the criterion defined by The Society for Vascular Surgery and the International Society for Cardiovascular Surgery Ad Hoc Committee on Standards in Reporting, if the infrarenal diameter becomes 1.5 times the normal diameter, it is considered aneurysmal [240].

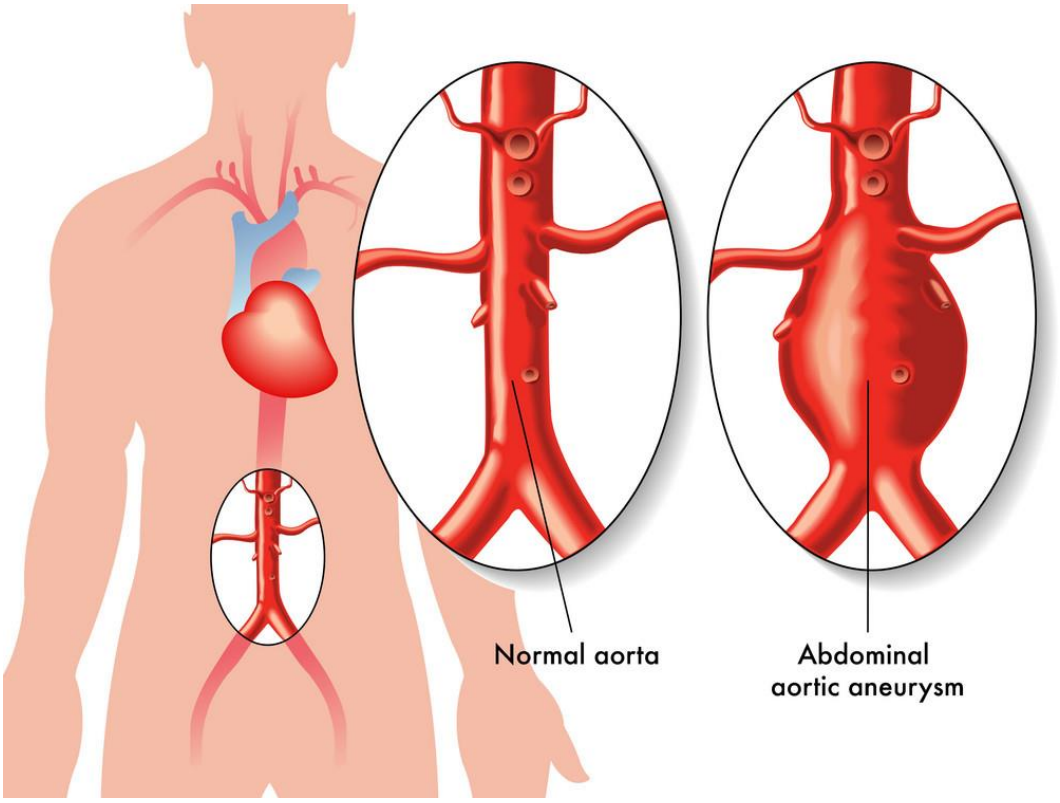

Fig. 6-4: Diagrammatic representation of an abdominal aortic aneurysm [241].

The most important risk factor for AAA is cigarette smoking [242]. Smoking causes an inflammatory reaction within the aortic wall [243] which leads to vessel dilation. Increase in biomechanical wall stress also causes aneurysms and at times, cause the aneurysms to rupture [244]. Genetics also contribute to the developments of AAAs, especially in first degree relatives [245].

AAA is a fairly common and usually fatal condition, especially in older patients. Owing to the increased number of smokers and ageing of the population, incidences of AAAs have increased over the last 20 years [236]. AAA is more common in men as compared to women, with prevalence rates estimated between $1.3\% - 8.9\%$ in men and between $1.0\% - 2.2\%$ in women [246]–[248]. However, as mentioned earlier, smoking is one of the most important risk factors for AAA [242].

With the increase in female smokers [249], the prevalence rates of AAA in women is expected to change in the near future [248], [250].

Although, a few patients have reported equivocal symptoms, most AAAs do not show symptoms and the methods of physical examinations are not sensitive enough to identify an aneurysm [251]. Of these asymptomatic aneurysms, a majority of aneurysms remain asymptomatic until they rupture [252]. The aneurysms that are identified by screening are usually small and do not require immediate surgical intervention [253]–[255]. However, untreated AAAs can become enlarged. The enlargement is usually very slow initially, but increases exponentially, later [256]. This enlargement increases the risk of rupture [249], [257]. Patients with a ruptured AAA have a mortality rate of $65\% - 85\%$ [252], [258], amongst which 50% of the ruptures occur before the patient even reaches the surgical room [259].

AAAs and aortic dissections cause approximately over 15,000 deaths annually in the USA and 8000 deaths annually in the UK [258], [260]. In 2000, these ranked 10^{th} in the list of leading causes of death in white men, aged between 65 and 74 years in the USA [261].

Presence of AAA affects the blood propagation in the aorta and causes changes in blood pressure and flow waveforms. According to Swillens et al. [262], if these changes in pressure and flow waveforms are identified through arteries which are close to the aneurysm while being accessible at the same time, AAAs can be detected well before they can rupture. Such arteries are the thoracic aorta and the common iliac arteries. It has been shown that the presence of an AAA causes pulse pressures to increases from the thoracic aorta towards the abdominal aorta [263].

In the following sections, an AAA is introduced in the arterial network and its effects on the pressure and flow waveforms in different anatomical locations are investigated. First, the AAA is introduced with normal stiffness parameters and then the stiffness of the AAA is gradually changed to quantify the effects of the different stiffness' on the pressure and flow waveforms. It is important to note here

that the AAA is introduced to simulate a pathophysiological condition for the creation of a pressure database, rather than studying the effects of the AAA. This database is used for GTF estimation, as will be seen in the next chapter. Nonetheless, the effects are still quantified to test the applicability and the robustness of the 1-D model to simulate a diseased arterial network.

6.4.2 Parametric study of AAA simulation

In this section an AAA is introduced and its effects on arterial hemodynamics are investigated. The AAA is introduced by increasing the diameter and hence the area of the infrarenal aorta (abdominal aorta V in **Table *6-2***). The diameter of a healthy infrarenal aorta defined in **Table *6-2*** is $1.46cm$ ($r = 0.73cm$). This value is increased gradually to a maximum value of $7\ cm$. **Table *6-2*** shows the range of diameters of the aneurysm used.

Table 6-2: Various AAA introduced into the 1-D model by increasing the diameter.

Diameter (cm)
1.46 (normal infrarenal diameter)
3.0
4.0
4.5
5.0
5.5
6.0
6.5
7

For simplicity and clarity of graphical representation, only three different conditions are compared. The first is a healthy human infrarenal aorta. The second condition is an AAA with a diameter of 5 cm and the third condition is an AAA with a diameter of 7cm. In addition to different diameters, the wall properties of an AAA also change. These changes in wall properties over time cause the dilation or enlargement of the infrarenal aorta. Most commonly the weakening of the arterial walls is the main reason for the dilation [264]. This is incorporated in the model by reducing the stiffness of the aneurysm to a maximum of 50% reduction, in increments of 10%.

The variation in diameter of the aneurysm remains the same for each incremental reduction of the aneurysmal stiffness. This give 54 different simulations considering that 9 different diameters are used for 6 different stiffness' which includes normal stiffness. For comprehension, a sample **Table *6-3*** is given to explain the structure of the 54 simulations. This table only describes one case of normal stiffness. This case generates 9 simulations.

Table 6-3: Description of the diamter variation of the AAA introduced in the 1-D model for an AAA with normal stiffness.

Stiffness of aneurysm	Diameter of aneurysm
Normal stiffness (0% reduction in stiffness)	1.46 (normal infrarenal diameter)
	3.0
	4.0
	4.5
	5.0
	5.5
	6.0
	6.5
	7

According to the data published by Swillens et al. [262], the key features to observe in the flow and pressure waveforms in the presence of an AAA are:

- A decrease in pulse pressure in the in the Iiiac artery, infrarenal aorta and the thoracic aorta.
- Increase in flow in the arteries above the AAA, while a decrease in flow in the external iliac artery.
- Inflection points in the pulse pressure in the thoracic aorta.
- More oscillations in the flow profile with larger amplitudes.

Fig. *6-5* shows the flow waveform and the pressure waveforms obtained from the 1-D simulation for three different diameters of the aneurysm with normal stiffness. **Fig. *6-5*** (a) represents the flow and pressure waveforms in the thoracic aorta while **Fig. *6-5*** (b) and (c) represent the waveforms in the infrarenal aorta and the external iliac artery, respectively.

Fig.*6-6* shows the flow and the pressure waveforms obtained from the 1-D simulation for a healthy subject and a subject with an AAA. The AAA in this figure has a diameter of 7 cm for all the cases. The stiffness of the AAA changes from normal to a reduction of 50%. **Fig.*6-6*** (a) represents the flow and pressure waveforms in the thoracic aorta, while **Fig.*6-6*** (b) and (c) represent the waveforms in the infrarenal aorta and the external iliac artery, respectively.

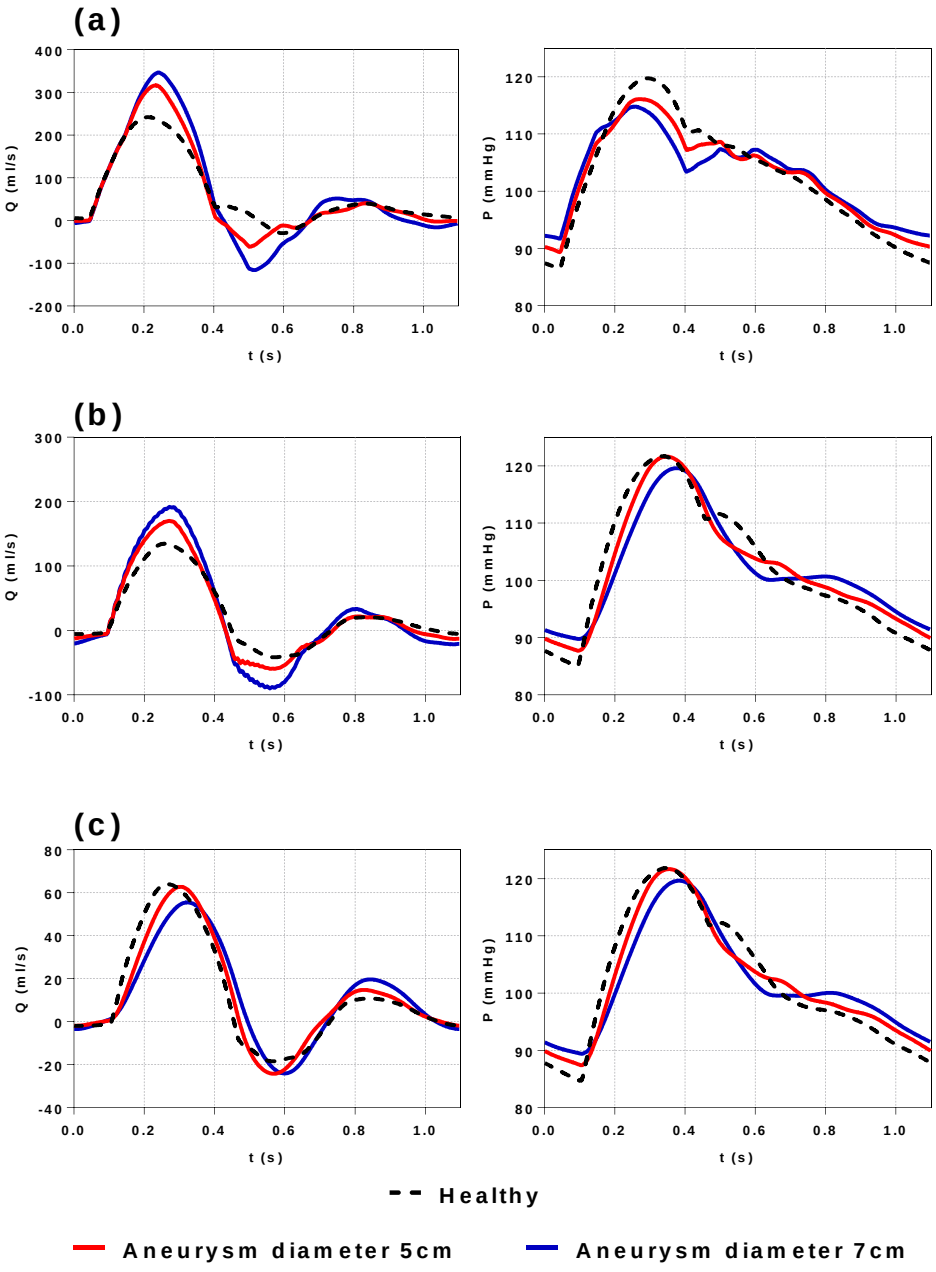

Fig. 6-5: Comparison of the flow (left) and pressure (right) waveform time histories obtained from the 1-D model by increasing AAA diameter. Selected increments $5cm$ (red) and $7cm$ (blue) in AAA diameter are compared with a healthy human subject without an AAA (black-dashed). The anatomical measurement locations are (a) thoracic aorta (b) infrarenal aorta (c) external iliac artery.

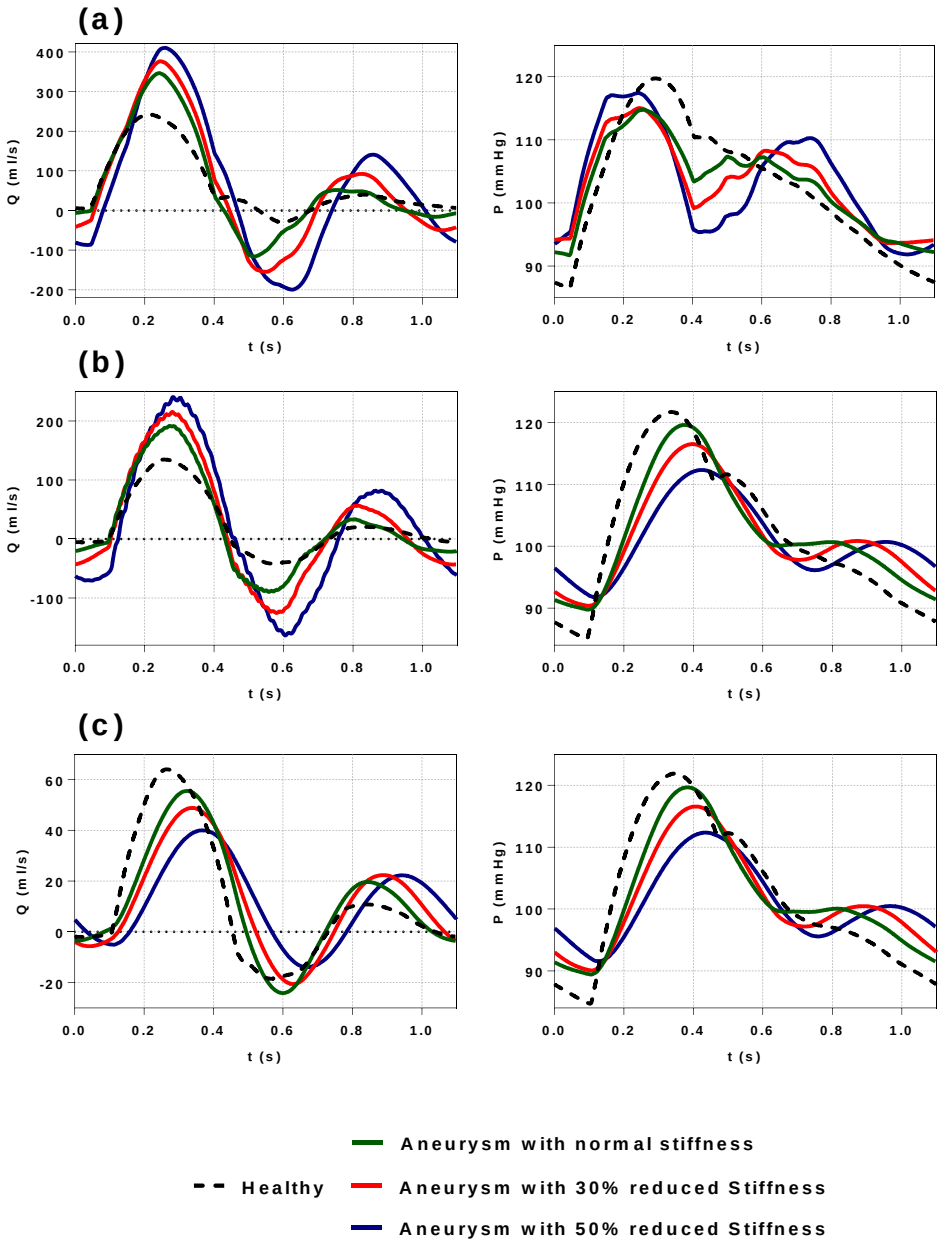

Fig.6-6: Comparison of the flow (left) and pressure (right) waveform time histories obtained from the 1-D model by decreasing the stiffness of AAA with a diameter of 7cm. Selected decrements of 30% (red) and 50% (blue) in AAA stiffness are compared with a healthy human subject without an AAA (black-dashed) as well as human subject with an AAA with diameter 7cm and normal stiffness (green). The anatomical measurement locations are (a) thoracic aorta (b) infrarenal aorta (c) external iliac artery.

6.4.3 Discussion

From the simulated results of increasing the size of an aneurysm without changing the stiffness (Fig. ***6-5***), it is observed that the flow rate increases in the thoracic aorta and in the infrarenal aorta while the flow decreases in the external iliac artery, which agrees well with literature [262].

Additionally, it is observed that each peak and nadir for the thoracic aorta as well as the abdominal aorta is amplified. The peak gets much higher as compared to a healthy patient and the nadir falls much lower when compared to a healthy patient. It has been mentioned earlier that wave reflections occur due to the tapering and bifurcating nature of the arteries. At discontinuities such as these, the impedance changes, which produces wave reflections. Hence, the amplification of the peaks and nadirs is the result of the sudden widening of the aneurysm which causes strong reflections. Once the flow exits the aneurysm, it enters the external iliac artery where the compliance returns to normal and hence , the flow decreases.

The pressure on the other hand decreases in all three arteries. Due to the presence of an aneurysm, the compliance of the system increases [262], this in turn reduces the pressure in the system. The greater the aneurysm, the greater the compliance leading to a greater decrease in pressure. The pressure contour of the thoracic aorta (Figure **Fig. *6-5*** (a)) also shows inflection points with the introduction of the aneurysm. This again shows complete agreement with literature [262]. These inflection points are, again, a result of the wave reflections due to the presence of an aneurysm. The aneurysm acts as a filter, which leads to reduced pressure in the iliac artery.

The 1-D model simulated results show excellent agreement with literature as to how the pressure and flow waveforms are affected due to the presence of an AAA. As mentioned earlier, the aim of this work is not to study AAA, rather to show the capability of the 1-D model with structured tree outflow condition to model an AAA. This capability has been demonstrated in this section.

On the other hand, when the aneurysmal stiffness is changed while keeping the diameter of the aneurysm constant (**Fig.*6*-*6***), the flow again increases in the thoracic aorta and the infrarenal aorta. However, the increase in flow with the change in stiffness is much higher because not only a compliance has been introduced in the system via an aneurysm, but the stiffness of the aneurysm is further reduced which further increases the compliance. In the iliac artery, the flow decreases again and decreases further with increased reduction in stiffness.

As with the case of an aneurysm with normal stiffness, reduced stiffness further decreases the pulse pressure in the infrarenal aorta as well in the iliac artery. The mean pressure also, very obviously decreases due to the increased compliance of the AAA. However, the pressure upstream, in the thoracic aorta starts increasing with decreasing stiffness. In the presence of an aneurysm with normal stiffness, the systolic pressure in the thoracic aorta decreases due to increased compliance because of the increase in volume of the infrarenal aorta. However, when the stiffness of this increased volume (AAA) is reduced, the pulse pressure starts increasing again. Without a comprehensive wave intensity analysis (WIA), it can only be assumed at this point that this increase in pulse pressure is due to a massive increase in wave reflections caused by the change in compliance. The reflected waves superimpose on the pressure waves, hence increasing the systolic pressure. It is emphasized again here that the AAA is introduced for the creation of the database rather than to study the AAA itself. However, the observations made here, open a new door of opportunities into the development and simulation of AAA using 1-D models to improve early detection of an AAA (reduced flow in the iliac artery). A WIA can be done from this point on to quantify the effects of wave reflections of the pulse pressure, upstream, due to the presence of an AAA with reduced stiffness. Such analysis has already been done [265] preliminarily and can be built upon further. The study undertaken here contributes 54 cases to the pressure database that is used in the next chapter for GTF estimation and validation.

6.5 Aortic Coarctation

6.5.1 Physiological problems associated with aortic coarctation

Coarctation is derived from the Latin word, *coarctatio*, which means narrowing. Clinically, a coarctation is narrowing of the lumen in a blood vessel, which in turn causes a hindrance to flow. If the narrowing of a vessel is focal, that is, concentrated at a specific point, it is termed a coarctation. In the case of a narrowing that is more diffused and covers more than a specific point, it is called tubular hypoplasia [266].

Aortic coarctation or coarctation of the aorta (CoA) is sometimes referred to congenital aortic stenosis and is a relatively common cardiovascular condition. The first observation of CoA goes back to 1750, where it was observed during an autopsy [267]. Although a series of 200 postmortems was published in 1928 [268], it was not until 1933 that CoA started being diagnosed more commonly [266].

COA comes under the umbrella of congenital heart diseases, which means it is a birth defect. The most common characteristic description of CoA is the narrowing of the segment of the descending aorta distal to the origin of the left subclavian artery [269] (Fig. ***6-7***). At times, CoA is simply defined as a systolic pressure gradient, greater than or equal to 20mm Hg, between the arm and leg [270].

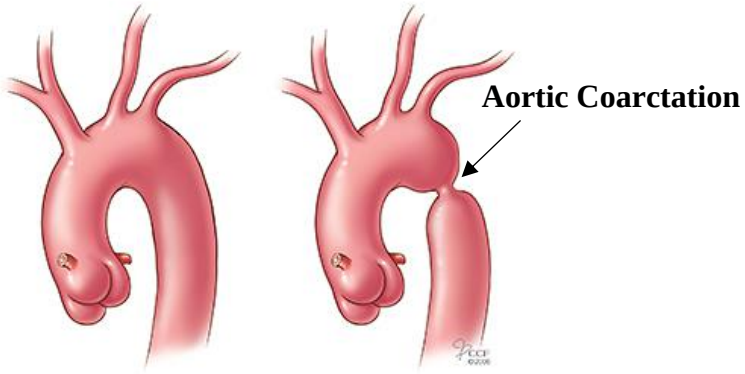

Fig. 6-7: Diagrammatic representation of an aortic coarctation [271].

CoA contributes 5–10% of all congenital heart diseases and signifies 7% of all critically ill infants with heart disease [266]. It is found in 1 in 1550 patients at necropsy [272] and is roughly three times more common in men [273]. Male-to-female predominance of CoA is in the range of 1.3–2.1 in most studies [266]. Additionally, females are in particular jeopardy during pregnancy and childbirth [274].

The set of causes of CoA are still unclear. CoA cases associated with bicuspid aortic valve lie in the range of $60\% - 85\%$ [266], [275] which support the theory that either, both these malformations have a similar cause [276] or the presence of a bicuspid aortic valve causes the development of CoA [266]. 50% of the patients with CoA have several other defects such as hypoplastic left-side heart syndrome, ventricular septal defects and obstructive defects [266]. $3\% - 10\%$ patients with CoA also develop intracranial aneurysms [266], [277]. Rosenquist et al. suggest CoA is a caused by abnormal development in the embryonic stages [277]. The higher prevalence in men of CoA suggests a relationship between X-chromosome defects and abnormal development of the aorta [276].

CoA can to lead to systemic hypertension, aortic insufficiency and secondary left ventricular hypertrophy with heart failure and if left untreated, the average life expectancy is 34 years [278]. CoA is one of the first successfully, surgically treated congenital heart diseases. However the surgical treatment does not solve the underlying vascular problem [279]. Long-term studies after the surgical repair of CoA have associated it with several late cardiovascular diseases such as aortic valve abnormalities, cerebral vascular mishaps, aneurysms in the aorta, coronary artery disease and hypertension [280]–[283]. Although, it has been shown that early repair of CoA reduces future morbidity [270], [284], all patients having undergone CoA repair need lifelong follow up [285], [286] as a lack of following up could lead to complications which might go undetected.

6.5.2 Parametric study of CoA simulation

As mentioned earlier, CoA is most common in the segment of the descending aorta distal to the origin of the left subclavian artery. A CoA is introduced into the 1-D model by reducing the diameter and hence the area of the descending aorta (thoracic aorta). The reduction is gradual, in order to comprehensively create a pressure database of mild CoA to severe CoA. **Table *6-4*** shows the cases simulated and their respective reduction in area. A 0% reduction in area signifies a healthy human subject at rest.

Table 6-4: Various degrees of aortic coarctation introduced into the 1-D model by reducing the area.

Reduction in area (%)
0
10
19
29

38
48
57
67
76.5

According to the data published in literature by various medical research groups and general practitioners [287]–[290], the key features to observe in the flow and pressure waveforms in the presence of CoA are:

- Abnormal flow and pressure in the femoral artery [288].
- Decreased pressure after the point of coarctation (decreased pressure in lower body) [287].
- Increased pressure before the point of coarctation. [287].
- Increased pressure in the upper limbs (upper limb hypertension) [288], [289].
- Weak or absent pulses in the femoral artery [289].
- Systolic pressure $\geq$ 20 $mmHg$ higher in the arms as compared to legs (pressure gradient) [290].

Fig. 6-8 is a diagrammatic representation of effects of the CoA on pressure before and after the point of CoA.

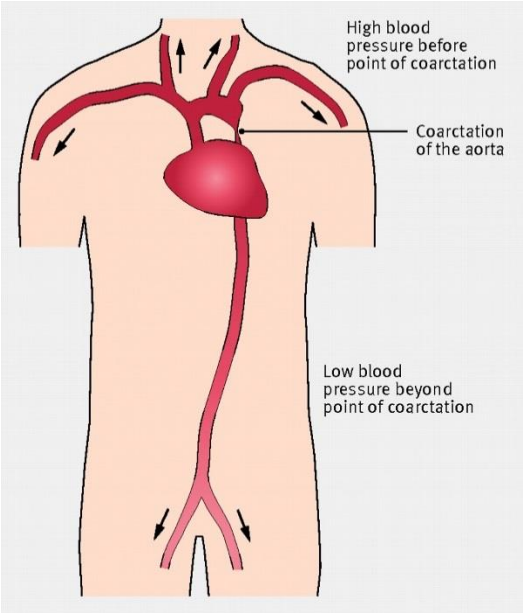

Fig. 6-8: Diagrammatic representation of effects of the aortic coarctation on pressure before and after the point of coarctation in the aorta [287].

The results for the CoA model are given in **Fig. *6-9***, **Fig. *6-10*** and **Table *6-5***. **Fig. *6-9*** shows the pressure waveforms in six different anatomical locations for various degrees of CoA. Each reduction in area signifies an increase in coarctation. At each location, the dotted line signifies a healthy human subject with no coarctation or any other pathological condition. Fig. ***6-9*** (a-d) show the pressure waveforms in the upper body, before the point of coarctation while Fig. ***6-9*** (e & f) show the pressure waveforms in the lower body, after the point of coarctation. More specifically, Fig. ***6-9*** (a-f), represent the waveforms in the ascending aorta (root of aorta), aortic arch II, brachial artery, radial artery, abdominal aorta I and the femoral artery, respectively. Aortic arch II is the segment of the aortic arch right before the origin of the subclavian artery while abdominal aorta I is the section of the aorta located right after the descending aorta where the coarctation is situated. The brachial artery is situated in the upper arm, where pressure measurements are routinely taken using a cuff while the radial artery follows the brachial artery. Measurements for the radial artery have been

taken near the wrist. The femoral artery resides in the leg.

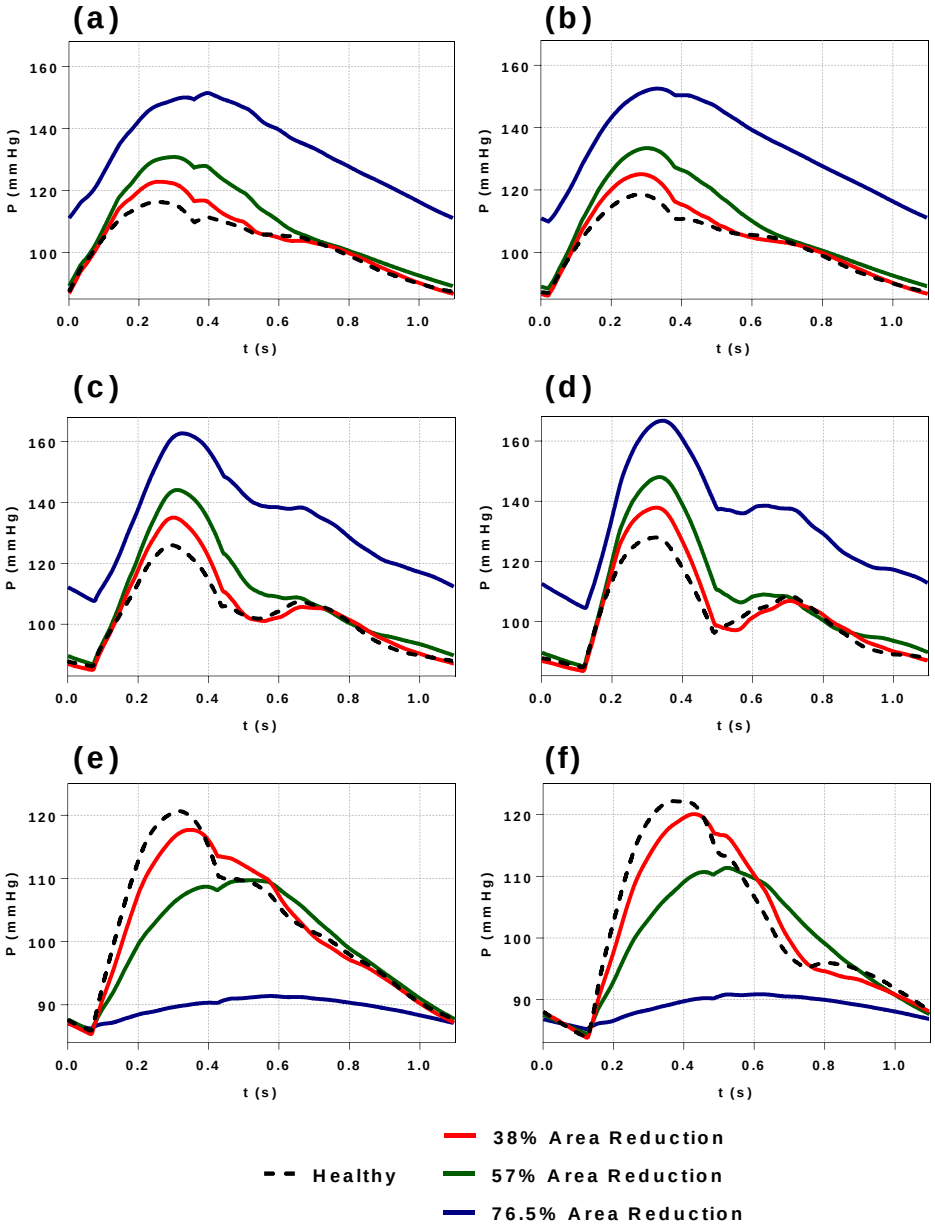

Fig. 6-9: Comparison of pressure waveform time histories obtained from the 1-D model by introducing various degrees of aortic coarctation. Selected increments 38% (red), 57% (green) and 76.5% (blue) in area reduction are compared with a healthy human subject without aortic

coarctation (black-dashed). The anatomical measurement locations are (a) ascending aorta (b) aortic arch (c) brachial artery (d) radial artery (e) abdominal aorta (f) femoral artery,

From **Fig. *6-9***, it can be observed that increasing the degree of CoA, the systolic pressure in all the locations before the coarctation increases, while the systolic pressure in all the locations after the coarctation decreases. The increase (or decrease, depending on the location) of pressure is highly related to the degree of coarctation. Greater the reduction in area (greater the coarctation), the greater the change in pressure.

Table *6-5* shows the comparison of the peak (systolic) pressure, P_S, in the brachial and femoral arteries. An increase in the systolic pressure in the brachial artery while a decrease in systolic pressure in the femoral artery is with the increase in coarctation. The pressure gradient is simply the difference between the systolic pressures in the brachial and femoral arteries. The pressure gradient keeps increasing with the increase in coarctation and is well above $20mmHg$ when the area of the descending aorta is reduced by 57%.

Table 6-5: Comparison of the peak (systolic) pressure, P_S, in the brachial and femoral arteries. The pressure gradient, ΔP_S is the difference in the peak pressures at the two locations.

Reduction (%)	**Brachial artery, P_S ($mmHg$)**	**Femoral artery, P_S ($mmHg$)**	**Pressure gradient, ΔP_S ($mmHg$)**
0	125.98	122.20	3.78
38	135.05	120.09	14.96
57	144.12	111.37	32.75
76.5	162.69	90.86	71.83

Fig. *6-10* shows the flow in the femoral artery. A significant decrease in flow with decreasing area of the descending aorta is observed. Along with a decrease in flow, the secondary undulations of flow also decrease, clearly seen by the decrease in the nadir following the initial peeking.

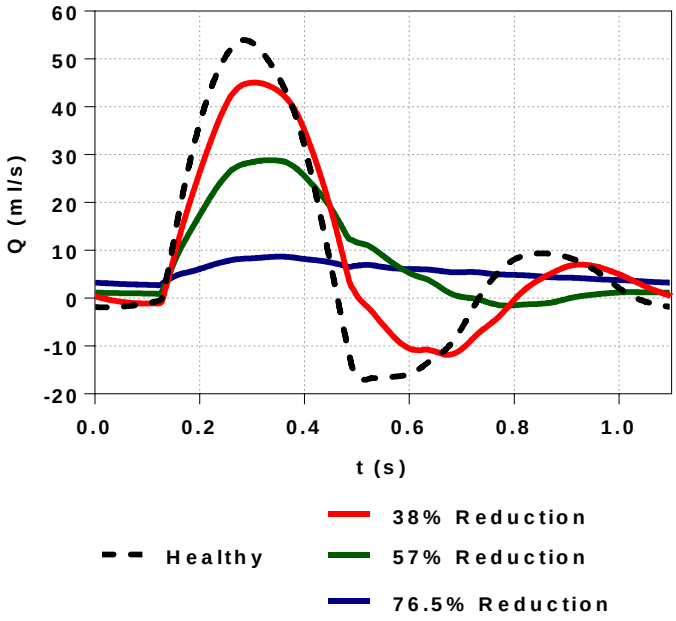

Fig. 6-10: Comparison of flow rate waveform time histories in the femoral artery at varios degrees of CoA. Selected increments 38% (red), 57% (green) and 76.5% (blue) in area reduction are compared with a healthy human subject without aortic coarctation (black-dashed).

6.5.3 Discussion

The simulation results show excellent agreement with literature. Due to the obstruction to flow caused by the decreasing area of the descending aorta, increased pressure in the upper limbs is observed (Fig. ***6-9***). Under normal circumstances, a healthy subject demonstrates systolic pressures of approximately 120 mmHg in the arms (brachial artery), however, when the area of the descending aorta is reduced by 50% or more, the systolic pressure exceeds 140mmHg in the arms while maintaining a normal diastolic pressure. This signifies hypertension in the upper limbs caused by

the coarctation. If the coarctation is increased further, the diastolic pressure also increases. The overall increase in pressure in the upper body is in complete agreement with literature [287]–[289]

Due to the obstruction introduced, flow is reduced to the lower body or more accurately the arteries beyond the point of coarctation [287]. This is again, excellently exhibited by the results of the simulation. A significant decrease in the pressure and flow to the lower body is seen. The decrease in flow was shown in Fig. ***6-10***. The pressure decrease was seen in Fig. **6-9**. The flow and pressure decrease in the femoral artery has been shown to be a characteristic of CoA [289] and was excellently demonstrated using the model. An interesting finding, is that the as long as the coarctation is a 38% reduction in the descending aorta, the pressure in the arms at this point still hasn't exceeded 140mmHg (Fig. ***6-9***). Even the pressure gradient as seen in Table 6-5, is approximately 15 mmHg between the arm and the leg. However, a further reduction in the area of the descending aorta, say a 58% reduction not only causes the systolic pressure in the arms to exceed 140 mmHg (Fig. ***6-9***) but also causes a pressure gradient of 32.75 mmHg (Table 6-5) between the arm and the leg. This not only signifies upper body hypertension but also exhibits the characteristic description of a clinically relevant CoA [290]. This finding is reinforced by observing the flow in the femoral artery (**Fig. *6-10***). Up until a 38% area reduction, the flow is reduced; however, it still has a secondary undulation with a nadir resembling that of a healthy patient. When the area reduction is at 58%, the oscillation stabilizes somewhat with a decreased amplitude of the nadir. The implication being, that the coarctation has to be in the range of $38\% - 58\%$ of area reduction of the descending aorta for it to have a pressure gradient $\geq 20\ mmHg$, thus requiring clinical intervention.

Although these findings are clinically significant, conclusive investigation of CoA still needs deliberation. It is emphasized yet again; the aim of this work is to simply prove the reliability of a 1-D model with structured tree outflow condition to simulate pathological conditions. The results

obtained from physiological and pathological conditions are used to create a pressure response database, which is used in the next chapter for GTF estimation and validation. Nonetheless, it has been demonstrated quite satisfactorily, that the 1-D model with a structured tree outlet condition can capture the key features and effects of CoA and can be further used to analyze these effects in greater depth.

6.6 Summary

In this chapter, the parameters of the one-dimensional model are varied to simulate a variety of physiological and pathological conditions. From the simulated response data of the cardiovascular system, the arterial pressure data is collected from various locations to form a pressure database for the next step, that is, GTF estimation. A variety of diseases are modelled such as Abdominal Aortic aneurysms, Aortic coarctation and arterial stiffening as in the case of hypertension and ageing. In addition to creating a pressure database for the next chapter, this chapter demonstrates the robustness of the 1-D model to capture the response of the cardiovascular system under the effects of these diseases or varied physiological parameters.

Key points from this chapter are as follows:

- 1-D models allow modelling various physiological and pathological conditions making them extremely attractive as research tools.
- In order to comprehensively take the range of the COs and the corresponding pressure responses of the cardiovascular system into account, simulations for thirteen cases are carried out. In these cases, the CO is increased from a minimum value of $3.1\ L/min$ to a maximum value of $6.83\ L/min$.
- In order to simulate arterial stiffening, stiffness of the arteries is increased by changing the parameters of the stiffness relation. The stiffness is increased from normal stiffness, which

to a 100% increase in stiffness. Ten simulations are carried out, generating ten different stiffness cases for the pressure response database.

- In order to consider subjects with lower arterial stiffness', the stiffness is reduced to a maximum of 50%. Five simulations are carried out, generating five different stiffness cases for the pressure response database.
- The AAA is introduced by increasing the diameter and hence the area of the infrarenal aorta. The diameter of a healthy infrarenal aorta is $1.46cm$ ($r = 0.73cm$). This value is increased gradually to a maximum value of 7 cm.
- Arterial wall weakening leading to arterial dilation is incorporated in the model by reducing the stiffness of the aneurysm to a maximum of 50% reduction, in increments of 10%.
- CoA is most common in the segment of the descending aorta distal to the origin of the left subclavian artery. A CoA is introduced into the 1-D model by reducing the diameter and hence the area of the descending aorta (thoracic aorta). The reduction is gradual, in order to comprehensively create a pressure database of mild CoA to severe CoA.

CHAPTER 7

GENERALIZED TRANSFER FUNCTION

7.1 Introduction

In clinical diagnoses, a very important physiological index is blood pressure at the aortic root. Initial reports of invasive blood pressure measurement date as far back as 1733. Hales made an opening in a horse's artery and inserted a glass tube in the opening. The force generated due to the pulsatile pumping of the heart caused the level of blood in the tube to rise. Such a technique, however, is dangerous for human subjects as it could lead to infection, injury and severe blood loss. Nowadays, blood pressure in human subjects is measured invasively in catheterization laboratories. There are various methods available for invasive blood pressure measurements among which using high fidelity catheter micro-tip pressure transducers is considered the most accurate. However, there are a number of limitations in measuring blood pressure using these methods. Due to their invasive nature, they can't be used for large scale clinical studies for instance for subjects who are healthy or even patients with hypertension, therefore these methods are deployed in subjects that are critically ill or already undergoing an invasive procedure such as a cardiopulmonary bypass [291]. Additionally, system damping leads to slower response times making it tedious to identify pressure wave features other than the systolic and diastolic pressure [291].

Owing to the limitations of the applicability of invasive blood pressure measurement techniques, the blood pressure is routinely measured at peripheral locations such the upper arm (brachial artery) or the wrist (radial artery). The measurements are carried out using a cuff sphygmomanometer in most instances. Introduced first in 1881, the sphygmomanometer has become readily available since.

However, blood pressure measured at peripheral locations does not represent the blood pressure at the aortic root or the carotid arteries. As shown in section 2.2, arterial pulse is produced when the

heart muscles contract and blood is ejected into the aorta. This pulse wave travels from the central aorta to peripheral arteries [32], [202]. While the arterial pulse is transmitted, the features of the pulse wave change progressively due to wave reflections from the vascular beds and arterial tapering and bifurcation. The central aortic blood pressure, is modified by the effects of the contraction of the left ventricle, the wave reflections from the entire arterial tree as well as the total compliance of the arterial tree [292]. On the other hand, peripheral blood pressure waves such as the pressure waves in the brachial artery, are effected by local wave reflections coming from its own terminal ends [32], [293]. Indeed, previous research has shown that the waveforms of peripherally measured pressure and central aortic pressures are significantly different in regards to the wave shapes as well as amplitude [17], [202], [294]. It has been shown that the peripheral systolic pressure such as the one in brachial and radial arteries, when compared to central aortic pressure is 11-22 mmHg higher [13] whereas mean blood pressure and diastolic blood pressure vary slightly (0.2 mmHg [295]). This amplification of the systolic pressure in the peripheral arteries is more prominent in young, healthy subjects [202], [296]–[300].

Research has also shown that administration of drugs [18], [301] and nutritional interventions [302]–[305] have different impacts on central and peripheral pressures.

Due to these reasons, it is believed that the central aortic pressure is a better representation of hemodynamic load and stress to the heart and large vessels at rest, during pharmacological intervention, and after exercise [27], [306]–[308]. There is substantial research demonstrating independent and additional clinical importance of central blood pressure as compared to peripherally measured blood pressure [18], [19], [21], [298], [309], [310] and that central aortic pressure is a better indicator physiologically for diagnosing diseases [19]–[21].

The last two decades have attracted a lot of research and interest from a clinical point of view into the central aortic blood pressure, which has been boosted by the development of non-invasive

techniques currently available for their estimation. The central aortic pressure can be assessed noninvasively by a number of techniques [291], [311]. In most of these techniques, peripheral pressure waveforms are acquired via arterial tonometry and are then transformed into the central pressure or directly analyzed to produce the central pressure [291], [311] (**Fig. *7-1***). Noninvasively estimated central aortic pressure has previously demonstrated its ability to forecast cardiovascular events better than peripherally measured pressures [21], [307], [308], [312], [313].

Central aortic pressure can be estimated non-invasively mainly using three methods [291]:

1. Recording the pressure in central arteries for instance the carotid artery and using that as a representation of the central aortic pressure.
2. Recording the pressure waveform at a peripheral location such as the brachial artery and deriving statistical relations using regression models between the peripheral pressure waveform and the central pressure waveform.
3. Recording pressure waveforms in peripheral arteries and estimating the central aortic pressure using transfer functions.

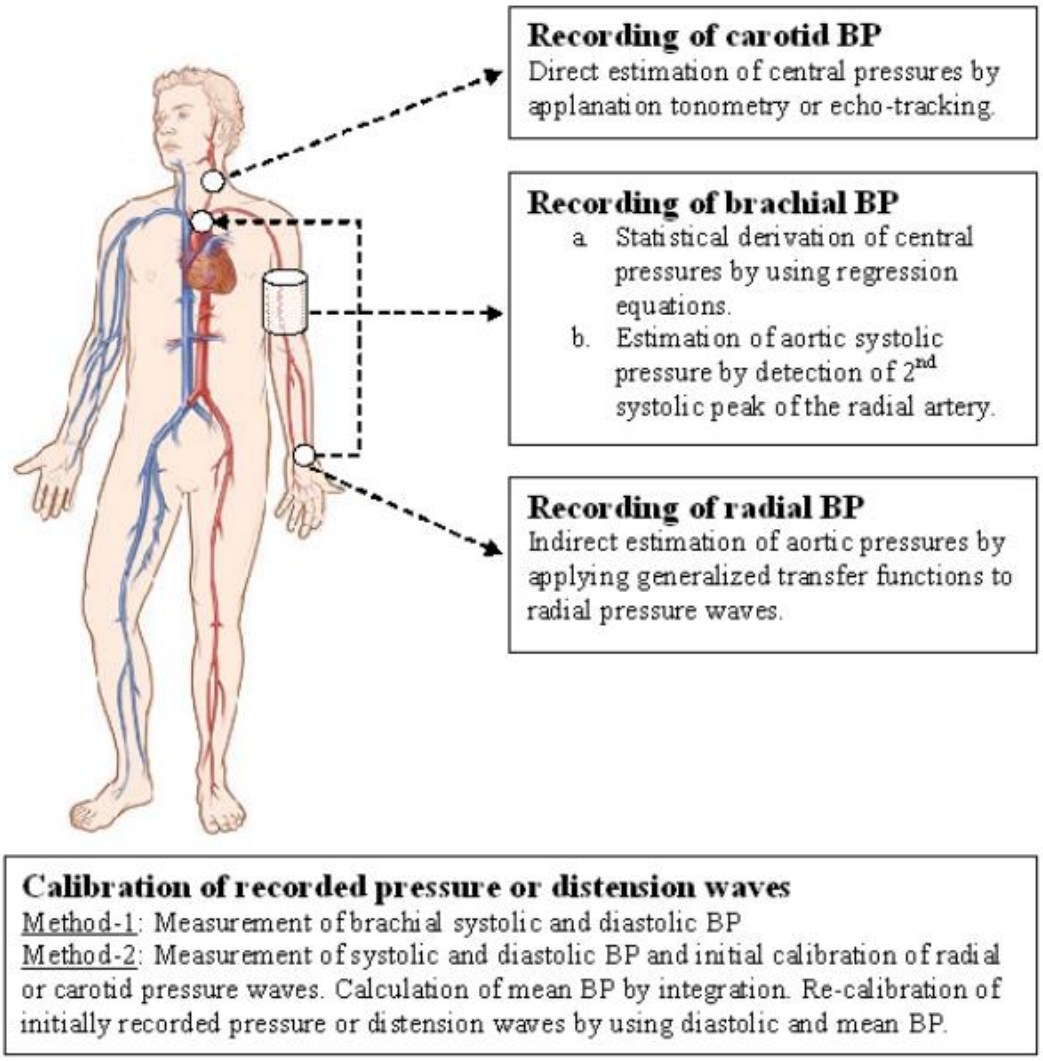

Fig. 7-1: Methods for the estimation of central blood pressures [291].

The evidence of the central aortic pressure being clinically more relevant as compared to peripheral pressure is still debatable [20], [21], [314], however, from a physiological point of view central pressures still forms the true afterload on the heart. The real problem lies in estimating the central aortic pressure and the limitations of the methods used to do that. One solution is to assess the

pressure in a location closest to the heart such as the carotid artery [315] using applanation tonometry. However, tonometry requires a stiff or bony structure to flatten the artery wall and a lean skin to avoid cushioning of the pressure pulse. Consequently, high quality waveforms are tedious to acquire especially in obese subjects, due to the physiological location of the carotid artery. Tonometry is also operator dependent and needs specialists [316]. Additionally, even though the carotid is close to the aorta, there still will be some amplification [202], [317], [318].

Therefore, the alternative is to measure blood pressure peripherally and to use a so-called transfer function (TF) to synthesize central pressure waveforms from the peripherally measured blood pressure [13], [22].

7.1.1 What is the generalized transfer function?

Transfer functions are mathematical functions that describe the behavior of a system by relating the input and output signals. Transfer functions (TFs) in cardiovascular studies, mathematically relate pressure waveforms at different arterial sites with each other [13], [22], [23], [40], [319]–[325] and are usually represented in the frequency domain [13], [22]. The pressure waveform is treated as a sum of a steady part and a sum of sinusoidal waves with increasing frequency [202]. The TF expressed in terms of modulus and phase [25] expresses the relationship between sine waves for a given frequency (also called harmonics) [326].

If the input is a flow waveform and the output is a pressure waveform from the same location, the TF between the two waveforms represents the impedance of the system [202], [327]. However, if the input and output signals are pressure waveforms from different locations but measured at the same time, the TF is the ratio of the frequency (ω) components of the output and input signal [328]. TFs are complex quantities, hence they are represented by the modulus and phase as a function of frequency [328].

In recent years, Generalized transfer functions (GTF) have been used to estimate central aortic pressure waveforms from peripherally measured waveforms obtained using non-invasive [13], [22], [329]. This GTF technique allows estimation of central aortic pressure from peripheral pressure measured non-invasively. Multiple central and peripheral pressures undergo a Fourier analysis and a generalized transfer function is calculated. This GTF relates the central and peripheral pressures. The central pressures of individual patients can be estimated by simply multiplying this GTF to peripheral pressures of these patients in the frequency domain and converting the results back to the time domain. [23]–[28] The patent to this technique [29] is in use of SphygmoCor® system (SphygmoCor®,AtCor Medical, West Ryde, NSW, Australia), a commercially available blood pressure measurement equipment. **Table *7-1*** summarizes a selection of the reported models.

Table 7-1: Tabulation of the reported models

Author (year)	Peripheral measurement location	Reference
Karamanoglu (1993)	Brachial & Radial artery	[13]
Fetics (1999)	Radial artery	[23]
Pauca (2001)	Radial artery	[24]
Söderström (2002)	Radial artery	[25]
Gallagher (2004)	Radial artery	[330]
Sharman (2006)	Radial artery	[27]
Cheng	Brachial artery	[306]

(2010)		
Weber (2011)	Brachial & Radial artery	[28]
Shih (2013)	Brachial artery	[331]
Wassertheurer (2010)	Brachial artery	[332]
Climie (2012)	Brachial artery	[11]
Brett (2012)	Brachial artery	[333]
Verberk (2016)	Brachial artery	[8]

7.1.2 GTF calculation

Each pressure wave comprises of harmonic waves at multiples of the frequency of the heart rate [27]. The generalized transfer function recreates the central aortic waveform from peripherally measured pressure waveform. Essentially, it is a ratio of the amplitudes and phase of the peripheral pressure waveform and the central pressure waveform [27]. A generalized transfer function of pressure waveforms between two sites is defined [13] as

$$H_{(A-B)} = \frac{P_B(\omega)}{P_A(\omega)} \tag{7.1}$$

where, $P_A(\omega)$ and $P_B(\omega)$ are the pressure waveforms represented in the frequency domain at sites A and B, respectively and ω is the angular frequency. If the moduli are denoted as

$M_A(\omega)\ and\ M_B(\omega)$ and phases denoted as $\varphi_A(\omega)\ and\ \varphi_B(\omega)$, the pressure waveforms can be written as $P_A(\omega) = M_A(\omega)e^{i\varphi}\ and\ P_B(\omega) = M_B(\omega)e^{i\varphi}$ for sites A and B, respectively.

Prior studies have shown that physiologically relevant data is contained within the first 15 harmonics [17], [23]. There is no fixed value for the magnitude (amplification) or phase of the transfer function estimated between the aorta and a peripheral location due to the variations in the arterial networks in each human subject and effects of cardiovascular dynamics due to dissimilarities of physiological and pathological conditions. However, most studies found in literature validate their transfer function by ensuring the magnitudes and the minimum phase angles stay within a certain range. Most studies simply compare the transfer function up to 4Hz after which a scatter is seen which can be attributed to the reduced power of frequency components of the pressure contours [13]. Approximately 96% of the power of the pressure pulse wave of the ascending aorta is confined in between the 0.8 and 4 Hz [17], [27]. For the current study, the benchmark for GTF validation are the GTFs estimated by Gallagher et al. [26] and Karamanoglu et al. for human subjects [13]. **Fig. *7-2*** shows the GTF estimated and validated by Gallagher et al. [26]. Out of the three TF amplifications, two are of significance in this work; the amplification at the top (AA-RA) and the amplification at the bottom (AA-CA). The top amplification is the amplification of the GTF estimated between the radial artery and the ascending aorta while the bottom amplification is for the GTF estimated between the carotid artery and the ascending aorta.

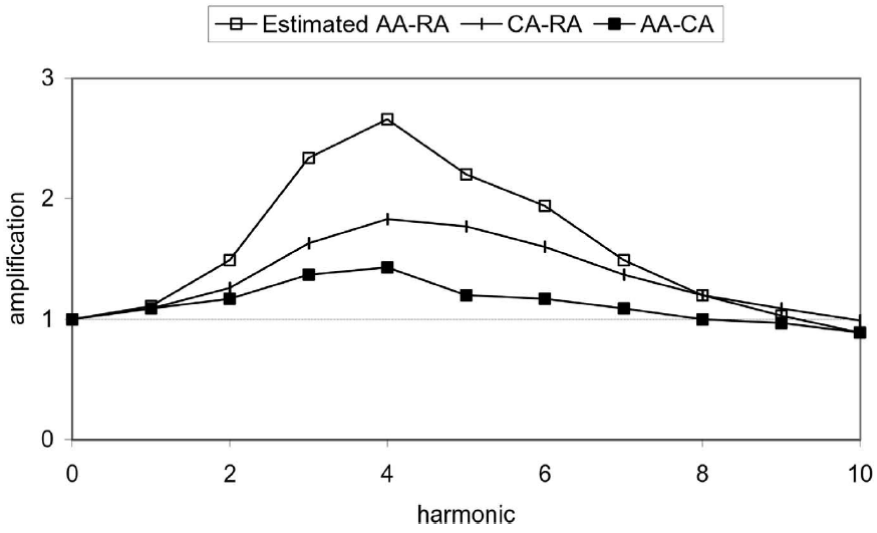

Fig. 7-2: Transfer functions estimated by Gallagher et al. between the ascending aorta and the radial artery (top) and between the ascending aorta and the carotid artery (bottom). The extracted figure also contains the transfer function between the carotid and radial artery. [330]

A summary of the amplification is shown in **Table *7-2***. For both the peripheral locations, the characteristic peeking occurs at 4 Hz, which has been to a certain extent, standardized as the optimal peaking frequency as demonstrated by multiple previous researchers [13], [16], [23], [26], [315], [334].

Table 7-2: Peak amplification and minimum phase of the GTFs estimated between the ascending aorta and the carotid and radial arteries by Gallagher et al. [330]

Peripheral location	Peak amplification
Carotid artery	1.431
Radial artery	2.658

Fig. *7-3* shows the GTF estimated and validated by Karamanoglu et al.[13]. The plots on the top depict the amplification and phase of the GTF estimated via the brachial artery while the bottom

plots depict the amplification and phase of the GTF estimated via the radial artery. The plots on the left are the control group, that is, under normal circumstances and the plots of the right depict the group under the influence of nitroglycerin. For the current study, the GTF amplitude and phase values of significance are from the plots on the left. The characteristic peaking, again, occurs at 4 Hz while the minimum phase takes place at 9Hz.These values are summarized in ***Table 7-3***.

Table 7-3: Peak amplification and minimum phase of the GTFs estimated between the ascending aorta and the brachial and radial arteries by Karamanoglu et al. [13]

Peripheral location	Peak amplification	Minimum Phase (rad)
Brachial artery	2.572	-3.627
Radial artery	3.049	-6.450

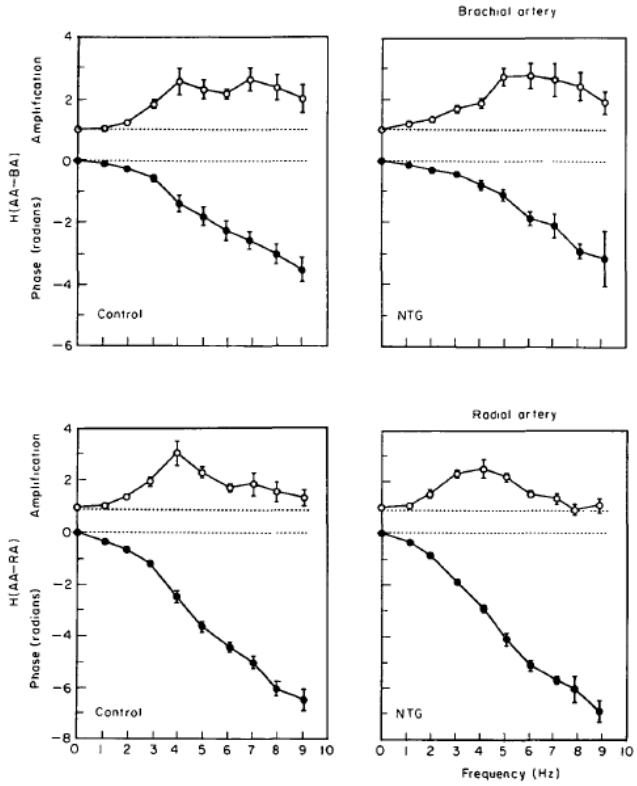

Fig. 7-3: Transfer function estimated by Karamanoglu et al. between the ascending aorta and the brachial artery under normal conditions (top-left) and under the influence of Nitroglycerin (top-right). The estimated transfer function between the ascending aorta and the radial artery under

normal conditions (bottom-left) and under the influence of Nitroglycerin (bottom-right) are shown here as well. [13]

The brachial and radial artery are by far, the most common peripheral locations used for GTF estimation. Femoral artery has mostly been used in studies conducting blind identification of the central aortic waveform [34]–[36], [335]–[337] rather that GTF estimation so it is tedious to generalize the characteristic peaking of the GTF estimated using the femoral artery.

7.1.3 Limitations of GTF

There has been some debate that the general transfer function varies from person-to-person due to a variety of physiological differences, making the general transfer function an unreliable tool of choice in such analyses as it lacks adaptability [30]–[32]. Cloud et al. [31] undertook a study with 30 patients and found that the SphygmoCor® system underestimated the systolic central aortic pressure and overestimated the diastolic central aortic pressure by 13.3mmHg and 11.5mmHg, respectively. To put things into perspective, a blood pressure measuring equipment should not have a standard deviation greater than ±8mmHg [33]. Consequently, individualized transfer functions (ITF) were introduced to account for individual differences amongst patients [34]–[37], and although promising, they still lack personalization.

With the on-going disagreement between the research groups for and against the GTF technique, it is essential to use an independent method to test the GTF technique, which also serves as an alternative to experimental studies. Numerical modeling provides such an alternative research method. Pressure changes in arteries can be more accurately analyzed by deriving and solving the mathematical equations that govern the pressure wave dynamics in the arteries [38]. This can serve as the judging tool to check the validity of the transfer function method.

Numerical modeling has been used comprehensively, to investigate a diverse range of problems in the study of cardiovascular dynamics. Research has already been carried out using numerical modelling of the pulse wave propagation to study the changes in flow as it goes from the heart towards the peripheral arteries. Stergiopulos et al.[39] used peripheral pressure and velocity to model the pulse wave transmission effect in a vessel segment. Based on the reflection coefficient in the periphery and the time taken for pulse wave transmission, a transfer function was defined that relates the central and peripheral pressures. Since the simulation is carried out on a vessel segment, it does not provide information about pressure in other parts of the arterial network. Segers et al. [40] and Thore et al. [41] used transmission line models to simulate pulse wave dynamics. Another study conducted by Jiang et al [42] extends the electrical circuits analogy to the entire human arterial network to predict the central aortic pressure. Although the entire network is simulated, the analogy to electrical circuits does not represent wave propagation effects satisfactorily. Additionally, important parameters such as Young's modulus, vascular thickness and cross-sectional areas of the arteries are assumed constant, which is not the case in physiological conditions.

All these studies use simplified models that either do not take into consideration non-linearities such as inhomogeneous vessel wall elasticity, vessel tapering etc. or consider stand-alone simulation cases. To our knowledge, a full-scale cardiovascular model that incorporates non-linearities as well, has not been used to systematically evaluate the GTF technique.

In this chapter, the pressure response database created in chapter 6 using the 1-D model is used to estimate, validate as well as study the GTF technique. The following section provides the protocol of the study followed by the results and the discussion of those results in sections 7.3 and 7.4.

7.2 Methods

This section reports the methodology of deriving the GTF as well as testing its validity. The approach adopted is summarized in a systematic manner as follows:

Step 1: Extracting the pressure waveforms from the response database for 5 anatomical locations, the ascending aorta, brachial artery, radial artery, common carotid artery and femoral artery.

Step 2: Dividing the database in half, randomly. One half forms the derivation database (97 datasets) while the other half forms the validation database (97 datasets). All the extracted waveforms are transformed into the frequency domain.

Step 3: Using the derivation half of the database to derive TFs between the aorta and each of the peripheral locations. Each of these TFs are averaged in order to generalize them.

Step 4: Using the validation half of the database to reconstruct the central aortic pressures of the validation database by multiplying the peripheral pressures with their respective GTFs obtained in the previous step. The reconstructed aortic pressure waveforms are transformed back into the time domain.

Steps 5: Comparing the reconstructed and model simulated central aortic pressure to test the validity of the transfer function.

These steps are further elaborated in the section that follows.

7.2.1 GTF Estimation

In order to estimate the GTF, the pressure response database created in the previous chapter is used. A total of 194 cases were simulated which give 194 different physiological and pathological responses of the cardiovascular system. Each of these 194 datasets, generates pressure and flow waveforms throughout the systemic arterial network which are measured at specific anatomical locations. For this particular study, pressure waveforms from 5 locations are of interest. These locations are the ascending aorta (root of the aorta), the brachial artery (upper arm), radial artery (wrist), the common carotid artery (neck) and the femoral artery (thigh).

As seen in the literature review for the GTF, for GTF estimation, the locations most commonly used for peripheral pressure measurement are the brachial and radial arteries. However, other locations have been used such as the carotid artery [6], [322] and the femoral artery [324], [338]. Numerical modelling allows pressure measurements in all these locations simultaneously, allowing the flexibility to generate a GTF for 4 different peripheral pressure measurement locations at the same time. It is noteworthy that other locations can be used to generate a GTF but for this study the GTFs between the ascending aorta and the main stream peripheral locations found in literature are estimated.

For GTF derivation, the pressure response database created in the previous chapter is randomly divided in half, that is, 97 cases are picked randomly. These 97 cases form the derivation database for the GTF. Each of these 97 cases consists of pressure waveforms from the 5 different locations. The pressure waveforms at the ascending aorta are termed derivation central aortic pressure (DCAP) while the pressure waveforms from peripheral locations (brachial, radial, carotid and femoral arteries) are termed derivation peripheral pressure (DPP). DPPS represent site B in equation (7.1) while DAPs represent site A.

The DPPs for each of these 97 datasets are used in conjunction with the DCAPs to estimate a transfer function for each of the respective sites. This is done by first transforming the DCAPs and the DPPs into the frequency domain by using a discrete Fourier transform (DFT). Once the pressure waveforms have been transformed, equation (7.1) is applied to estimate the transfer function for each of these locations. This yields 388 TFs (97 TFs per site B, yielding $4 \times 97 = 388$ TFs). The individual TFs are then averaged in order to estimate the GTF for each site.

A diagrammatic representation of the DPPs and the DCAPs is shown in **Fig. *7-4***. The DPPs are the pressure waveforms form the peripheral measurement locations while the DCAPs are the pressure waveforms from a single location, the aortic root which is of interest for this study.

The averaged TFs derived can now be used to reconstruct the central aortic pressure by from peripherally measured pressures. This is covered in the next section.

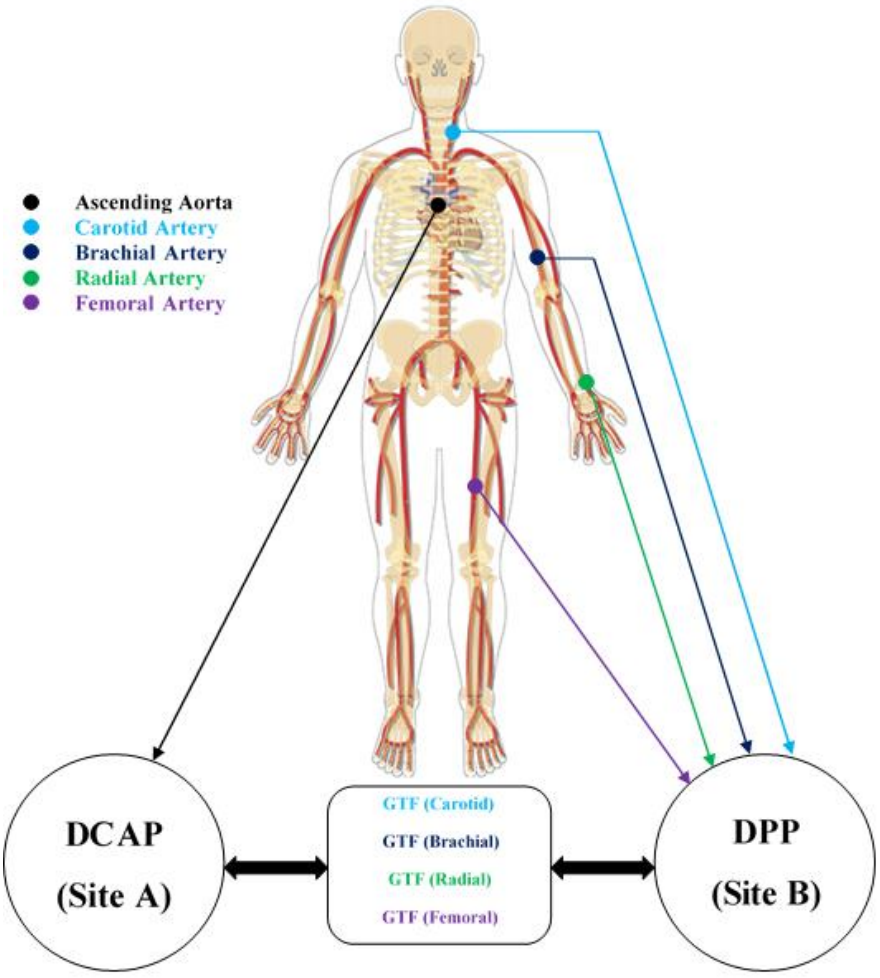

Fig. 7-4: Central and peripheral sites of GTF estimation.

7.2.2 Reconstruction of central aortic pressure

In order to test the validity and performance of the derived GTF, the other half of the database (the remaining 97 cases out the 194 cases simulated) is used. For the reconstruction, only peripherally

measured pressures are required. The peripherally measured pressures (pressures measured at the brachial, radial, carotid and femoral arteries) of the remaining database are now termed as the validation peripheral pressures (VPP) for simplicity.

The VPPs are first converted into the frequency domain, again, using a DFT. The VPPs expressed in the frequency domain are then multiplied with their respective GTF. For instance, if a VPP in consideration is taken from the brachial artery, it is multiplied with the GTF derived using the DPPs from the brachial artery. This product yields the estimated central aortic pressure (ECAP) in the frequency domain. The ECAP in the frequency domain is transformed to the time domain using an inverse DFT, which gives the reconstructed central aortic pressure waveform.

Since the database was created using the 1-D model, the central aortic pressures for the remaining 97 cases are already known. These are compared to the ECAP, hence they are called validation central aortic pressure (VCAP). This comparison is carried out to test the validity of the estimated transfer functions. Section 7.3 details the statistical analysis carried out to compare the ECAPs and the VCAPs to judge the effectiveness of the GTFs.

7.2.3 Statistical Analysis

Statistical analysis was carried out using GraphPad Prism version 7.0 (GraphPad Software Inc.). Pearson correlation coefficient *(r)* was used to determine the correlation between the pressure responses, which were estimated using GTF as well as pressure responses produced using the 1-D model. A linear regression was then performed to investigate the relationship between the pressure responses that were estimated (using GTF) and the pressure responses from the 1-D model. Bland-Altman plots were used to assess the agreement between the two chosen methods. Data was expressed as mean$\pm$ SD and significance was taken at $p < 0.05$.

7.3 Results

Fig. *7-5* shows examples of the comparison of the reconstructed central aortic waveforms using the GTF and the model-generated waveforms. It is tedious to quantify the similarity by just looking at the figure; hence a detailed statistical analysis is carried out in the sections that follow. However, by inspection of **Fig. *7-5***, it can be clearly seen that the estimated waveforms correspond well with the model generated waveforms even though the peripheral pressure contours differ significantly when compared to the central aortic pressure waveforms.

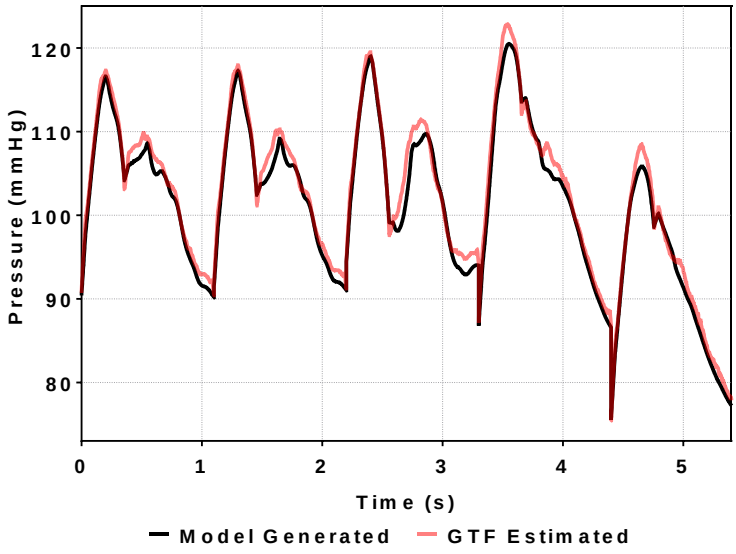

Fig. 7-5: Comparison of model generated central aortic pressure waveforms (black) and GTF estimated central aortic pressure waveforms (red) from 5 randomly chosen subjects.

One such example of the difference in pressure contours is shown in **Fig. *7-6***. The pressure waveform from the femoral artery is compared with the central aortic waveform from a randomly selected subject. The dicrotic notch is evidently diminished in the pressure contour of the femoral artery and the systolic pressure is markedly different. The initial time delay between the waveforms

signifies the distance between the two measurement locations which is also demonstrated by the delayed peeking of the pressure contour of the femoral artery.

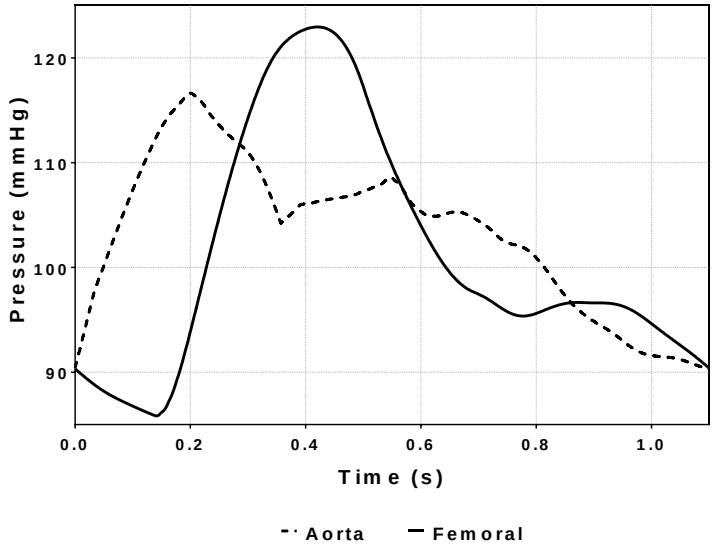

Fig. 7-6: Comparison of model generated pressure waveforms in the ascending aorta (dotted) and the femoral artery (solid).

As mentioned earlier, the TF is expressed in terms of modulus and phase expresses the relationship between sine waves for a given frequency (also called harmonics). The pressure transfer functions between the carotid artery, brachial artery, radial artery, femoral artery and the ascending aorta peak at 1.567, 2.114, 3.018 and 1.112, respectively while the minimum phase angles are -3.012, -3.747, -6.569 and -6.874 rad, respectively (***Fig. 7-7***).

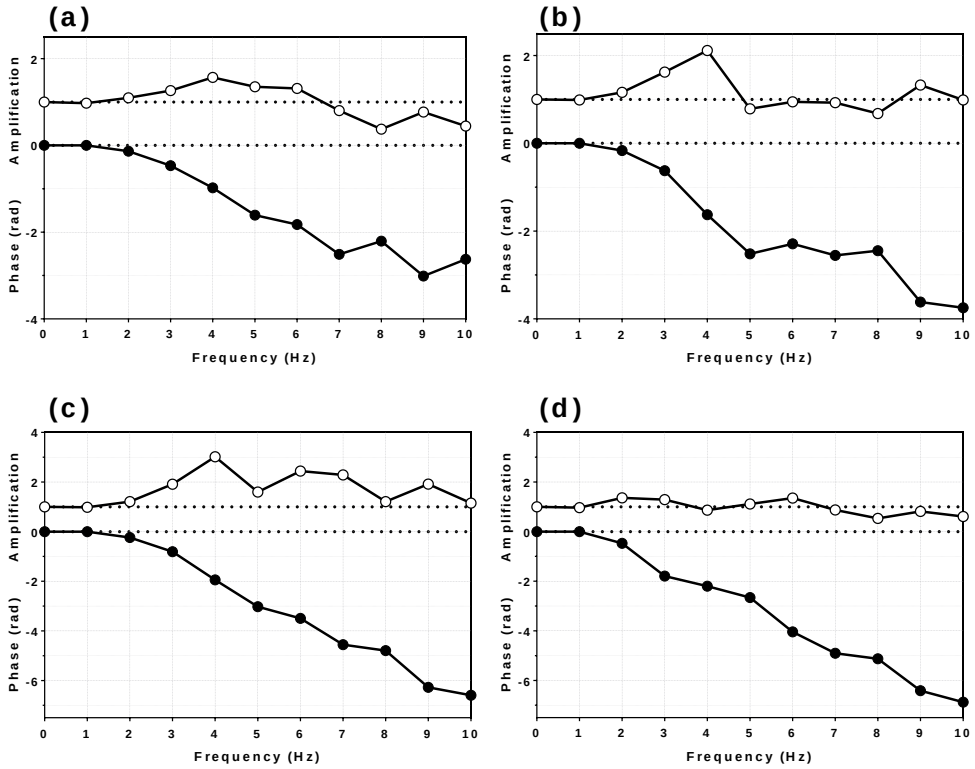

Fig. 7-7: Averaged transfer functions estimated between the ascending aorta and (a) carotid artery, (b) brachial artery, (c) radial artery and (d) femoral artery.

The data from the GTF plots can be summarized as follows:

Table 7-4: Summary of the peak amplification and minimum phase of the GTFs estimated between the ascending aorta and the four peripheral locations.

Peripheral location	Peak amplification	Minimum Phase (rad)
Carotid artery	1.567	-3.012
Brachial artery	2.114	-3.747
Radial artery	3.018	-6.594
Femoral artery	1.112	-6.874

7.3.1 Correlation of model generated and estimated central waveforms

Pearson's correlation coefficients were calculated for the systolic, diastolic and mean pressures at the root of aorta (ascending aorta), between the pressures estimated using GTF and the pressures predicted by the model for the remaining 97 cases. **Table *7-5*** shows the correlation coefficient values calculated along with the mean pressure values (systolic, diastolic and mean pressures) from each of the arteries, including the *p* values for each location.

For the systolic pressure, the model generated mean value was 116.700 ± 8.996 mmHg while the mean values estimated using GTF from the carotid artery was 117.600 ± 8.151 mmHg, from the brachial artery was 117.700 ± 7.309 mmHg, from the radial artery was 117.600 ± 7.176 mmHg and the femoral artery was 118.600 ± 9.175 mmHg. It can be seen from these mean values that GTF estimated values from each location slightly overestimates the systolic pressure at the root of the aorta as compared to the mean systolic pressure values generated by the 1-D model. The Pearson's *r* values are 0.991, 0.981, 0.978 and 0.873 *($p < 0.001$)* for the carotid, brachial, radial and femoral arteries, respectively. These *r* values indicate that the highest correlation is between the values estimated from the carotid artery followed closely by the brachial and radial arteries. The least correlated value was the one estimated using the femoral artery.

For the diastolic pressure, the model generated mean value was 86.560 ± 4.995 mmHg while the mean values estimated using GTF from the carotid artery was 87.130 ± 4.983 mmHg, from the brachial artery was 86.860 ± 5.132 mmHg, from the radial artery was 86.390 ± 5.056 mmHg and the femoral artery was 84.250 ± 5.928 mmHg. It can be seen from these mean values that GTF estimated values from the carotid and brachial arteries slightly overestimates the diastolic pressure while the values estimated from the radial and femoral arteries underestimates the diastolic pressure at the root of the aorta when compared to the mean diastolic pressure values generated by the 1-D model. The Pearson's *r* values for the carotid, brachial, radial and femoral arteries are 0.996, 0.996,

0.993 and 0.971 *(p* < 0.001*)*, respectively. These *r* values indicate that the highest correlation is between the values estimated from the carotid and brachial arteries followed closely by the radial and femoral arteries. The least correlated value was the one estimated using the femoral artery.

For the mean pressure, the model generated mean value was 101.800 ± 5.495 mmHg while the mean values estimated using GTF from the carotid artery was 102.800 ± 5.401 mmHg, from the brachial artery was 102.800 ± 5.522 mmHg, from the radial artery was 102.800 ± 5.457 mmHg and the femoral artery was 103.100 ± 5.563 mmHg. As seen from these mean values, the GTF estimated values from each location slightly overestimates the mean pressure at the root of the aorta as compared to the mean pressure values generated by the 1-D model. The Pearson's *r* values are 0.999, 1.000, 1.000 and 0.934 *(p* < 0.001*)* for the carotid, brachial, radial and femoral arteries, respectively. These *r* values indicate that the mean pressure values estimated from the carotid, brachial and radial arteries are highly correlated with the mean pressures generated from the 1-D model. As seen with the mean systolic and diastolic pressure values, the lowest correlation was found from the pressure values estimated using the femoral artery.

Table 7-5: Comparison of the model generated and GTF estimated central aortic systolic, diastolic and mean pressures from the four locations.

Variable	P_S	P_D	P_m
Model Generated (mmHg)	116.700 ± 8.996	86.560 ± 4.995	101.800 ± 5.495
Carotid			
GTF estimated (mmHg)	117.600 ± 8.151	87.130 ± 4.983	102.800 ± 5.401
Pearson's *r* value	0.991	0.996	0.999
Brachial			
GTF estimated (mmHg)	117.70 ± 7.309	86.860 ± 5.132	102.800 ± 5.522
Pearson's *r* value	0.981	0.996	1.000
Radial			
GTF estimated (mmHg)	117.600 ± 7.176	86.390 ± 5.056	102.800 ± 5.457
Pearson's *r* value	0.978	0.993	1.000
Femoral			
GTF estimated (mmHg)	118.600 ± 9.175	84.250 ± 5.928	103.100 ± 5.563
Pearson's *r* value	0.873	0.971	0.934
***p* for association**	< 0.001	< 0.001	< 0.001

7.3.2 Linear regression

Fig. 7-8, ***Fig. 7-9*** and ***Fig. 7-10*** show the relationship between the systolic, diastolic and mean pressures estimated using GTF from multiple locations and the systolic, diastolic and mean pressures generated by the 1-D model for the remaining 97 cases of the database.

Estimated systolic pressures (ESP) from the (a) carotid, (b) brachial, (c) radial and (d) femoral arteries are shown in figure ***Fig. 7-8***. The figure shows the data points with the regression line. There was a significant difference between the systolic pressures estimated using the femoral artery and the model generated systolic pressures ($y = 0.8902\,x + 14.79, r^2 = 0.762,\ p < 0.001$). However, there is little difference between the systolic pressures estimated using the carotid artery ($y = 0.8982\,x + 12.85, r^2 = 0.983, p < 0.001$), brachial artery ($y = 0.7971\,x + 24.68, r^2 = 0.963,\ p < 0.001$), radial artery ($y = 0.7800\,x + 26.57, r^2 = 0.956,\ p < 0.001$) and the model-generated systolic pressures (VSP).

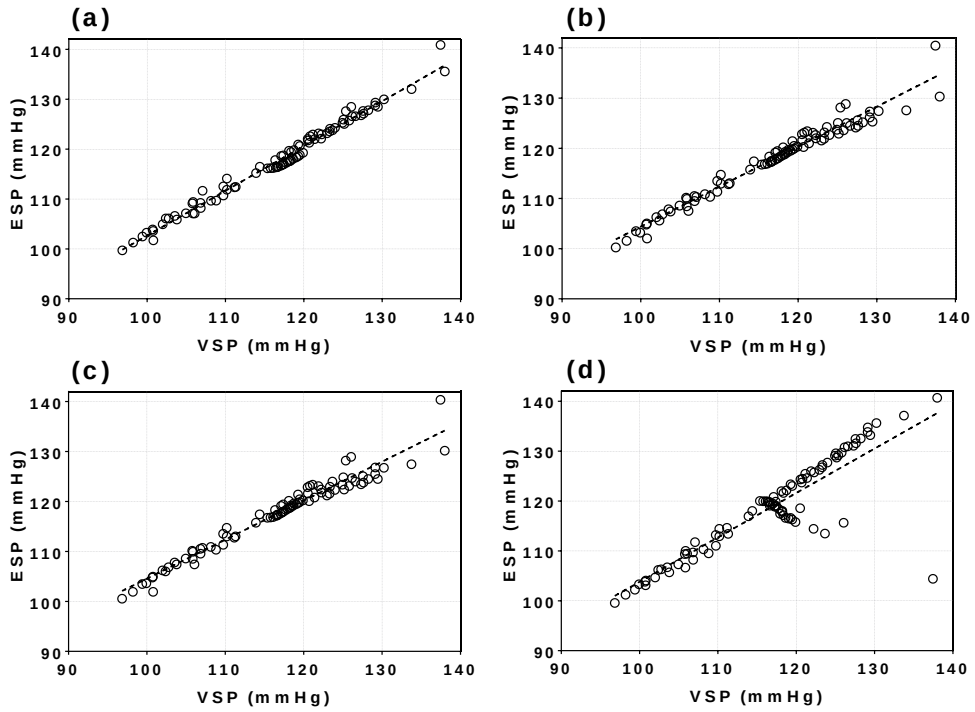

Fig. 7-8: Relationship between the model generated (validated) central systolic pressures (VSP) and GTF estimated central systolic pressures (ESP) associated with (a) carotid artery, (b) brachial artery, (c) radial artery and (d) femoral artery. The dotted line is the line of best fit.

Estimated diastolic pressures (EDP) from the (a) carotid, (b) brachial, (c) radial and (d) femoral arteries are shown in ***Fig. 7-9***. There is little difference between the systolic pressures estimated using the carotid artery ($y = 0.9935\,x + 1.13, r^2 = 0.992,\ p < 0.001$), brachial artery ($y = 1.023\,x - 1.728, r^2 = 0.992,\ p < 0.001$), radial artery ($y = 1.005\,x - 0.5894, r^2 = 0.985,\ p < 0.001$), femoral artery ($y = 1.153\,x - 15.55, r^2 = 0.944,\ p < 0.001$) and the model generated diastolic pressures (VDP).

Estimated mean pressures (EMP) from the (a) carotid, (b) brachial, (c) radial and (d) femoral arteries are shown in ***Fig. 7-10***. The figure shows the data points with the regression line. There was a significant difference between the mean pressures estimated using the femoral artery and the model

generated mean pressures ($y = 0.9454\,x + 6.829, r^2 = 0.872,\ p < 0.001$). However, there is little difference between the mean pressures estimated using the carotid artery ($y = 0.9819\,x + 2.876, r^2 = 0.998,\ p < 0.001$), brachial artery ($y = 1.005\,x + 05462, r^2 = 1.000,\ p < 0.001$), radial artery ($y = 0.9928\,x + 1.776, r^2 = 1.000,\ p < 0.001$) and the model generated mean pressures (VMP).

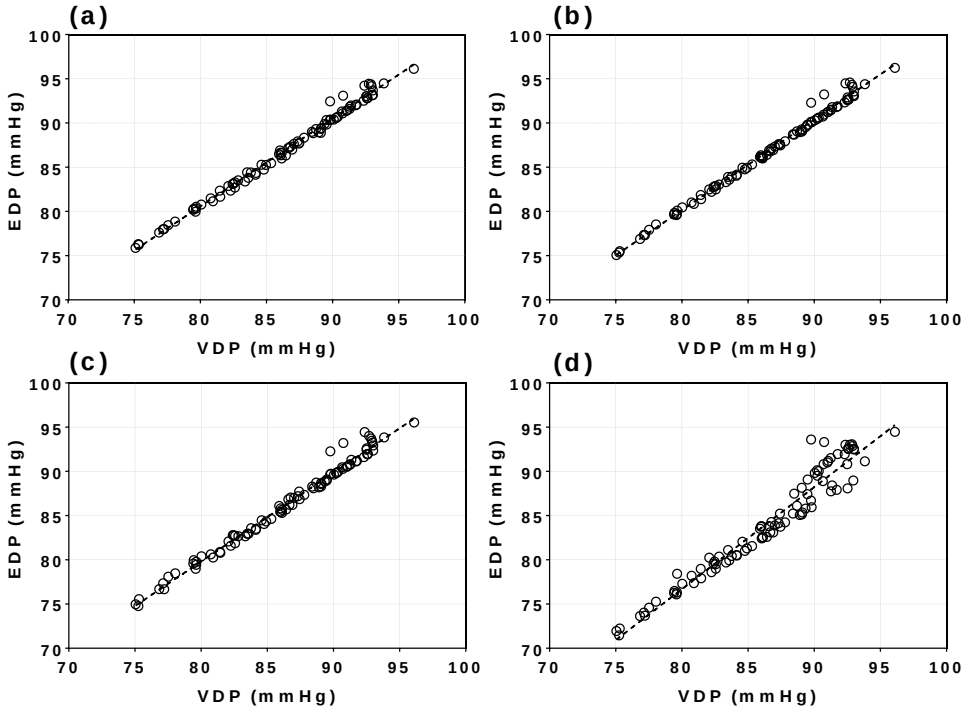

Fig. 7-9: Relationship between the model generated (validated) central diastolic pressures (VDP) and GTF estimated central diastolic pressures (EDP) associated with (a) carotid artery, (b) brachial artery, (c) radial artery and (d) femoral artery. The dotted line is the line of best fit.

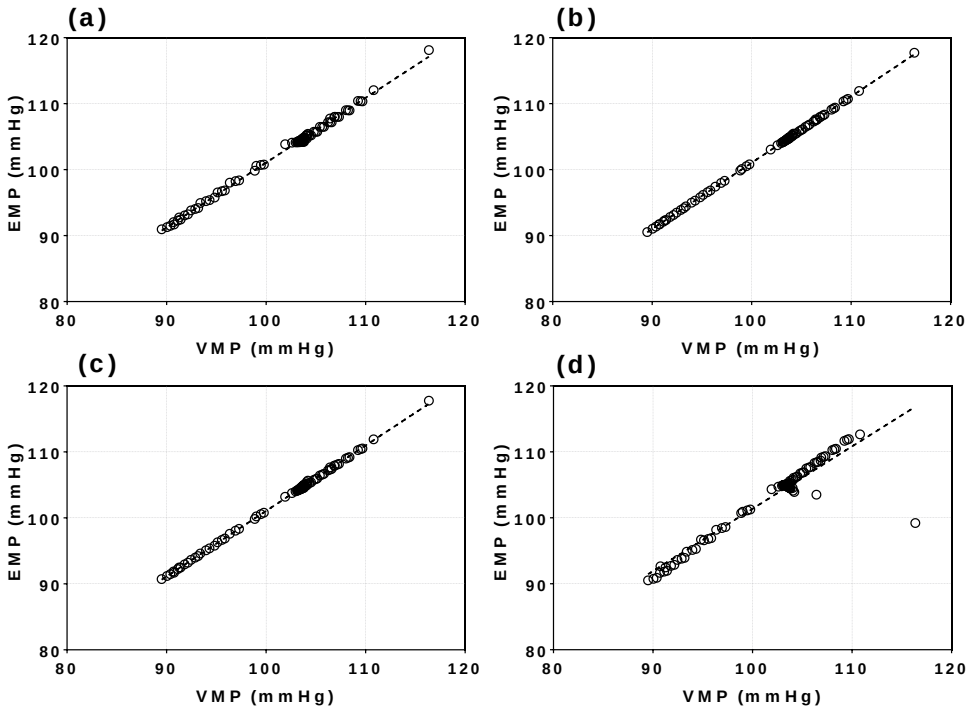

Fig. 7-10: Relationship between the model generated (validated) central mean pressures (VMP) and GTF estimated central mean pressures (EMP) associated with (a) carotid artery, (b) brachial artery, (c) radial artery and (d) femoral artery. The dotted line is the line of best fit.

7.3.3 Bland-Altman analysis

The relative performance of the GTF estimated pressure responses can be visually comprehended with relative ease using the Bland-Altman plots depicted in ***Fig. 7-11***, ***Fig. 7-12*** and ***Fig. 7-13*** for the systolic, diastolic and mean pressures. The y-axis represents the mean difference (bias) of measures between the model generated and GTF estimated pressure responses (systolic, diastolic or mean) while the x-axis represents the average of the measures from the two method [339].

Fig. *7-11* depicts the Bland-Altman plot of the central aortic systolic pressures generated using the 1-D model and estimated using the GTF technique. Bland-Altman analysis showed that the bias was

0.9733 mmHg (95% limits of agreement: -1.78 to 3.727), 1.006 mmHg (95% limits of agreement: -3.521 to 5.532), 0.896 mmHg (95% limits of agreement: -3.976 to 5.769), and 1.974 mmHg (95% limits of agreement: -7.013 to 10.96) for the estimation carried out using the carotid artery, brachial artery, radial artery and femoral artery, respectively.

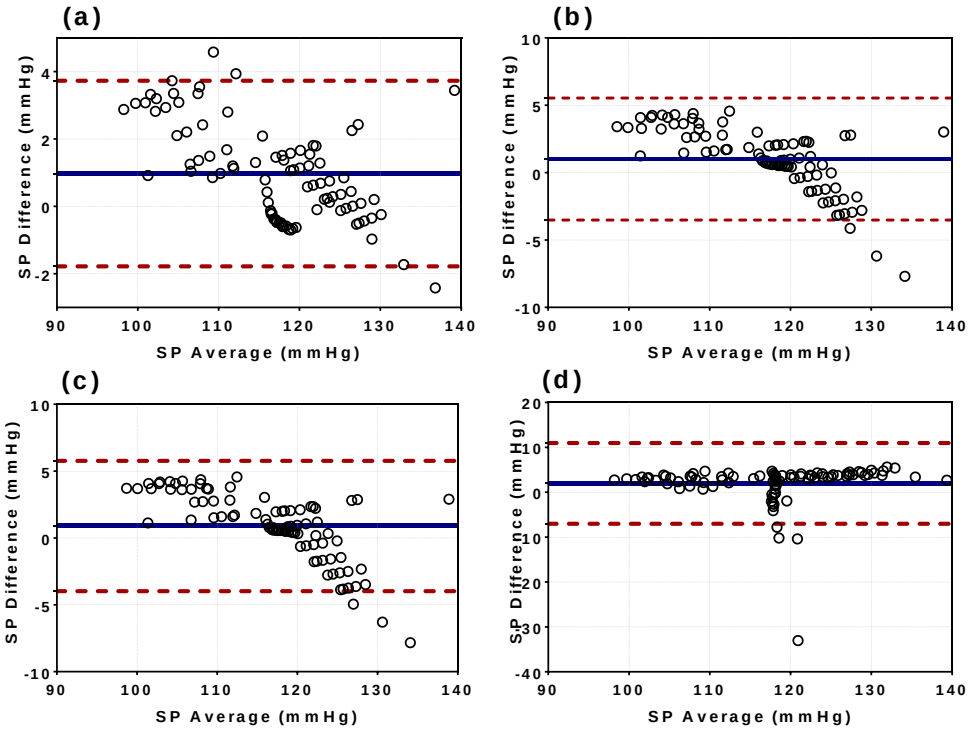

Fig. 7-11: Bland Altman plots for the model generated and GTF estimated central systolic pressures (SP) associated with (a) carotid artery, (b) brachial artery, (c) radial artery and (d) femoral artery. The solid blue line represents the mean difference (bias) and the dotted red lines represent the 95% limits of agreement.

Fig. *7-12* shows the Bland-Altman plot of the central aortic diastolic pressures generated using the 1-D model and estimated using the GTF technique. Bland-Altman analysis showed that the bias was 0.569 mmHg (95% limits of agreement: -0.321 to 1.459), 0.3002 mmHg (95% limits of agreement: -0.618 to 1.218), -0.1674 mmHg (95% limits of agreement: -1.364 to 1.029), and -2.311 mmHg

(95% limits of agreement: -5.449 to 0.826) for the estimation carried out using the carotid artery, brachial artery, radial artery and femoral artery, respectively.

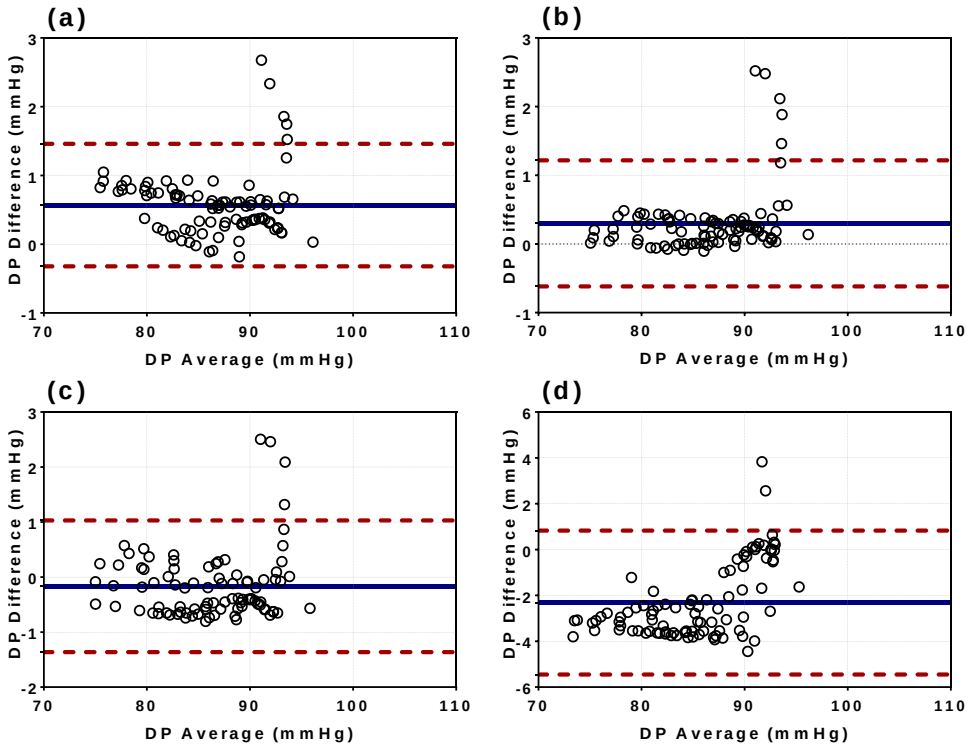

Fig. 7-12: Bland Altman plots for the model generated and GTF estimated central diastolic pressures (DP) associated with (a) carotid artery, (b) brachial artery, (c) radial artery and (d) femoral artery. The solid blue line represents the mean difference (bias) and the dotted red lines represent the 95% limits of agreement.

Fig. *7-13* depicts the Bland-Altman plot of the central aortic mean pressures generated using the 1-D model and estimated using the GTF technique. Bland-Altman analysis showed that the bias was 1.03 mmHg (95% limits of agreement: 0.501 to 1.559), 1.045 mmHg (95% limits of agreement: -0.929 to 1.160), 1.039 mmHg (95% limits of agreement: 0.778 to 1.300), and 1.275 mmHg (95% limits of agreement: -2.670 to 5.219) for the estimation carried out using the carotid artery, brachial artery, radial artery and femoral artery, respectively.

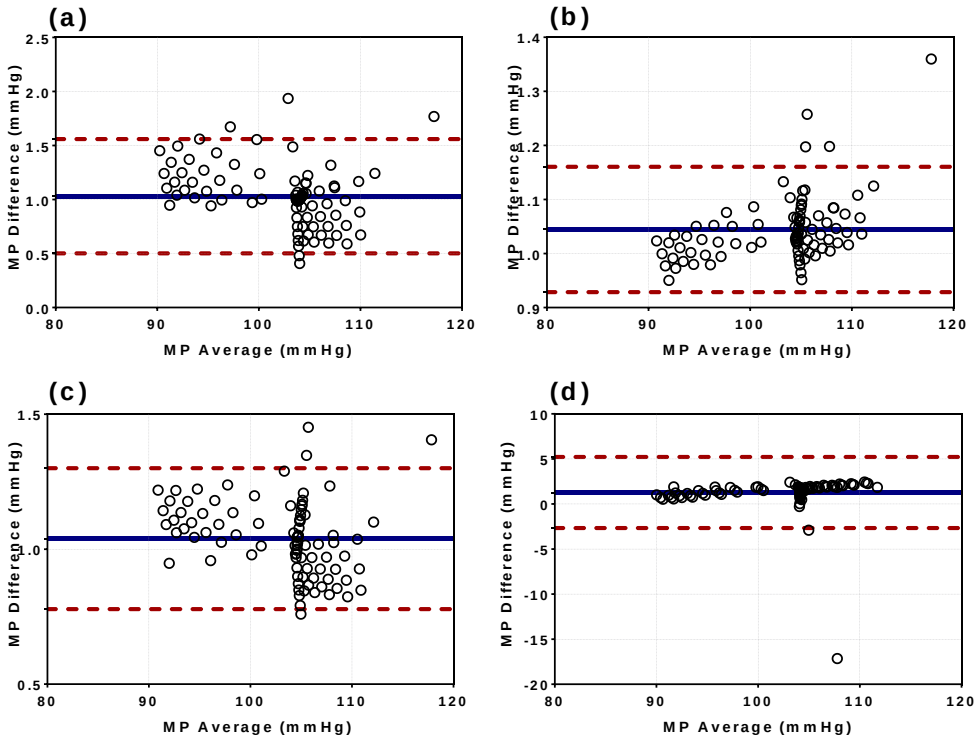

Fig. 7-13: Bland Altman plots for the model generated and GTF estimated central mean pressures (MP) associated with (a) carotid artery, (b) brachial artery, (c) radial artery and (d) femoral artery. The solid blue line represents the mean difference (bias) and the dotted red lines represent the 95% limits of agreement.

7.4 Discussion

It has been previously shown that the waveforms in the ascending aorta and the waveforms in peripheral locations are markedly different [13], [17], [18]. The systolic pressure in the peripheral location is higher due to wave reflections that occur because of the tapering and bifurcating nature of the arteries and most importantly due to the impedances at the terminal ends of the arteries due to arterioles [67]. The reflected waves superimpose on the pressure waves, hence increasing the systolic pressure. The diastolic wave is also more prominent and due to the distance from the heart, the foot of the wave is delayed in peripheral locations. [340]. This is demonstrated in **Fig. *7-6*** and shows the difference in pressure contours [17], [202], [294]. This difference is one of many reasons

that makes peripheral blood pressure measurement a less than preferable indicator of cardiac function/abnormality leading to a need for central aortic pressure estimation [18], [19], [21], [298], [309], [310].

For this study, TFs between the carotid, brachial, radial, femoral arteries and the ascending aorta were estimated (**Fig. *7-7***) for half the database created in the previous chapter and used to reconstruct the aortic waveforms for the remaining half of the database from each of these locations (***Fig. 7-4***). The results discussed in the previous section show that the transfer function reconstructs the aortic waveform with good accuracy. However, the accuracy decreases the farther away the peripheral site is from the heart. The best estimation comes from the carotid artery because it is closest to the heart hence the waveform has not been modified as much as the other peripheral sites [341].

In order to validate the GTFs estimated from the various locations, the peak amplification and minimum phase of each GTF is compared with GTFs validated in literature using human subjects. **Table *7-4*** shows the peak amplification and minimum phase of each of the estimated GTF, which can also be seen in **Fig. *7-7***. Karamanoglu et al. [13] used two separate GTFs, one for the radial artery and the other for the brachial artery. The peak amplification for the brachial GTF they used (**Fig. *7-3*** & **Table *7-3***) occurred at 4 Hz and the value of the amplitude was 2.572, while the peak amplification for the radial GTF they used occurred at 4 Hz and the value of the amplitude was 3.049. In comparison, the GTFs estimated in the current study (**Fig. *7-7***) had a peak amplification at 4 Hz and had values of 2.114 and 3.018 for the brachial GTF and the radial artery GTF, respectively. These values showed extremely good agreement with the values used by Karamanoglu et al. The minimum phase' Karamanoglu et al. reported occurred at 9 Hz and had a value of -3.627 rad and -6.450 rad for the brachial artery and radial artery GTF, respectively. In this study, the minimum phase at the same frequency had a value of -3.747 rad and -6.594 rad for the brachial and radial artery GTFs, respectively. The phase values show satisfactory agreement as well.

As for the GTF estimated for the carotid artery waveforms, a separate study conducted by Gallagher et al. [330] is used as a benchmark. In their review, Gallagher et al. report a peak amplification of 1.431 occurring at 4 Hz for the GTF estimated via the carotid artery (**Fig. *7-2*** & **Table *7-2***). In comparison, the GTF estimated via the carotid artery in the current study demonstrates characteristic peaking at 4 Hz and has an amplitude of 1.567, which agrees well with the value reported by Gallagher et al.

The phase' for all the arteries are negative as there is a delay between the frequency components of the pressure waves in the aorta and the respective arteries. All the phase' tend to reach an asymptotic values representing a constant group delay [13].

For the systolic pressure generated by the model and estimated using GTF, the Bland-Altman plots shown in **Fig. *7-11*** reveal that most of the data points lie within the 95% limits of agreement for all four locations. This indicates that by enlarge all the arteries are capable enough to estimate the CAP with good accuracy. However, the limits of agreement for the femoral artery (***Fig. 7-11***) are wider as compared to the rest of the arteries signifying femoral artery to be the least preferable site of CAP estimation using GTF. The narrowest limits of agreement are for the carotid artery (***Fig. 7-11***), signifying that the most preferable peripheral location to estimate CAP is the carotid artery. This agrees well with literature [291] and is due to the proximity of the carotid artery to the ascending aorta. Looking at the bias, it can be concluded that the four locations lead to a slight over estimation of the systolic pressure. The carotid artery by 0.9733 mmHg, the brachial artery by 1.006 mmHg, the radial artery by 0.896 mmHg and the femoral artery by 1.974 mmHg. This data is tabulated in **Table *7-6***.

These finding are further complimented by the linear regression (**Fig. *7-8***) and Pearson's *r* values (**Table *7-5***) calculated for the systolic pressures. The CAP waveforms estimated from the carotid artery waveforms have the highest correlation (**Table *7-5***) with the model generated CAP

waveforms (r=0.991) while the least correlated are the waveforms estimated via the femoral artery (r = 0.873). The r^2 values from the linear regression (**Fig. *7-8***) cements that the carotid artery is the most preferable site for estimating systolic CAP as the highest r^2 value (r^2 =0.983) are for the systolic CAP waveforms estimated via the carotid artery. The femoral artery estimated CAP waveforms have the lowest r^2 value (r^2=0.762) confirming that the femoral artery is the least preferable site. The brachial and radial arteries establish excellent statistical relevance and demonstrate that these locations are excellent choices for systolic CAP estimation.

As for the diastolic and mean pressures, the same reasoning applied for the systolic pressures can be used to justify that the best estimation site is the carotid artery and the least preferable site is the femoral artery (**Fig. *7-9***, **Fig. *7-10***, **Fig. *7-12*** and **Fig. *7-13***). It must be noted that the diastolic pressure is estimated with excellent accuracy ($r > 0.9$, $r^2 > 0.9$) from all the four locations (**Fig. *7-9***) but in purely quantitative terms, the carotid, brachial and radial arteries have higher r and r^2 values, making them relatively preferable in comparison to the femoral artery. Also noteworthy, by looking at the bias via the Bland-Altman plot (**Fig. *7-12***) and **Table *7-6***, is that the CAP waveforms estimated via carotid and brachial arteries slightly overestimate the diastolic pressure by 0.569 mmHg and 0.3002 mmHg, respectively. The radial and femoral arteries on the other hand underestimate the diastolic pressure by 0.167 mmHg and 2.311 mmHg, respectively. The mean pressure of the estimated CAP waveforms (**Fig. *7-13***) is overestimated slightly. 1.03 mmHg from the waveforms via the carotid artery, 1.045 mmHg via the brachial artery, 1.039 mmHg via the radial artery and 1.275 mmHg via the femoral artery.

For the GTFs derived via the four locations, the mean difference between the estimated and model generated systolic, diastolic and mean pressures are given in **Table *7-6***. The mean systolic differences lie in a range of 0.9 to 1.9 mmHg while the mean diastolic difference lies in the range

of -2.31 to 0.57 mmHg. These differences are similar to the mean differences reported in literature [13], [22], [334].

Table 7-6: Summary of the mean differences between GTF estimated and model generated central systolic, diastolic and mean pressures.

Artery	Mean Difference (mmHg)		
	P_S	P_D	P_m
Carotid	0.973	0.569	1.030
Brachial	1.006	0.300	1.045
Radial	0.896	−0.167	1.039
Femoral	1.974	−2.311	1.275

Since the evaluation method used here, that is, evaluation of the GTF technique using a comprehensive model, is novel and independent, it is not comparable to results from literature. In the majority of past studies conducted to evaluate the GTF technique [11], [13], [342]–[344], [23], [24], [27], [31], [315], [329], [330], [334], the subjects used have been human patients and the study protocols have been much different to the ones used here. In the mentioned clinical studies, there is loss of high-frequency information due to the fluid-filled catheter used for invasive measurements [334]. Another source of error reported in most of these studies is that, due to the nature of catheter-recorded waveforms from the various arteries (peripheral and aortic), and the further study protocols such as applanation of the radial artery, there is an introduction of a variation in the time-interval between the estimated and measured waveforms. This means the estimated and measured waveforms are not actually measured simultaneously [31]. A further source of error reported in these clinical studies is the calibration of the peripheral pressures to central pressures by assuming that the diastolic and (or) mean pressures in the peripheral sites is the same as the diastolic and (or) mean pressure in the ascending aorta [334].

Much of the criticism directed towards the GTF technique pertains to the inaccurate methods used to measure waveforms peripherally and the calibration/time-interval errors associated with them [330]. However, these issues are a separate entity and the GTF technique in itself is simply confined to the manipulation of peripheral waveforms to estimate central waveforms rather than rectifying these errors [330]. The evaluation method used in this study does not use clinically measured values, nor needs calibration assumptions. This reduces a significant amount of the errors associated with central and peripheral waveform measurement.

7.5 Summary

In this chapter, the pressure response database for various physiological and pathological conditions, created in chapter 6, is used to evaluate the GTF technique. Half of the database is used to estimate and validate the GTF between the ascending aorta and four peripheral locations, namely the carotid artery, brachial artery, radial artery and the femoral artery. The remaining half of the database is used to reconstruct central aortic pressure waveforms in order to compare them with model generated central waveforms. A statistical analysis is carried out to test the validity of the GTF technique.

Key points from this chapter are as follows:

- Nowadays, blood pressure in human subjects is measured invasively in catheterization laboratories. There are various methods available for invasive blood pressure measurements among which using high fidelity catheter micro-tip pressure transducers is considered the most accurate.

- There are a number of limitations in measuring blood pressure using these methods. Due to their invasive nature, they can't be used for large scale clinical studies for instance subject who are healthy or even patients with hypertension, therefore these methods are deployed in subjects that are critically ill or already undergoing an invasive procedure such as a cardiopulmonary bypass

- Waveforms of peripherally measured pressure and central aortic pressures are significantly different in regards to the wave shapes as well as amplitude. It is believed that the central aortic pressure is a better representation of hemodynamic load and stress to the heart and large vessels at rest

- Noninvasively estimated central aortic pressure has previously demonstrated its ability to forecast cardiovascular events better than peripherally measured pressures

- Transfer functions are mathematical functions that describe the behavior of a system by relating the input and output signals. The transfer function is expressed in terms of modulus and phase. Prior studies have shown that physiologically relevant data is contained within the first 15 harmonics

- There has been some debate that the general transfer function varies from person-to-person due to a variety of physiological differences, making the general transfer function an unreliable tool of choice in such analyses as it lacks adaptability

- With the on-going disagreement between the research groups for and against the GTF technique, it is essential to use an independent method to test the GTF technique, which also serves as an alternative to experimental studies. While numerical modeling provides such an alternative research method, a full-scale cardiovascular model that incorporates non-linearities as well, has not been used to systematically evaluate the GTF technique.

- In this chapter, GTFs are estimated and used to re-synthesize central waveforms, which have already been generated from a comprehensive 1-D model. Correlation, linear regression and Bland Altman analyses are then carried out to test the validity of GTFs.

CHAPTER 8

CONCLUSIONS AND PERSPECTIVES

8.1 Conclusions

The work carried out in this thesis aimed to test the validity of the GTF technique by using a well-validated and comprehensive numerical model of the human arterial network as an alternative to experimental studies. In order to achieve the primary objective, certain aims and objectives had to be met successfully which were described in section.

In this chapter, the achievement of these objectives as well as the conclusions from each of the working chapters is outlined. In the following sections, summary of important observations made while achieving these objectives, followed by the some of the limitations of the current study that pave way for the future directions in this area of study are provided. The chapter is concluded with the significant contributions to literature of this work.

Objective 1: ***Developing a one-dimensional fluid dynamical model that takes into consideration realistic features of blood flow propagation such as vessel tapering, vessel branching, inhomogeneous vessel wall elasticity etc.***

A 1-D based on physiological principles, which simulates blood propagation in the human arterial network, is developed in chapter 4. This model can predict flow and pressure in the large systemic arteries of the human cardiovascular system. The objective has been successfully achieved by further developing the fluid dynamical model developed by Olufsen et al [43]. The model includes both large arteries as well as smaller arteries.

The geometrical properties of the large arteries is based on actual data for each vessel in the arterial network. The non-linear, incompressible, axisymmetric form of the Navier-Stokes equations govern blood flow in the large arteries while the state or constitutive equation governs the elastic properties of the vessels. The coupling of these equations predicts the pressure and flow in the large arteries.

The smaller arteries on the other hand, are modelled as asymmetric structured trees, where a specified minimum radius governs the number of bifurcations, $r_{\min}$. The fluid flow and fluid-structure interaction in smaller arteries is governed by the linearized form of the Navier-Stokes equations coupled with the constitutive equation used for the large arteries. These equations predict the ratio of pressure to flow to give the impedance in the smaller arteries, which forms the outlet boundary condition for large arteries. This boundary condition allows a more dynamical impedance to be calculated which is physiological in nature.

Through the development of the mathematical model, new insights into the variation of parameters has been achieved. These insights proved immensely important in disease modelling which is an integral part of this work.

Objective 2: ***Carrying out a systematic, multi-level validation against data published in literature to increase the reliability of the code and its capability to simulate various clinical conditions.***

The objective has been successfully achieved by validating the numerical model developed in chapter 4 against data published in literature. The validation carried out is a multi-level one, in that, the model is altered in each of the validation case to test its robustness and the general agreement of model predictions with a variety of published literature. The first of its kind, a multi-level validation of a 1-D model with structured tree outflow condition, provides a significant contribution to the research community, at large, as it demonstrates the reliability of the model to simulate simple cases such as pulse wave propagation in a single vessel to more complex cases such as the pulse wave propagation in an entire arterial network.

The simplest validation carried out is the propagation of blood flow in a single vessel. For this case, propagation along the aorta is simulated. The vessel parameters are for a healthy and young adult, taken from literature [63], [80]. The RCR model used by Alastruey [2] is used as the benchmark for the validation along with in-vivo data published by Simon et al [198]. The simulation results showed excellent agreement with the model (***Fig. 5-4***) as well as the in-vivo data (***Table 5-3***). Key features of the pressure waveforms namely the dicrotic notch and the diastolic delay are captured excellently by the model, as well. Overall, the agreement of the results with the validation data is excellent and the exhibition of the key features of the pressure and flow waveforms ensures the capability of the model with structured tree outflow condition, to simulate blood flow in a single vessel.

A second level of validation is carried out by comparing the current 1-D model to a 3-D model developed by Kim et al. [199]. The 3-D model starts at the root of the aorta and includes the main upper body branches. This 3-D model (***Fig. 5-6***) is significantly more complex when compared to the first validation case as the vessels branch into other vessels. Since the 3-D model represents the entire arterial network in a lumped manner (RCR), the model for a single vessel, used in the first validation was extended to simulate an entire arterial network with a few variations in elastic parameters to match the parameters used for the 3-D model. Not only is the 1-D model capable of reproducing the results achieved from the 3-D model quantitatively but also qualitatively. The error analysis carried out in **Table *5-6*** shows that the percentage errors lie in the range of 0% to 2.5%. Noting that a 1-D model being compared to a 3-D model has such a low percentage error, increases confidence in the robustness of the 1-D model. The brachial pressure simulated using the 1-D model (***Fig. 5-11***) shows excellent agreement with the data measured for an actual human subject by Kim et al. [199] further reinforcing the competence of the 1-D model with a structured tree outflow condition.

A final validation is carried out by simulating the pulse wave propagation in an entire arterial network, the same as the second validation. However, the validation data used in the third validation are flow waveforms at multiple physiological locations in an actual human subject. The validation data was measured using MRI and was reported by Olufsen et al. [82]. The model used here is the same model developed by Olufsen et al. [43], [47], [82], mitigating the need to validate the current model against the simulated data of Olufsen's model as well. The only difference in the two models is the ejection profile used. By using a simple equation (half sinusoid equation), a consistent and generic inflow profile for all cases is produced which reduces the complexity of modelling and at the same time reduces the number of subject-specific parameters required for the inflow profile. When the model predictions are compared to the measured flow data, the shape of the computed flow waveforms show extremely good agreement along with excellent computation of the peak flowrates in all the locations (**Fig. *5-13***), conclusively validating the 1-D model at each level of validation.

Objective 3: ***Conducting a parametric study of the one-dimensional model to simulate various physiological and pathological conditions, to create a pressure response data.***

An added advantage of mathematically modelling the cardiovascular system using the formulation presented in chapter 4 is the flexibility with which the parameters of the model can be varied. This variation allows disease modelling with relative ease and the reliability of such a model has been tested at multiple levels in chapter 5. The fulfillment of this particular objective has a substantial contribution to the research community; it demonstrates the effectiveness and the robustness of the 1-D model with structured outflow condition to simulate pathological as well as variations of physiological conditions.

In chapter 6, the parameters of the 1-D model (geometric, elastic and boundary parameters) are varied to simulate a variety of physiological and pathological conditions. These include

hypertension, varying heart ejection profiles, arterial stiffening, vasodilation, abdominal aortic aneurysms and coarctation of the aorta. Key findings from these variations is as follows:

- From **Fig. *6-1***, with each increment in the cardiac output, the flow in the entire system increases causing pressure to increase in all arteries. However, the shape of the waveforms is preserved.
- From **Fig. *6-2***, in all the arteries, increasing the stiffness not only increases the systolic pressure but also decreases the diastolic pressure. The greater the increase in stiffness, the greater the increase in pulse pressure. Decreased stiffness has the opposite effect (**Fig. *6-3***).
- The 1-D model simulated results of abdominal aortic aneurysm show excellent agreement with literature as to how the pressure and flow waveforms are affected due to the presence of an AAA. Increasing the size of an aneurysm (Fig. ***6-5***), the flow rate increases in the thoracic aorta and in the infrarenal aorta but decreases in the external iliac artery, which agrees well with literature [262]. The peaks and nadirs are amplified due to the sudden widening of the aneurysm, which causes strong reflections. The pressure on the other hand decreases in all three arteries due to increased compliance as a result of the introduction of the AAA. The greater the aneurysm, the greater the compliance leading to a greater decrease in pressure. Reducing the stiffness of the AAA increases the flow in the thoracic aorta and the infrarenal aorta (**Fig.*6-6***). The increase in flow with the reduction in stiffness is much higher because not only a compliance has been introduced in the system via an aneurysm, but the stiffness of the aneurysm is further reduced which further increases the compliance.

- The simulation results of the coarctation of aorta show excellent agreement with literature [287]–[289]. As a results of CoA, an obstruction to flow is introduced which causes the pressure in the upper limbs to decrease and the opposite in the lower body (Fig. ***6-9***). A

50% CoA (50% reduction in area of the descending aorta) causes the systolic pressure in the arm to exceed 140 mmHg. As long as the coarctation is a 38% reduction in the descending aorta, the pressure in the arms at this point still doesn't exceeded 140mmHg (Fig. ***6-9***). A further reduction (58%) causes upper body hypertension and a pressure gradient of 32.75 mmHg between the upper and lower body.

It is of utmost importance to note that the purpose of disease modelling is to create a pressure response database to study the GTF technique rather than to study the disease itself. Conclusions were drawn based on literature on the behavior of modelled diseases and it has been demonstrated that the 1-D model with structured tree outflow condition is extremely robust in accurately modelling these diseases.

Objective 4: ***Carrying out a Fourier analysis on half of the central and peripheral pressure response data to estimate transfer functions between ascending aorta and multiple physiological peripheral locations.***

This objective has been successfully achieved by using the pressure response database created in chapter 6. 194 physiological and pathological cases are simulated, out of which half of them (97 cases) are used to estimate the GTFs. The 97 cases are selected at random and waveforms from only five arteries are taken into consideration, the ascending aorta, carotid artery, brachial artery, radial artery and femoral artery. The ascending aorta is where the central pressure is measured while the four other arteries are peripheral sites from which the central pressure is estimated via separate GTFs. Other locations can be used to generate a GTF but for this study, the GTFs between the ascending aorta and the mainstream peripheral locations found in literature are estimated. The waveforms from each of these locations is first transformed into the frequency domain using discrete Fourier transform after which equation (7.1) is applied to estimate the TF between the central

waveform (ascending aorta) and a peripheral location. The individual TFs are then averaged in order to estimate the GTF for each site (**Fig. *7-4***).

In order to validate the GTFs estimated from the various locations, the peak amplification and minimum phase of each GTF is compared with GTFs validated in literature using human subjects. The peak amplification for the brachial and radial GTFs used by Karamanoglu et al. [13] occurred at 4 Hz with amplitude values of 2.572 and 3.049, respectively. Gallagher et al. [330] report a peak amplification of 1.431 occurring at 4 Hz for the GTF estimated via the carotid artery. In contrast, the carotid, brachial and radial GTFs estimated in the current study had a peak amplification at 4 Hz and had values of 1.567, 2.114 and 3.018, respectively. These values show extremely good agreement with the values used by Karamanoglu et al. and Gallagher et al.

The minimum phase' for the GTFs estimated via the brachial and radial artery occurred at 9 Hz and had a value of -3.627 rad and -6.450 rad, respectively in the study conducted by Karamanoglu et al [13]. In this study, the minimum phase at the same frequency had a value of -3.747 rad and -6.594 rad for the brachial and radial artery GTFs, respectively. The phase values show excellent agreement as well.

The GTF from the femoral artery can not as yet be validated as most studies using the femoral artery use blind identification of the central aortic waveform [34]–[36], [335]–[337] rather that GTF estimation.

The validation of the GTFs means that they can be used to estimate the central aortic waveforms with the same or higher accuracy as the studies found in literature. More importantly, the amplification and phase values demonstrate that the GTFs estimated using the 1-D model and the GTFs estimated in literature using human subjects are in extremely close agreement. This cements the applicability of the mathematical models as independent alternatives to in-vitro and in-vivo

studies especially because mathematical model measurements do not need to be calibrated as opposed their experimental counterparts.

Objective 5: ***Using the estimated GTFs to estimate central aortic waveforms from multiple peripheral locations for the remaining half of the pressure response database.***

This objective has been successfully achieved by using the GTFs estimated from the four peripheral locations. The remaining half of the pressure response database (97 cases) is used for this particular objective.

Each of the averaged GTFs is multiplied with the waveforms (in frequency domain) from their respective peripheral location. This product between a particular peripheral waveform and its GTF yields the central aortic waveform in the frequency domain. Since there are four peripheral locations (therefore four GTFs), a total of 388 central waveforms (97 from each peripheral site) are estimated. These central aortic waveforms are transformed back in the time domain using the inverse discrete Fourier transform.

As the central aortic pressure waveforms of the remaining database is known as well, these estimated waveforms can be statistically compared with the known central aortic pressures (model generated) to test the validity of the GTF technique and its performance from each peripheral location.

Objective 6: ***Carrying out a statistical analysis on the GTF estimated central aortic waveforms to test the validity of the GTF technique.***

Chapter 7 details the statistical analysis carried out to test the validity of the GTF technique. The methods used to analyze and compare the estimated and model generated waveforms are Pearson's correlation coefficient, linear regression and the Bland-Altman method. The ultimate aim of this study is to test the validity of the GTF technique with the use of a comprehensive numerical method.

The estimated accuracy of the systolic, diastolic and mean pressures are evaluated separately for the four peripheral locations.

For the systolic pressure generated by the model and estimated using GTF, the Bland-Altman plots reveal that all the arteries are adept enough to estimate the CAP with good accuracy. The bias, 0.9733 mmHg, 1.006 mmHg, 0.896 mmHg and 1.974 mmHg of the carotid, brachial, radial and femoral arteries, respectively demonstrates a slight over estimation. The r^2 values from the linear regression of 0.983, 0.963, 0.956 and 0.762 and the Pearson's *r* values of 0.991, 0.981, 0.978 and 0.873 *($p < 0.001$)* for the carotid, brachial, radial and femoral arteries, respectively establish carotid artery as the most preferable site for systolic pressure estimation while femoral artery as the least preferable site. The brachial and radial arteries show extremely satisfactory estimation results as well. Overall, the strong significance shown statistically confirms the GTF technique as an excellent estimator of the central aortic systolic pressure, especially from the carotid, brachial and radial arteries.

The diastolic pressure is estimated with excellent accuracy *($r > 0.9, r^2 > 0.9$)* from all the four locations. With r^2 values from the linear regression of 0.992, 0.992, 0.985 and 0.944 and the Pearson's *r* values of 0.996, 0.996, 0.993 and 0.971 *($p < 0.001$)* for the carotid, brachial, radial and femoral arteries, respectively, the diastolic pressure is predicted with an even higher accuracy as compared to the systolic pressure from all arteries. The brachial and carotid arteries are the most preferable sites followed by the radial and femoral arteries. Bias values of 0.569 mmHg, 0.3002 mmHg, -0.1674 mmHg and -2.311 mmHg reveal that the carotid and brachial arteries overestimate the diastolic pressures slightly while the radial and femoral arteries underestimate the diastolic pressure slightly. Again, the high correlation between the estimated and model generated values demonstrate GTF as an excellent estimator of central aortic diastolic pressure.

Finally, the mean pressure bias of 1.03 mmHg, 1.045 mmHg, 1.039 mmHg and 1.275 mmHg for the carotid, brachial, radial and femoral arteries, respectively, shows a slight overestimation by all four locations. r^2 values from the linear regression of 0.998, 1.000, 1.000 and 0.872 and the Pearson's *r* values of 0.999, 1.000, 1.000 and 0.934 *($p < 0.001$)* for the carotid, brachial, radial and femoral arteries, respectively, reveal that the central aortic mean pressure is estimated most accurately by the GTF technique.

The high correlation and minimal bias's with narrow 95% limits of agreement make it evident that the GTF technique is extremely accurate in predicting central aortic pressure from peripheral locations. The order of preference of the peripheral location from the statistical analysis is the carotid artery followed by the brachial artery, trailed closely by the radial artery with femoral artery as the least preferable site. The mean differences in the central aortic pressures shown in **Table *7-5*** and the extensive statistical analysis testifies to this conclusion. These preferences are in complete agreement with literature as well since carotid artery is the closest to the aorta. However, due to the ease with which the brachial and radial waveforms can be acquired as compared to the carotid artery and factually having almost the same estimation capabilities, the brachial and (or) the radial arteries are recommended as the preferable peripheral sites.

The study conducted here is unique, in that, it has used a full-scale numerical model to replace data acquisition from human subjects. The numerical model acts as human subject, so to speak and the flexibility of parameter variation allows modelling of various pathological and physiological conditions. The GTFs estimated using this comprehensive model resemble the GTFs estimated using human subjects which supplement the already comprehensive validation carried out. The performance of these GTFs demonstrate the accuracy of the GTF technique and acts as a rebuttal to the criticism of the GTF technique. In doing so, it also reiterates the importance of errors that are inherent in waveform acquisition from human subjects and the further manipulation of these

waveforms (such as calibration) before carrying out the GTF estimation of the central aortic pressures.

A summary of the major findings of the study is stated as follows:

- Structured tree outflow boundary condition is capable of modelling blood flow in a single vessel with improved accuracy as compared to the RCR model.
- The 1-D model with structured tree outflow condition is capable of quantitatively and qualitatively produce results attained from a 3-D model (Percentage errors lie in the range of 0% to 2.5%).
- Generic inflow profile reduces the complexity of modelling, that is, the number of subject-specific parameters are reduced without compromising much on the accuracy of the results achieved.
- With each increment in the cardiac output, the flow in the entire system increases causing pressure to increase in all arteries.
- The greater the increase in stiffness, the greater the increase in pulse pressure. Decreased stiffness has the opposite effect.
- Increasing the size of an aneurysm causes the flow rate to increase in the thoracic aorta and in the infrarenal aorta but decrease in the external iliac artery.
- The greater the aneurysm, the greater the compliance leading to a greater decrease in pressure
- Reducing the stiffness of the AAA increases the flow in the thoracic aorta and the infrarenal aorta
- As a results of CoA, an obstruction to flow is introduced which causes the pressure in the upper limbs to decrease and the opposite in the lower body

- A coarctation greater than 38% but less than 57% causes upper body hypertension and a pressure gradient $\geq$ 20 mmHg between the upper and lower body.
- 1-D model with structured tree outflow condition is extremely robust in accurately modelling these diseases.
- GTFs estimated using the 1-D model generated pressure response database and the GTFs estimated in literature using human subjects are in extremely close agreement.
- The bias between model generated and GTF estimated P_S demonstrates a slight over estimation using the GTF technique (0.896 mmHg to 1.974 mmHg).
- Bias values of 0.569 mmHg, 0.3002 mmHg, -0.1674 mmHg and -2.311 mmHg reveal that for P_D estimated using GTFs from the carotid and brachial arteries, it is overestimated slightly while the P_D estimated using GTFs from radial and femoral arteries underestimate it slightly.
- Finally, P_M bias of 1.03 mmHg, 1.045 mmHg, 1.039 mmHg and 1.275 mmHg between model generated and GTF estimated CSAP from carotid, brachial, radial and femoral arteries, respectively, shows a slight overestimation by all four locations.
- The high correlation and minimal bias's with narrow 95% limits of agreement make it evident that the GTF technique is extremely accurate in predicting central aortic pressure from peripheral locations.
- The order of preference of the peripheral location from the statistical analysis is the carotid artery, brachial artery, radial artery and femoral artery as the least preferable site.

8.2 Study limitations and future work

The work conducted here shows the capabilities and robustness of the 1-D numerical model as well as how it can be used to test the validity of the GTF technique. However, before integrating these

systems in real life applications, there is still significant room for improvement and further investigations.

The validations carried out in this work have been using studies published in literature. Although comparisons were drawn from models/in-vivo data already found in literature, it is recommended that the current validation studies be taken a step forward and in-house in-vivo analyses be introduced as an additional validation. In addition to a complete MRI study to measure flow rates in different anatomical location, pressure waveforms from that specific subject should be acquired. Before the experiment is conducted, the geometrical properties of the said subject should be measured/approximated. It has been well established that the geometry of arteries in the network have a great impact on hemodynamics. Knowing the geometry of the arteries of the validation subject as well as the flow and pressure waveforms and validating the current model against such data would make the model a truly subject-specific model.

The structured tree used in the current model terminates at a certain minimum radius. This minimum radius coincides with the resistance from a certain organ. The minimum radii used here should be adjusted depending on where the specific artery terminates. Alteration of other parameters of the structured tree such as the radius exponent and the asymmetry ratio enhances model predictions as these parameters reveal the true impedance within the vascular beds.

In this work, a generic inflow profile has been used. The inflow profile works well as seen when compared with data published in literature. However, physiological ejection profile are more complicated than the one model here. More so because physiologically, there is a slight backflow into the ventricle from the aorta as the aortic valves close. The inflow profile should include this effect to provide more information on the wave reflections introduced due to this backflow. Another possible solution to this is making a separate heart model and integrating it with the current model.

It has been shown in this work that the vessels in the human cardiovascular system change gradually downstream. The elasticity of the arteries in this work has been defined using a state equation that is based on linear elasticity. Depending on the function of the vessel, the elastic properties vary and the model needs to reflect this. The model is flexible enough to allow elastic parameters to be varied according to function, which should be taken into consideration in future studies. An empirically based relation that allows elastic properties to be altered depending on the artery can be introduced [43].

For the pressure response database, although the geometric properties were varied slightly, physiologically each individual subject does not necessarily have the same geometrical/ elastic properties. This should be taken into consideration. Although tedious and time consuming, geometrical and elastic properties from a large enough human subject sample can be used to create a virtual database that can be implemented in the model.

Addition of the venous circulation such as that modelled by Vaughan and Qureshi et al. [53], [188]. This expands the scope of study of the cardiovascular system and the non-linearities introduced due to the venous system can be taken into consideration.

Integrating the pulmonary, coronary and cerebral circulations in the current model will further enhance the real life applicability of the model.

Since the GTF technique estimates the central aortic waveforms, a simple but significant study can be conducted by using a subject specific model. In that, the model will use parameters that reflect physiological geometry and elastic properties of a particular subject. The GTFs estimated from the database created here can then be used in the validated subject specific model to estimate the central aortic pressure. The central aortic waveforms from the said subject can be used to test the validity of the GTF estimated central waveforms.

8.3 Scientific achievements

- Demonstration of the structured tree outflow condition to provide a dynamic and physiological downstream boundary condition in the simulation of a single vessel. Data published in literature indicates that the structured tree outflow condition has been used for full scale arterial networks and (or) networks comprising of more than a few vessels. In this work, simulation for a single vessel has been carried out and validated against a single vessel model with RCR downstream condition. An additional, in-vivo validation further cements the applicability of the structured tree outflow condition in a single vessel model. The significant contribution to literature is the demonstration that such a model can be used to study hemodynamics in a specific vessel, given that the geometric, elastic and downstream parameters can be defined accurately.
- A multi-level validation of the 1-D model with structured tree outflow boundary condition. This validation ensures the capability of the code and demonstrates the robustness of the 1-D numerical model of the cardiovascular system with structured tree outflow condition to accurately model extremely simple cases with only a single vessel to more complex arterial networks. The 1-D model is validated against in-vivo data, previous 1-D model data as well as 3-D model data, which increases confidence in the 1-D numerical model. The significant scientific achievement here is the factual identification of 1-D model with structured tree outflow conditions as an alternative to experimental studies and higher dimension models to study pressure and flow waveforms.
- The validated 1-D model has been used to model a variety of arterial stiffness'. Vasoconstriction as well as vasodilation with varying peripheral resistances have been modelled to good effect. Effects of stiffness variations which range from low to high stiffness' have been added to literature.

- The 1-D model is used to model two relatively common diseases, abdominal aortic aneurysm and coarctation of the aorta. The modelling demonstrates the robustness of the 1-D model with structured tree outflow condition to model both of these diseases with accuracy. The results are compared with published literature and show excellent agreement. The effects of increasing the size of the aneurysm, decreasing the aneurysm diameter and increasing the coarctation of the aorta are studied with the ultimate aim to create a pressure response database. This demonstration of disease modelling and effects of disease variation has a significant contribution to literature as it carves way for 1-D model to be used for an in-depth analysis of diseases to improve diagnostics.
- A pressure response database has been created which includes cardiovascular responses to physiological and pathological conditions. The next obvious step is to make this database public and add more diseases to increase the size of the database and provide a comprehensive database for future research.
- The ultimate novelty and goal of this work is to use an alternative approach to in-vivo and in-vitro studies to evaluate the GTF technique. This has been successfully achieved by using a numerical model in lieu of experimental studies to create a database of different cardiovascular responses to varying physiological and pathological conditions which is then used to evaluate the GTF technique. The numerical method and measurement is free from calibration and human errors and provides an excellent platform to test the validity of the GTF technique. A significant finding added to literature is the accuracy of the GTF without the inherent errors involved in experiment studies.

REFERENCES

[1] W. H. O. World Heart Federation; World Stroke Organization, *Global Atlas on Cardiovascular Disease Prevention and Control*. 2012.

[2] S. Epstein, M. Willemet, P. J. Chowienczyk, and J. Alastruey, "Reducing the number of parameters in 1D arterial blood flow modeling: less is more for patient-specific simulations," *Am. J. Physiol. - Hear. Circ. Physiol.*, vol. 309, no. 1, pp. H222–H234, 2015.

[3] M. K. Patricia, W. Megan, R. Kristi, M. Paul, K. W. Paul, and J. He, "Global burden of hypertension--analysis of worldwide data," *Lancet*, vol. 365, pp. 217–223, 2005.

[4] S. C. Smith, A. Collins, R. Ferrari, D. R. Holmes, S. Logstrup, D. V. McGhie, J. Ralston, R. L. Sacco, H. Stam, K. Taubert, D. A. Wood, and W. A. Zoghbi, "Our Time: A Call to Save Preventable Death From Cardiovascular Disease (Heart Disease and Stroke)," *Circulation*, vol. 126, no. 23, pp. 2769–2775, 2012.

[5] G. M. Drzewiecki, J. Melbin, and A. Noordergraaf, "Arterial tonometry: Review and analysis," *J. Biomech.*, vol. 16, no. 2, pp. 141–152, 1983.

[6] R. P. Kelly, M. Karamanoglu, H. Gibbs, A. P. Avolio, and M. F. O'Rourke, "Noninvasive carotid pressure wave registration as an indicator of ascending aortic pressure," *J. Vasc. Med. Biol.*, vol. 1, pp. 241–247, 1989.

[7] R. P. Kelly, C. Hayward, J. Ganis, J. Daley, A. P. Avolio, and M. F. O"Rourke, "Noninvasive registration of the arterial pressure pulse waveform; using high-fidelity applanation tonometry," *J. Vasc. Med. Biol.*, vol. 1, pp. 142–149, 1989.

[8] W. J. Verberk, H. Cheng, L.-C. Huang, C.-M. Lin, Y.-P. Teng, and C.-H. Chen, "Practical

Suitability of a Stand-Alone Oscillometric Central Blood Pressure Monitor: A Review of the Microlife WatchBP Office Central," *Pulse*, vol. 3, no. 3–4, pp. 205–216, 2016.

[9] J. E. Lewis, P. Williams, and J. H. Davies, "Non-invasive assessment of peripheral arterial disease: Automated ankle brachial index measurement and pulse volume analysis compared to duplex scan," *SAGE Open Med.*, vol. 4, no. 5, p. 205031211665908, 2016.

[10] Y. Watanabe, H. Masaki, Y. Yunoki, A. Tabuchi, I. Morita, S. Mohri, and K. Tanemoto, "Ankle-Brachial Index, Toe-Brachial Index, and Pulse Volume Recording in Healthy Young Adults," *Ann. Vasc. Dis.*, vol. 8, no. 3, pp. 227–235, 2015.

[11] R. E. D. Climie, M. G. Schultz, S. B. Nikolic, K. D. K. Ahuja, J. W. Fell, and J. E. Sharman, "Validity and reliability of central blood pressure estimated by upper arm oscillometric cuff pressure," *Am. J. Hypertens.*, vol. 25, no. 4, pp. 414–420, 2012.

[12] G. P. Gravlee, A. B. Wong, T. G. Adkins, L. Douglas Case, and A. L. Pauca, "A comparison of radial, brachial, and aortic pressures after cardiopulmonary bypass," *J. Cardiothorac. Anesth.*, vol. 3, no. 1, pp. 20–26, Feb. 1989.

[13] M. Karamanoglu, M. F. O'Rourke, a P. Avolio, and R. P. Kelly, "An analysis of the relationship between central aortic and peripheral upper limb pressure waves in man.," *Eur. Heart J.*, vol. 14, no. 2, pp. 160–167, 1993.

[14] R. P. Kelly, H. H. Gibbs, M. F. O'Rourke, J. E. Daley, K. Mang, J. J. Morgen, and A. P. Avolio, "Nitroglycerin has more favourable effects on left ventricular afterload than apparent from measurement of pressure in a peripheral artery," *Eur. Heart J.*, vol. 11, no. 2, pp. 138–144, 1990.

[15] N. Stergiopulos, D. F. Young, and T. R. Rogge, "Computer simulation of arterial flow with applications to arterial and aortic stenoses," *J. Biomech.*, vol. 25, no. 12, pp. 1477–

1488, 1992.

[16] M. Karamanoglu, D. E Gallagher, A. Avolio, and M. F O'Rourke, "Pressure wave propagation in a multibranched model of the human upper limb," *Am. J. Physiol.*, vol. 269, pp. H1363-9, 1995.

[17] W. Nichols, M. O'Rourke, and C. Vlachopoulos, "Mcdonald's Blood Flow in Arteries," *Shock*, vol. 9, no. 6, p. 456, 1998.

[18] B. Williams, P. S. Lacy, S. M. Thom, K. Cruickshank, A. Stanton, D. Collier, A. D. Hughes, H. Thurston, and M. O'Rourke, "Differential impact of blood pressure-lowering drugs on central aortic pressure and clinical outcomes: Principal results of the Conduit Artery Function Evaluation (CAFE) study," *Circulation*, vol. 113, no. 9, pp. 1213–1225, 2006.

[19] M. E. Safar, J. Blacher, B. Pannier, A. P. Guerin, S. J. Marchais, P.-M. Guyonvarc\textquoterighth, and G. M. London, "Central Pulse Pressure and Mortality in End-Stage Renal Disease," *Hypertension*, vol. 39, no. 3, pp. 735–738, 2002.

[20] T. K. Waddell, A. M. Dart, T. L. Medley, J. D. Cameron, and B. A. Kingwell, "Carotid Pressure Is a Better Predictor of Coronary Artery Disease Severity Than Brachial Pressure," *Hypertension*, vol. 38, no. 4, pp. 927–931, 2001.

[21] M. J. Roman, R. B. Devereux, J. R. Kizer, E. T. Lee, J. M. Galloway, T. Ali, J. G. Umans, and B. V. Howard, "Central pressure more strongly relates to vascular disease and outcome than does brachial pressure: The strong heart study," *Hypertension*, vol. 50, no. 1, pp. 197–203, 2007.

[22] C. H. Chen, E. Nevo, B. Fetics, P. H. Pak, F. C. P. Yin, W. L. Maughan, and D. A. Kass, "Estimation of Central Aortic Pressure Waveform by Mathematical Transformation of

Radial Tonometry Pressure," *Circulation*, vol. 95, no. 7, pp. 1827–1836, 1997.

[23] B. Fetics, E. Nevo, C. H. Chen, and D. A. Kass, "Parametric model derivation of transfer function for noninvasive estimation of aortic pressure by radial tonometry," *IEEE Trans. Biomed. Eng.*, vol. 46, no. 6, pp. 698–706, 1999.

[24] A. L. Pauca, M. F. O'Rourke, and N. D. Kon, "Prospective evaluation of a method for estimating ascending aortic pressure from the radial artery pressure waveform.," *Hypertension*, vol. 38, no. 4, pp. 932–937, 2001.

[25] S. Soderstrom, G. Nyberg, M. F. O'Rourke, J. Sellgren, and J. Pontén, "Can a clinically useful aortic pressure wave be derived from a radial pressure wave?†," *Br. J. Anaesth.*, vol. 88, no. 4, pp. 481–488, 2002.

[26] D. Gallagher, A. Adji, and M. O'Rourke, "Validation of the transfer function technique for generating central from peripheral upper limb pressure waveform," *Am. J. Hypertens.*, vol. 17, no. 11, pp. 1059–1067, 2004.

[27] J. E. Sharman, R. Lim, A. M. Qasem, J. S. Coombes, M. I. Burgess, J. Franco, P. Garrahy, I. B. Wilkinson, and T. H. Marwick, "Validation of a generalized transfer function to noninvasively derive central blood pressure during exercise," *Hypertension*, vol. 47, no. 6, pp. 1203–1208, 2006.

[28] T. Weber, S. Wassertheurer, M. Rammer, E. Maurer, B. Hametner, C. C. Mayer, J. Kropf, and B. Eber, "Validation of a brachial cuff-based method for estimating central systolic blood pressure," *Hypertension*, vol. 58, no. 5, pp. 825–832, 2011.

[29] M. F. O'Rourke, "Method for Ascertaining the Pressure Pulse and Related Parameters in the Ascending Aorta from the Contour of the Pressure Pulse in the Peripheral Arteries," US 5,265,011, 1993.

[30] W. J. Stok, “Changes in finger-aorta pressure transfer function during and after exercise,” *J. Appl. Physiol.*, vol. 101, no. 4, pp. 1207–1214, 2006.

[31] G. C. Cloud, C. Rajkumar, J. Kooner, J. Cooke, and C. J. Bulpitt, “Estimation of central aortic pressure by SphygmoCor requires intra-arterial peripheral pressures.,” *Clin. Sci. (Lond).*, vol. 105, no. 2, pp. 219–225, 2003.

[32] P. Segers, D. Mahieu, J. Kips, E. Rietzschel, M. De Buyzere, D. De Bacquer, S. Bekaert, G. De Backer, T. Gillebert, P. Verdonck, and L. Van Bortel, “Amplification of the pressure pulse in the upper limb in healthy, middle-aged men and women,” *Hypertension*, vol. 54, no. 2, pp. 414–420, 2009.

[33] W. B. White, A. S. Berson, C. Robbins, M. J. Jamieson, L. M. Prisant, E. Roccella, and S. G. Sheps, “National standard for measurement of resting and ambulatory blood pressures with automated sphygmomanometers,” *Hypertension*, vol. 21, no. 4, pp. 504–509, 1993.

[34] G. Swamy, Q. Ling, T. Li, and R. Mukkamala, “Blind identification of the aortic pressure waveform from multiple peripheral artery pressure waveforms.,” *Am. J. Physiol. Heart Circ. Physiol.*, vol. 292, no. 5, pp. H2257-64, 2007.

[35] J. O. Hahn, A. T. Reisner, F. A. Jaffer, and H. H. Asada, “Subject-specific estimation of central aortic blood pressure using an individualized transfer function: A preliminary feasibility study,” *IEEE Trans. Inf. Technol. Biomed.*, vol. 16, no. 2, pp. 212–220, 2012.

[36] G. Swamy, D. Xu, N. B. Olivier, and R. Mukkamala, “An adaptive transfer function for deriving the aortic pressure waveform from a peripheral artery pressure waveform,” *Am. J. Physiol. Circ. Physiol.*, vol. 297, no. 5, pp. H1956–H1963, 2009.

[37] N. Fazeli, M. Rashedi, A. Chappell, S. Wang, R. Macarthur, M. S. Mcmurtry, B. Finegan, and J. Hahn, “Subject-specific estimation of aortic blood pressure via system

identification: Preliminary in-human experimental study," in *2013 American Control Conference*, 2013, pp. 740–745.

[38] Y. Shi, P. Lawford, and R. Hose, "Review of zero-D and 1-D models of blood flow in the cardiovascular system.," *Biomed. Eng. Online*, vol. 10, no. 1, p. 33, 2011.

[39] N. Stergiopulos, B. E. Westerhof, and N. Westerhof, "Physical basis of pressure transfer from periphery to aorta: a model-based study," *Am. J. Physiol. Circ. Physiol.*, vol. 274, no. 4, pp. H1386–H1392, 1998.

[40] P. Segers, S. Carlier, a Pasquet, S. I. Rabben, L. R. Hellevik, E. Remme, T. De Backer, J. De Sutter, J. D. Thomas, and P. Verdonck, "Individualizing the aorto-radial pressure transfer function: feasibility of a model-based approach.," *Am. J. Physiol. Heart Circ. Physiol.*, vol. 279, no. 2, pp. H542-9, 2000.

[41] C. J. Thore, J. Stålhand, and M. Karlsson, "Toward a noninvasive subject-specific estimation of abdominal aortic pressure.," *Am. J. Physiol. Heart Circ. Physiol.*, vol. 295, no. 3, pp. H1156–H1164, 2008.

[42] S. Jiang, Z.-Q. Zhang, F. Wang, and J.-K. Wu, "A personalized-model-based central aortic pressure estimation method," *J. Biomech.*, vol. 49, no. 16, pp. 4098–4106, 2016.

[43] M. S. Olufsen, "Structured tree outflow condition for blood flow in larger systemic arteries.," *Am J Physiol*, vol. 276, no. 1 Pt 2, pp. H257--H268, 1999.

[44] F. N. van de Vosse and M. E. H. Van Dongen, *Cardiovascular Fluid Mechanics: Lecture Notes*. Technische Universiteit Eindhoven, 1998.

[45] J. R. Levick, "Chapter 1 - Overview of the cardiovascular system," in *An Introduction to Cardiovascular Physiology*, J. R. Levick, Ed. Butterworth-Heinemann, 1991, pp. 1–12.

[46] W. K. Purves, D. Sadava, and G. H. Orians, *Life: The Science of Biology*, Seventh ed. Sinauer Associates and W. H. Freeman, 2003.

[47] M. S. Olufsen, "Modeling of the Arterial System with Reference to an Anesthesia Simulator," *Dep. Math.*, vol. PhD, p. 199, 1998.

[48] P. A. Iaizzo, *Handbook of Cardiac Anatomy, Physiology, and Devices*. Newyork, USA: Humana Press, 2009.

[49] R. E. Klabunde, "Cardiovascular Physiology Concepts," 2016. [Online]. Available: http://www.cvphysiology.com/Blood Pressure/BP006.

[50] S. Vogel and R. A. Calvert, *Vital circuits: on pumps, pipes, and the workings of circulatory systems*. Oxford University Press, 1993.

[51] N. Best, C; Taylor, *The Physiological Basis of Medical Practice*, 11th ed. Newyork, USA: Williams and Wilkins, 1985.

[52] M. Thiriet, *Biology and Mechanics of Blood Flows*. Newyork , USA: Springer-Verlag New York, 2008.

[53] M. U. Qureshi, G. D. A. Vaughan, C. Sainsbury, M. Johnson, C. S. Peskin, M. S. Olufsen, and N. A. Hill, "Numerical simulation of blood flow and pressure drop in the pulmonary arterial and venous circulation," *Biomech. Model. Mechanobiol.*, vol. 13, no. 5, pp. 1137–1154, 2014.

[54] E. Le, "Biology notes for IGCSE 2014," 2014. [Online]. Available: http://biology-igcse.weebly.com/arteries-veins-and-capillaries---structure-and-functions.html.

[55] M. S. Olufsen, "Structured tree outflow condition for blood flow in larger systemic arteries.," *Am J Physiol*, vol. 276, no. 1 Pt 2, pp. H257--H268, 1999.

[56] D. A. McDonald, “Profiles in cardiology.,” *Clin. Cardiol.*, vol. 16, pp. 842–843, 1993.

[57] Y. Tardy, J. J. Meister, F. Perret, H. R. Brunner, and M. Arditi, “Non-invasive estimate of the mechanical properties of peripheral arteries from ultrasonic and photoplethysmographic measurements,” *Clin. Phys. Physiol. Meas.*, vol. 12, no. 1, pp. 39–54, 1991.

[58] G. A. Holzapfel, T. C. Gasser, and R. W. Ogden, “A new constitutive framework for arterial wall mechanics and a comparative study of material models,” *J. Elast.*, vol. 61, no. 1–3, pp. 1–48, 2000.

[59] P. L. Williams and R. Warwick, *Gray’s Anatomy*, 36th ed. Newyork, USA: Churchill Livingstone, 1980.

[60] P. R. Wheater, H. G. Burkitt, and V. G. Daniels, *Functional histology : a text and colour atlas*. Edinburgh,G.B.: Churchill Livingstone, 1979.

[61] S. S. DeLoach and R. R. Townsend, “Vascular Stiffness: Its measurement and significance for epidemiologic and outcome studies,” *Clin. J. Am. Soc. Nephrol.*, vol. 3, no. 1, pp. 184–192, 2008.

[62] W. Caro, C G, Pedley, T, Schroter,R and Seed, *The Mechanics of the Circulation*. Oxford,G.B.: Oxford University Press, 1978.

[63] A. J. Alastruey, “Numerical modelling of pulse wave propagation in the cardiovascular system: development, validation and clinical applications.,” Imperial College London (University of London), 2006.

[64] X. Wang, “1D modeling of blood flow in networks : numerical computing and applications,” Université Pierre et Marie Curie-Paris VI, 2014.

[65] T. Pedley, *The Fluid Mechanics of Large Blood Vessels*. Cambridge,G.B.: Cambridge University Press, 1980.

[66] N. Westerhof, J.-W. Lankhaar, and B. E. Westerhof, "The arterial Windkessel," *Med. Biol. Eng. Comput.*, vol. 47, no. 2, pp. 131–141, 2009.

[67] M. F. O'Rourke, *Arterial function in health and disease*. Newyork , USA: Churchill Livingstone, 1982.

[68] R. G. Richardson, *The surgeon's heart.* Cox & Wyman Ltd., 1969.

[69] K. Walker, *The story of blood*. London: Jenkins, 1958.

[70] M. ElMaghawry, A. Zanatta, and F. Zampieri, "The discovery of pulmonary circulation: From Imhotep to William Harvey," *Glob. Cardiol. Sci. Pract.*, vol. 2014, no. 2, p. 31, 2014.

[71] D. W. R. Alfred P. Fishman, Ed., *Circulation of the blood: men and ideas*. Oxford University Press, 1964.

[72] L. Euler, *Principia pro motu sanguinis per arterias determinando*, vol. 2:814-823, no. 1844 detecta. 1775.

[73] Y. C. Fung, *Biomechanics: Circulation*, Second Edi. Springer, 1997.

[74] D. L. Kline, *Thomas Young, Forgotton Genius: An Annotated Narrative Biography*. Cincinnati: Vidan Press, 1993.

[75] T. Young, "Hydraulic investigations, subservient to an intended Croonian lecture on the motion of the blood," *Phil. Trans. Roy. Soc., London*, no. 98, pp. 164–186, 1808.

[76] A. I. Moens, "Over de voortplantingssnelheid von del pols (on the speed of propagation of

the pulse),” Leiden, 1877.

[77] P. Chemie and A. T. D. Korteweg, “Fortpflanzungsgeschwindigkeit des Schalles in elastischen R ¨ ohren (Sur la transmission du son par les fluides renferm ´ es dans les tubes ` a parois ´ elastiques); Ann . der,” vol. 9, no. 1, pp. 127–134, 1880.

[78] B. Riemann, “Gesammelte mathematische Werke und wissenschaftlicher Nachlass,” Liepzig, 1876.

[79] J. R. Womersley, “An elastic tube theory of pulse transmission and oscillatory flow in mammalian arteries,” 1957.

[80] N. Westerhof, F. Bosman, C. J. De Vries, and A. Noordergraaf, “Analog studies of the human systemic arterial tree,” *J. Biomech.*, vol. 2, no. 2, pp. 121–143, 1969.

[81] A. Avolio, “Multi-branched model of the human arterial system,” *Med. Biol. Eng. Comput.*, vol. 18, no. 6, pp. 709–718, 1980.

[82] M. S. Olufsen, C. S. Peskin, W. Y. Kim, E. M. Pedersen, A. Nadim, and J. Larsen, “Numerical simulation and experimental validation of blood flow in arteries with structured-tree outflow conditions,” *Ann. Biomed. Eng.*, vol. 28, no. 11, pp. 1281–1299, 2000.

[83] S. J. Sherwin, V. Franke, J. Peiró, and K. Parker, “One-dimensional modelling of a vascular network in space-time variables,” *J. Eng. Math.*, vol. 47, no. 3–4, pp. 217–250, 2003.

[84] P. Kakar and G. Y. H. Lip, “Towards understanding the aetiology and pathophysiology of human hypertension: Where are we now?,” *Journal of Human Hypertension*, vol. 20, no. 11. pp. 833–836, 2006.

[85] J. Alastruey, A. W. Khir, K. S. Matthys, P. Segers, S. J. Sherwin, P. R. Verdonck, K. H. Parker, and J. Peiró, "Pulse wave propagation in a model human arterial network: Assessment of 1-D visco-elastic simulations against in vitro measurements," *J. Biomech.*, vol. 44, no. 12, pp. 2250–2258, 2011.

[86] J. P. Mynard, "One-dimensional Blood Flow Modelling with the Locally Conservative Galerkin (LCG) Method," no. November, 2007.

[87] P. Reymond, F. Merenda, F. Perren, D. Rüfenacht, and N. Stergiopulos, "Validation of a one-dimensional model of the systemic arterial tree.," *Am. J. Physiol. Heart Circ. Physiol.*, vol. 297, no. 1, pp. 208–222, 2009.

[88] L. Formaggia, F. Nobile, and A. Quarteroni, "A One Dimensional Model for Blood Flow: Application to Vascular Prosthesis," in *Mathematical Modeling and Numerical Simulation in Continuum Mechanics*, 2002, pp. 137–153.

[89] I. E. Vignon and C. A. Taylor, "Outflow boundary conditions for one-dimensional finite element modeling of blood flow and pressure waves in arteries," *Wave Motion*, vol. 39, no. 4, pp. 361–374, 2004.

[90] I. E. Vignon-Clementel, C. A. Figueroa, K. E. Jansen, and C. A. Taylor, "Outflow boundary conditions for three-dimensional finite element modeling of blood flow and pressure in arteries," *Comput. Methods Appl. Mech. Eng.*, vol. 195, no. 29, pp. 3776–3796, 2006.

[91] P. J. Blanco, M. R. Pivello, S. A. Urquiza, and R. A. Feijóo, "On the potentialities of 3D-1D coupled models in hemodynamics simulations," *J. Biomech.*, vol. 42, no. 7, pp. 919–930, 2009.

[92] I. E. Vignon-Clementel, A. L. Marsden, and J. A. Feinstein, "A primer on computational

simulation in congenital heart disease for the clinician," *Prog. Pediatr. Cardiol.*, vol. 30, no. 1–2, pp. 3–13, 2010.

[93] S. Sankaran, M. E. Moghadam, A. M. Kahn, E. E. Tseng, J. M. Guccione, and A. L. Marsden, "Patient-specific multiscale modeling of blood flow for coronary artery bypass graft surgery," *Ann. Biomed. Eng.*, vol. 40, no. 10, pp. 2228–2242, 2012.

[94] F. Cuomo, S. Roccabianca, D. Dillon-Murphy, N. Xiao, J. D. Humphrey, and C. A. Figueroa, "Effects of age-associated regional changes in aortic stiffness on human hemodynamics revealed by computational modeling," *PLoS One*, vol. 12, no. 3, pp. 1–21, 2017.

[95] F. C. Xiao N, Alastruey J, "A systematic comparison between 1-D and 3-D hemodynamics in compliant arterial models.," *Int. J. Numer. Methods Biomed. Eng.*, vol. 30, pp. 204–231, 2014.

[96] B. N. Steele, J. Wan, J. P. Ku, T. J. R. Hughes, and C. A. Taylor, "In vivo validation of a one-dimensional finite-element method for predicting blood flow in cardiovascular bypass grafts," *IEEE Trans. Biomed. Eng.*, vol. 50, no. 6, pp. 649–656, 2003.

[97] K. Devault, P. A. Gremaud, V. Novak, M. S. Olufsen, G. V. Eres, and P. Zhao, "Blood flow in the circle of willis: Modelling and Calibration," *Multiscale Model. Simul.*, vol. 7, no. 2, pp. 888–909, 2008.

[98] P. Reymond, Y. Bohraus, F. Perren, F. Lazeyras, and N. Stergiopulos, "Validation of a patient-specific one-dimensional model of the systemic arterial tree," *Blood*, pp. 1173–1183, 2011.

[99] B. N. Steele, C. A. Taylor, J. Wan, J. P. Ku, and T. J. R. R. Hughes, "In vivo validation of a one-dimensional finite element method for simulation-based medical planning for

cardiovascular bypass surgery," in *Annual Reports of the Research Reactor Institute, Kyoto University*, 2001, vol. 1, no. 5, pp. 120–123.

[100] M. Willemet, V. Lacroix, and E. Marchandise, "Validation of a 1D patient-specific model of the arterial hemodynamics in bypassed lower-limbs: Simulations against in vivo measurements," *Med. Eng. Phys.*, vol. 35, no. 11, pp. 1573–1583, 2013.

[101] C. Audebert, P. Bucur, M. Bekheit, E. Vibert, I. E. Vignon-Clementel, and J.-F. Gerbeau, "Kinetic scheme for arterial and venous blood flow, and application to partial hepatectomy modeling," *Comput. Methods Appl. Mech. Eng.*, vol. 314, 2017.

[102] E. Marchandise, M. Willemet, and V. Lacroix, "A numerical hemodynamic tool for predictive vascular surgery," *Med. Eng. Phys.*, vol. 31, no. 1, pp. 131–144, 2009.

[103] A. R. Ghigo, S. Abou Taam, X. Wang, P. Lagrée, and J. M. Fullana, "A one-dimensional arterial network model for bypass graft assessment," *Med. Eng. Phys.*, vol. 43, pp. 39–47, 2017.

[104] M. Saito, P. Marie-curie, and I. Jean, "One-dimensional modeling of pulse wave for a human artery model," 2010.

[105] A. X. Wang, O. Delestre, J.-M. Fullana, M. Saito, Y. Ikenaga, M. Matsukawa and P.-Y. Lagee., "Comparing different numerical methods for solving arterial 1d flows in networks.," *Comput. Methods Biomech. Biomed. Engin.*, vol. 15(sup1), pp. 61–62, 2012.

[106] C. A. D. A. D. D. Leguy, E. M. H. M. H. H. Bosboom, H. Gelderblom, A. P. G. P. G. G. Hoeks, F. N. N. van de Vosse, and F. N. Van De Vosse, "Estimation of distributed arterial mechanical properties using a wave propagation model in a reverse way," *Med. Eng. Phys.*, vol. 32, no. 9, pp. 957–967, 2010.

[107] C. M. Quick, W. L. Young, and A. Noordergraaf, “Infinite number of solutions to the hemodynamic inverse problem.,” *Am. J. Physiol. Heart Circ. Physiol.*, vol. 280, no. 4, pp. H1472--9, 2001.

[108] C. M. Quick, D. S. Berger, R. H. Stewart, G. A. Laine, C. J. Hartley, and A. Noordergraaf, “Resolving the Hemodynamic Inverse Problem,” *Biomed. Eng. IEEE Trans.*, vol. 53, no. 3, pp. 361–368, 2006.

[109] S. Čanić and E. H. Kim, “Mathematical analysis of the quasilinear effects in a hyperbolic model blood flow through compliant axi-symmetric vessels,” *Math. Methods Appl. Sci.*, vol. 26, no. July 2002, pp. 1161–1186, 2003.

[110] V. L. Streeter, W. F. Keitzer, and D. F. Bohr, “Pulsatile Pressure and Flow Through Distensible Vessels,” *Circ. Res.*, vol. 13, no. 1, pp. 3–20, 1963.

[111] A. P. Schaaf B, “Digital computer simulation of human systemic arterial pulse wave transmission: a nonlinear model.,” *J. Biomech.*, vol. 5, pp. 345–364, 1972.

[112] A. H. Shapiro, “Steady Flow in Collapsible Tubes,” *J. Biomech. Eng.*, vol. 99, pp. 126–147, 1977.

[113] C. W. Li and H. D. Cheng, “A nonlinear fluid model for pulmonary blood circulation,” *J. Biomech.*, vol. 26, no. 6, pp. 653–664, 1993.

[114] S. J. Sherwin, L. Formaggia, and J. Peiró, “Computational modelling of 1D blood flow with variable mechanical properties and its application to the simulation of wave propagation in the human arterial system,” *Int. J. Numer. Methods Fluids*, vol. 700, no. April 2002, pp. 673–700, 2003.

[115] J. Wan, B. Steele, S. A. Spicer, S. Strohband, G. R. Feijo´o, T. J. R. Hughes, C. A. Taylor,

G. R. Feijóo, T. J. R. Hughes, and C. A. Taylor, “A one-dimensional finite element method for simulation-based medical planning for cardiovascular disease,” *Comput. Methods Biomech. Biomed. Engin.*, vol. 5, no. 3, pp. 195–206, 2002.

[116] B. S. Brook and T. J. Pedley, “A model for time-dependent flow in (giraffe jugular) veins: Uniform tube properties,” *J. Biomech.*, vol. 35, no. 1, pp. 95–107, 2002.

[117] L. Formaggia, J. F. Gerbeau, F. Nobile, and A. Quarteroni, “On the coupling of 3D and 1D Navier-Stokes equations for flow problems in compliant vessels,” *Comput. Methods Appl. Mech. Eng.*, vol. 191, no. 6–7, pp. 561–582, 2001.

[118] J. J. Wang and K. H. Parker, “Wave propagation in a model of the arterial circulation,” *J. Biomech.*, vol. 37, no. 4, pp. 457–470, 2004.

[119] J.-J. Wang, A. B. O’Brien, N. G. Shrive, K. H. Parker, and J. V Tyberg, “Time-domain representation of ventricular-arterial coupling as a windkessel and wave system.,” *Am. J. Physiol. Heart Circ. Physiol.*, vol. 284, no. 4, pp. H1358–H1368, 2003.

[120] G. Pontrelli and E. Rossoni, “Numerical modelling of the pressure wave propagation in the arterial ow,” *Int. J. Numer. Methods Fluids*, vol. 671, no. March 2002, pp. 651–671, 2003.

[121] K. H. Parker and C. J. H. Jones, “Forward and Backward Running Waves in the Arteries: Analysis Using the Method of Characteristics,” *J. Biomech. Eng.*, vol. 112, no. 3, p. 322, 1990.

[122] E. Rooz, D. F. Young, and T. R. Rogge, “A finite-element simulation of pulsatile flow in flexible tubes,” *J. Biomech. Eng.*, vol. 104, no. May 1982, pp. 119–124, 1982.

[123] G. Porenta, D. F. Young, and T. R. Rogge, “A Finite-Element Model of Blood Flow in

Arteries Including Taper, Branches, and Obstructions," *J. Biomech. Eng.*, vol. 108, no. 2, p. 161, 1986.

[124] I. Surovtsova, "Effects of compliance mismatch on blood flow in an artery with endovascular prosthesis," *J. Biomech.*, vol. 38, no. 10, pp. 2078–2086, 2005.

[125] D. Elad, D. Katz, E. Kimmel, and S. Einav, "Numerical schemes for unsteady fluid flow through collapsible tubes," *J. Biomed. Eng.*, vol. 13, no. 1, pp. 10–18, 1991.

[126] B. S. Brook, S. A. E. G. Falle, and T. J. Pedley, "Numerical solutions for unsteady gravity-driven flows in collapsible tubes: evolution and roll-wave instability of a steady state," *J. Fluid Mech.*, vol. 396, pp. 223–256, 1999.

[127] W. E. Bodley, "The non-linearities of arterial blood flow," *Phys. Med. Biol.*, vol. 16, no. 4, pp. 663–672, 1971.

[128] A. J. Pullan, N. P. Smith, and P. J. Hunter, "An anatomically based model of transient coronary blood flow in the heart," *SIAM J. Appl. Math.*, vol. 62, no. 3, pp. 990–1018, 2002.

[129] S. A. Urquiza, P. J. Blanco, M. J. Vénere, and R. A. Feijóo, "Multidimensional modelling for the carotid artery blood flow," *Comput. Methods Appl. Mech. Eng.*, vol. 195, no. 33–36, pp. 4002–4017, 2006.

[130] J. K. Raines, M. Y. Jaffrin, and A. H. Shapiro, "A computer simulation of arterial dynamics in the human leg," *J. Biomech.*, vol. 7, no. 1, pp. 77–91, 1974.

[131] P. J. Reuderink, H. W. Hoogstraten, P. Sipkema, B. Hillen, N. Westerhof, N. One-dimensional, O. F. Pulse, W. Transmission, and A. T. High, "Linear and nonlinear one-dimensional models of pulse wave transmission at high womersley numbers," *J. Biomech.*,

vol. 22, no. 819, pp. 819–827, 1989.

[132] G. Perdikaris, P, Grinberg, L, Karniadakis, “An Effective Fractal-Tree Closure Model for Simulating Blood Flow in Large Arterial Networks,” *Ann. Biomed. Eng.*, vol. 43, no. 6, pp. 1432–1442, 2015.

[133] T. Sochi, “The flow of power law fluids in elastic networks and porous media,” *Comput. Methods Biomech. Biomed. Engin.*, vol. 19, no. 3, pp. 324–329, 2016.

[134] J. Wan, B. Steele, S. A. Spicer, S. Strohband, G. R. Feijo´o, T. J. R. Hughes, C. A. Taylor, and G. R. Feij O, “A One-dimensional Finite Element Method for Simulation-based Medical Planning for Cardiovascular Disease) A One-dimensional Finite Element Method for Simulation-based Medical Planning for A One-dimensional Finite Element Method for Simulation- based Medic,” *Comput. Methods Biomech. Biomed. Engin.*, vol. 53, no. November 2014, pp. 195–206, 2010.

[135] B. S. Brook, S. A. E. G. Falle, and T. J. Pedley, “Numerical solutions for unsteady gravity driven flows in collapsible tubes{:} evolution and roll wave instability of a steady state,” *J. Fluid Mech.*, vol. 396, pp. 223–256, 1999.

[136] J. Alastruey, S. R. Nagel, B. A. Nier, A. A. E. E. Hunt, P. D. Weinberg, J. Peiró, D. Peter, and J. Peiró, “Modelling pulse wave propagation in the rabbit systemic circulation to assess the effects of altered nitric oxide synthesis,” *J. Biomech.*, vol. 42, no. 13, pp. 2116–2123, 2009.

[137] J. Wang, K. I. M. H. Parker, J. V Tyberg, and K. H. Parker, “Left ventricular wave speed,” *Science (80-.).*, pp. 2531–2536, 2001.

[138] Z. Wang, “Assessment of left ventricular diastolic suction in dogs using wave-intensity analysis,” *AJP Hear. Circ. Physiol.*, vol. 288, no. 4, pp. H1641–H1651, 2004.

[139] A. Zambanini, “Wave-energy patterns in carotid, brachial, and radial arteries: a noninvasive approach using wave-intensity analysis,” *AJP Hear. Circ. Physiol.*, vol. 289, no. 1, pp. H270–H276, 2005.

[140] Y. H. Sun, T. J. Anderson, K. H. Parker, and J. V Tyberg, “Wave-intensity analysis: a new approach to coronary hemodynamics,” *J Appl Physiol*, vol. 89, no. 4, pp. 1636–1644, 2000.

[141] E. H. Hollander, J. J. Wang, G. M. Dobson, K. H. Parker, and J. V Tyberg, “Negative wave reflections in pulmonary arteries.,” *Am. J. Physiol. Heart Circ. Physiol.*, vol. 281, no. 2, pp. H895-902, 2001.

[142] E. H. Hollander, G. M. Dobson, J. Wang, K. H. Parker, and J. V Tyberg, “Direct and series transmission of left atrial pressure perturbations to the pulmonary artery: a study using wave-intensity analysis.,” *Am. J. Physiol. Heart Circ. Physiol.*, vol. 286, no. 1, pp. H267-75, 2004.

[143] P. J. Blanco, R. A. Feijóo, and S. A. Urquiza, “A unified variational approach for coupling 3D-1D models and its blood flow applications,” *Comput. Methods Appl. Mech. Eng.*, vol. 196, no. 41–44, pp. 4391–4410, 2007.

[144] L. Formaggia, A. Quarteroni, and C. Vergara, “On the physical consistency between three-dimensional and one-dimensional models in haemodynamics,” *J. Comput. Phys.*, vol. 244, no. July 2015, pp. 92–112, 2013.

[145] M. Anliker, R. L. Rockwell, and E. Ogden, “Nonlinear analysis of flow pulses and shock waves in arteries,” *Zeitschrift für Angew. Math. und Phys. ZAMP*, vol. 22, no. 2, pp. 217–246, Mar. 1971.

[146] J. C. Stettler, P. Niederer, and M. Anliker, “Theoretical analysis of arterial hemodynamics

including the influence of bifurcations. Part I: mathematical models and prediction of normal pulse patterns.," *Ann. Biomed. Eng.*, vol. 9, no. 2, pp. 145–64, 1981.

[147] L. Formaggia, D. Lamponi, A. Quarteroni, and P. Leonardo, "One dimensional models for blood flow in arteries," *J. Eng. Math.*, vol. 47, no. 3–4, pp. 251–276, 2003.

[148] C. Sheng, S. N. Sarwal, K. C. Watts, and a E. Marble, "Computational simulation of blood flow in human systemic circulation incorporating an external force field.," *Med. Biol. Eng. Comput.*, vol. 33, no. January, pp. 8–17, 1995.

[149] G. A. Sod, "A survey of several finite difference methods for systems of nonlinear hyperbolic conservation laws," *J. Comput. Phys.*, vol. 27, no. 1, pp. 1–31, 1978.

[150] P. Moczo, J. O. A. Robertsson, and L. Eisner, "The Finite-Difference Time-Domain Method for Modeling of Seismic Wave Propagation," in *Advances in Wave Propagation in Heterogenous Earth*, vol. 48, R.-S. Wu, V. Maupin, and R. Dmowska, Eds. Elsevier, 2007, pp. 421–516.

[151] A. Taflove, "Computational Electrodynamics," *Artech House, Norwood, MA*, 1998.

[152] S. Mazumder, "Chapter 2 - The Finite Difference Method," in *Numerical Methods for Partial Differential Equations*, S. Mazumder, Ed. Academic Press, 2016, pp. 51–101.

[153] P. C. Azer K, "A one-dimensional model of blood flow in arteries with friction and convection based on the Womersley velocity profile.," *Cardiovasc. Eng.*, vol. 7, pp. 51–73, 2007.

[154] L. H. Liang F, Takagi S, Himeno R, "Biomechanical characterization of ventricular–arterial coupling during aging: a multi-scale model study.," *J. Biomech.*, vol. 42, pp. 692–704, 2009.

[155] N. P. Smith, A. J. Pullan, and P. J. Hunter, “An Anatomically Based Model of Transient Coronary Blood Flow in the Heart,” *SIAM J. Appl. Math.*, vol. 62, no. 3, pp. 990–1018, 2002.

[156] B. Etienne, N. Perumal, P. J. Blanco, L. O. Müller, F. E. Fossan, L. R. Hellevik, W. P. Donders, W. Huberts, M. Willemet, and A. J. Alastruey, “A benchmark study of numerical schemes for one-dimensional arterial blood flow modelling,” *Int. j. numer. method. biomed. eng.*, vol. 31, no. 10, 2015.

[157] X. Wang, “1D modeling of blood flow in networks: numerical computing and applications,” Université Pierre et Marie Curie-Paris VI, 2014.

[158] L. R. Hellevik, J. Vierendeels, T. Kiserud, N. Stergiopulos, F. Irgens, E. Dick, K. Riemslagh, and P. Verdonck, “An assessment of ductus venosus tapering and wave transmission from the fetal heart,” *Biomech. Model. Mechanobiol.*, vol. 8, no. 6, pp. 509–517, 2009.

[159] S. A. Toro E, “Flow in collapsible tubes with discontinuous mechanical properties: mathematical model and exact solutions,” *Commun. Comput. Phys.*, vol. 13, pp. 361–385, 2013.

[160] T. E. Müller L, “Well balanced high order solver for blood flow in networks of vessels with variable properties.,” *Int. J. Numer. Methods Biomed. Eng.*, vol. 29, pp. 1388–1411, 2013.

[161] E. F. Toro, “The Equations of Fluid Dynamics,” *Riemann Solvers Numer. Methods Fluid Dyn.*, no. 1, pp. 1–40, 2009.

[162] R. Eymard, T. Gallouet, and R. Herbin, “Finite Volume Methods,” vol. M, no. January, 2006.

[163] R. J. LeVeque, “Finite Volume Methods for Hyperbolic Problems,” *Cambridge Univ. Press*, vol. 54, p. 258, 2002.

[164] J. N. Reddy, *An Introduction to Nonlinear Finite Element Analysis: with applications to heat transfer, fluid mechanics, and solid mechanics*. Oxford,G.B.: Oxford University Press, 2015.

[165] D. L. Logan, *A First Course In The Finite Element Method*. 2012.

[166] O. C. Zienkiewicz, R. L. Taylor, and J. Z. Zhu, *The Finite Element Method: Its Basis and Fundamentals*, 7th ed. Oxford,G.B.: Butterworth-Heinemann, 2013.

[167] D. Bessems, M. Rutten, and F. Van De Vosse, “A wave propagation model of blood flow in large vessels using an approximate velocity profile function,” *J. Fluid Mech.*, vol. 580, pp. 145–168, 2007.

[168] F. R. Watanabe S, Blanco P, “Mathematical model of blood flow in an anatomically detailed arterial network of the arm.,” *ESAIM Math. Model. Numer. Anal.*, vol. 47, pp. 961–985, 2013.

[169] D. J. Brown, “Brown - Input Impedance and Reflection Coefficient in Fractal-Like Models of Asymmetrically Branching Compliant Tubes.PDF,” vol. 43, no. 7, 1996.

[170] Y. Huo and G. S. Kassab, “A hybrid one-dimensional/Womersley model of pulsatile blood flow in the entire coronary arterial tree,” *AJP Hear. Circ. Physiol.*, vol. 292, no. 6, pp. H2623–H2633, 2007.

[171] D. Bessems, C. G. Giannopapa, M. C. M. Rutten, and F. N. van de Vosse, “Experimental validation of a time-domain-based wave propagation model of blood flow in viscoelastic vessels,” *J. Biomech.*, vol. 41, no. 2, pp. 284–291, 2008.

[172] N. Stergiopulos, “Computer simulation of arterial blood flow,” 1990.

[173] A. Noordergraaf, P. D. Verdouw, and H. B. K. Boom, “The use of an analog computer in a circulation model,” *Prog. Cardiovasc. Dis.*, vol. 5, no. 5, pp. 419–439, 1963.

[174] M. Matsumori, H. Tanaka, Y. Kawanishi, T. Onishi, K. Nakagiri, T. Yamashita, K. Okada, and Y. Okita, “Comparison of distensibility of the aortic root and cusp motion after aortic root replacement with two reimplantation techniques: Valsalva graft versus tube graft☆,” *Interact. Cardiovasc. Thorac. Surg.*, vol. 6, no. 2, pp. 177–181, 2007.

[175] W. B. Cousins, “Boundary Conditions and Uncertainty Quantification for Hemodynamics,” North Carolina State University, 2013.

[176] B. N. Steele, “A Simulation-based Medical Planning System for Occlusive Cardiovascular Disease Using One-dimensional Analysis Techniques,” Stanford University, Stanford, CA, USA, 2003.

[177] B. Steele, M. Olufsen, and C. Taylor, “Fractal Network model for simulating abdominal and lower extremity blood flow during resting and exercise conditions,” *Comput. Methods Biomech. Biomed. Engin.*, vol. 10, pp. 39–51, 2007.

[178] R. Spilker, J. Feinstein, D. W Parker, V. Reddy, and C. Taylor, “Morphometry-Based Impedance Boundary Conditions for Patient-Specific Modeling of Blood Flow in Pulmonary Arteries,” *Ann. Biomed. Eng.*, vol. 35, pp. 546–559, 2007.

[179] L. Grinberg and G. E. Karniadakis, “Outflow boundary conditions for arterial networks with multiple outlets,” *Ann. Biomed. Eng.*, vol. 36, no. 9, pp. 1496–1514, 2008.

[180] P. J. Blanco, S. M. Watanabe, E. A. Dari, M. A. R. F. Passos, and R. A. Feijóo, “Blood flow distribution in an anatomically detailed arterial network model: criteria and

algorithms," *Biomech. Model. Mechanobiol.*, vol. 13, no. 6, pp. 1303–1330, 2014.

[181] S. J. Sherwin, L. Formaggia, J. Peiró, and V. Franke, "Computational modelling of 1D blood flow with variable mechanical properties and its application to the simulation of wave propagation in the human arterial system," *Int. J. Numer. Methods Fluids*, vol. 43, no. 6–7, pp. 673–700, 2003.

[182] H. B. M. Uylings, "Optimization of diameters and bifurcation angles in lung and vascular tree structures," *Bull. Math. Biol.*, vol. 39, no. 5, pp. 509–520, 1977.

[183] C. D. Murray, "The physiological principle of minimum work applied to the angle of branching of arteries," *J. Gen. Physiol.*, vol. 9, no. 6, pp. 835–841, 1926.

[184] M. S. Pollanen, "Dimensional optimization at different levels of the arterial hierarchy," *J. Theor. Biol.*, vol. 159, no. 2, pp. 267–270, 1992.

[185] G. L. Papageorgiou, B. N. Jones, V. J. Redding, and N. Hudson, "The area ratio of normal arterial junctions and its implications in pulse wave reflections," *Cardiovasc. Res.*, vol. 24, no. 6, pp. 478–484, 1990.

[186] H. B. B. Atabek and H. S. S. Lew, "Wave Propagation through a Viscous Incompressible Fluid Contained in an Initially Stressed Elastic Tube," *Biophys. J.*, vol. 6, no. 11, pp. 481–503, 1966.

[187] H. B. Atabek, "Wave Propagation through a Viscous Fluid Contained in a Tethered, Initially Stressed, Orthotropic Elastic Tube," *Biophys. J.*, vol. 8, no. 5, pp. 626–649, 1968.

[188] G. D. A. Vaughan, "Pulse propagation in the pulmonary and systemic arteries," 2010.

[189] R. B. Clipp and B. N. Steele, "An evaluation of dynamic outlet boundary conditions in a 1D fluid dynamics model," *Mathematical Biosciences and Engineering*, vol. 9. pp. 61–74,

2012.

[190] R. B. Clipp and B. N. Steele, “Impedance boundary conditions for the pulmonary vasculature including the effects of geometry, compliance, and respiration,” *IEEE Trans Biomed Eng*, vol. 56, no. 3, pp. 862–870, 2009.

[191] M. U. Qureshi, “Simulating the pulse wave in the human pulmonary circulation,” University of Glasgow, 2013.

[192] K. Matthys, J. Alastruey, J. Peiro, A. W. Khir, P. Segers, P. R. Verdonck, K. H. Parker, and S. J. Sherwin, “ulse wave propagation in a model human arterial network: assessment of 1-D numerical simulations against in vitro measurements,” *J. Biomech.*, vol. 40, no. 15, pp. 3476–3486, 2007.

[193] P. Reymond, F. Merenda, F. Perren, D. Ru, N. Stergiopulos, P. Reymond, F. Merenda, F. Perren, D. Rüfenacht, N. Stergiopulos, D. Ru, N. Stergiopulos, P. Reymond, F. Merenda, F. Perren, D. Rüfenacht, and N. Stergiopulos, “Validation of a one-dimensional model of the systemic arterial tree.,” *Am. J. Physiol. Heart Circ. Physiol.*, vol. 297, no. 1, pp. 208–222, 2009.

[194] K. Laganà, R. Balossino, F. Migliavacca, G. Pennati, E. L. Bove, M. R. de Leval, and G. Dubini, “Multiscale modeling of the cardiovascular system: application to the study of pulmonary and coronary perfusions in the univentricular circulation,” *J. Biomech.*, vol. 38, no. 5, pp. 1129–1141, 2005.

[195] A. Quarteroni, S. Ragni, and A. Veneziani, “Coupling between lumped and distributed models for blood flow problems,” *Comput. Vis. Sci.*, vol. 4, pp. 111–124, 2001.

[196] A. Quarteroni and A. Veneziani, “Analysis of a Geometrical Multiscale Model Based on the Coupling of ODE and PDE for Blood Flow Simulations,” *Multiscale Model. Simul.*,

vol. 1, pp. 173–195, 2003.

[197] G. Mulder, A. Marzo, A. C. B. Bogaerds, S. C. Coley, P. Rongen, D. R. Hose, and F. N. van de Vosse, "Patient-Specific Modeling of Cerebral Blood Flow: Geometrical Variations in a 1D Model," *Cardiovasc. Eng. Technol.*, vol. 2, no. 4, pp. 334–348, Dec. 2011.

[198] A. C. Simon, M. E. Safar, J. A. Levenson, G. M. London, B. I. Levy, and N. P. Chau, "An evaluation of large arteries compliance in man," *Am. J. Physiol. Circ. Physiol.*, vol. 237, no. 5, pp. 550–554, 1979.

[199] H. J. Kim, I. E. Vignon-Clementel, C. A. Figueroa, J. F. Ladisa, K. E. Jansen, J. A. Feinstein, and C. A. Taylor, "On coupling a lumped parameter heart model and a three-dimensional finite element aorta model," *Ann. Biomed. Eng.*, vol. 37, no. 11, pp. 2153–2169, 2009.

[200] Edwards Lifesciences LLC, "Normal Hemodynamic Parameters and Laboratory – Adult," 2009.

[201] J. Doohan, "Cardiac Output and Blood Pressure," *McGraw-Hill*, 2000. [Online]. Available: http://www.biosbcc.net/doohan/sample/htm/COandMAPhtm.htm.

[202] W. Nichols, M. O'Rourke, and C. Vlachopoulos., *McDonald's blood flow in arteries: theoretical, experimental and clinical principles.* CRC Press, 2011.

[203] M. F. O'Rourke and J. Hashimoto, "Mechanical Factors in Arterial Aging: A Clinical Perspective," *J. Am. Coll. Cardiol.*, vol. 50, no. 1, pp. 1–13, 2007.

[204] S. Franklin, M. Jacobs, and N. Wong, "Predominance of isolated systolic hypertension among middle-aged and elderly US hypertensives analysis based on National Health and

Nutrition Examination," *Hypertension*, vol. 37, no. 3, pp. 869–874, 2001.

[205] C. Dechanet, A. Fort, E. Barbero-Camps, H. Dechaud, S. Richard, and A. Virsolvy, "Endothelin-Dependent Vasoconstriction in Human Uterine Artery: Application to Preeclampsia," *PLoS One*, vol. 6, no. 1, pp. 1–8, 2011.

[206] F. U. S. Mattace-Raso, T. J. M. Van Der Cammen, A. Hofman, N. M. Van Popele, M. L. Bos, M. A. D. H. Schalekamp, R. Asmar, R. S. Reneman, A. P. G. Hoeks, M. M. B. Breteler, and J. C. M. Witteman, "Arterial stiffness and risk of coronary heart disease and stroke: The Rotterdam Study," *Circulation*, vol. 113, no. 5, pp. 657–663, 2006.

[207] A. Amery, R. Fagard, C. Guo, J. Staessen, and L. Thus, "Isolated systolic hypertension in the elderly: An epidemiologic review," *Am. J. Med.*, vol. 90, no. 3, Supplement 1, pp. S64–S70, 1991.

[208] D. A. Kass, "Ventricular arterial stiffening: Integrating the pathophysiology," *Hypertension*, vol. 46, no. 1, pp. 185–193, 2005.

[209] I. B. Wilkinson, C. M. McEniery, and J. R. Cockcroft, "Arteriosclerosis and atherosclerosis: Guilty by association," *Hypertension*, vol. 54, no. 6, pp. 1213–1215, 2009.

[210] E. G. Lakatta and D. Levy, "Arterial and cardiac aging: Major shareholders in cardiovascular disease enterprises: Part I: Aging arteries: A 'set up' for vascular disease," *Circulation*, vol. 107, no. 1, pp. 139–146, 2003.

[211] A. P. Avolio, S. G. Chen, R. P. Wang, C. L. Zhang, M. F. Li, and M. F. O'Rourke, "Effects of aging on changing arterial compliance and left ventricular load in a northern Chinese urban community.," *Circulation*, vol. 68, no. 1, pp. 50–58, 1983.

[212] C.-H. Chen, M. Nakayama, E. Nevo, B. J. Fetics, W. L. Maughan, and D. A. Kass,

"Coupled systolic-ventricular and vascular stiffening with age: Implications for pressure regulation and cardiac reserve in the elderly," *J. Am. Coll. Cardiol.*, vol. 32, no. 5, pp. 1221–1227, 1998.

[213] R. Asmar, R. A., and B. J., "Pulse pressure and aortic pulse wave are markers of cardiovascular risk in hypertensive populations," *Am.J.Hypertens*, vol. 14, no. 2, pp. 91–97, 2001.

[214] A. W. Haider, M. G. Larson, S. S. Franklin, and Levy, D, "Systolic blood pressure, diastolic blood pressure, and pulse pressure as predictors of risk for congestive heart failure in the framingham heart study," *Ann. Intern. Med.*, vol. 138, no. 1, pp. 10–16, 2003.

[215] I. Hajjar and T. A. Kotchen, "Trends in prevalence, awareness, treatment, and control of hypertension in the united states, 1988-2000," *JAMA*, vol. 290, no. 2, pp. 199–206, 2003.

[216] R. S. Vasan, A. Beiser, and S. Seshadri, "Residual lifetime risk for developing hypertension in middle-aged women and men: The framingham heart study," *JAMA*, vol. 287, no. 8, pp. 1003–1010, 2002.

[217] E. Pinto, "Blood pressure and ageing," *Postgraduate Medical Journal*, vol. 83, no. 976. pp. 109–114, Feb-2007.

[218] E. L. Schiffrin, "Vascular stiffening and arterial complianceImplications for systolic blood pressure," *Am. J. Hypertens.*, vol. 17, no. S3, p. 39S–48S, 2004.

[219] R. Asmar, "Benefits of blood pressure reduction in elderly patients," *J. Hypertens.*, vol. 21, 2003.

[220] J. Stamler, R. Stamler, and J. D. Neaton, "Blood pressure, systolic and diastolic, and

cardiovascular risks: Us population data," *Arch. Intern. Med.*, vol. 153, no. 5, pp. 598–615, 1993.

[221] M. F. O'Rourke, J. A. Staessen, C. Vlachopoulos, D. Duprez, and G. E. Plante, "Clinical Application of Arterial Stiffness; Definition and Reference Values," *Am. J. Hypertens.*, vol. 15, no. 5, pp. 426–444, 2002.

[222] G. F. Mitchell, Y. Lacourcière, J. P. Ouellet, J. L. Izzo, J. Neutel, L. J. Kerwin, A. J. Block, and M. A. Pfeffer, "Determinants of elevated pulse pressure in middle-aged and older subjects with uncomplicated systolic hypertension: The role of proximal aortic diameter and the aortic, pressure-flow relationship," *Circulation*, vol. 108, no. 13, pp. 1592–1598, 2003.

[223] M. AlGhatrif and E. G. Lakatta, "The Conundrum of Arterial Stiffness, Elevated blood pressure, and Aging," *Current hypertension reports*, vol. 17, no. 12. Feb-2015.

[224] R. P. Wildman, R. H. Mackey, A. Bostom, T. Thompson, and K. Sutton-Tyrrell, "Measures of obesity are associated with vascular stiffness in young and older adults," *Hypertension*, vol. 42, no. 4 I, pp. 468–473, 2003.

[225] R. M. A. Henry, P. J. Kostense, A. M. W. Spijkerman, J. M. Dekker, G. Nijpels, R. J. Heine, O. Kamp, N. Westerhof, L. M. Bouter, and C. D. A. Stehouwer, "Arterial stiffness increases with deteriorating glucose tolerance status: The Hoorn study," *Circulation*, vol. 107, no. 16, pp. 2089–2095, 2003.

[226] M. F. O'Rourke, "Vascular impedance in studies of arterial and cardiac function.," *Physiol. Rev.*, vol. 62, no. 2, pp. 570–623, 1982.

[227] A. Siddiqui, "Effects of Vasodilation and Arterial Resistance on Cardiac Output," *J. Clin. Exp. Cardiolog.*, vol. 02, no. 11, 2011.

[228] I. Tuleta, G. Bauriedel, M. Peuster, R. Andrié, and S. Pabst, “FKBP12+ S100+ Dendritic Cells as Novel Cellular Targets for Rapamycin in Post Stent Neointima,” *J. Clin. Exp. Cardiolog.*, vol. 02, no. 06, pp. 10–12, 2011.

[229] N. D. Brunetti, A. Centola, E. G. Campanale, A. Cuculo, and L. Ziccardi, “Combined Finding of Left Ventricular Non-Compaction and Dilated Cardiomyopathy,” *J. Clin. Exp. Cardiolog.*, vol. 01, no. 03, pp. 1–2, 2010.

[230] Y. Tanaka, K. Matsuo, and S. Yuzuriha, “Near-Infrared Irradiation Nonthermally Induces Long-lasting Vasodilation by Causing Apoptosis of Vascular Smooth Muscle Cells,” *Eplasty*, vol. 11. 2011.

[231] A. M. Evans, D. G. Hardie, C. Peers, and A. Mahmoud, “Hypoxic Pulmonary Vasoconstriction: mechanisms of oxygen-sensing,” *Current opinion in anaesthesiology*, vol. 24, no. 1. pp. 13–20, Feb-2011.

[232] N. Charkoudian, “Mechanisms and modifiers of reflex induced cutaneous vasodilation and vasoconstriction in humans,” *J. Appl. Physiol.*, vol. 109, no. 4, pp. 1221–1228, 2010.

[233] J. Cui, M. Shibasaki, D. A. Low, D. M. Keller, S. L. Davis, and C. G. Crandall, “Heat stress attenuates the increase in arterial blood pressure during the cold pressor test,” *J. Appl. Physiol.*, vol. 109, no. 5, pp. 1354–1359, 2010.

[234] R. P. Kelly, R. Tunin, and D. A. Kass, “Effect of reduced aortic compliance on cardiac efficiency and contractile function of in situ canine left ventricle,” *Circ. Res.*, vol. 71, no. 3, pp. 490–502, 1992.

[235] J. Koch-Weser, “Vasodilator drugs in the treatment of hypertension,” *Arch. Intern. Med.*, vol. 133, no. 6, pp. 1017–1027, 1974.

[236] N. Sakalihasan, R. Limet, and O. D. Defawe, “Abdominal aortic aneurysm,” *Lancet*, vol. 365, no. 9470, pp. 1577–1589, 2005.

[237] H. Bengtsoon, B. Sonesson, and D. Bergqvist, “Incidence and Prevalence of Abdominal Aortic Aneurysms, Estimated by Necropsy Studies and Population Screening by Ultrasounda,” *Ann. N. Y. Acad. Sci.*, vol. 800, no. 1, pp. 1–24, 1996.

[238] G. R. Upchurch and T. A. Schaub, “Abdominal aortic aneurysm,” *Am. Fam. Physician*, vol. 73, no. 7, pp. 1198–1206, 2006.

[239] F. A. Lederle, G. R. Johnson, S. E. Wilson, I. L. Gordon, E. P. Chute, F. N. Littooy, W. C. Krupski, D. Bandyk, G. W. Barone, L. M. Graham, and others, “Relationship of age, gender, race, and body size to infrarenal aortic diameter,” *J. Vasc. Surg.*, vol. 26, no. 4, pp. 595–601, 1997.

[240] K. W. Johnston, R. B. Rutherford, M. Tilson, D. M. Shah, L. Hollier, and J. C. Stanley, “Suggested standards for reporting on arterial aneurysms. Subcommittee on Reporting Standards for Arterial Aneurysms, Ad Hoc Committee on Reporting Standards, Society for Vascular Surgery and North American Chapter, International Society for Cardiovascular,” *J. Vasc. Surg. Off. Publ. Soc. Vasc. Surg. [and] Int. Soc. Cardiovasc. Surgery, North Am. Chapter*, vol. 13, pp. 452–458, 1991.

[241] familydoctor. or. editorial Staff, “Abdominal Aortic Aneurysm (AAA).,” 2017. [Online]. Available: https://familydoctor.org/condition/abdominal-aortic-aneurysm/.

[242] S. T. R. MacSweeney, M. Ellis, P. C. Worrell, R. M. Greenhalgh, and J. T. Powell, “Smoking and growth rate of small abdominal aortic aneurysms,” *Lancet*, vol. 344, no. 8923, pp. 651–652, 1994.

[243] T. E. Rasmussen, J. W. Hallett Jr, H. D. Tazelaar, V. M. Miller, S. Schulte, W. M.

O'Fallon, and C. M. Weyand, "Human leukocyte antigen class II immune response genes, female gender, and cigarette smoking as risk and modulating factors in abdominal aortic aneurysms," *J. Vasc. Surg.*, vol. 35, no. 5, pp. 988–993, May 2002.

[244] M. Wassef, B. T. Baxter, R. L. Chisholm, R. L. Dalman, M. F. Fillinger, J. Heinecke, J. D. Humphrey, H. Kuivaniemi, W. C. Parks, W. H. Pearce, C. D. Platsoucas, G. K. Sukhova, R. W. Thompson, M. D. Tilson, and C. K. Zarins, "Pathogenesis of abdominal aortic aneurysms: A multidisciplinary research program supported by the National Heart, Lung, and Blood Institute," *J. Vasc. Surg.*, vol. 34, no. 4, pp. 730–738, 2001.

[245] C. J. van Vlijmen-van Keulen, G. Pals, and J. A. Rauwerda, "Familial Abdominal Aortic Aneurysm: a Systematic Review of a Genetic Background," *Eur. J. Vasc. Endovasc. Surg.*, vol. 24, no. 2, pp. 105–116, 2002.

[246] F. A. Lederle, G. R. Johnson, and S. E. Wilson, "The aneurysm detection and management study screening program: Validation cohort and final results," *Arch. Intern. Med.*, vol. 160, no. 10, pp. 1425–1430, 2000.

[247] J. S. Lindholt, S. Vammen, S. Juul, H. Fasting, and E. W. Henneberg, "Optimal Interval Screening and Surveillance of Abdominal Aortic Aneurysms," *Eur. J. Vasc. Endovasc. Surg.*, vol. 20, no. 4, pp. 369–373, 2000.

[248] S. H. Forsdahl, K. Singh, S. Solberg, and B. K. Jacobsen, "Risk factors for abdominal aortic aneurysms: a 7-year prospective study: the tromsø study, 1994 2001," *Circulation*, vol. 119, no. 16, pp. 2202–2208, 2009.

[249] L. C. Brown and J. T. Powell, "Risk Factors for Aneurysm Rupture in Patients Kept Under Ultrasound Surveillance," *Annals of Surgery*, vol. 230, no. 3. p. 289, Sep-1999.

[250] F. A. Lederle, G. R. Johnson, and S. E. Wilson, "Abdominal aortic aneurysm in women,"

J. Vasc. Surg., vol. 34, no. 1, pp. 122–126, 2001.

[251] F. A. Lederle and D. L. Simel, "Does this patient have abdominal aortic aneurysm?," *JAMA*, vol. 281, no. 1, pp. 77–82, 1999.

[252] H. W. Kniemeyer, T. Kessler, P. U. Reber, H. B. Ris, H. Hakki, and M. K. Widmer, "Treatment of Ruptured Abdominal Aortic Aneurysm, a Permanent Challenge or a Waste of Resources? Prediction of Outcome Using a Multi-organ-dysfunction Score," *Eur. J. Vasc. Endovasc. Surg.*, vol. 19, no. 2, pp. 190–196, 2000.

[253] F. A. Lederle, S. E. Wilson, G. R. Johnson, D. B. Reinke, F. N. Littooy, C. W. Acher, D. J. Ballard, L. M. Messina, I. L. Gordon, E. P. Chute, W. C. Krupski, S. J. Busuttil, G. W. Barone, S. Sparks, L. M. Graham, J. H. Rapp, M. S. Makaroun, G. L. Moneta, R. A. Cambria, R. G. Makhoul, D. Eton, H. J. Ansel, J. A. Freischlag, and D. Bandyk, "Immediate Repair Compared with Surveillance of Small Abdominal Aortic Aneurysms," *N. Engl. J. Med.*, vol. 346, no. 19, pp. 1437–1444, 2002.

[254] "Long-Term Outcomes of Immediate Repair Compared with Surveillance of Small Abdominal Aortic Aneurysms," *N. Engl. J. Med.*, vol. 346, no. 19, pp. 1445–1452, 2002.

[255] R. A. P. Scott, "The Multicentre Aneurysm Screening Study (MASS) into the effect of abdominal aortic aneurysm screening on mortality in men: a randomised controlled trial," *Lancet*, vol. 360, no. 9345, pp. 1531–1539, 2002.

[256] R. Limet, N. Sakalihassan, and A. Albert, "Determination of the expansion rate and incidence of ruptur of abdominal aortic aneurysms," *J. Vasc. Surg.*, vol. 14, no. 4, pp. 540–548, 1991.

[257] M. P. Nevitt, D. J. Ballard, and J. W. Hallett, "Prognosis of Abdominal Aortic Aneurysms," *N. Engl. J. Med.*, vol. 321, no. 15, pp. 1009–1014, 1989.

[258] M. M. Thompson, “Controlling the expansion of abdominal aortic aneurysms,” *Br. J. Surg.*, vol. 90, no. 8, pp. 897–898, 2003.

[259] R. A. P. Scott, H. A. Ashton, and D. N. Kay, “Abdominal aortic aneurysm in 4237 screened patients: Prevalence, development and management over 6 years,” *Br. J. Surg.*, vol. 78, no. 9, pp. 1122–1125, 1991.

[260] R. F. Gillum, “Epidemiology of aortic aneurysm in the United States,” *J. Clin. Epidemiol.*, vol. 48, no. 11, pp. 1289–1298, 1995.

[261] R. N. Anderson, “Deaths: Leading Causes for 2000,” *Natl. Vital Stat. Reports*, vol. 50, no. 16, p. 86, 2002.

[262] A. Swillens, L. Lanoye, J. De Backer, N. Stergiopulos, P. R. Verdonck, F. Vermassen, and P. Segers, “Effect of an Abdominal Aortic Aneurysm on Wave Reflection in the Aorta,” *IEEE Trans. Biomed. Eng.*, vol. 55, no. 5, pp. 1602–1611, May 2008.

[263] L. M. Prisant and J. S. Mondy, “Abdominal Aortic Aneurysm,” *J. Clin. Hypertens.*, vol. 6, no. 2, pp. 85–89, 2004.

[264] L. Formaggia, J. F. Gerbeau, F. Nobile, and A. Quarteroni, “Numerical Treatment of Defective Boundary Conditions for the Navier--Stokes Equations,” *SIAM J. Numer. Anal.*, vol. 40, no. 1, pp. 376–401, 2002.

[265] A. Swillens and P. Segers, “Assessment of arterial pressure wave reflection: Methodological considerations,” *Artery Res.*, vol. 2, no. 4, pp. 122–131, 2008.

[266] F. Secchi, A. Iozzelli, G. D. E. Papini, A. Aliprandi, G. Di Leo, and F. Sardanelli, “MR imaging of aortic coarctation,” *Radiol. Med.*, vol. 114, no. 4, pp. 524–537, Jun. 2009.

[267] S. Jarcho, “Coarctation of the aorta (Meckel, 1750; Paris, 1791),” *Am. J. Cardiol.*, vol. 7,

no. 6, pp. 844–852, 1961.

[268] M. E. Abbott, “Coarctation of the aorta of the adult type: II. A statistical study and historical retrospect of 200 recorded cases with autopsy, of stenosis or obliteration of the descending arch in subjects above the age of two years,” *Am. Heart J.*, vol. 3, no. 5, pp. 574–618, 1928.

[269] Z. Keshavarz-Motamed, J. Garcia, and L. Kadem, “Fluid Dynamics of Coarctation of the Aorta and Effect of Bicuspid Aortic Valve,” *PLoS One*, vol. 8, no. 8, 2013.

[270] M. A. Hamdan, S. Maheshwari, J. T. Fahey, and W. E. Hellenbrand, “Endovascular stents for coarctation of the aorta: initial results and intermediate-term follow-up,” *J. Am. Coll. Cardiol.*, vol. 38, no. 5, pp. 1518–1523, 2001.

[271] Cleveland Clinic: Health Library, “Coarctation of the Aorta,” *Cleveland Clinic: Health Library*. [Online]. Available: https://my.clevelandclinic.org/health/diseases/16876-coarctation-of-the-aorta.

[272] B. L, “Coarctation of the aorta,” *Arch. Intern. Med.*, vol. 41, no. 5, pp. 702–735, 1928.

[273] M. Campbell and J. H. Baylis, “The Course and Prognosis of Coarctation of the Aorta,” *Heart*, vol. 18, no. 4, pp. 475–495, 1956.

[274] D. S. Celermajer and K. Greaves, “Survivors of coarctation repair: fixed but not cured,” *Heart*, vol. 88, no. 2, pp. 113–114, 2002.

[275] P. S. Rao, “Coarctation of the aorta,” *Curr. Cardiol. Rep.*, vol. 7, no. 6, pp. 425–434, Nov. 2005.

[276] C. A. Warnes, “Bicuspid aortic valve and coarctation: two villains part of a diffuse problem,” *Heart*, vol. 89, no. 9. pp. 965–966, Sep-2003.

[277] T. H. Rosenquist, A. C. Beall, L. Módis, and R. Fishman, “Impaired elastic matrix development in the great arteries after ablation of the cardiac neural crest,” *Anat. Rec.*, vol. 226, no. 3, pp. 347–359, 1990.

[278] L. M. Prisant, K. Mawulawde, D. Kapoor, and C. Joe, “Coarctation of the Aorta: A Secondary Cause of Hypertension,” *J. Clin. Hypertens.*, vol. 6, pp. 347–352, 2004.

[279] J. P. De Bono and L. J. Freeman, “Long term follow up of patients with repaired aortic coarctations,” *Heart*, vol. 91, no. 4, pp. 537–538, 2005.

[280] P. Presbitero, D. Demarie, M. Villani, E. A. Perinetto, G. Riva, F. Orzan, M. Bobbio, M. Morea, and A. Brusca, “Long term results (15-30 years) of surgical repair of aortic coarctation.,” *Heart*, vol. 57, no. 5, pp. 462–467, 1987.

[281] P. M. Clarkson, M. R. Nicholson, B. G. Barratt-Boyes, J. M. Neutze, and R. M. Whitlock, “Results after repair of coarctation of the aorta beyond infancy: A 10 to 28 year follow-up with particular reference to late systemic hypertension,” *Am. J. Cardiol.*, vol. 51, no. 9, pp. 1481–1488, 1983.

[282] M. Koller, M. Rothlin, and Å. Senning, “Coarctation of the aorta: review of 362 operated patients. Long-term follow-up and assessment of prognostic variables,” *Eur. Heart J.*, vol. 8, no. 7, pp. 670–679, 1987.

[283] A. B. Stewart, R. Ahmed, C. M. Travill, and C. G. Newman, “Coarctation of the aorta life and health 20-44 years after surgical repair.,” *British Heart Journal*, vol. 69, no. 1. pp. 65–70, Jan-1993.

[284] M. E. Brickner, L. D. Hillis, and R. A. Lange, “Congenital Heart Disease in Adults,” *N. Engl. J. Med.*, vol. 342, no. 4, pp. 256–263, 2000.

[285] J. W. Roos-Hesselink, B. E. Schölzel, R. J. Heijdra, S. E. C. Spitaels, F. J. Meijboom, E. Boersma, A. J. J. C. Bogers, and M. L. Simoons, "Aortic valve and aortic arch pathology after coarctation repair," *Heart*, vol. 89, no. 9. pp. 1074–1077, Sep-2003.

[286] S. Venning, L. J. Freeman, and K. Stanley, "Two cases of pregnancy with coarctation of the aorta," *Journal of the Royal Society of Medicine*, vol. 96, no. 5. pp. 234–236, May-2003.

[287] M. Punukollu, A. Harnden, and R. Tulloh, "Coarctation of the aorta in the newborn," *BMJ*, vol. 343, no. 7832, pp. 1063–1065, 2011.

[288] K. E. Ward, R. W. Pryor, J. R. Matson, J. D. Razook, W. M. Thompson, and R. C. Elkins, "Delayed Detection of Coarctation in Infancy: Implications for Timing of Newborn Follow-up," *Pediatrics*, vol. 86, no. 6, pp. 972–976, 1990.

[289] F. F. Ing, T. J. Starc, S. P. Griffiths, and W. M. Gersony, "Early Diagnosis of Coarctation of the Aorta in Children: A Continuing Dilemma," *Pediatrics*, vol. 98, no. 3, pp. 378–382, 1996.

[290] D. S. Crossland, J. C. Furness, M. Abu-Harb, S. N. Sadagopan, and C. Wren, "Variability of four limb blood pressure in normal neonates," *Arch. Dis. Child. - Fetal Neonatal Ed.*, vol. 89, no. 4, pp. F325--F327, 2004.

[291] T. Papaioannou, A. D Protogerou, K. Stamatelopoulos, M. Vavouranakis, and C. Stefanadis, "Non-Invasive Methods and Techniques for Central Blood Pressure Estimation: Procedures, Validation, Reproducibility and Limitations," *Curr. Pharm. Des.*, vol. 15, pp. 245–253, 2009.

[292] H. Smulyan, R. Mukherjee, P. R Sheehe, and M. E Safar, "Cuff and aortic pressure differences during dobutamine infusion: A study of the effects of systolic blood pressure

amplification," *Am. Heart J.*, vol. 159, pp. 399–405, 2010.

[293] A. Mahmud and J. Feely, "Spurious systolic hypertension of youth: Fit young men with elastic arteries," *Am. J. Hypertens.*, vol. 16, no. 3, pp. 229–232, 2003.

[294] M. F. O'Rourke, "Wave travel and reflection in the arterial system.," *J. Hypertens. Suppl.*, vol. 17 5, pp. S45-7, 1999.

[295] A. L. Pauca, S. L. Wallenhaupt, N. D. Kon, and W. Y. Tucker, "Does Radial Artery Pressure Accurately Reflect Aortic Pressure?," *Chest*, vol. 102, no. 4, pp. 1193–1198, 1992.

[296] E. J. Kroeker and E. H. Wood, "Comparison of Simultaneously Recorded Central and Peripheral Arterial Pressure Pulses During Rest, Exercise and Tilted Position in Man EDWIN J. KROEKER and EARL H. WOOD Circ. Res. 1955;3;623-632," *Respiration*, vol. III, 2007.

[297] R. D. Latham, N. Westerhof, P. Sipkema, B. J. Rubal, P. Reuderink, and J. P. Murgo, "Regional wave travel and reflections along the human aorta: A study with six simultaneous micromanometric pressures," *Circulation*, vol. 72, no. 6, pp. 1257–1269, 1985.

[298] A. D. Protogerou, T. G. Papaioannou, J. Blacher, C. M. Papamichael, J. P. Lekakis, and M. E. Safar, "Central blood pressures: do we need them in the management of cardiovascular disease? Is it a feasible therapeutic target?," *J Hypertens*, vol. 25, no. 2, pp. 265–272, 2007.

[299] A. D Protogerou, T. Papaioannou, J. P Lekakis, J. Blacher, and M. E Safar, "The Effect of Antihypertensive Drugs on Central Blood Pressure Beyond Peripheral Blood Pressure. Part I: (Patho)-Physiology, Rationale and Perspective on Pulse Pressure Amplification,"

Curr. Pharm. Des., vol. 15, pp. 267–271, 2009.

[300] C. Vlachopoulos and M. O'Rourke, "Genesis of the normal and abnormal arterial pulse," *Curr. Probl. Cardiol.*, vol. 25, no. 5, pp. 303–367, 2000.

[301] A. D Protogerou, G. S Stergiou, C. Vlachopoulos, J. Blacher, and A. Achimastos, "The Effect of Antihypertensive Drugs on Central Blood Pressure Beyond Peripheral Blood Pressure. Part II: Evidence for Specific Class-Effects of Antihypertensive Drugs on Pressure Amplification," *Curr. Pharm. Des.*, vol. 15, pp. 272–289, 2009.

[302] T. G. Papaioannou, K. Karatzi, E. Karatzis, C. Papamichael, and J. P. Lekakis, "Acute effects of caffeine on arterial stiffness, wave reflections, and central aortic pressures," *Am. J. Hypertens.*, vol. 18, no. 1, pp. 129–136, 2005.

[303] C. Vlachopoulos, K. Hirata, and M. F. O'Rourke, "Pressure-altering agents affect central aortic pressures more than is apparent from upper limb measurements in hypertensive patients: The role of arterial wave reflections," *Hypertension*, vol. 38, no. 6, pp. 1456–1460, 2001.

[304] C. M Papamichael, K. Karatzi, T. Papaioannou, E. N Karatzis, P. Katsichti, V. Sideris, N. Zakopoulos, A. Zampelas, and J. P Lekakis, "Acute combined effects of olive oil and wine on pressure wave reflections: Another beneficial influence of the Mediterranean diet antioxidants?," *J. Hypertens.*, vol. 26, pp. 223–229, 2008.

[305] K. Karatzi, T. Papaioannou, C. Papamichael, J. Lekakis, C. Stefanadis, and A. Zampelas, "Red Wine, Arterial Stiffness and Central Hemodynamics," *Curr. Pharm. Des.*, vol. 15, pp. 321–328, 2009.

[306] H. Cheng, K.-L. Wang, Y.-H. Chen, S.-J. Lin, L.-C. Chen, S.-H. Sung, P. Yu-An Ding, wen-chung yu, J.-W. Chen, and C.-H. Chen, "Estimation of central systolic blood pressure

using an oscillometric blood pressure monitor," *Hypertens. Res.*, vol. 33, pp. 592–599, 2010.

[307] C. Vlachopoulos, K. Aznaouridis, M. F. O'Rourke, M. E. Safar, K. Baou, and C. Stefanadis, "Prediction of cardiovascular events and all-cause mortality with central haemodynamics: A systematic review and meta-analysis," *Eur. Heart J.*, vol. 31, no. 15, pp. 1865–1871, 2010.

[308] B. Williams and P. S. Lacy, "Central haemodynamics and clinical outcomes: Going beyond brachial blood pressure?," *Eur. Heart J.*, vol. 31, no. 15, pp. 1819–1822, 2010.

[309] M. Sabovic, M. E Safar, and J. Blacher, "Is there any Additional Prognostic Value of Central Blood Pressure Wave Forms Beyond Peripheral Blood Pressure?," *Curr. Pharm. Des.*, vol. 15, pp. 254–266, 2009.

[310] J. A. Chirinos, J. P. Zambrano, S. Chakko, A. Veerani, A. Schob, G. Perez, and A. J. Mendez, "Relation Between Ascending Aortic Pressures and Outcomes in Patients With Angiographically Demonstrated Coronary Artery Disease," *Am. J. Cardiol.*, vol. 96, no. 5, pp. 645–648, 2005.

[311] H. Smulyan and M. E. Safar, "Blood pressure measurement: Retrospective and prospective views," *Am. J. Hypertens.*, vol. 24, no. 6, pp. 628–634, 2011.

[312] R. Pini, M. Chiara Cavallini, V. Palmieri, N. Marchionni, M. Di Bari, R. B Devereux, G. Masotti, and M. J Roman, "Central But Not Brachial Blood Pressure Predicts Cardiovascular Events in an Unselected Geriatric Population. The ICARe Dicomano Study," *J. Am. Coll. Cardiol.*, vol. 51, pp. 2432–2439, 2008.

[313] K.-L. Wang, H. Cheng, S.-Y. Chuang, H. A Spurgeon, C.-T. Ting, E. G Lakatta, F. C.P. Yin, P. Chou, and C.-H. Chen, "Central or peripheral systolic or pulse pressure: Which

best relates to target organs and future mortality?," *J. Hypertens.*, vol. 27, pp. 461–467, 2009.

[314] A. Dart, C. D Gatzka, B. Kingwell, K. Willson, J. Cameron, Y.-L. Liang, K. L Berry, L. Wing, C. Reid, P. Ryan, L. Beilin, G. L R Jennings, C. I Johnston, J. J McNeil, G. J Macdonald, T. O Morgan, and M. J West, "Brachial Blood Pressure But Not Carotid Arterial Waveforms Predict Cardiovascular Events in Elderly Female Hypertensives," *Hypertension*, vol. 47, pp. 785–790, 2006.

[315] C.-H. Chen, C.-T. Ting, A. Nussbacher, E. Nevo, D. A. Kass, P. Pak, S.-P. Wang, M.-S. Chang, and F. C. P. Yin, "Validation of Carotid Artery Tonometry as a Means of Estimating Augmentation Index of Ascending Aortic Pressure," *Hypertension*, vol. 27, no. 2, pp. 168–175, 1996.

[316] C. M. McEniery, J. R. Cockcroft, M. J. Roman, S. S. Franklin, and I. B. Wilkinson, "Central blood pressure: Current evidence and clinical importance," *Eur. Heart J.*, vol. 35, no. 26, pp. 1719–1725, 2014.

[317] C. M. McEniery, Yasmin, I. R. Hall, A. Qasem, I. B. Wilkinson, and J. R. Cockcroft, "Normal Vascular Aging: Differential Effects on Wave Reflection and Aortic Pulse Wave Velocity: The Anglo-Cardiff Collaborative Trial (ACCT)," *J. Am. Coll. Cardiol.*, vol. 46, no. 9, pp. 1753–1760, 2005.

[318] L. Bortel, E. Balkestein, J. van der Heijden-Spek, F. H. Vanmolkot, J. A. Staessen, J. Kragten, J. W. Vredeveld, M. E. Safar, H. Struijker-Boudier, and A. P. Hoeks, "Non-invasive assessment of local arterial pulse pressure: Comparison of applanation tonometry and echo-tracking," *J. Hypertens.*, vol. 19, pp. 1037–1044, 2001.

[319] M. Karamanoglu and M. P. Feneley, "On-line synthesis of the human ascending aortic

pressure pulse from the finger pulse," *Hypertens. (Dallas, Tex. 1979)*, vol. 30, no. 6, p. 1416—1424, Dec. 1997.

[320] H. A. J. Lasance, K. H. Wesseling, and C. A. Ascoop, "Peripheral pulse contour analysis in determining stroke volume," pp. 59–62, 1976.

[321] M. F. O'Rourke, "Influence of ventricular ejection on the relationship between central aortic and brachial pressure pulse in man," *Cardiovasc. Res.*, vol. 4, no. 3, pp. 291–300, 1970.

[322] M. Karamanoglu and M. P. Feneley, "Derivation of the ascending aortic-carotid pressure transfer function with an arterial model," *Am. J. Physiol. Circ. Physiol.*, vol. 271, no. 6, pp. H2399–H2404, 1996.

[323] M. Sugimachi, T. Shishido, K. Miyatake, and K. Sunagawa, "A New Model-Based Method of Reconstructing Central Aortic Pressure from Peripheral Arterial Pressure," *Jpn. J. Physiol.*, vol. 51, no. 2, pp. 217–22, 2001.

[324] D. H. Fitchett, "Aortofemoral transfer function: a method to determine the instantaneous aortic valve gradient in aortic valve stenosis," *J. Am. Coll. Cardiol.*, vol. 22, no. 7, pp. 1909–1914, 1993.

[325] M. Sugimachi, T. Kawada, T. Shishido, N. Matsumoto, J. Alexander, and K. Sunagawa, "Estimation of Arterial Mechanical Properties from Aortic and Tonometric Arterial Pressure Waveforms," *Methods Inf. Med.*, vol. 36, pp. 250–253, 1998.

[326] P. Segers, D. Mahieu, J. Kips, and L. M. Van Bortel, "The use of a generalized transfer function: different processing, different results!," *J.Hypertens.*, vol. 25, no. 0263–6352 (Print), pp. 1783–1787, 2007.

[327] W. R. Milnor, *Hemodynamics*, 2nd ed. Baltimore: Williams and Wilkins, 1989.

[328] A. P. Avolio, M. Butlin, and A. Walsh, "Arterial blood pressure measurement and pulse wave analysis--their role in enhancing cardiovascular assessment," *Physiol. Meas.*, vol. 31, no. 1, pp. R1–R47, 2010.

[329] S. A. Hope, I. T. Meredith, D. Tay, and J. D. Cameron, "'Generalizability' of a radial-aortic transfer function for the derivation of central aortic waveform parameters," *J. Hypertens.*, vol. 25, no. 9, pp. 1812–1820, 2007.

[330] D. GALLAGHER, A. Adji, M. F. O'Rourke, and M. OROURKE, "Validation of the transfer function technique for generating central from peripheral upper limb pressure waveform," *Am. J. Hypertens.*, vol. 17, no. 11, pp. 1059–1067, 2004.

[331] Y.-T. Shih, H.-M. Cheng, S.-H. Sung, W.-C. Hu, and C.-H. Chen, "Comparison of two generalized transfer functions for measuring central systolic blood pressure by an oscillometric blood pressure monitor," *J. Hum. Hypertens.*, vol. 27, p. 204, 2012.

[332] S. Wassertheurer, J. Kropf, T. Weber, M. van der Giet, J. Baulmann, M. Ammer, B. Hametner, C. C. Mayer, B. Eber, and D. Magometschnigg, "A new oscillometric method for pulse wave analysis: comparison with a common tonometric method," *J. Hum. Hypertens.*, vol. 24, no. 8, pp. 498–504, 2010.

[333] S. Emma Brett, A. Guilcher, B. Clapp, and P. Chowienczyk, "Estimating central systolic blood pressure during oscillometric determination of blood pressure: Proof of concept and validation by comparison with intra-aortic pressure recording and arterial tonometry," *Blood Press. Monit.*, vol. 17, pp. 132–136, 2012.

[334] S. A. Hope, D. B. Tay, I. T. Meredith, and J. D. Cameron, "Use of arterial transfer functions for the derivation of aortic waveform characteristics," *J. Hypertens.*, vol. 21, no.

7, pp. 1299–1305, 2003.

[335] G. Swamy and R. Mukkamala, “Estimation of the aortic pressure waveform and beat-to-beat relative cardiac output changes from multiple peripheral artery pressure waveforms,” *IEEE Trans. Biomed. Eng.*, vol. 55, no. 5, pp. 1521–1529, 2008.

[336] G. Swamy, D. Xu, and R. Mukkamala, “Estimation of the aortic pressure waveform from a radial artery pressure waveform via an adaptive transfer function: Feasibility demonstration in swine,” *Proc. 31st Annu. Int. Conf. IEEE Eng. Med. Biol. Soc. Eng. Futur. Biomed. EMBC 2009*, pp. 2362–2364, 2009.

[337] J.-O. Hahn, A. T. Reisner, and H. Asada, “Blind Identification of Two-Channel IIR Systems With Application to Central Cardiovascular Monitoring,” *J. Dyn. Syst. Meas. Control. Asme - J DYN SYST MEAS CONTR*, vol. 131, 2009.

[338] F. Haddad, C. Zeeni, I. El Rassi, A. Yazigi, S. Madi-Jebara, G. Hayeck, V. Jebara, and P. Yazbeck, “Can Femoral Artery Pressure Monitoring Be Used Routinely in Cardiac Surgery?,” *J. Cardiothorac. Vasc. Anesth.*, vol. 22, no. 3, pp. 418–422, 2008.

[339] V. Chhapola, S. K. Kanwal, and R. Brar, “Reporting standards for Bland–Altman agreement analysis in laboratory research: a cross-sectional survey of current practice,” *Ann. Clin. Biochem.*, vol. 52, no. 3, pp. 382–386, 2015.

[340] M. F. O’Rourke and T. Yaginuma, “Wave reflections and the arterial pulse.,” *Arch. Intern. Med.*, vol. 144, no. 2, pp. 366–371, 1984.

[341] S. C. Millasseau, S. J. Patel, S. R. Redwood, J. M. Ritter, and P. J. Chowienczyk, “Pressure wave reflection assessed from the peripheral pulse: Is a transfer function necessary?,” *Hypertension*, vol. 41, no. 5, pp. 1016–1020, 2003.

[342] S. A. Hope, D. B. Tay, I. T. Meredith, and J. D. Cameron, “Comparison of generalized and gender-specific transfer functions for the derivation of aortic waveforms,” *Am. J. Physiol. Circ. Physiol.*, vol. 283, no. 3, pp. H1150–H1156, 2002.

[343] S. A. Hope, I. T. Meredith, and J. D. Cameron, “Effect of non-invasive calibration of radial waveforms on error in transfer-function-derived central aortic waveform characteristics.,” *Clin. Sci. (Lond).*, vol. 107, no. 2, pp. 205–11, 2004.

[344] C. H. Chen, E. Nevo, B. E. Fetics, P. H Pak, F. C.P. Yin, W. L Maughan, and D. Kass, “Estimation of Central Aortic Pressure Waveform by Mathematical Transformation of Radial Tonometry Pressure : Validation of Generalized Transfer Function,” *Circulation*, vol. 95, pp. 1827–1836, 1997.

APPENDIX A FLUID AND ELASTIC PARAMETERS FOR THE 1-D MODEL

Table A-1: Elastic, fluid and boundary condition parameter definition for the 1-D model to simulate pulse wave propagation for various cases.

Model	ρ $\left(\frac{g}{cm^3}\right)$	μ $\left(\frac{g}{cm\ s}\right)$	k_1 $\left(\frac{g}{s^2 cm}\right)$	k_1 (cm^{-1})	k_3 $\left(\frac{g}{s^2 cm}\right)$	r_{min} (cm)
Aorta model (Single Vessel)	1.050	0.040	2×10^7	-22.53	8.0×10^5	0.001
3-D model	1.055	0.0488	2×10^7	-22.53	8.0×10^5	0.01
Full arterial network	1.055	0.0488	2×10^7	-22.53	8.65×10^5	0.01

APPENDIX B WORK FLOW OF 1-D MODEL SIMULATIONS

The work flow of simulations has been adapted from the pseudocode presented by Olufsen et al [82]. A total of 4 algorithms are used that setup the arterial network, solve the governing equations in large arteries, solve the equations in small arteries and find the root impedance.

Algorithm 1: The arterial tree

- Define number of vessels in the arterial network (arteries=A)
- Define starting time of simulation ($T_S = B$)
- Define ending (final) time of simulation ($T_F = C$)
- Initialize the arterial tree (arterialtree= newvessel[arteries])
- Artery[1]=newvessel $[L, r_{in}, r_{out}, Artery[2], Artery[3], r_{min}, \#, k_1, k_2, k_3, K_1, K_2]$

For each artery, the parameter specification in the order given is as follows:

- Length, L
- Proximal or inlet radius, r_{in}
- Distal or outlet radius, r_{out}
- Left daughter and right daughters (if they exist, that is, it is a bifurcating artery) otherwise a value of 0 is set as it is a terminal vessel. In the pseudocode the left and right daughters are $Artery[2]$ & $Artery[3]$, respectively
- If it a terminal vessel, the truncation criteria of the structured tree has to be specified, r_{min}. Otherwise, if it is a bifurcating artery, r_{min} is set as 0.
- Number of points per vessel, #
- Parameters that define the stiffness of vessel, k_1, k_2, k_3
- Loss coefficients where necessary, K_1, K_2

Algorithm 2: Solving governing equations for large arteries

- While $t < T_F$
    - For all arteries do

- Check application of CFL condition.
- Use Lax-Wendroff scheme in order to solve governing equations for the interior points.
- Update Q_{in} for artery next to inlet (heart).
- Apply bifurcation conditions if the artery is bifurcating (has daughters) otherwise apply structured tree outflow condition as the artery is terminal.

The following algorithm compute the root impedance recursively. Assumptions made here for the algorithm to run are number of time steps, N, the truncation or minimum radius, r_{min} and the root radius, r_{root} have been given.

Algorithm 3: Determination of the impedance at the root of the structured tree $\boldsymbol{Z(x=0,\omega)}$

- Compute root impedance for all frequencies. Compute the impedance for N values of ω. Impedance can be computed using two steps as follows:
  - For $k = N/2 + 1, N + 1$ do
    - Reset all computed results and store results temporarily.
    - Compute $Z(x = 0, \omega)$ recursively using Z_0 from algorithm 4.
  - Apply self-adjointness $\left(Z(0, \omega_k) = \overline{Z(0, \omega_{k+N/2})}\right)$
- Use IFT to transform root impedance from frequency domain to time domain.

Algorithm 4: Recursive computation of impedance

- Compute all parameters for the vessel
  - $r_0 = \alpha^{n_\alpha}\beta^{n_\beta}r_{root}$.
  - $A_0 = \pi r_0^2$
  - $f(r_0) = 4Eh/3r_0$

- $L = r_0 l_{rr}$

- Compute c (wave propagation velocity) and g (equation). Both these values depend of F_J (and hence on the womersley number)
- Run recursive algorithm
  - If $r_0 < r_{min}$ then
    - $Z_L(\omega_k, n_\alpha, n_\beta) = terminal\ resistance$
  - else
    - If root impedance of left daughter has been computed, store it in a temporary array.
    - Else
    - Compute root impedance of left daughter
    - If root impedance root impedance of right daughter has been computed, store it in a temporary array.
    - Else
    - Compute root impedance of right daughter
    - $Z_L(\omega_k, n_\alpha, n_\beta) = 1/[Z_0^{-1}(\omega_k, n_\alpha + 1, n_\beta) + Z_0^{-1}(\omega_k, n_\alpha, n_\beta + 1)$
- If $\omega_k \neq 0$
  - $Z_0(\omega_k, n_\alpha, n_\beta) = \frac{ig^{-1}\sin(\omega L/c) + Z(L,\omega)\cos(\omega L/c)}{\cos(\omega L/c) + igZ(L,\omega)\sin(\omega L/c)}$
- Else if $\omega_k = 0$
  - $Z_0(\omega_k, n_\alpha, n_\beta) = \frac{8\mu l_{rr}}{\pi r_0^3} + Z_L(\omega_k, n_\alpha, n_\beta)$
- Update the temporary array

APPENDIX C MATLAB ROUTINES FOR DATA

EXTRACTION AND GTF ESTIMATION

Matlab program that reads data from arteries of diseased subject

The diseased subject used in this sample code has an AAA.

```
clear % clears all variables in workspace

base_dir='C:\sample_directory\ Abdominal Aortic Aneurysm';
% Define path of directory containing AAA files

stiff_dir={'\normal stiffness',
    '\Reduced stiffness 10%',
    '\Reduced stiffness 20%',
    '\Reduced stiffness 30%',
    '\Reduced stiffness 40%',
    '\Reduced stiffness 50%'};
% Define path of directory containing files of varying stiffness'
of AAA

dis_dir={'\Diseased 1.5cm\',
    '\Diseased 2.5cm\',
    '\Diseased 2.25cm\',
    '\Diseased 2.75cm\',
    '\Diseased 2cm\',
    '\Diseased 3.5cm\',
    '\Diseased 3.25cm\',
    '\Diseased 3cm\',
    '\Healthy\'};
% Define path of directory containing files of varying radii of
AAA

art_dir={'artery1.2d', 'artery2.2d', 'artery3.2d' ,'artery4.2d',
    'artery5.2d','artery6.2d', 'artery7.2d', 'artery8.2d'
,'artery9.2d',
    'artery10.2d', 'artery11.2d', 'artery12.2d', 'artery13.2d'
,'artery14.2d',
    'artery15.2d','artery16.2d', 'artery17.2d', 'artery18.2d'
,'artery19.2d',
    'artery20.2d','artery21.2d', 'artery22.2d' ,'artery23.2d',
'artery24.2d'};
% Define content of directory that needs to be extracted


 for s=1:1:length(stiff_dir)
```

```
% For loop to go through all stiffness' directories

    for d=1:1:length(dis_dir)
% For loop to go through all radii directories


        for a=1:1:length(art_dir)
% For loop to go through all arteries in current directory
            temp_dir=strcat(base_dir,stiff_dir(s),dis_dir(d)) %
create a temporary directory

cd(temp_dir{1}); % Moving into the current directory


out=art_dir{a}; % Creating a new variable 'out' that reads the
data inside a specific artery


dataV1 = load (out); % Loads a specific artery onto the workspace

[t1,x1,p1,q1,A1,C1] = datacontainer(dataV1);  % Calls out
'datacontainer' which defines the columns of each file called

P_p1 = p1(:,1);  % Defines range of proximal pressures

P_m1 = p1(:,floor((end)/2)); % Defines range of mid pressures

P_d1 = p1(:,end);  % Defines range of distal pressures

Q_p1 = q1(:,1); % Defines range of proximal flow rates

Q_m1 = q1(:,floor((end)/2)); % Defines range of mid flow rates

Q_d1 = q1(:,end); % Defines range of distal flow rates

A=[P_p1 P_m1 P_d1 Q_p1 Q_m1 Q_d1]; % Creates a generic array 'A'
that contains all the pressures and flow rates


save(['artery' num2str(a) '.mat'],'A') % Saves array 'A' as a mat
file in the current directory

        end % end of artery directory for loop

    end % end of radii directory for loop

 end % end of stiffness' directory for loop

%------------------ End of Program -----------------%
```

Matlab program that estimates the GTF between ascending aorta and peripheral site pressure waveforms.

```
clear % clears all variables from workspace

clc % clears everything on command window

base_dir='C:\Sample_directory\Aorta\';
% Define path of directory containing Ascending Aorta files

base_dir2='C:\Sample_directory\Brachial\';
% Define path of directory containing peripheral pressure
measurement site (carotid/brachial/radial/femoral) files

GTF_A_B=[];
% Create empty array for GTF (GTF estimated between aorta and
brachial pressure waveforms in this example)

j=1; % Define value of counter starting value

for i=1:2:194
% Counter of the for loop (Half of the database)

    cd(base_dir);
    % Moving into ascending aorta files directory

    aorta = strcat(base_dir,'artery1-',' ',num2str(i),'')
    % Extract artery 1-1/2/3/4... (ascending aorta)- The second
    number i.e. 1/2/3/4 is the definition of case number so
    artery 1-24 means the first artery (ascending aorta) and case
    24

    load(aorta); % Load artery onto workspace

    A= A(:,1);
    % A is the generic name of the mat files for each artery

    X=fft(A); % DFT of ascending aorta waveform data


    cd(base_dir2);
    % Moving into peripheral artery files directory

    brachial = strcat(base_dir2,'artery4-',' ',num2str(i),'')
    % Extract artery 4-1/2/3/4...
    (carotid/radial/brachial/femoral)-Brachial in this example
```

```
    load(brachial); % Load artery onto workspace

    A= A(:,2);

    Y=fft(A); % DFT of peripheral waveform data

      TF=Y./X;
      % Find transfer function according to equation (7.1), See
      Thesis Chapter 7- GTF calculation

    GTF_A_B(:,j)=TF;
    % Redefine GTF name (A_B represents Aorta-Brachial)

    j=j+1; % Increment in counter

end % End of for loop

clc  % clear everything on command window

GTF_A_B=sum(GTF_A_B,2); % Sum of GTFs

GTF_A_B=GTF_A_B/j; % Avergae of GTFs

save('C:\Sample_directory\GTF_A_B.mat','GTF_A_B')
% Save GTF file as mat file in a specific directory to use in
estimating CAPs

%------------------ End of Program -----------------%
```

Matlab program that estimates CAP waveforms from peripheral waveforms using the GTF estimated in the previous program.

```
clear % clears all variables from workspace

clc % clears everything on command window

base_dir='C:Sample_directory\Aorta\';
% Define path of directory containing Ascending Aorta files

base_dir2='C:\Sample_directory\Brachial\';
% Define path of directory containing peripheral pressure
measurement site (carotid/brachial/radial/femoral) files

ECAP=[];
% Create empty array for estimated central aortic pressure (GTF
estimated pressures)

VCAP=[];
```

```
% Create empty array for validated central aortic pressure (model
generated pressures)

maxECAP=[];
% Create empty array for maximum estimated central aortic
pressure values

minECAP=[];
% Create empty array for minimum estimated central aortic
pressure values

meanECAP=[];
% Create empty array for mean estimated central aortic pressure
values

maxVCAP=[];
% Create empty array for maximum validated central aortic
pressure values

minVCAP=[];
% Create empty array for minimum validated central aortic
pressure values

meanVCAP=[];
% Create empty array for mean validated central aortic pressure
values

similarity=[];
% Create empty array for similarity (between ECAP and VCAP)

j=1; % Define value of counter starting value

for i=2:2:194
% Counter of the for loop (remaining half of the database)

    cd(base_dir);
    % Moving into ascending aorta files directory

    aorta = strcat(base_dir,'artery1-',' ',num2str(i),'');
    % Extract artery 1-1/2/3/4... (ascending aorta)- The second
    number i.e. 1/2/3/4 is the definition of case number so
    artery 1-24 means the first artery (ascending aorta) and case
    24


    load(aorta); % Load artery onto workspace

    A= A(:,1);
    % A is the generic name of the mat files for each artery
```

```
VCAP(:,j)=A;
% create an array with incremental VCAPs

cd(base_dir2);
% Moving into peripheral artery files directory


radial = strcat(base_dir2,'artery4-',' ',num2str(i),'');
% Extract artery 4-1/2/3/4...
(carotid/radial/brachial/femoral)-Brachial in this example

load(radial); % Load artery onto workspace

A= A(:,2);

Y=fft(A); % DFT of waveform data

cd 'C:\Sample_directory\GTF_A_B'
% Moving into directory where the GTF is saved as a mat file

load ('GTF_A_B'); % Load GTF onto workspace

GTF_B_A=1./GTF_A_B;
% Find the GTF from peripheral to central direction

ECAP_frequency=Y.*GTF_B_A;
% Multiply GTF with peripheral waveform in the frequency
domain (Example, Brachial data (in frequency) X
GTF_Brachial_aorta)

ECAP_time=ifft(ECAP_frequency);
% Inverse DFT to convert estimated freqeuncy domain waveform
to time domain

ECAP(:,j)= ECAP_time;
% Define the estimated time domain data as ECAP

maxECAP(:,j)=max(ECAP(:,j));
% Find max (systolic) pressure values of ECAP

minECAP(:,j)=min(ECAP(:,j));
% Find min (diastolic) pressure values of ECAP

meanECAP(:,j)=mean(ECAP(:,j));
% Find mean pressure values of ECAP

maxVCAP(:,j)=max(VCAP(:,j));
% Find max (systolic) pressure values of VCAP

minVCAP(:,j)=min(VCAP(:,j));
```

```
    % Find min (diastolic) pressure     values of VCAP

    meanVCAP(:,j)=mean(VCAP(:,j));
    % Find mean pressure values of VCAP


      similarity(:,j)=corr(ECAP(:,j),VCAP(:,j));
      %Find 2-D correlation coefficient between VCAP and ECAP

    j=j+1; % Increment in counter

end % End of for loop


% Transpose all arrays for ease
    similarity=similarity';

    maxECAP=maxECAP';

    minECAP=minECAP';

    meanECAP=meanECAP';

    maxVCAP=maxVCAP';

    minVCAP=minVCAP';

    meanVCAP=meanVCAP';

% Save all files in a directory as matfiles

save('C:\Sample_directory\Similarity.mat','similarity')

save('C:\Sample_directory\maxVCAP.mat','maxVCAP')

save('C:\Sample_directory\meanVCAP.mat','meanVCAP')

save('C:\Sample_directory\minVCAP.mat','minVCAP')

save('C:\Sample_directory\maxECAP.mat','maxECAP')

save('C:\Sample_directory\meanECAP.mat','meanECAP')

save('C:\Sample_directory\minECAP.mat','minECAP')

save('C:\Sample_directory\ECAP.mat','ECAP')

save('C:\Sample_directory\VCAP.mat','VCAP')

%------------------ End of Program -----------------%
```